UNIVERSITY OF
LIVERPOOL

Department of Chemistry

METAL NANOPARTICLES IN AGAROSE HYDROGELS: PREPARATION, CHARACTERISATION AND PROPERTIES

Thesis submitted in accordance with the requirements of the University of Liverpool for the degree of Doctor in Philosophy

by

Erwan Faoucher

Supervisor: Prof. M. Brust

September 2010

Abstract

The preparation of gold nanoparticles has been achieved inside an agarose gel and the nanoparticles and clusters obtained have been characterized. The results show the presence of polydispersed nanoparticles decorating the gel network. This decoration is hierarchical with the primary, secondary and tertiary structural features of the gel presenting single atoms and small clusters, small nanoparticles in the size range of 1 to 4nm and larger nanoparticles respectively. The average size of the larger particles depends on the metal salt concentration in the initial feed solution. Following analogous procedures, silver, platinum, ruthenium and palladium particles have also been obtained.

The electronic properties of the Au-gel composite have been investigated at different particle loading and upon dehydration of the gel, and the existence of dynamic percolation point has been established. The charge transport across the material at these percolation points has been related to a counterbalance between the Brownian motion of the nanoparticles and the de-wetting of the gel. The ohmic behaviour of the composite beyond the percolation point has been also shown. Partial reversibility of the electronic properties of the gel has been observed upon rehydration.

The application of an Ag-gel composite as a recyclable substrate for Surface Enhanced Raman Spectrometry (SERS) has been also explored. The trapping of molecules in addition to the formation of dynamic hotspots upon the dehydration of the gel are unique features of this material. Detection of DDT by SERS is also reported here for the first time. Finally, this substrate was employed for the SERS analysis of molecules that comprise the ligand shell of gold nanoparticles (GNPs). This technique presents a new approach to confirm the functionalisation of GNPs.

Acknowledgement

Firstly, I would like to thank my supervisor Professor Mathias Brust for having accepted me as a PhD student in his group and for the many helpful discussions and explanations on my subject during the last four years. I would also like to express my gratitude to him for having changed my PhD subject as the original one did not start on time.

Secondly, I am grateful for the assistance provided by the many collaborators I have had over the last four years. Thanks to Professor Andrew Bleloch and his team, Dr Kasim Sader, Dr Mhairi Gass and Dr Simon Romani for their help on the microscopy analyses of my samples. I would also like to thank Professor Paul Chalker for the many helpful discussions on the electronic and SERS investigations carried on my samples and for giving me access to his Raman spectroscope. I would also like to express my gratitude to the research group of Professor Luiz-Marzan and more particularly to Dr Ramon Alvarez-Puebla for the collaboration on the SERS study of our gel. I appreciate also the help of Miss Samia Saleemi for providing the functionalized GNPs for the second SERS study. In a more general way, I would like to thank co-workers and collaborators who assisted my research at different levels in the last four years.

Finally, I cannot thank enough my partner, Miss Lisa Scullion, who has been a massive support during my entire PhD and the writing of the thesis. I could have not managed to hand this thesis without her and I cannot wait for the 23rd of October.

Contents

Chapter 1: Introduction

1.1 Nanotechnology

Nanoscience or nanotechnology has been one of the major topics of study in the 21st century so far, even though technically this science dates back to the 5th century BC. For example, the making of steel, painting and even pottery all involved the manipulation of materials at the nanoscale. The strong interest over the last decades in this field originates from key dates and specific individuals. While the concept of nanotechnology was introduced by Richard Feynman in 1959 during a talk entitled "There's plenty of room at the bottom" the term "nanotechnology" was first used in 1974 by Norio Tanigushi[1]. His definition was simply that "nano-technology' mainly consists of the processing of, separation, consolidation, and deformation of materials by one atom or by one molecule". This definition was developed further by Dr. K. Eric Drexler in 1986:[2]. In general, this science can be described as the study of objects or structures which have at least one of their dimensions in the range of 1-100nm[(3)]. The principle is that the properties (mechanical, optical, electrical, etc.) of these structures or objects due to their small size differ from properties of the same material of bulk size. Nanomaterials include fullerenes (tubical, ellipsoidal or spherical molecules composed only of carbon) and nanoparticles of metals, semiconductors, polymers, etc. The applications based on nanotechnology are wide and cover different areas including medicine[4-7], chemistry (for instance in catalysis[8-10]), industry (for example washing powders or cosmetics, Sigma Aldrich with already prepared colloids solutions for research purpose, etc.), energies[11-14] and even in consumer goods (for example aerosols, etc.). In this thesis, nanoparticles of different metals are studied, in particular those of gold and silver. This introduction will present some general information on these materials which is relevant for a proper understanding of our research. The second part of this chapter is dedicated to the investigation of nanoparticles in gels followed by a presentation of the hydrogel used during our research. Finally the outline of this thesis and the methods of characterization are described.

1.2 Gold and silver nanoparticles

A nanoparticle can be defined generally as a small entity with a size between 1 and 100nm which is made of any material. Most of the properties and applications of nanoparticles have been discovered over the second half of the 20th century even though their interesting optical properties, in particular those of gold and silver particles, were already applied to the decoration of ornamental structures long before. Colloidal gold was used to make ruby glass (the famous example is the Lycurgus Cup from the 5th century A.D.[95] which appears ruby red when light shines through it, this is due to more scattering of blue light than the red; it appears green under direct light also due to the presence of gold/silver alloys) and for colouring ceramics during ancient times, silver nanoparticles were employed during the middle ages (5th to 14th century A.D.)[15] and the renaissance (14th to 17th A.D.) to give a metallic, glittery aspect to pottery. Silver nanoparticles were obtained by mixing vinegar, ochre and clay then heating the mixture at 600°C to form a metallic film[15]. These first applications show how the quest for beauty yields important discoveries even though in this case the complex principle behind the creation of these nanoparticles was not understood at the time they were made.

1.3 Nanoparticle formation

The formation of nanoparticles can be described as a three step process consisting of nucleation, growth and stabilisation[16]. The nucleation step comprises the coming together of a few atoms or ions to form a small nucleus of a cluster, which continues to grow steadily during the growth phase[17]. This growth is decelerated by the adsorption of stabilizing agents to the surface of the particle. Monodispersed nanoparticles can therefore be obtained by a burst of nucleation followed by a slow growth is implemented.

1.4 Colloidal stability

Fortunately for the archaeologists who found the different ornaments made with nanoparticles, the stabilization of the clusters were provided by the glass or glaze surrounding them. The clusters are trapped in the highly organised structures of their respective matrices providing excellent stabilisation. A weakness of this stabilisation strategy is the poor accessibility of the surface of the nanoparticles for molecular interaction. Therefore, other stabilisation methods have been developed that allow for the preparation of stable colloids in solution. These are discussed below.

1.4.1 Electrostatic stabilization

The surfaces of silver and gold nanoparticles can interact with anionic species such as citrate, acrylate and chloride ions, which adsorb to the surface of the particles rendering colloids negative. This charge is compensated in the electrochemical double layer formed around the particles in electrolyte solutions[19,20]. The attractive Van der Waals interactions will be counteracted by the repulsive interactions between the charged nanoparticles. The mechanism of this stabilization method has been described though the DLVO theory so-called after the researchers who found it (Dejaguin, Landau[21] and Verwey and Overbeek[22]). It is reported that the total energy involved in this electrostatic mechanism can be related to the interparticle distance by:

$$V_T = V_A - V_R = 2\pi \in_0 \in_\tau r\varphi_0^2 . e^{-kD} - \frac{Ar}{12D}$$

Where V_T is the total potential energy function, V_A is the energy from the Van der Waals attractions forces, V_R is the energy from the electrostatic repulsive forces, $\in_0$ is the permittivity of the vacuum, $\in_\tau$ is the permittivity of the medium, φ_0 the surface potential, k^{-1} the double layer thickness, r the particle radius and D the inter-particle distance. Knowing that the Van der Waals interaction is inversely proportional to r^2 and the evolution of the repulsion forces are constrained to be e^{-r}, the difference between stable and unstable particles can described by the graphs presented in Figure1.1[23].

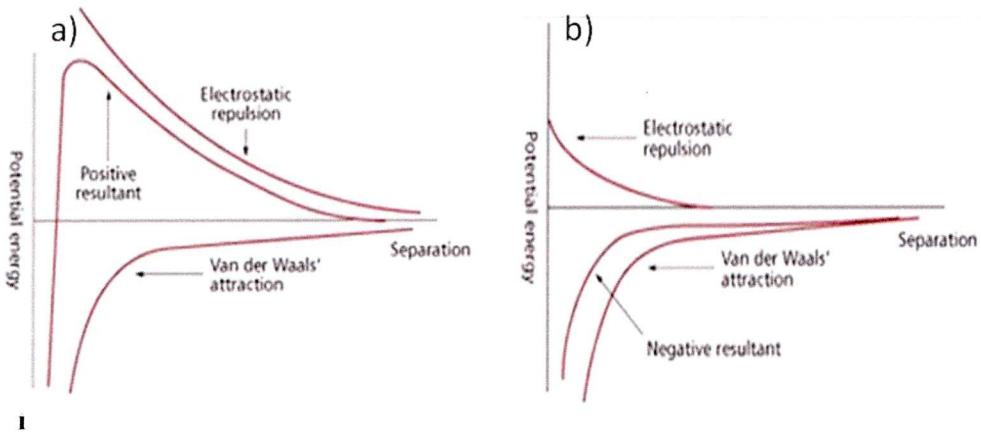

gure 1.1 Potential energy curves for stable 1.1(a) and unstable 1.1(b) dispersions. Reproduced from ref. 23.

However, the screening of the electrostatic repulsion with an increase of the medium ionic strength will results in nanoparticle aggregation. Likewise, the replacement of ionic charge from the particle surface will have the same net effect.

1.4.2 Example

The most commonly used application of electrostatic stabilization is the Turkevich[16]/Frens[24] method. A boiling aqueous solution of $HAuCl_4$ is mixed quickly with a hot solution of sodium citrate and stirred vigorously. The citrate molecules act as both stabilizing and reducing agent[25,26]. The addition of the sodium citrate produces a change in the colour of the solution from yellow to ruby red. The particles obtained are monodispersed and can be prepared in the size range from 5 to 30 nm. Above this size, the particles start to exhibit different shapes and the size dispersion becomes less uniform. Also, this method only yields relatively low concentrations of nanoparticles (around 2nM). Even though this method presents some shortcomings, it is often used when the nanoparticle surface is to be modified at a subsequent stage[18,27-28] (addition of functionality).

1.4.3 Steric stabilisation

The second stabilisation method, involves the absorption of surfactants and sometimes polymers to the surface of the nanoparticles[29]. Most of these molecules have a terminal-functionality which can bind chemically on the surface of the nanoparticles[3]. In this case, the repulsion force preventing the system from aggregation is comprised of entropic and enthalpic phenomena. The entropic repulsion emanates from the incapacity of the stabilizing molecules to desorb or migrate when two nanoparticles approach each other. The enthalpic repulsion is provided by an osmotic effect (diffusion of the solvent) appearing as the concentration of the surfactant or polymer chains increases in some localized areas between approaching particles.

1.4.4 Example

A popular method using steric stabilisation is the Brust/Schiffrin method[30] published in 1994 following the study by Giersig and Mulvaney[31] on the stabilization of gold nanoparticles with alkanethiols. Basically, $AuCl_4^-$ is transferred from an aqueous phase to toluene using tetraoctylammonium bromide as phase-transfer reagent. The system is then reduced by sodium borohydride ($NaBH_4$) in the presence of an alkanethiol. The monolayer protected clusters (MPCs) obtained are extremely small and moderately polydispersed (range of 1.5 to 5.2nm). Nowadays, these MCPs are still considered as the most stable clusters and intensive research has been focused on the subject[3, 32-35] following the method described above.

It is also possible to combine the two stabilization methods. The use of both long chain surfactants[36] and charged species[37] results in steric and electrostatic stabilisation.

1.4.5 Stabilisation in gels and hydrogels

A gel can be described as a material which behaves like a solid but is mostly composed of liquid. This behaviour emanates from the cross-linked three dimensional network (made of polymeric chains) which crosses through the liquid medium after gelification of the sample. When the

polymeric chains are hydrophilic and the liquid phase is water the gel obtained is called a hydrogel.

The use of polymers, hydrogels and microgels as matrices for the formation of nanoparticles has been a subject of much interest in the past ten years, the most important motivation being that these new materials could combine the chemical accessibility of a solvent and the stabilization properties of solid matrices. The combination of the nanoparticles with these materials presents in itself the creation of a new type of composites having interesting physical and chemical properties for different applications such as biosensor[38] , optical sensor[38-40], catalysis[41,42], electronic devices[43-48] (with sometimes switchable properties[49-51] and antibacterial system[52-56]. This field of science, called matrix chemistry by Gomez-Romero *et al.*[57], has a wide range of uses due to the diversity of the nature of such composites. For example, with a different matrix, the nanoparticles can be synthesized inside the pores or attached onto the network of the polymer used. They are respectively called nanocasting and nanocoating[58]. The final result will be the inverse replica of the gel structure for the first case and the hollow replica in the latter (Figure 1.2).

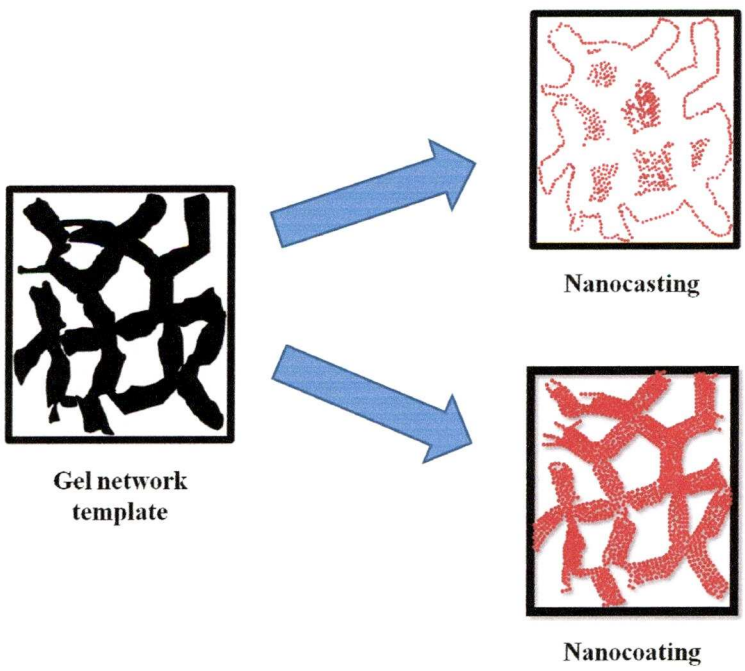

Figure 1.2 Principle of nanocoating and nanocasting developed by Caruso *and al.*[58]

This could also be affected by the synthesis method used to create the nanoparticles. For instance, if nanoparticles are synthesized before being added to the matrix[59,60], the nanoparticles will be either in the gel pores or on the top of the network by electrostatic or hydrogen bonding[58]. If the nanoparticles are generated *in-situ*, they interact and bind to the molecules forming the polymer gel network or become trapped between the cross-linkage of the gel chains (so-called nanoreactor[61]). In fact, the *in-situ* preparation of the nanoparticles is possible inside most polymer gels due to three key parameters: (i) the hydrogel network can stabilize sterically the particles and so allow the synthesis of very small and stable nanoparticles,(ii) some hydrogels can act as the stabilizing and as the reducing agent depending on their functionalities[60] and finally (iii) the morphology of the nanoparticles can be controlled through the polymer concentration and the temperature of the experiment (influence of the pore size as well as nanoreactor size[61]).

The choice of the polymer gel used is also an important factor that influences the properties of the newly created composite. The gels can be a dense polymer[62,63] or a porous material[60,61,64]. While the first category of matrices will provide smaller nanoreactor sites the second will facilitate the diffusion of the metal salt through the matrix and so its impregnation in the gel structure. The polymer gels can also be synthetic[65-69] or natural[54,68,70]. The advantage of using the synthetic polymers is the possibility of integration of any functional groups to stabilize the nanoparticles during the synthesis step of the molecule. Additionally, the architecture of the molecule can be altered in order to obtain the desired pattern. The drawback to using these kinds of gel is that the synthesis of the network structure can be time consuming and we are generally obliged to add cross-linkers during the reaction in order to obtain a three-dimensional template[41,61]. On the other hand the use of natural polymers does not offer a wide variety of functional groups that may increase strong binding to the gold. However, they are inexpensive, environmentally friendly and biocompatible[70].

In the category of natural polymer gels, polysaccharides are very often used with dextran[71], cellulose[54], agar[70] and agarose[42,60,72] being the most common. In the majority of these studies, the nanoparticles are synthesized in-situ by addition of the metal salt solution to the powder gel, the hydrogel acts as the stabilizing agent and reducing agent. All studies are in agreement with the formation of polydispersed nanoparticles nanocoating the hydrogel network with an average size of 10 to 20nm. On the other hand, there is a discrepancy in the theory of the nanoparticles formation between the two studies on the synthesis of nanoparticles by soaking[70,72] (immersion of hydrogel solid matrix in a metal salt solution). In the first study, Ayyad *et al.* claim that the nanoparticles formed follow a nanocasting decoration of the template while the second study shows a nanocoating decoration of the network. The difference in the nature of the reducing agent (agar and sodium borohydride) and in the nature of the matrices cannot explain this contradiction. Indeed, the agar molecule is composed of an agarose and an agaropectin monomer. The structure of these two monomers is very similar, the differences being that the agaropectin is slightly sulphated and branched.

In this thesis, the concept of nanocoating (by soaking in metal salt) of the agarose structure by gold and silver nanoparticles is developed and applications of such kind of material are presented. In order to fully understand the concept proposed here, the agarose compound and hydrogel structure are discussed in the following part of the chapter.

1.5 Agarose

1.5.1 Molecule and strand

The agarose hydrogel was first obtained through an acetylation method of the polysaccharide agar by Araki[73] in 1956. Later, this scientist and others determined that this neutral polymer was composed of agarobiose repeating disaccharide units alternating with 1, 3-linked-β-D-galactopyranose and 1, 4-linked-3, 6-anhydro-α-L-galactopyranose (Figure 1.3).

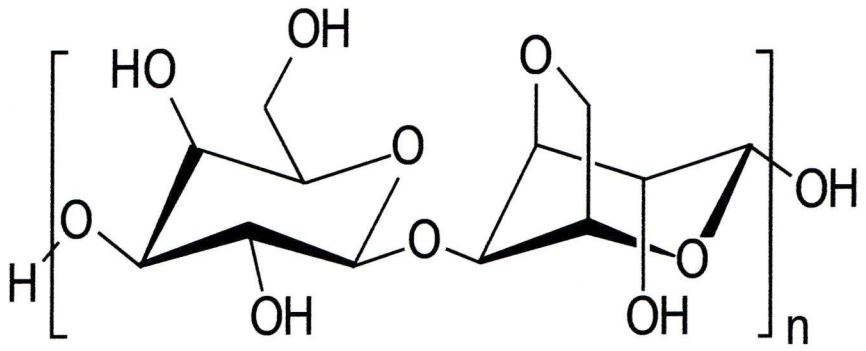

Figure 1.3 Structure of the agarose molecule.

It appears in a powder form and the addition of water followed by an increase of the temperature of the mixed solution provides a complete dissolution of the powder. A cooling of the mixed solution results in a gelation of the sample. The network of macromolecules formed entraps the dispersion medium and thus leads to the formation of a hydrogel. While the composition of the gel approaches that of the pure liquid its mechanical properties correspond to those of a solid. After gelation, the hydrogel retains the shape of the vessel used during the processing due to its elastic properties. At the microscale, the network is made of aggregations of three-folded double helices. Previous work described qualitatively and quantitatively these double helices (Figure 1.4). The helices are left-handed and are related by a 0.95nm translation along the helix axis. The interior cavity between the helices is 0.45nm. Each chain of the double helices develops a left handed three fold helix with a pitch of 1.9nm and contains molecules of agarose having a width between 1and 1.6nm[74] .

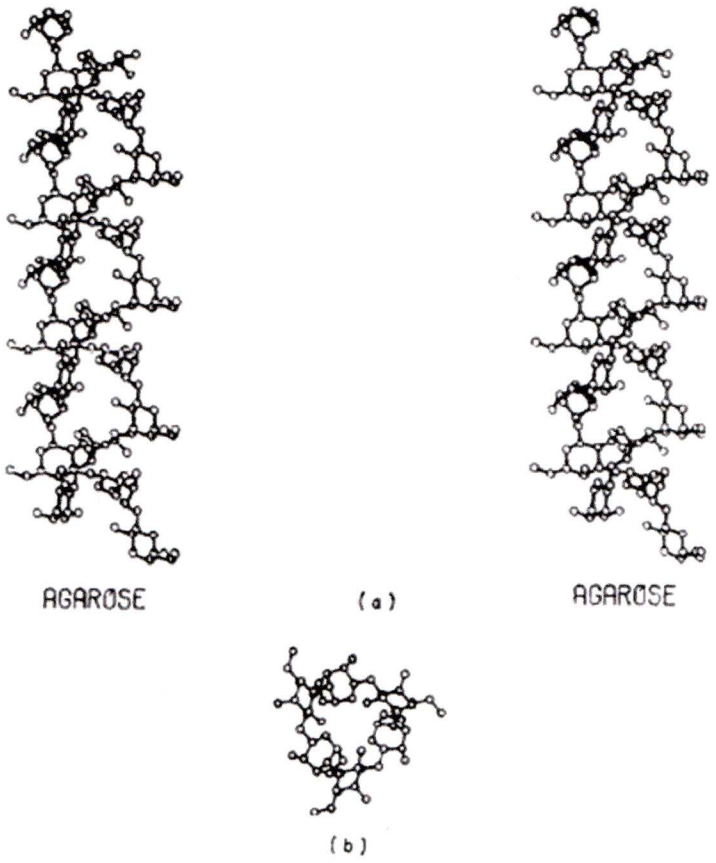

Figure 1.4: (a) Structure of the agarose double helix in XY plane. (b) The agarose double helix along the Z-axis. Reproduced from ref.74

As reported previously by Arnott *et al.*[74], the O(2) of galactose and the O(5) of 3,6-anhydrogalactose on each strand of the helix are situated inside the cavity and these oxygen atoms are frequently engaged in hydrogen bonding. It is stipulated that a water molecule could be positioned in the cavity at a distance of 0.27nm from each oxygen atom. To explain the important stability of the chains of the network, Arnott *et al.* suggest that three or four hydroxyl group point outwards for hydrogen bonding with the solvent system and/or neighbouring helices.

Finally a perfectly pure agarose gel does not display any defects through its entire network. Unfortunately it is impossible to obtain a completely pure agarose gel. Residues of sulphate are always present in small quantities

(0.1%<). This results in kinks in some localised areas of the network which prevent the formation of double helices[75,76].

1.5.2 Gelation

As described by San Biaggo *et al*[77]when the mixed and homogeneous solution of agarose/water is cooled down, a thermodynamic instability results in the appearance of rich-polymer regions (still free chains of polymer) and rich solvent regions solution state). This phenomenon occurs during the solution state. This effect is called spinodal demixing and has been reported in different studies of gelation[78,79]. After a period of time the number of free polymers decreases which corresponds to the transition from the single coil to the double helix system. These double helices aggregate, then branch out to each other (called the percolation point) and cross link. In addition, Leone *et al.*[79] reported that the final structure of the hydrogel resembles this form in solution during the spinodal demixing phenomenon.

1.5.3 Fractal structure

This structural comparison reveals the erratic nature of the agarose hydrogel network. This lack of homogeneity in the matrix has motivated much research on diffusion of nanoparticles or complexes[80,81] in this biopolymer for applications such as electrophoresis. Fortunately, several groups have studied the evolution of the agarose pattern under the influence of different parameters such as temperature quenching and concentration of the gel in the matrix via SANS[82-86]. All, these studies define the gel network as "fractal" which corresponds to the presence of self similarities at different scales of the growing process of the gel and can be defined by:

$$M = r^{-d_f}$$

Where M defines the mass of objects within the radius r and d_f the fractal dimension of the sytem[87]. This fractal dimension corresponds to a numerical measure which is preserved across the scale.

Manno *et al.*[83] have pointed out that the rate of decrease in temperature during the quenching does not affect the fractal dimension of the network and that this value is identical at the two different scales of the gel (nanoscale for the coils and microscale for the fibers made of double helix aggregates). Krueger *et al.*[82] on the other hand show that at higher gel concentration the fractal dimension at the microscale is around 2.1 and barely dependant of the gel concentration. The lack of dependence on gel concentration has been also validated by the study of another gel[88].

1.6 Thesis outline

The study reported here presents the *in-situ* preparation of network-forming metal nanoparticles. We demonstrate the stabilisation of different nanoparticles by a gel, which as a matrix material combines the optical and stabilisation characteristics of glass with the chemical accessibility of a solvent.

Chapter 2 describes the synthesis and characterization of gold nanoparticles inside the hydrogel. The detection of the presence of the gold nanoparticles in the matrix is first characterized by uv-visible spectroscopy, X-ray diffraction and MALDI-TOF (section 2.3.1) followed by a discussion on the best sample preparation method to visualize these nanoparticles by Transmission Electron Microscopy (TEM) (section 2.3.2). A structural model of the matrix-nanoparticles system is then proposed according to the Scanning Transmission Electron microscopy images obtained (section 2.3.4). Finally, the preparative method is applied to different metals including silver, platinum, palladium and ruthenium (section 2.3.5). A comparison between the results obtained with different metals concludes the chapter.

Chapter 3 focuses on the tunability of the electronic properties of the Au-gel introduced in the previous chapter. A theoretical estimation of the electronic properties of the gel loaded with gold nanoparticles is achieved based on the structure the gel network (section 3.2). The electronic properties of the Au-gel and their dependency on the concentration of gold and dehydration of the matrix are then investigated (section 3.4.1). The evolution of the

percolation point, the charge transport and the electronic behaviour of the gel (whether or not it adheres to ohms law) are also inspected (section 3.4.2). Finally, an electron microscopic characterisation of the Au-gel at and above the percolation point is carried out in order to corroborate the quantitative data obtained previously in this chapter. In conclusion of the chapter, the comparison between the results obtained with theory is discussed.

Chapter 4 introduces the use of an agarose hydrogel loaded with silver nanoparticles as a substrate for the detection of different molecules (by SERS). The chapter begins with a description the concept of SERS (section 4.2). This section, presenting the influence of several parameters on the quality and the intensity of the SERS signal, gives important information on the general interest of using our material as a substrate for Raman spectroscopy. The experimental results are then discussed with a presentation of the dynamic hotspot (section 4.3.3.3), the molecular trapping (section 4.3.3.4) and the reusability of the substrate (section 4.3.3.5).

Chapter 5 focuses on the functionalisation of gold nanoparticles and the subsequent analysis of their ligand shells by SERS. This is first carried out by different methods of characterization (section 5.4.1) and then by Raman spectroscopy at different excitation wavelengths (section5.4.4). A discussion on the quality of the results is proposed as a conclusion of the chapter.

Finally, chapter 6 presents a general conclusion of the work presented in this thesis. The results are discussed and future improvements are proposed (section 6.1 and 6.2). Future work and applications of this gel are also discussed in this chapter (section 6.3).

1.7 Characterization methods

Here the main experimental techniques used are briefly introduced specifically in view of their importance for their importance for the characterisation of nanoparticles.

1.7.1 Uv-visible spectroscopy

Nanoparticle solutions can exhibit different colour depending on the size and the shape of the colloids. The colouration of the solution corresponds to the collective coherent oscillation of conduction band electrons induced by electromagnetic radiation from the light (in the UV-visible range here). The colloids can absorb this light when its frequency is in resonance with the plasma oscillations at their surfaces. This phenomenon can be characterised and quantified by Uv-visible spectroscopy. The principle of this method is to excite the absorbing material with a light beam, the wavelength of which is scanned across in the Uv-visible range using a monochromator. The light will not interact with the solution in most of this range and therefore will be scattered but will absorb at precise wavelength bands. This absorption corresponds to the Surface Plasmon Resonance of the system studied. The spectrum obtained, related to the nature of the clusters, can provide important information such as their concentration in solutions[90], their average size[89] and size dispersion (width of the band: qualitative measurement), an estimation of their stability (wavelength for which the absorbance is maximum) and an idea of their shapes (wavelength for which the absorbance is maximum and the amount of distinctive absorption band[91].

1.7.2 X-Ray powder diffraction

This method provides data on the crystalline structure of the system studied. Basically, an X-ray beam strikes the sample which will then diffract it. The pattern of spots obtained through the detector relates to the position of the atoms in the lattice forming the crystals of the sample. The intensity of the spots and the angles between them are checked by the rotation of the sample (so-called X-ray scans). Each X-ray signal detected corresponds to a reflection (called Bragg reflection) from successive planes of the crystal and is defined by Bragg's law:

$$2dsin\theta = n\lambda$$

Where d is the spacing between planes, θ is the angle between the X-ray beam and the plane, n is an integer (usually equal to 1) and λ is the wavelength of the X-ray.

In the case of the nanoparticles, the signal can give information of the arrangement of the atoms and an estimation of the average size of the cluster (monodispersed) following the Scherrer equation[92] (will be presented in Chapter 2).

1.7.3 Mass spectrometry

This technique gives the exact mass of the nanoparticles present on the sample studied by providing a mass/charge ratio of the charged particles. After vaporisation of the sample, the gas obtained is ionized with positive and negatives charges. For this many different methods are available and have to be chosen according to the nature of the sample. The charged clusters are then accelerated in an electric field and deviated by a magnetic field. The deviation of each charged particle is related to their respective mass (light fragments will be deviated more than heavy fragments).These data are presented in spectrum form with each peak corresponding to the isotopes of the system in relation to their mass/charge ratio ($^{m}/_{z}$). However, in the clusters case, the fragmentation of the core does not provide the overall mass. In order to keep the core of the nanoparticles/clusters intact Matrix Assisted Laser Desorption/Ionized (MALDI MS) can be employed. In this technique, the sample is first embedded in a polymer to protect the system from a direct interaction with the laser beam and to facilitate the vaporization and ionization. The nature of these polymers can differ providing their molecular weight is small (for the vaporization step), and large enough to prevent evaporation before the measurement. In addition their acidic character provides an ionization of the compound studied and their absorbance at the uv-light encourage the absorption of the laser radiation. The protonation or deprotonation is then applied to the entire system polymer/metal NPs-gel (in our case) and allows the core of the clusters to remain intact.

1.7.4 Electron microscopy

1.7.4.1 TEM

This popular technique is one of the most often used methods to characterize the size of metal nanoparticles. Briefly, a tungsten filament producing an electron flux (by connection to a high voltage source) is focused into a thin beam by a magnetic condenser lensing system. The beam hits the sample and the electrons transmitted through the specimen (which has to be between 20 and 100nm in order to obtain sufficient intensity from the beam transmitted to be detected) are projected via a system of projector lenses on a fluorescent screen. The image obtained can be magnified by reducing the distance between the sample and the objective lenses. The shadow areas on the image correspond to the spots on the sample where electrons have been absorbed and lighter areas to the regions where most of the electrons have been transmitted. The resolution r of this kind of microscope is defined by:

$$r = 0.61\ x\ \lambda\ x\ \mu(\alpha)$$

Where λ is the wavelength of the incident beam and μ the index of the sample medium, α is the semi-angle of the microscope aperture which corresponds to a thin disc that allows restriction of the beam and is situated after the condensing and objective lensing stages)[93].

Knowing that electron wavelengths are 10^4 smaller than the photon wavelength this equation explains the high resolution obtained with this technique compared to optical microscopy. Clusters made of few atoms can be detected via the use of this microscope.

1.7.4.2 SEM

Scanning transmission electron microscopy is governed by the same basic principle as the TEM presented above. An electron gun provides a monochromatic electron stream which is focused into a thin electron beam by several condenser lenses. The difference is that a set of scanning coils moves the focused beams onto different areas of the sample surface. When

an electron hits a spot of the sample a secondary electron is emitted (or scattered). The secondary electrons emitted from each of the sample are then counted through a detector and amplified. An image is then created based on the amount of electrons detected on each spot of the samples. Nanoparticles as small as 1-2 nm can be detected through this method (due to the beam energy of the electron gun).

1.7.4.3 STEM

Scanning Transmission Electron Microscopy is a type of TEM. This method also involves the analysis of electrons transmitted through the specimen. The differences between STEM and TEM are that in STEM the beam is focused before hitting the specimen to facilitate the detection of the scattered electrons or transmitted through the sample, also the beam scans the entire surface of the samples moving row by row (spot by spot). These changes allow analysis of the sample in the transmission mode (bright field) or scattering mode (dark field) in addition to an improved resolution of the diffracted or scattered electrons and therefore of the image obtained. If the objective aperture (located in the diffraction plane) is replaced by a high annular angle detector many more electrons can be detected. The annular dark field image obtained at very high angles is based on the incoherently scattered electrons which provides atomic resolution of the samples due to the Z-contrast (contrast defined by the number of atoms in the sample)[94].

1.7.4 Raman spectroscopy

When polarised light excites a RAMAN active molecule (change of polarisability or distortion of the electron cloud during a vibration), the molecule reaches a very short-lived virtual exited state (10^{-14}s). When the molecule relaxes, it emits a photon, most of the time at the the same wavelength as the excitation source (elastic scattering). A small proportion of photons (1 per million) show frequency shifts (inelastic or Raman scattering). These correspond in energy to changes in vibrational states of the molecule, i.e. to transitions in the infrared region. After the filtration of

the elastic scattering (Rayleigh scattering), the Raman scattered light can be detected and analysed. Raman shifts can be either to lower (Stokes) or to higher energy (anti-Stokes) depending of the vibrational state of the molecule before and after the scattering event. Since the majority of the molecules are in their vibrational ground state under normal conditions the Stokes bands are predominant (Fig1.5). Vibrations are Raman active if they are concurrent with a change in polarisability of the molecule. In comparison to infrared spectroscopy, Raman spectroscopy can detect vibrations that are not associated with permanent dipole moments and is thus useful for the analysis of non-polar molecules. It is also useful for the characterisation of vibrational bands at low frequency (for example stretching frequency of compounds containing heavy elements or particularly weakly chemical bonds).

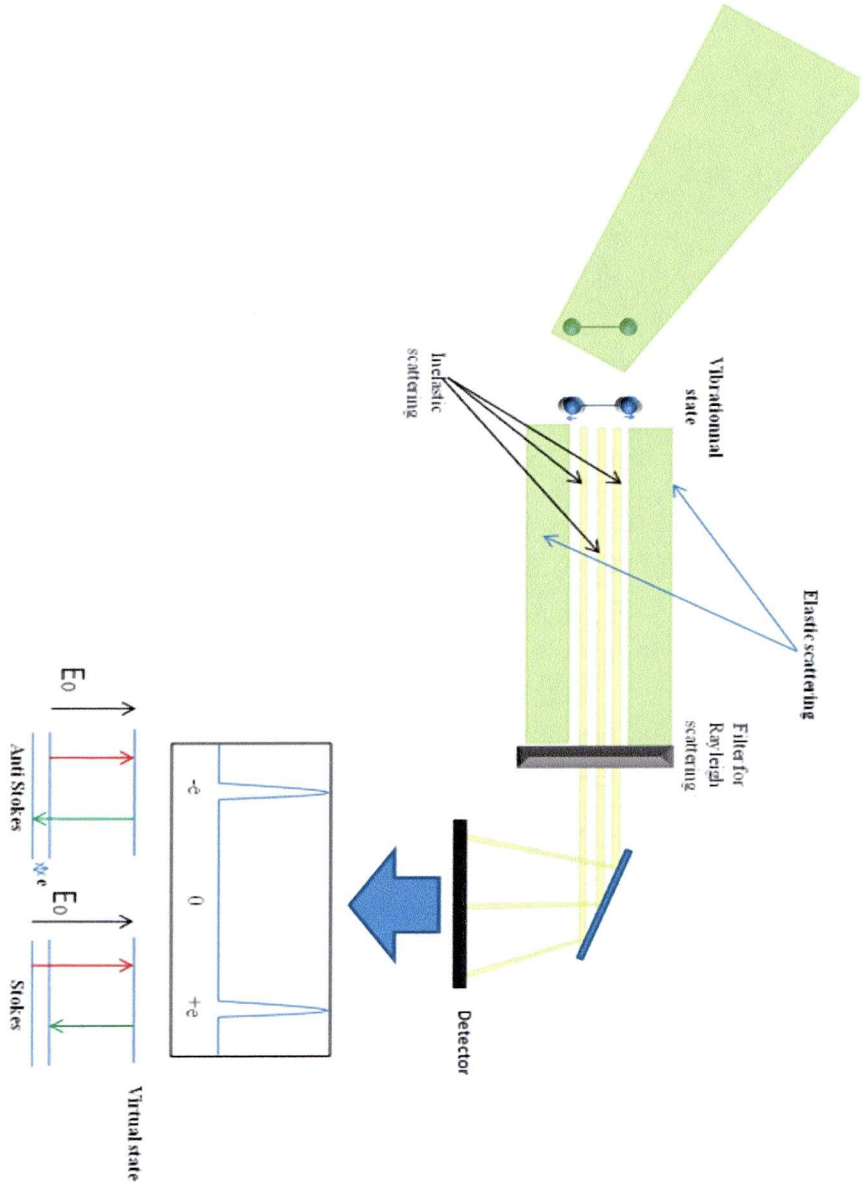

Figure 1.5 Principle of Raman spectroscopy: A laser beam hits the sample. The electron cloud of the molecule contained in the sample will start to stretch. The relaxation of the molecule after the stretching will involves the emission of photons at a different frequency for the photons provides by the laser beam. The difference is analysed through a detector. The filtration of the laser beams scattered provides specific information on the vibrational state

References

1. N. Taniguchi, *Proc. Intl. Conf. Prod. London, Part II.* British Society of Precision Engineering,**1974.**

2. E.Drexler, (1991). "Nanosystems: Molecular Machinery, Manufacturing, and Computation, MIT PhD thesis". New York: Wiley, **1991**.

3. M. C. Daniel, D. Astruc, *Chemical Reviews* **2004**, *104*, 293.

4. S. M. Moghimi, A. C. Hunter, J. C. Murray, *Pharmacological Reviews* **2001**, *53*, 283.

5. P. K. Jain, I. H. El-Sayed, M. A. El-Sayed, *Nano Today* **2007**, *2*, 18.

6. J. F. Hainfeld, D. N. Slatkin, H. M. Smilowitz, *Physics in Medicine and Biology* **2004**, *49*, N309.

7. P. Nativo, I. A. Prior, M. Brust, *ACS Nano* **2008**, *2*, 1639.

8. M. Q. Zhao, R. M. Crooks, *Angewandte Chemie-International Edition* **1999**, *38*, 364.

9. M. Haruta, M. Date, *Applied Catalysis a-General* **2001**, *222*, 427.

10. M. Haruta, *Cattech* **2002**, *6*, 102.

11. J. A. He, R. Mosurkal, L. A. Samuelson, L. Li, J. Kumar, *Langmuir* **2003**, *19*, 2169.

12. W. J. E. Beek, M. M. Wienk, R. A. J. Janssen, *Advanced Materials* **2004**, *16*, 1009.

13. Z. L. Liu, X. Y. Ling, X. D. Su, J. Y. Lee, *Journal of Physical Chemistry B* **2004**, *108*, 8234.

14. Z. L. Liu, L. M. Gan, L. Hong, W. X. Chen, J. Y. Lee, *Journal of Power Sources* **2005**, *139*, 73.

15. T. Pradell, J. Molera, A. D. Smith, M. S Tite, *Journal of Archaeological Sciences* **2008**, 35,1201-1215.

16. J. Turkevich, P. C. Stevenson *et al. Discussions of the Faraday Society* **1951**, 11 55.

17. B. K. Teo, H. Zhang, X. B. Shi, *Journal of the American Chemical Society* **1990**, *112*, 8552.

18. M. A. Hayat, *Colloidal Gold Vol. 1. Principles Methods and Applications* **1989**.

19. M. K. Chow, C. F. Zukoski, *Journal of Colloid and Interface Science* **1994**, *165*, 97.

20. I. Hussain, M. Brust, A. J. Papworth, A. I. Cooper, *Langmuir* **2003**, *19*, 4831.

21. B. V. Derjaguin and L. Landau, *Acta Physico chemica URSS* **1941**, 14, 633.

22. E. J. W. Verwey and J. Th. G Overbeek "Theory of the stability of lyophobic colloids." **1948**, Elsevier, Amsterdam

23. M. Garvey, (February 2003). Chemistry World.

24. G. Frens, *Nature-Physical Science* **1973**, *241*, 20.

25. J. Turkevich, *Gold Bulletin* **1985**, 18 (3), 86-91.

26. J. Turkevich,(1985) "Colloidal gold Part II: colour, coagulation, adhesion, alloying and catalytic properties." Gold Bulletin **18** (4): 125-131.

27. S. Gomez, K. Philippot, V. Colliere, B. Chaudret, F. Senocq, P. Lecante, *Chemical Communications* **2000**, 1945.

28. W. W. Weare, S. M. Reed, M. G. Warner, J. E. Hutchison, *Journal of the American Chemical Society* **2000**, *122*, 12890.

29. D. H. Napper, *Polymeric stabilization of colloidal dispersions*, Academic Press, London . New York, **1983**.

30. M. Brust, M. Walker, D. Bethell, D. J. Schiffrin, R. Whyman, *Journal of the Chemical Society-Chemical Communications* **1994**, 801.

31. M. Giersig, P. Mulvaney, *Langmuir* **1993**, *9*, 3408.

32. A. Ulman, *Chemical Reviews* **1996**, *96*, 1533.

33. C. B. Murray, C. R. Kagan, M. G. Bawendi, *Annual Review of Materials Science* **2000**, *30*, 545.

34. A. C. Templeton, M. P. Wuelfing, R. W. Murray, *Accounts of Chemical Research* **2000**, *33*, 27.

35. J. C. Love, L. A. Estroff, J. K. Kriebel, R. G. Nuzzo, G. M. Whitesides, *Chemical Reviews* **2005**, *105*, 1103.

36. J. D. Aiken, R. G. Finke, *Journal of Molecular Catalysis a-Chemical* **1999**, *145*, 1.

37. K. Esumi, S. Sarashina, T. Yoshimura, *Langmuir* **2004**, *20*, 5189.

38. P. Aldeanueva-Potel, E. Faoucher, R. A. Alvarez-Puebla, L. M. Liz-Marzan, M. Brust, *Analytical Chemistry* **2009**, *81*, 9233.

39. T. Endo, R. Ikeda, Y. Yanagida, T. Hatsuzawa, *Analytica Chimica Acta* **2008**, *611*, 205.

40. I. Tokarev, I. Tokareva, S. Minko, *Advanced Materials* **2008**, *20*, 2730.

41. D. G. Shchukin, J. H. Schattka, M. Antonietti, R. A. Caruso, *Journal of Physical Chemistry B* **2003**, *107*, 952.

42. X. D. Wang, D. R. G. Mitchell, K. Prince, A. J. Atanacio, R. A. Caruso, *Chemistry of Materials* **2008**, *20*, 3917.

43. A. Wakabayashi, Y. Sasakawa, T. Dobashi, T. Yamamoto, *Langmuir* **2007**, *23*, 7990.

44. S. H. Ko, I. Park, H. Pan, N. Misra, M. S. Rogers, C. P. Grigoropoulos, A. P. Pisano, *Applied Physics Letters* **2008**, *92*.

45. X. N. Xie, Y. L. Xie, X. Y. Gao, C. H. Sow, A. T. S. Wee, *Advanced Materials* **2009**, *21*, 3016.

46. A. Garai, S. Chatterjee, A. K. Nandi, *Polymer Engineering and Science* **2010**, *50*, 446.

47. B. K. Jena, C. R. Raj, *Talanta* **2010**, *80*, 1653.

48. X. N. Xie, Y. L. Zhong, M. S. Dhoni, Y. L. Xie, K. P. Loh, C. H. Sow, W. Ji, A. T. S. Wee, *Journal of Applied Physics* **2010**, *107*.

49. L. Sheeney-Haj-Ichia, G. Sharabi, I. Willner, *Advanced Functional Materials* **2002**, *12*, 27.

50. M. Ikeda, N. Tanifuji, H. Yamaguchi, M. Irie, K. Matsuda, *Chemical Communications* **2007**, 1355.

51. K. Matsuda, H. Yamaguchi, T. Sakano, M. Ikeda, N. Tanifuji, M. Irie, *Journal of Physical Chemistry C* **2008**, *112*, 17005.

52. V. Thomas, M. M. Yallapu, B. Sreedhar, S. K. Bajpai, *Journal of Colloid and Interface Science* **2007**, *315*, 389.

53. P. S. K. Murthy, Y. M. Mohan, K. Varaprasad, B. Sreedhar, K. M. Raju, *Journal of Colloid and Interface Science* **2008**, *318*, 217.

54. A. Travan, C. Pelillo, I. Donati, E. Marsich, M. Benincasa, T. Scarpa, S. Semeraro, G. Turco, R. Gennaro, S. Paoletti, *Biomacromolecules* **2009**, *10*, 1429.

55. K. Vimala, K. S. Sivudu, Y. M. Mohan, B. Sreedhar, K. M. Raju, *Carbohydrate Polymers* **2009**, *75*, 463.

56. Y. M. Mohan, K. Vimala, V. Thomas, K. Varaprasad, B. Sreedhar, S. K. Bajpai, K. M. Raju, *Journal of Colloid and Interface Science* **2010**, *342*, 73.

57. P. Gomez-Romero, *Advanced Materials* **2001**, *13*, 163.

58. R. A. Caruso, in *Colloid Chemistry 1, Vol. 226*, Springer-Verlag Berlin, Berlin, **2003**, pp. 91.

59. M. Yamada, A. Kuzume, M. Kurihara, K. Kubo, H. Nishihara, *Chemical Communications* **2001**, 2476.

60. X. D. Wang, C. E. Egan, M. F. Zhou, K. Prince, D. R. G. Mitchell, R. A. Caruso, *Chemical Communications* **2007**, 3060.

61. Y. M. Mohan, K. Lee, T. Premkumar, K. E. Geckeler, *Polymer* **2007**, *48*, 158.

62. R. D. Deshmukh, R. J. Composto, *Chemistry of Materials* **2007**, *19*, 745.

63. N. Singh, P. K. Khanna, *Materials Chemistry and Physics* **2007**, *104*, 367.

64. V. Kattumuri, M. Chandrasekhar, S. Guha, K. Raghuraman, K. V. Katti, K. Ghosh, R. J. Patel, *Applied Physics Letters* **2006**, *88*.

65. M. Tanaka, R. Fujita, H. Nishide, *Polymer* **2007**, *48*, 5884.

66. H. Basit, A. Pal, S. Sen, S. Bhattacharya, *Chemistry-a European Journal* **2008**, *14*, 6534.

67. C. R. Hansen, F. Westerlund, K. Moth-Poulsen, R. Ravindranath, S. Valiyaveettil, T. Bjornholm, *Langmuir* **2008**, *24*, 3905.

68. V. Thomas, M. Namdeo, Y. M. Mohan, S. K. Bajpai, M. Bajpai, *Journal of Macromolecular Science Part a-Pure and Applied Chemistry* **2008**, *45*, 107.

69. L. M. Guiney, A. D. Agnello, J. C. Thomas, K. Takatori, N. T. Flynn, *Colloid and Polymer Science* **2009**, *287*, 601.

70. O. Ayyad, D. Munoz-Rojas, J. Oro-Sole, P. Gomez-Romero, *Journal of Nanoparticle Research* **2010**, *12*, 337.

71. L. LaConte, N. Nitin, G. Bao, *Materials Today* **2005**, *8*, 32.

72. E. Faoucher, P. Nativo, K. Black, J. B. Claridge, M. Gass, S. Romani, A. L. Bleloch, M. Brust, *Chemical Communications* **2009**, 6661.

73. C. Araki, *Bulletin of the Chemical Society of Japan* **1956**, *29*, 543.

74. S. Arnott, A. Fulmer, W. E. Scott, I. C. M. Dea, R. Moorhouse, D. A. Rees, *Journal of Molecular Biology* **1974**, *90*, 269.

75. D. A. Rees, in *Advances in Carbohydrate Chemistry and Biochemistry, Vol. Volume 24* (Eds.: R. S. T. Melville L. Wolfrom, H. Derek), Academic Press, **1970**, pp. 267.

76. N. S. Anderson, J. W. Campbell, M. M. Harding, D. A. Rees, J. W. B. Samuel, *Journal of Molecular Biology* **1969**, *45*, 85.

77. P. L. SanBiagio, D. Bulone, A. Emanuele, M. B. PalmaVittorelli, M. U. Palma, *Food Hydrocolloids* **1996**, *10*, 91.

78. P. L. San Biagio, F. Madonia, J. Newman, M. U. Palma, *Biopolymers* **1986**, *25*, 2255.

79. M. Leone, F. Sciortino, M. Migliore, S. L. Fornili, M. B. P. Vittorelli, *Biopolymers* **1987**, *26*, 743.

80. K. Starchev, J. Sturm, G. Weill, C. H. Bogren, *Journal of Physical Chemistry B* **1997**, *101*, 5659.

81. N. Fatin-Rouge, K. Starchev, J. Buffle, *Biophysical Journal* **2004**, *86*, 2710.

82. S. Krueger, A. P. Andrews, R. Nossal, *Biophysical Chemistry* **1994**, *53*, 85.

83. M. Manno, M. U. Palma, *Physical Review Letters* **1997**, *79*, 4286.

84. D. Bulone, D. Giacomazza, V. Martorana, J. Newman, P. L. San Biagio, *Physical Review E* **2004**, *69*.

85. N. Fatin-Rouge, K. J. Wilkinson, J. Buffle, *Journal of Physical Chemistry B* **2006**, *110*, 20133.

86. S. Boral, A. Saxena, H. B. Bohidar, *Journal of Physical Chemistry B* **2008**, *112*, 3625.

87. S. K. Sinha, *Physica D* **1989**, *38*, 310.

88. L. J. Tan, S. P. Liu, D. Pan, N. Pan, *Soft Matter* **2009**, *5*, 4297.

89. S. Link, M. A. El-Sayed, *Journal of Physical Chemistry B* **1999**, *103*, 8410.

90. W. Haiss, N. T. K. Thanh, J. Aveyard, D. G. Fernig, *Analytical Chemistry* **2007**, *79*, 4215.

91. J. Perez-Juste, L. M. Liz-Marzan, S. Carnie, D. Y. C. Chan, P. Mulvaney, *Advanced Functional Materials* **2004**, *14*, 571.

92. Scherrer, P. (1918). Göttinger Nachrichten; 98.

93. Goodhew, P. J. and Humphreys, F. J. (1988). "Electron Microscopy and Analysis" Taylor and Francis

94. D. E. Jesson, S. J. Pennycook, *Proceedings of the Royal Society of London Series a-Mathematical and Physical Sciences* **1995**, *449*, 273.

95. I. Freestone, N. Meeks, M. Sax, C. Higgitt, *Gold Bulletin* **2007**, *40*, 270.

.

Chapter 2: preparation of network forming metal nanoparticles in agarose

2.1 Introduction

Spurred by the unabated interest in nanoscale science, tremendous advances have been made in metal nanoparticle synthesis over the past two decades. Detailed protocols for the control of the key parameters, particle composition, size and shape are now widely available and further methods are being published virtually every day with a clear dominance of wet chemical approaches over vapour phase deposition and other physical methods.[1-5] As the field gains maturity, increasing attention is being paid to the production of nanoparticles that are tailored as components of functional composite materials for applications in optics, catalysis, energy conversion, drug delivery, sensors and other areas.[6-11] Stability, longevity and controlled interaction with other components are thus important secondary parameters that determine the relative usefulness of the particles for any given application. These can be addressed by chemically controlling the interface between the particles and their surrounding medium, *i.e.* usually by the choice of stabilizing and functionalizing ligand molecules, often thiols.[12,13] A potential drawback of this approach is that the primary functionality of the high area clean metal surface of the nanoparticles is usually lost. For applications that rely on the chemical accessibility of this interface, alternative strategies need to be found. The exciting developments in catalysis by Au nanoparticles illustrate this problem.[14-16] Although many methods exist to generate size selectively a range of Au nanoparticles that could in principle, be excellent catalysts, they all use some form of ligand chemistry to control particle size and stability, which is incompatible with the targeted application.[17,18] For this reason, catalyst nanoparticles are more commonly generated *in situ* by the reduction of a Au(III) precursor compound adsorbed to the support material and often followed by a heat treatment step to ensure the cleanliness of the metal surface and intimate chemical contact with the support[16]. This example shows that it can be advantageous to depart from established preparative protocols if it is possible to create the nanoparticles directly as part of a composite structure that can impart stability and size-control also in the absence of a well-defined molecular ligand shell.

Here we describe a conceptually similar approach by reducing a metal precursor compound inside a matrix formed by an agarose hydrogel. This results in the formation of interesting composite materials with metal nanoparticle inclusions both inside the water cells of the gel and within its polymeric framework structure. Since apart from the agarose framework no further stabilizing agents are used, it is expected that the surface of the metal particles remains accessible to water-soluble reactants in a way not achievable with particles stabilized by a ligand-shell. While there are many reports on the entrapment of pre-prepared metal nanoparticles in gels including several studies on particle separation by gel electrophoresis[19-21], comparatively moderate attention has been paid recently to the use of gels as the actual reaction medium in which nanoparticle synthesis takes place[22-29].

In this chapter, we will first introduce the method used for the *in-situ* preparation of nanoparticles in agarose hydrogel (see Figure 2.1). Then, we present the characterization of the nanoparticles by different techniques (such as UV-vis, XRD, MALDI, Electron microscopy), discuss the different difficulties encountered and suggest a general model of the new composite material obtained. Finally, we characterize and describe the system obtained with other metals following the same preparative procedure.

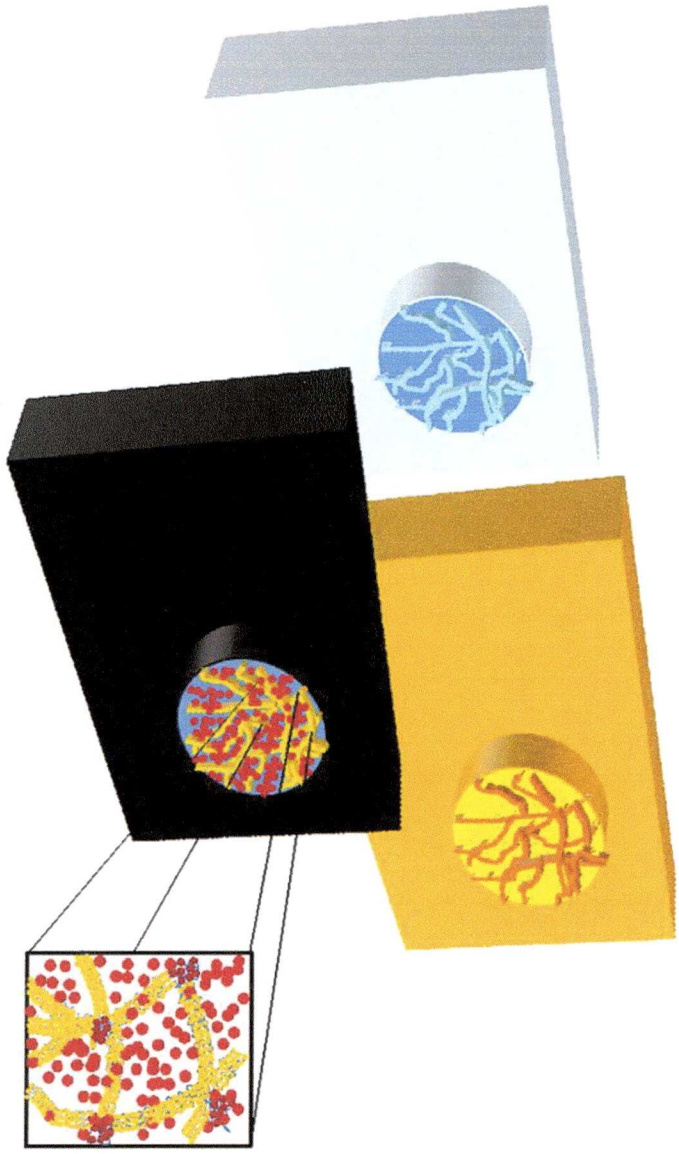

Figure 2.1 Cartoon presenting a hypothetical model of the composite material. The change in colour of the agarose corresponds to the decoration of its networks by polydispersed nanoparticles.

2.2 Experimental

2.2.1 Materials

Hydrogen tetrachloroaurate ($HAuCl_4$) trihydrate, ruthenium (III) chloride ($RuCl_3$) hydrate, sodium hexachloropalladate (Na_2PdCl_6) tetrahydrate, sodium hexachloroplatinate (Na_2PtCl_6) hexahydrate and silver nitrate ($AgNO_3$) were purchased from Sigma Aldrich. Hexanedithiol (1,6-Dimercaptohexane: HDT) was also purchased in Sigma Aldrich. Sodium borohydride ($NaBH_4$) was obtained from BDH, agarose (molecular grade) from Bioline and monohydroxy(1-mercaptoundec-11-yl)tetraethylene glycol (PEG-OH) from Prochimia. All chemicals were used as received. In all experiments water deionised with a Milli-Q plus 185 system was used.

2.2.2 Methods

2.2.2.1 Gold nanoparticles in agarose gel

Agarose hydrogels (5.4%w) were prepared by dissolving 285mg of agarose in 5ml of water at 90°C in a glass vial of 20 mm inner diameter followed by sonication until all gas bubbles were removed, and storage for at least one hour at 4°C. The vial was then carefully destroyed with a small metal hammer (caution!) to isolate the resultant hydrogel, which was rinsed with water and cut with a razor blade into discs of ca. 3.2mm thickness. A wedge shaped quarter of an agarose hydrogel disc was immersed in 3 ml of a 20 mM feed solution of the respective metal salt, here hydrogen tetrachloroaurate for 24 hours. The hydrogels were then removed from the feed solution, quickly rinsed with water and immediately transferred to 3ml of a freshly prepared 500 mM solution of sodium borohydride to reduce the metal salt. After 24 hours, the particle-loaded gels were removed from the sodium borohydride solution. The sample was finally dialysed in ca. 50 ml of water for 48 hours changing the water every 12 hours thus preventing any presence of sodium borohydride. Other Au-gel samples were prepared following the same protocol but with an increase in concentration of the feed solution.

Ruthenium, palladium, platinum and silver nanoparticles were prepared following the same procedure but changing obviously the nature of the metal salt used in the feed solution. The concentration of the feed solution used for these metals here was 20mM for all.

2.2.2.2 Determination of the gold salt concentration

The Au (III) concentration inside the gel after the immersion for 24 hours in the feed solution was determined using UV-visible spectroscopy. An increase of the Au (III) concentration involves a more pronounced yellow color in the solution and therefore a more intense absorption. The peak which characterizes this absorption is located at 298nm (as shown in Figure 2.2).

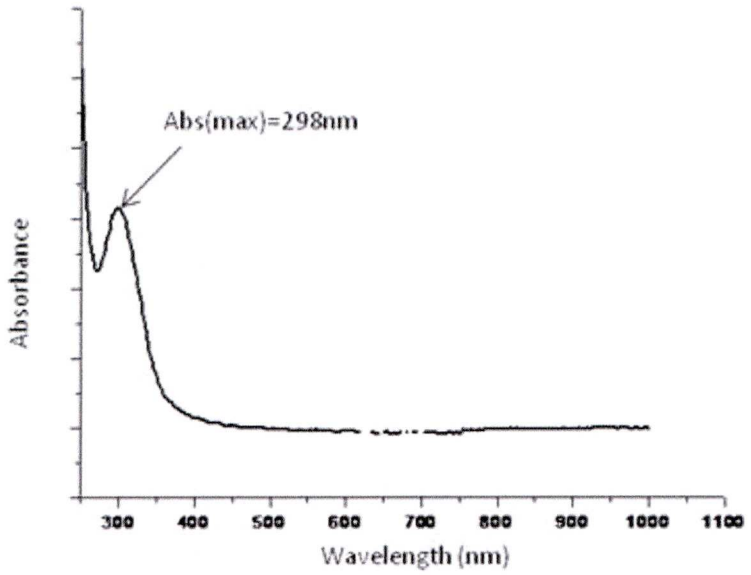

Figure 2.2 Absorbance spectrum of a Au (III) solution diluted. The maximum absorbance is obtained at 298nm wavelength.

Therefore, the unknown concentration of an Au (III) solution can be determined by comparing the absorbance value obtained at 298nm with the one of a standard solution of Au (III) with a known concentration. In our study, the concentration of Au (III) in the agarose gel could not be determined in one step as the agarose matrix absorbs within the 250-1100 wavelength range. Instead, we measured the difference of the Au (IIII) concentration in the feed solution before and after the soaking step using

UV-visible spectroscopy. This difference of concentration is then converted in weight and considered as the total amount of gold in the piece of gel. A correlation of these values to the volume of the pure piece of gel employed in each single experiment provides the concentration of Au (III) in the gel.

2.2.2.3 Characterization of the nanoparticles

An initial visual inspection of the hydrogel was followed by UV-visible spectroscopic and X-ray diffraction analysis to confirm the presence of nanoparticles in the agarose gel. Mass spectrometry was performed and added to the X-Ray diffraction data to fully describe the size range of the nanoparticles present in the matrix. Finally, examination of the samples using electron microscopy was performed to validate the previous results obtained using three different techniques: TEM, STEM and Super-STEM.

UV-visible spectroscopy. UV-vis solid state spectra were recorded with a Perkin Elmer Lambda 650 S UV/Vis Spectrometer equipped with a Labsphere integrating sphere over the spectral range 190-900nm (6.53-1.38eV) using $BaSO_4$ reflectance standards. Samples were prepared by compressing a small piece of gel between two glass slides. A sample of unloaded gel was used as a reference. UV-vis liquid state spectra were recorded on a Genesys 10-S spectrophotometer(Thermospectronic USA).

X-ray Powder Diffraction (XRD). Data were collected on a Stoe STADI P diffractometer using Cu $K\alpha_1$ radiation in transmission foil geometry. Measurements were carried out on ca. 1 mm slices of gel cut with a razor blade. They were held in place between acetate films in order to prevent shrinkage of the sample by the beam due to dehydration.

Mass spectrometry. The wet samples were rubbed across the sample plate (stainless steel) in order to deposit some material, with matrix solutions pipetted on top. The dry samples were pre ground for one hour prior to the mix with the matrix to eliminate the presences of clamps. The

mixing with the matrix was achieved following the vortex/smearing method[30]. Basically, each analyte and the au-gel powder were transferred into a vial and mixed with a vortex mixer for 15 seconds and four times. After each time, the mixeage was smeared on the sample plate (stainless steel). Different analytes has been used in this study in order to detect the different size of clusters present in the hydrogel. These analytes are SA[31], DHB[32], CHCA[33], DCTB[34], terthiophene[35], dithranol[36], PFBA and PFCA[37] are commonly used in MALDI studies.

MALDI-TOFMS spectra were acquired using an Applied Biosystems Voyager DE-STR spectrometer (Foster City, CA), equipped with a nitrogen laser (λ) 337 nm). Both positive and negative ions were achieved in reflection mode. The accelerating voltage was 20 kV, while the grid voltage was maintained at 65.5%. The delay time was 100 ns and the laser fluence was optimized for each sample. The data were acquired using Data Explorer V4.0 software supplied by Applied Biosystems[30]. This was done at EPSRC National Mass Spectrometry Service Centre (NMSSC), School of Medicine, Swansea University, by Dr. Mark Wyatt.

Electron Microscopy. For a full TEM characterization of the nanoparticles prepared inside the agarose gel, three different types of sample preparation have been used (i) embedding in epoxy resin, (ii) dissolution of the gel and (iii) freeze drying.

(i) Embedding in epoxy resin

Before embedding in pure epoxy resin the gel (0.23cm^3 cut in small pieces) was first dehydrated in a graded series of ethanol solutions (30, 60, 70, 90 and 100%v) for 30 min at each concentration and then infiltrated by a graded series of epoxy resin in absolute ethanol (proportion of resin was ¼, ½ and ¾ of the total volume) each step lasting for 1 hour. The resin was then polymerised at 60°C for one week. This unusually time consuming step was necessary in order to avoid irreversible adhesion of the sample to the diamond blade during the subsequent cutting process. Ultrathin sections (20-200 nm) were cut using a LKB ultramicrotome. The hydrogel samples were fixed in a 0.1M PBS (phosphate buffer

solution) solution of 25% gluteraldehyde and ruthenium red (1mg/ml) for 1 hour. The samples were then rinsed with 0.1M PBS, stained in a 4% osmium tetroxide solution and ruthenium red (1mg/ml) for 1 hour. They were then rinsed with 0.1M PBS, dehydrated in a graded series of ethanol solutions (30, 60, 70, 90 and 100%v) for 30 min at each concentration, stained with a mix of propylene oxide and epoxy resin (1:1) and embedded in epoxy resin; 1 hour each step. The resin was polymerised at 60°C for 48 hours[38]. Ultrathin sections (20-90 nm) were stained with 5% aqueous uranyl acetate and 2% aqueous lead citrate. The sections were placed on a carbon-coated copper grid and dried at room temperature.

(ii) Dissolution of the gel

A piece of gel ($0.23cm^3$) was soaked in 5 ml of 1.7 µl of hexanedithiol (HDT) and 50 µl of monohydroxy 1-mercaptoundec-11-yl tetraethylene glycol[39] (PEG) (HDT/PEG 1:2) for 24 hrs. The mixture was prepared in ethanol in order to increase the solubility of the hexanedithiol and PEG in the hydrogel. The hydrogel was then dissolved in a dilute hydrochloric acid solution at 70-80 C for 24 hours. A drop of each solution obtained was evaporated on a standard copper grid for TEM imaging.

(iii) Freeze drying

For freeze drying, the gels were first frozen for one hour at -20°C, then for 3 hours at -80°C and dried overnight in a Modulyo vaccum dryer. They were then crushed with pestel and mortar and a sample of the resultant dust was carefully picked up with a holey carbon TEM sample grid.

Microscopy methods related to the preparation mode employed

Samples dissolved in HCl were analysed by TEM whilst the embedded samples were also characterised by TEM in addition to STEM. The freeze dried samples were visualized by Super STEM. TEM images were obtained using a 120kV FEI technai Spirit TEM and STEM images were

obtained using a JEOL 2100F (S)TEM with aberration corrector . Samples were inspected by HAADF imaging on the Super STEM 1 microscope at Daresbury Laboratories, UK.

2.2.2.4 Quantification of number of atoms along Z-axis

The STEM and HAADF-STEM used here present both a z-constrast system. It means that the intensity of each spot of the sample surface is provided by the electrons scattered along the X and Y axis as well as the different electrons scattered along the Z-axis. A Three dimensional assembly of atoms or nanoparticles could therefore be analysed qualitatively as well as quantitatively.

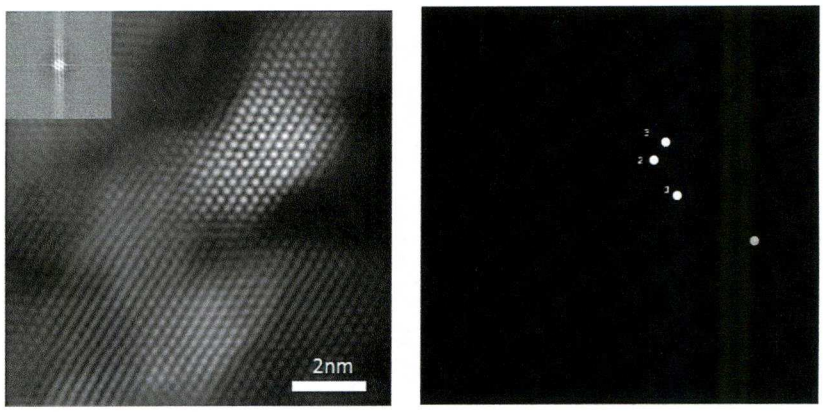

Figure 2.3 STEM picture of ruthenium atomic layers on the left shows difference of intensity from the atoms along the surface of the sample studied. The different intensities can be measure locally (right picture) and number of atoms aligned along the Z-axis can be determined.

Indeed, the number of atoms along the Z-axis can be determined using the equation:

$$N_{atoms} = \frac{(I_{av}zone1 - I_{av}background)}{I_{av}atom}$$

Where $I_{av}zone1$correspond to the average of intensity in the localized area studied, $I_{av}background$ to the average intensity of the image background and $I_{av}atom$ to the average intensity of a single atom. The intensity of each element of the equation has been determined by their

respective discretisation of their surface in 452 pixels. The average intensity of per pixel in zole 1, per pixel in the background and per pixel in a single atom were then used for the calculation (Figure 2.3).

2.3 Results and discussion

In this section of the chapter, the detection and characterization of the nanoparticles synthesized in the gel are first investigated through the use of different techniques such as UV-vis, XRD, MALDI and different electron microscopies. A structural model of the composite is then proposed based on the best STEM and HAADF-STEM pictures obtained. Finally, the synthesis method is applied to other metals. The different nanoparticles obtained are characterized by STEM, and the patterns acquired for the different gels are discussed.

2.3.1 Detection of the presence of gold nanoparticles

Figure 2.4 exhibits the changing colour of the gel following the experimental procedure. Transfer of the Au loaded gel to an aqueous solution of sodium borohydride leads to the immediate reduction of the Au (III) complex to Au (0), which is manifested by a rapid colour change of the gel from yellow to black.

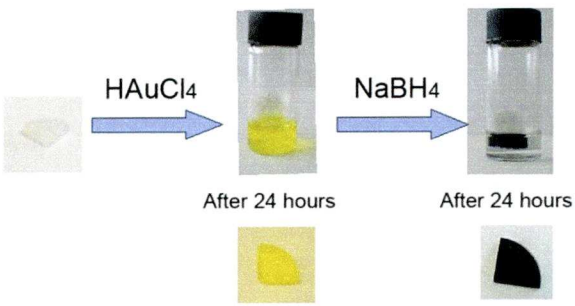

Figure 2.4 Scheme of the synthesis of gold nanoparticles in agarose gel. The Hydrogel is soaked in Au salt solution for 24hrs followed by immersion in a solution of sodium borohydride for 24hrs. The gel was rinsed with milli-Q water between the two steps.

In order to confirm the presence of Au nanoparticles, the sample was analysed by UV-vis spectroscopy, X-ray powder diffraction (XRD), mass spectrometry and electron microscopy. The UV-visible spectra obtained

with three different concentrations of feeding solution are shown in the appendix (appendix 2.1). The results are extremely poor due to the excessive absorption of the agarose. Even a normalization of these spectra by subtracting the absorbance of a pure piece of agarose gel within the same wavelength range does not improve the quality of the Au-gels characterisation. The only detail obtained from these spectra is a slightly bigger absorption of the gel at 500-520nm as the concentration of the feed solution increases. This could mean an increase in the average nanoparticles size. The absorbance at 800nm can be due to the agarose as the thickness of the slices analysed are not exactly identical, it can also be due to the shape of the nanoparticles (see page 109).

This hypothesis is consistent with the XRD data of the gel. XRD patterns of gels prepared with three different Au loadings are shown in Figure 2.5. The spectra of the gel obtained with a 20 mM, 200mM and 500mM feed solution clearly indicate the presence of fcc Au nanocrystals[40,41]. The approximate size of the particles is estimated by line broadening analysis using the Scherrer equation[42] :

$$\tau = \frac{K\lambda}{\beta cos\theta}$$

Where K is the shape factor, λ is the x-ray wavelength, β is the line broadening at half the maximum intensity (FWHM) in radians, and θ is the Bragg angle. τ is the mean size of the ordered (crystalline) domains which in our case correspond to the nanoparticles.

The nanoparticle size increases with increasing Au loading as shown in the inset of Figure 2.5. Importantly, the absence of narrow peaks in the XRD spectra rules out the formation of bulk Au, which, at the salt concentrations used, would be the only product if the reaction had been carried out in

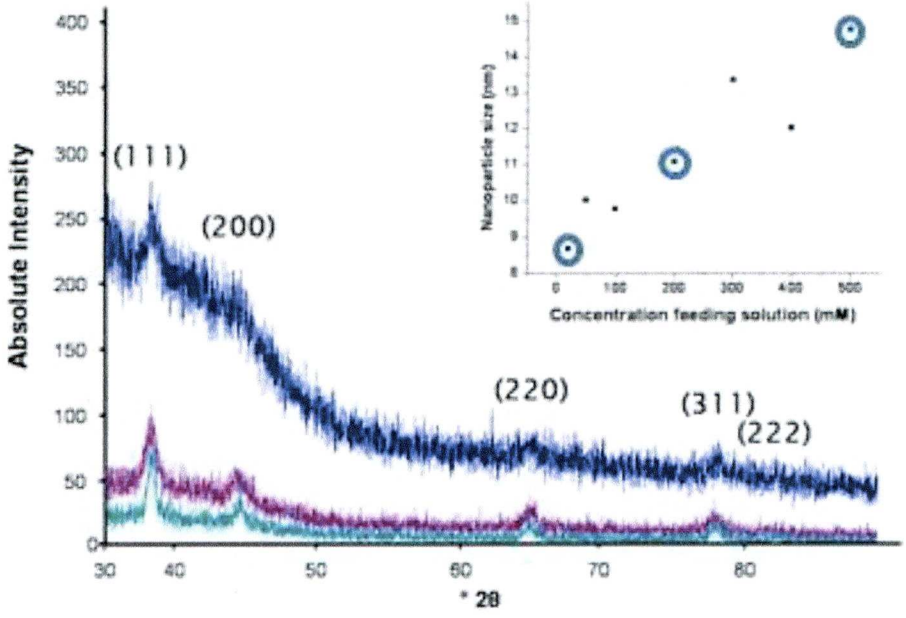

Figure 2.5 X-ray diffraction patterns of Au nanoparticle-loaded agarose gel obtained with feed solutions of $HAuCl_4$ of different concentrations (20mM, 200mM and 500mM feeding solutions) and evolution of nanoparticles size estimated by line broadening analysis using the Scherrer equation (20mM, 200mM and 500mM being circled in blue).

aqueous solution in the absence of any stabilising agents. The larger signal intensity at low concentration results from the fact that more X-rays are transmitted through the sample when only small nanoparticles are present at low concentration. The intensity of the noise on the spectrum obtained is also related to the matrix. If the concentration of nanoparticles in the gel is small, the X-ray will be less diffracted and the structure of the nanocrystal will be less defined. In addition to the XRD data, mass spectrometry measurements have been carried out to confirm the presence of small clusters in the matrix and estimate their size. MALDI measurements give an indication of the size of the gold clusters decorating the network. As the clusters are polydispersed in size, this method is particularly useful for this study.

These measurements have been performed on both the "wet" (gel without any treatment after dialysis) and the "dry" (freeze dried following the

procedure presented in the experimental part of the chapter) samples. All gels were prepared using a feed solution concentration of 20mM ($HAuCl_4$). For the "wet" gel, initial positive and negative ion LDI data show Au_4 and Au_5 ions (Figure 2.6). Only background ions (from the matrix) were observed in the 5-30kDa mass range. A very low intensity polymeric series is also observed (Figure 2.7 A and B); the species separation is ~24 Da which may indicate that there are several overlapping series, however, the poor resolution precludes a more accurate interpretation. Previous studies[43,44] have reported that these peaks are corresponding to different $CxHy^+$ and $CxHyOz^+$ fragment ions, as expected from the carbohydrate structure of these materials which could explained the Mn~24kDa(number average molecular weight), much lower than the expected 300kDa. Similar analyses focussing on the <1kDa mass range also show Au ions and Au_2 and Au_3 ions (Figure 2.8 in negative mode and appendix 2.2 in positive mode).

Further analysis involved layering matrix solutions on top of the smeared sample, beginning with common protic matrices SA (appendix 2.3A), DHB (appendix 2.3B) and CHCA (appendix 2.4). All spectra show the Au_3 ion, while only negative ion DHB and CHCA show higher order clusters. However, all three positive ion spectra show a resolved, polymeric series of species in the ~700-900 mass range and the isotope pattern would indicate the presence of a multi-isotopic element. This could also correspond to the Au_4 clusters attached to some specific fragments of the agarose unit (such as $CxHyOz^+$).Next, two electron transfer matrices, DCTB and terthiophene were used, as well as dithranol capable of both proton and electron transfer ionisation. Only matrix ions were observed for all analyses.

Finally, two fluorinated protic matrices, pentafluorobenzoic acid (PFBA) (appendix 2.5) and pentafluorocinnamic acid (PFCA) (Figure 2.9 in negative mode and appendix 2.6 in positive mode), were used. The results were similar to the LDI data, with Au_{3-5} clusters and extremely weak unresolved polymeric series were observed with PFBA. Most notably, Au_7

and Au_9 clusters were observed with PFCA in negative ion mode, but there was no evidence for the Au_6 or Au_8 clusters.

It is important to note that the m/z 862 species in negative ion mode should be disregarded as it corresponds to a boron anion contaminant from somewhere inside the instrument that we were unable to remove.

For the dry hydrogel, the powder did not adhere to the sample holder, so LDI analysis could not be carried out. Also, the powder did not homogenise well with the matrices during the solvent-free preparation stage, this is likely to have had a negative effect upon the resultant data. Matrices SA, CHCA, DHB, DCTB and TCNQ in positive and negative ion modes were evaluated; no Au_n particles were observed in all cases. Au_n particles (for n = 1-5) were observed in positive and negative modes for PFBA and PFCA matrices.

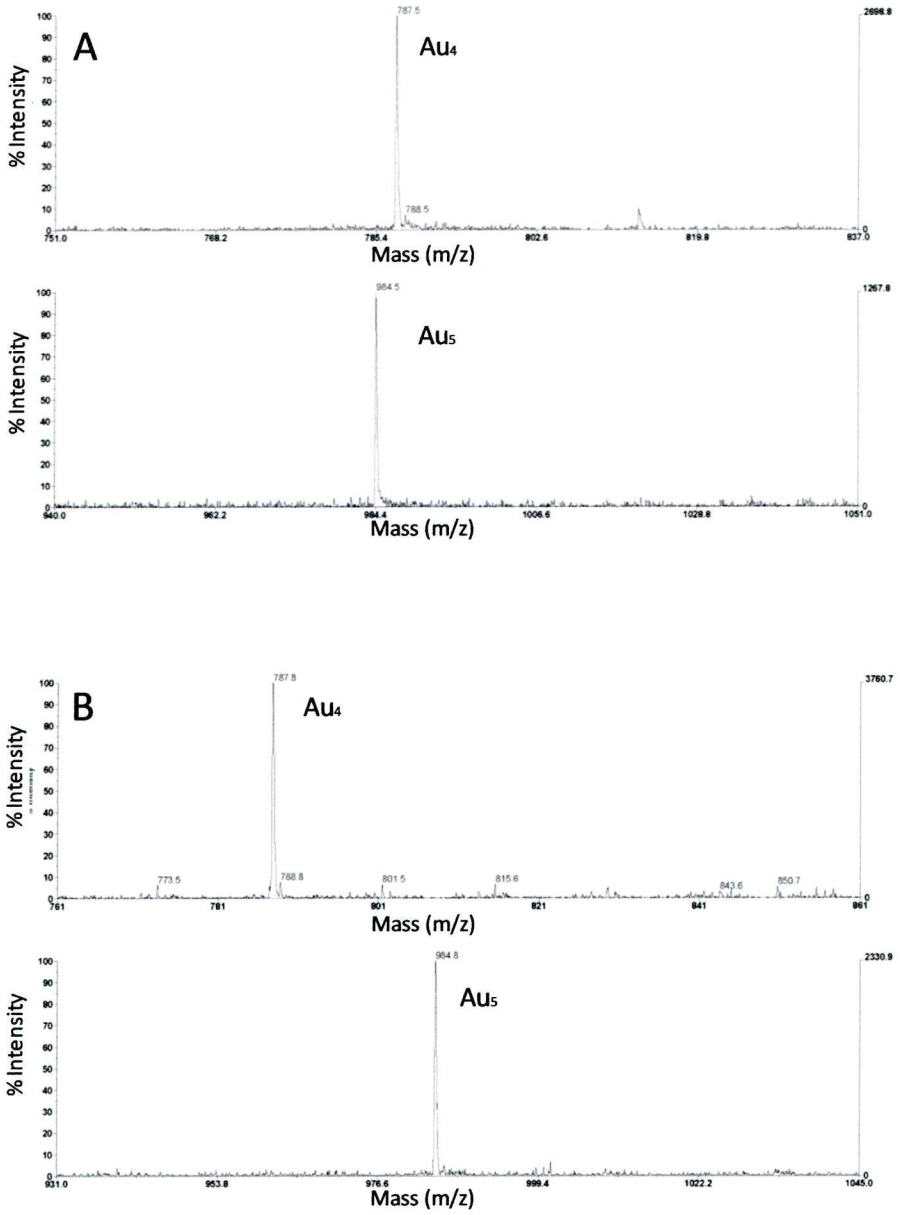

Figure 2.6 (A) Negative ion solvent-free MALDI-TOFMS spectrum for Au-gel in LDI mode and (B) positive ion solvent-free MALDI-TOFMS spectrum for Au-gel in LDI mode both presenting Au_4 and Au_5 clusters

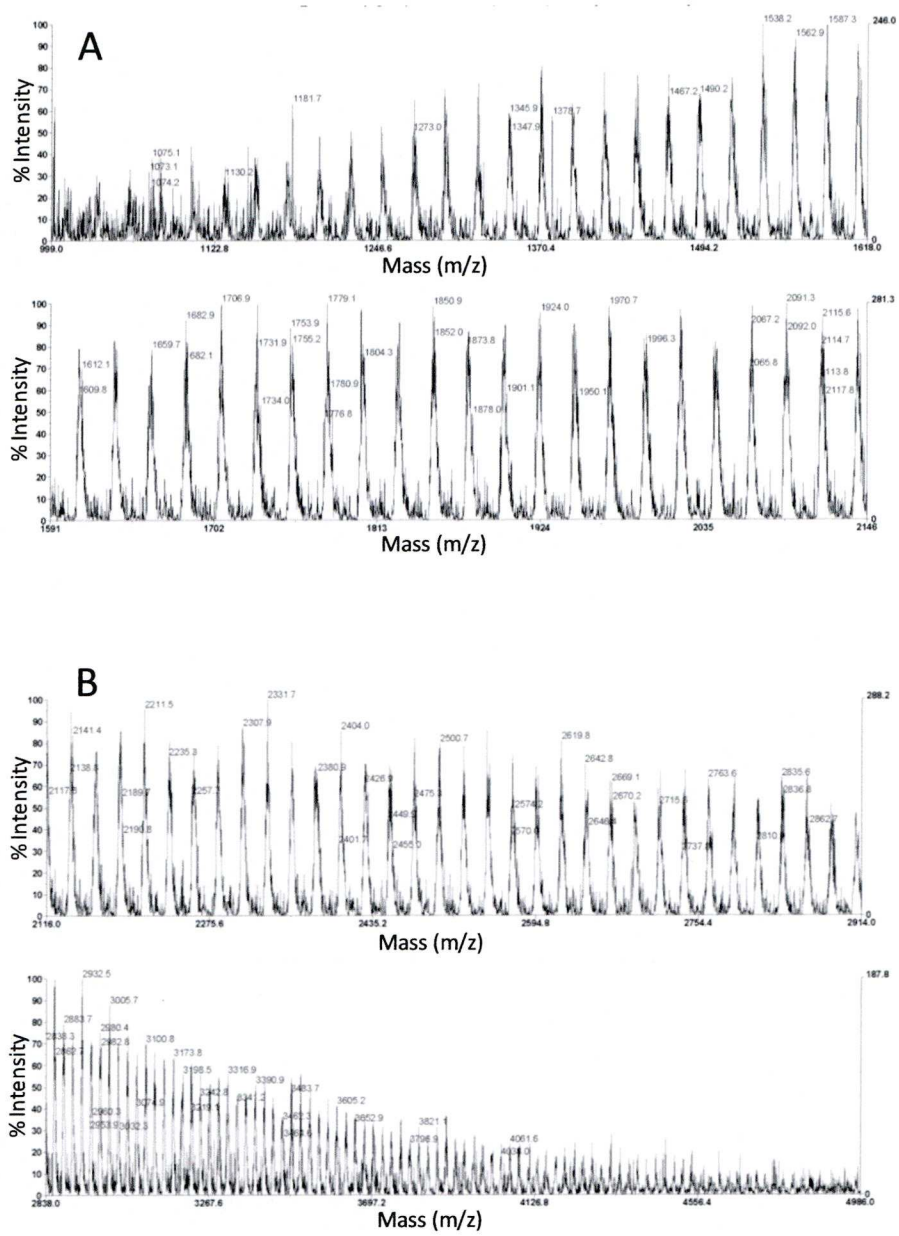

Figure 2.7 (A) positive ion solvent-free MALDI-TOFMS spectrum for Au-gel in LDI mode (1000-2100 mass range) and (B) positive ion solvent-free MALDI-TOFMS spectrum for Au-gel in LDI mode (2100-5000 mass range). These spectra show low intensity polymeric series

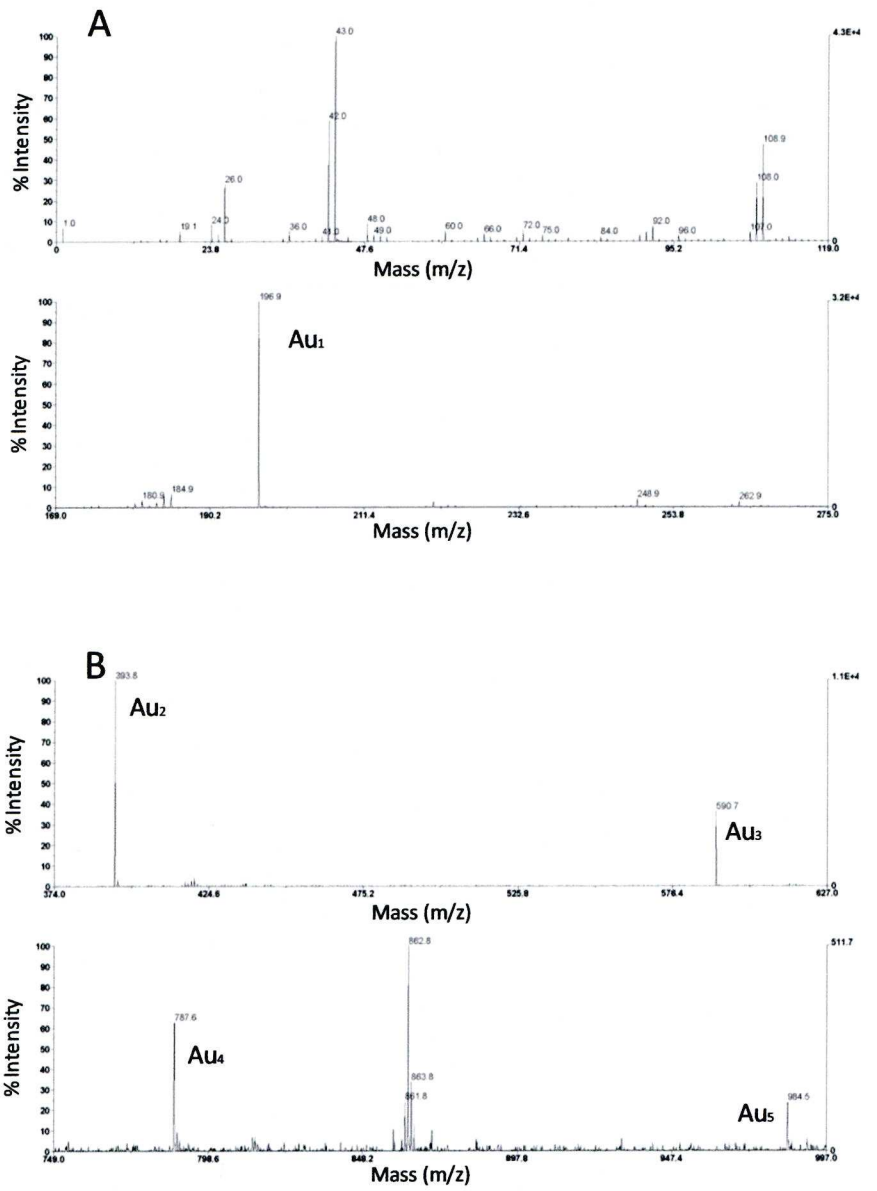

Figure 2.8 (A) and (B): negative ion solvent-free MALDI-TOFMS spectrum for Au-gel in LDI mode and showing the presence of Au_1, Au_2, Au_3, Au_4 and Au_5 inside the hydrogel matrix.

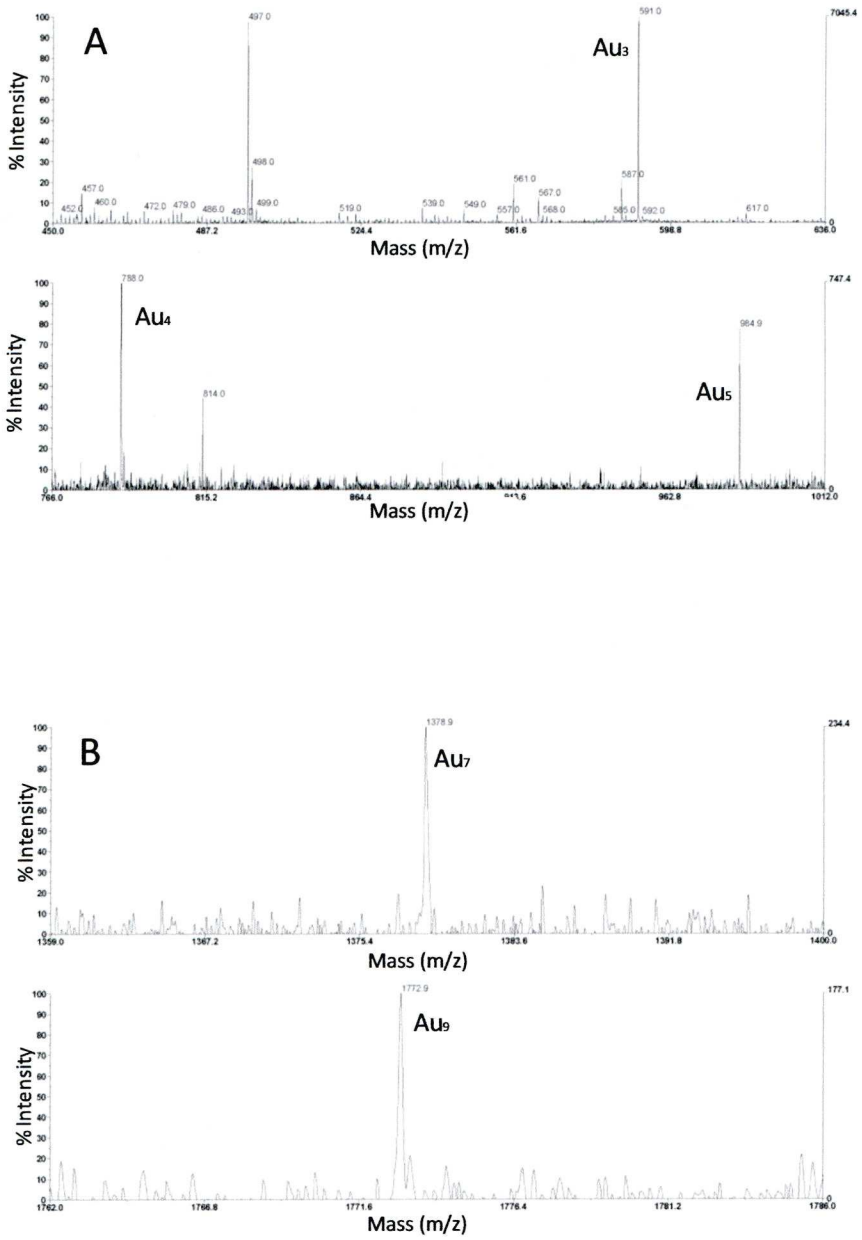

Figure 2.9 (A) negative ion solvent-free MALDI-TOFMS spectrum for Au-gel with PCFA matrix showing Au_3, Au_4 and Au_5 cluters while (B) is a negative ion solvent-free MALDI-TOFMS spectrum for Au-gel with PCFA both exhibiting the presence of Au_7 and Au_9 clusters.

The correlation between the UV-vis spectra, the XRD patterns and the mass spectrometry data provides a first picture of the nanoparticles synthesized in the agarose gel. The following preliminary model is suggested to describe this composite material: Single atoms and very small clusters of two to nine atoms are present in the material. In addition, nanoparticles with an average diameter of 8nm but possibly very polydisperse are found. Analysis of the UV-vis spectra shows that the slight size dispersion found for each category at low concentrations of feed solution increase dramatically when higher concentration of metal salt are used. To test the validity of this model the samples were also characterized by electron microscopy.

2.3.2 Electron Microscopy

2.3.2.1 Pure gel

As most polymers, agarose gel is hard to image by electron micrsoscopy due to its low density and the correspondingly high quantity of electrons transmitted through the material. The contrast between the gel network and the water phase (void) is therefore really poor. This contrast can be enhanced by the staining of the gel structure with dyes or stains [38,45]. These highly charged compounds bind to the polymer chains and therefore can absorb some electons coming from the electron beam of the microscope. In order to optimize this contrast, the thickness of the sample should be between 20 and 100nm for a partial transmission of the electrons. For the analysis of a pure piece of gel, these conditions are fulfilled when the polymer is beaten with silica beads in a bead mill followed by staining with urenyl acetate and lead citrate (Figure 2.10). The hydrogel network is then visualized and corresponds to a cross-linking of strands of 30nm diameter. Unfortunately this method could not be applied to the different Au-gel as the beating of the polymer altered the stabilization of the nanoparticles. The liquification of the gel under this beating process involves a change of color from black to purple.

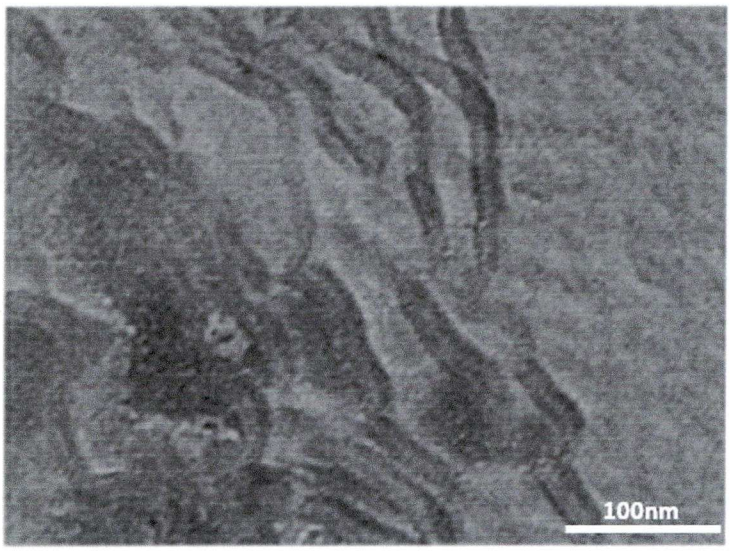

Figure 2.10 TEM picture of a pure piece of gel beaten by silicon bead followed and stained with urenyl acetate and lead citrate.

Different methods were then employed to characterize the gel decorated with gold nanoparticles (Au-gel): (i) staining and embedding, (ii) dissolution of the gel and stabilisation of the nanoparticles by "ligand exchange" and (iii) dissolution of the gel and preservation of the structure by cross-linking of the nanoparticles.

2.3.2.2 Au-gel

(i) Staining and embedding

Several methods can be used to prepare a hydrogel for an electron microscopic characterization. Here, the hydrogel is first soaked in a solution of ethanol in order to expel the water phase from the sample. The gel is then immersed in a chosen metal salt solution (the nature of this solution depends on the hydrogel analysed). The metal ions interact with the gel network and staining of the gel pattern is thus achieved. Finally, the hydrogel is embedded in an epoxy resin which is polymerized within few days in an oven. Once the embedding of the gel is achieved, the sample can be cut in ultra thin section with a microtome.

Since the presence of GNPs in the Au-gel (fed with a solution of 20mM gold salt) processed by embedding only could not be visualized by TEM

(no entities could be resolved), this sample was stained with ruthenium red[46], urenyl acetate and lead citrate which is the most common method for staining a sugar.

TEM image of the hydrogel after processing displays partially the structure of the agarose but there is no visual proof of the presence of the particles (Figure 2.11). The limit of efficiency of this method can be explained by the poor quality of the network staining and by a possible staining of the GNP surface. It was thus impossible to detect the presence of any colloids in our gel in this way.

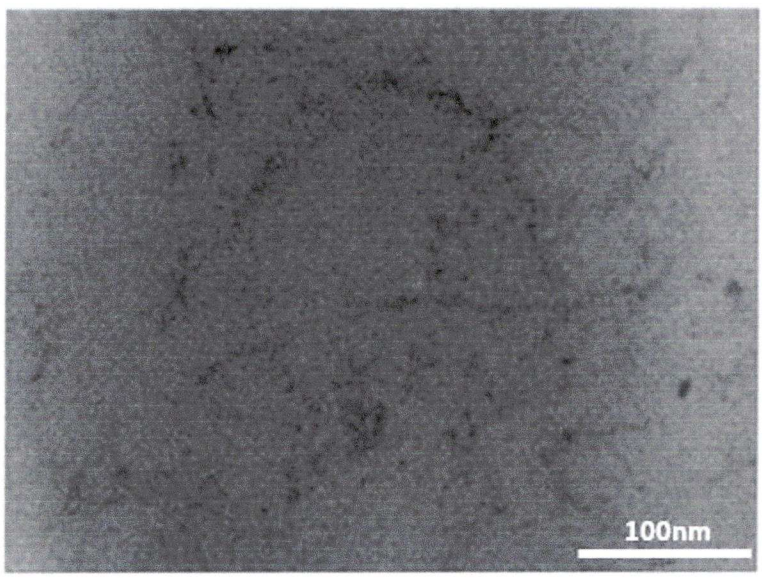

Figure 2.11 TEM picture of the Au-gel stained with ruthenium red. The network is visible but this does not represent evidence for the presence of nanoparticles.

(ii) Dissolution of the gel and "ligand exchange"

The second method employed here to attempt to visualize the nanoparticles by TEM is based on the dissolution of the gel after stabilization of the GNPs with thiolated PEG-OH ligands. The idea behind this method is to replace stabilization of the GNPs provided by the network of the gel with another ligand having strong stabilization properties. After the addition of the ligands, the dissolution of the hydrogels was obtained by the addition of a few drops of hydrochloric acid which breaks the hemiacetal linking the two monomers forming

the agarose, combined with heating which alters the cross-linking of the molecules inside the hydrogel. The solutions obtained showed the existence of small nanoparticles with an average size of 2 to 5nm (Figure 2.12). As the previous UV-vis results confirmed the presence of nanoparticles, this indicates that the particles were probably hidden by the staining and so decorate the network of the agarose matrix.

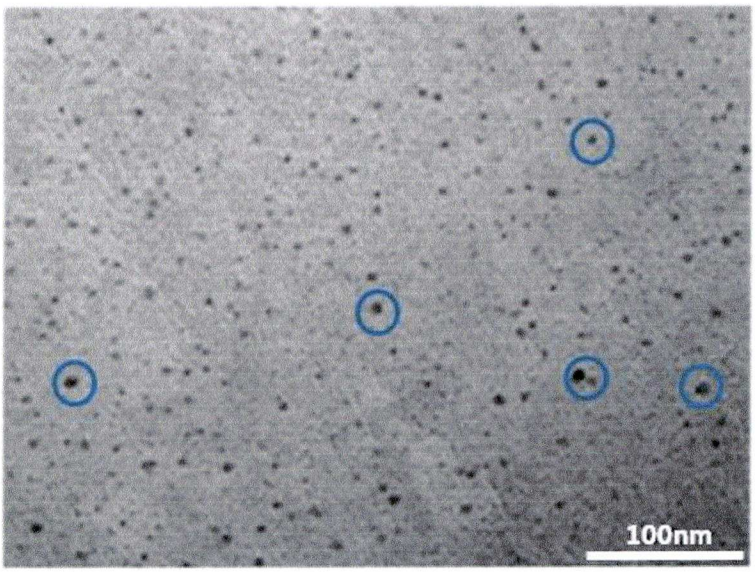

Figure 2.12 TEM picture of a piece of gel dissolved in hydrochloric acid exhibits the presence of nanoparticles in the size range of 2 to 5nm. Aggregates possibly formed during the dissolution of the gel are circled in blue.

Even though this method allows the detection of nanoparticles, it cannot be infered with certainty that theses colloids have the same size as the ones present in the gel before its dissolution. The "ligand exchange" could involve a heterogeneity in the stabilization of the GNP surface and so lead to the formation of small aggregates. The Figure 2.12 tends to support this possibility with some non spherical specks (circled in blue).

(iii) Dissolution of the gel and preservation of the structure by cross-linking of nanoparticles

In order to allow the partial or complete dissolution of the hydrogel whilst simultaneously retaining the network structure, the use of hexanedithiol as an interparticle cross-linking agent was added to the method described above. Immersion of the gel in ethanol containing hexanedithiol and monohydroxy 1-mercaptoundec-11-yl tetraethylene glycol followed by a dissolution of the material in hydrochloric acid solution proved to be a suitable method. While the thiolated ligands stabilize (partially) the GNP surface[39,47], the HDT allows to keep the "organisation" of these colloids by bonding its two thiol group on the surface of two neigbouring particles[48-51]. At a large scale, the addition of the HDT before the dissolution of the gel should make a partial or total print of the crossinlinked organisation of GNPs possible. The reactions here is:

$$(Au)m + (SHCH_2(CH_2)_4CH_2SH)n + p(SH(CH_2)_{11}(OCH_2CH_2)_4OH) \rightarrow ((Au)m(SH(CH_2)_{11}(SHCH_2(CH_2)_4CH_2SH)n)(OCH_2CH_2)_4OH)$$

between Au(0), PEG-OH and HDT. There is no limitation on the diffusion of the molecule in the hydrogel (24hrs soaking) and there is no distance limitation as the hexanedithiol is incorporated inside the gel before its dissolution. The position of the GNPs is not dependent of the length of the hexanedithiol molecule but to the crosslinking between all the hexanedithiol molecules.While Figure 2.13 schematically presents the reactions described above, Figure 2.14 displays the TEM picture obtained with an Au-gel (20mM feed solution) proccessed in this way. Curved strings of 5-10nm formed by an accumulation of small specks appeared homogeneously through the entire surface of the copper grid. These small black specks (3nm) are visible (as entities) in some localized area of these strings and seemed to reside inside the strings. At the centre of the picture, two different strings join each other and form a wider string. By correlation with the picture 2.9 obtained on a pure piece of gel, the nature of these string can be associated with the helices forming the network of the hydrogel. The

width of each string correponds to the widths of the gel helices presented in Figure 2.14 and the joining of the strings could correspond to the cross-linkage of the helices. Knowing that the pictures in Figure 2.10 and Figure 2.14 were obtained at a similar scale their correlation would indicate a decoration of the helices of the network by the nanoparticles which results from the staining of the pattern by the Au salt.

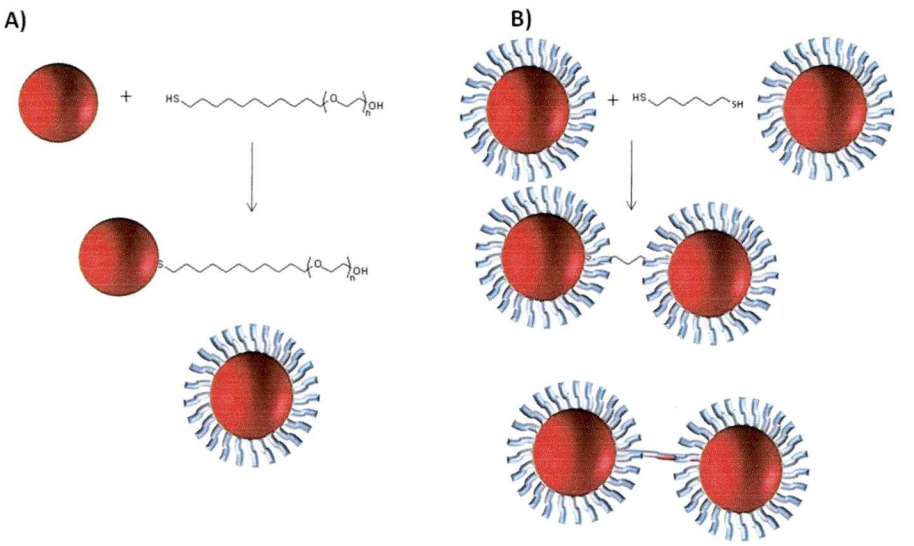

Figure 2.13 Scheme of the stabilization of the GNPs with PEG-OH-thiol (A) and the preservation of their localizations on the gel network with HDT (B) after the dissolution of the matrix

The staining of the hydrogel network by the gold salt has been investigated through the analysis of a gel soaked in a gold salt solution (concentration of the feeding solution: 20mM) and dissolved (diluted solution of HCl) without any reducing step involved in the procedure.

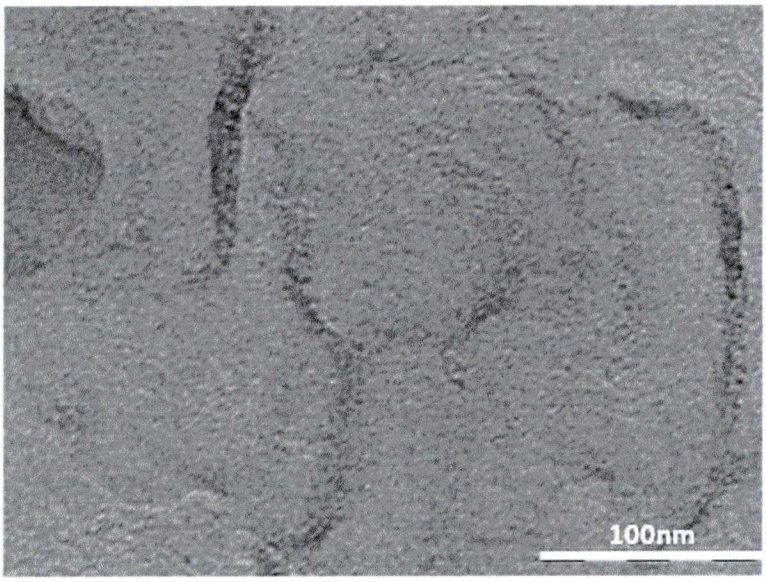

Figure 2.14 TEM picture of the Au-gel after dissolution of the matrix, stabilization and cross-linking of the nanoparticles by dithiol.

Figure 2.15 shows a TEM picture obtained on a Au-gel dissolved before reduction with BH_4 leading to a yellow solution. The network of the gel is clearly observed and stained by the gold. Many black spots can also be seen on this picture which were not distinguishable in Figure 2.14, however, both pictures show the same pattern which corresponds to the gel network (see figure 2.10 p 53). Their presence corresponds to the amount of gold that was staining the part of the network dissolved by the HCl. These large black spots may correspond to particles formed during the TEM investigation. Athough gold nanoparticles can be damaged by HCl and even disappear the Au salt is not altered in the presence of this acid. In Figure 2.15 the total amount of the Au salt initially present in the piece of gel remains on the grid after dissolution.

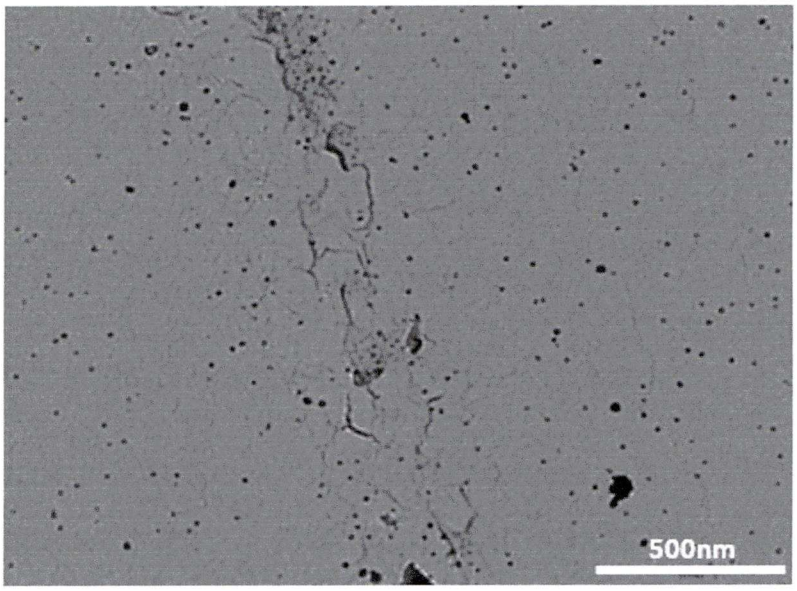

Figure 2.15 TEM picture of Au- gel before reduction dissolved in hydrochloric acid solution.

Many studies[54-60] have reported the possible complexation of the metal ions to the carbohydrates and polysaccarides structure though the hydroxyl groups which are abundant in the agarose case. The hydroxyl group gives a pair of electrons to the metal ions through the oxygen atom which wich results in the creation of a coordinate covalent bond. The double helix of agarose molecules becomes then a coordination complex for the formation of metal clusters following the chemical reaction:

$$m\,AuCl_4^-(aq) + n(C24H38O19) + 3me^- \rightarrow 4mCl^-(aq) + (Au)m(C24H38O19)n$$

$$oxidation\ state\ of\ the\ gold:\ Au(III) \rightarrow Au(0)$$

With BH_4 providing the electrons. The bonding will be then Au-OH and Au-O.

2.3.3 Structural model

The previous part of the study has showns the difficulties to characterise our system by electron microscopy. While the staining of the gel appears to be ineffective, the dissolution of the gel provides some information on the decoration of the gel structure but restricted and erroneous data on the GNPs size. The embedding (without staining procedure) and freeze drying appear to be the two best methods to characterize the GNPs as they dont alter the colloid morphologies.

A more detailed characterization of the freeze dried and embedded gels were performed and form the basis for the suggested structural model of the nanoparticle loaded gel. The images in 2.16.A and B were obtained by scanning transmission electron microscopy (STEM) in dark field mode of a 60 nm thin section of the gel embedded in epoxy resin. Dark field mode was employed here in order to distinguish more accurately the GNPs from the gels. In 2.16.A the agarose network of the gel is clearly visible as an electron dense (light) cloud that suggests the presence of Au atoms or clusters decorating the polymeric framework. In addition, ca. 8nm Au particles appear as bright spots on the surface of the network and to a lesser degree also free in the water phase (void) of the gel. A high resolution image of a representative particle is shown in Figure 2.16.B exhibiting a multiply twinned structure commonly observed in Au nanoparticles of this size.[52]

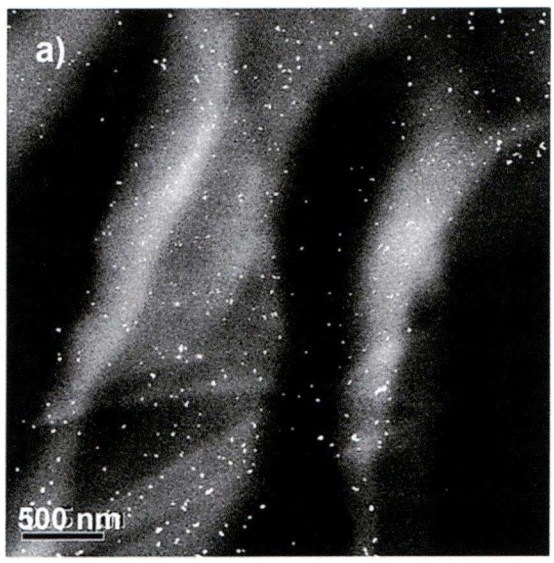

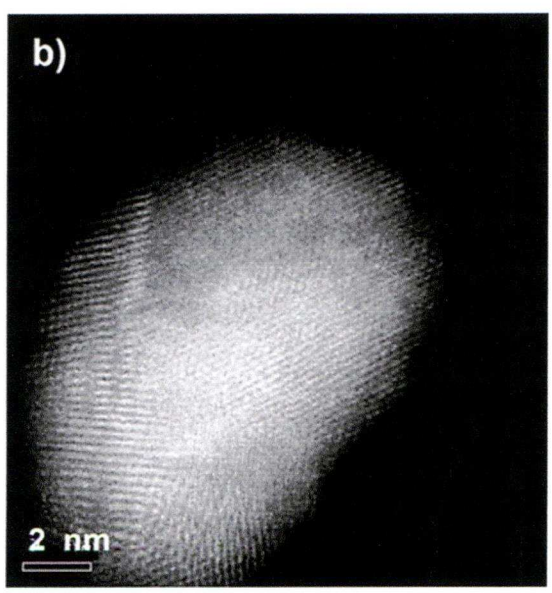

Figure 2.16 STEM image of a 60 nm thin epoxy embedded section of an agarose gel loaded with gold nanoparticles showing the agarose network structure coated with gold clusters (a) and a single gold nanoparticle dispersed within the water phase (void) of the gel (b).

To confirm our hypothesis that the polymeric framework of the gel is decorated by Au atoms and/or small clusters, a freeze-dried sample of the gel was inspected by high angle annular dark field scanning transmission electron microscopy HAADF-STEM. The result shown in Figure 2.17 reveals the presence of Au clusters in the range of 0.5 to 4 nm plus electron dense material not resolved as particulate matter. This observation is consistent with a decoration of the agarose framework by Au atoms and clusters. The smallest discernible clusters are likely to be Au_{13}[33-35] and correspond to 0.5 nm in diameter (circled in the picture). This cluster diameter corresponds exactly to the size of the cavities between the strands of the double helix system. Oxygen atoms and hydroxyl groups are present in this cavity and could explain the stabilization of these clusters while the cavity would restrict their size. The other electron dense areas correspond to the decoration of the strands by single Au atom to Au_9 clusters by correlation with the MALDI results. On the other hand, the larger nanoparticles seem to only decorate the surface of the hydrogel structure. Moreover, a focus on these particles shows that they are not spherical and even have some holes in their atomics structures (Figure 2.17 A, B and C). This could be explained by a partial organization of their atoms and therefore these nanoparticles can be considered as "amorphous" and could be called "metal glass nanoparticles". From our knowledge, this is the first time that "glassy metal colloids" have been reported anywhere.

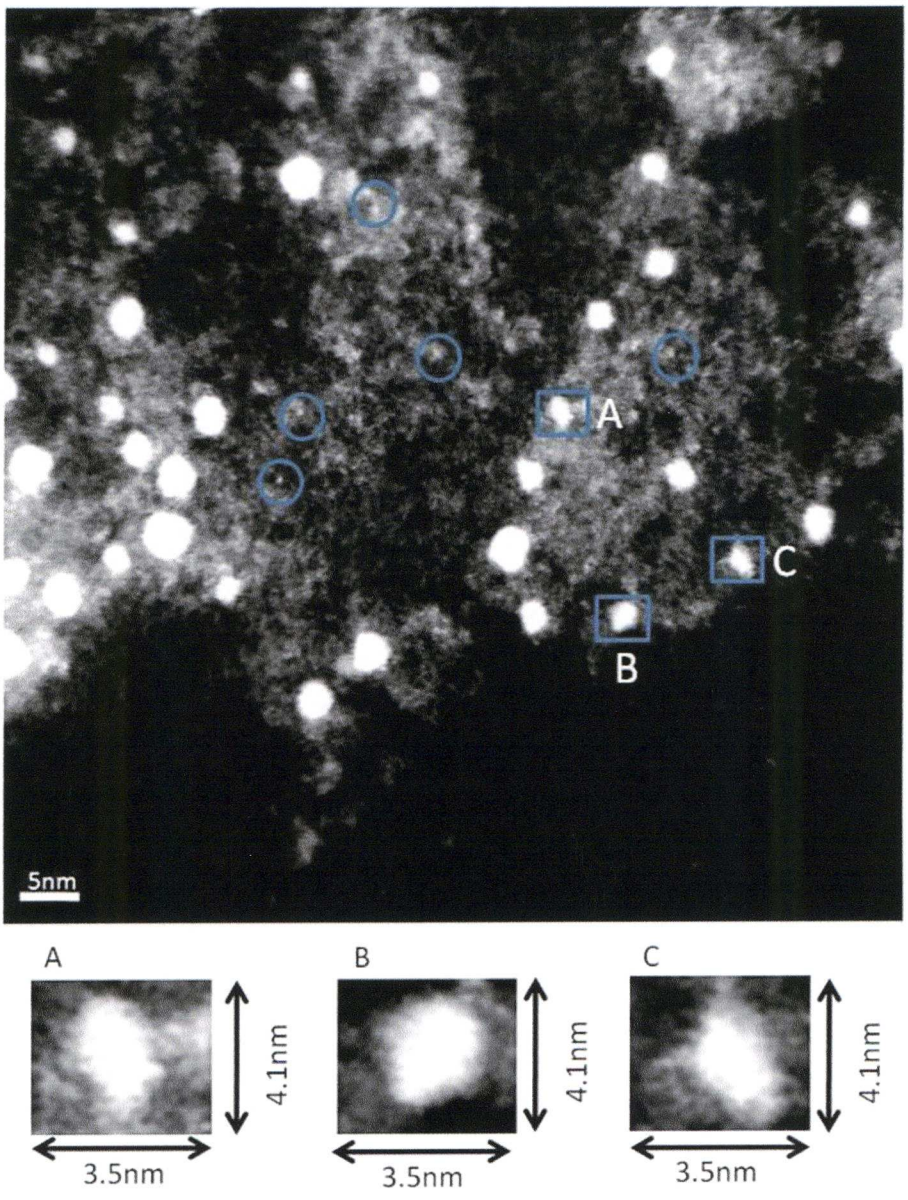

Figure 2.17 HAADF "Super-STEM" image of freeze dried sample showing decoration of the agarose network with Au atoms and clusters ranging from a size below the resolution limit to nearly 5 nm. Note the blue circles indicating the smallest discernible clusters, probably Au_{13}. Three areas with small nanoparticles have been enlarged and are presented as picture A, B and C. In every case, the atoms, composing the nanoparticles, do not seem to exhibit any order between them. These colloids are called glassy colloids in the chapter.

2.3.4 Evolution of the Au (III) concentration in the gel

The next step was to validate the evolution of the nanoparticles size as a function of the feed solution concentration determined before through the XRD characterization. The evolution of Au (III) concentration in the gel as a function of the concentration of the feed solution used has been obtained following the method described in section 2.2.2.2.The results are reported in Figure 2.18. The three samples measured between 400 and 500 mM (concentration feed solution) seem to be incorrect. This can be due to inaccurate measurements at one level of the method employed here. The rest of the data shows a logarithmic relationship between the concentration of gold in the gel and the concentration of the feed solution. At low concentration, the concentration in the gel is bigger than in the soaking solution. This corresponds to the impregnation to the gel structure at the nanoscale and microscale which react like a "sponge". The increase of the concentration starts to slow down after 150mM (concentration of the feed solution). It corresponds on Figure 2.18 to a lower gradient of the slope. This slow down could be interpreted as the saturation in Au (III) of the nanoscale structure with the continuous impregnation of the microscale structure of the hydrogel. At really high concentration (above 500mM), the gradient of the slope decrease again which correspond to the close saturation of the gel saturation at the microscale. The results presented below should correspond to an increase in number and size of the large nanoparticles on the microscale structure of the gel. Au-gel at 500mM of feed solution was then characterized by STEM. The sample was embedded as described above (without any staining). The STEM pictures are shown in Figure 2.20.a and b.

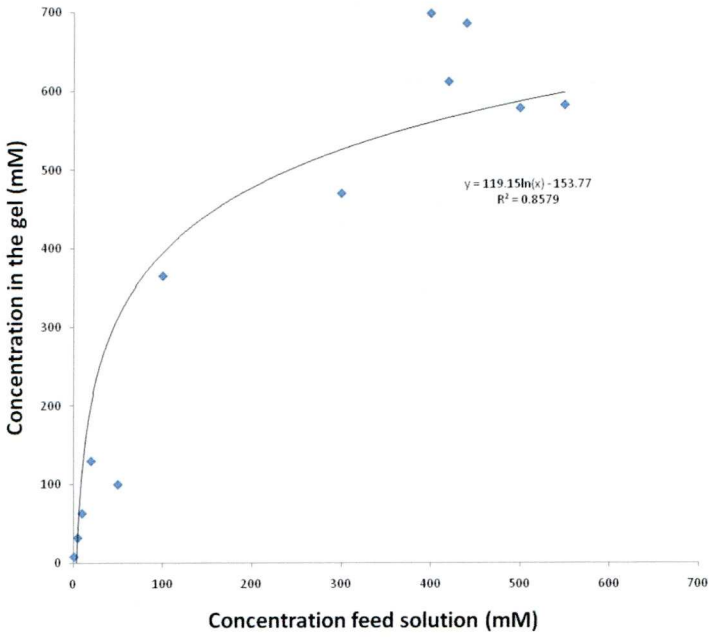

Figure 2.18 Concentration of Au (III) in the gel (mM) *vs.* concentration of Au (III) in the feed solution (mM).

From the extensively studied structure of agarose gel[37] and the present electron microscopic analysis the following structural model is proposed for the composite material. As illustrated in Figure 2.19 the gel is composed of interwoven helices (blue lines) of agarose polymer strands stabilised by water pockets in the helical cavities[53].

It is suggested that upon reduction of the metal ions in the gel very small clusters (yellow dots) form and lodge in these cavities thereby decorating the gel framework. The agarose polymer thus acts as a template for the formation of the clusters. The upper limit of particle size appears to be *ca.* 5nm (small brown dots).

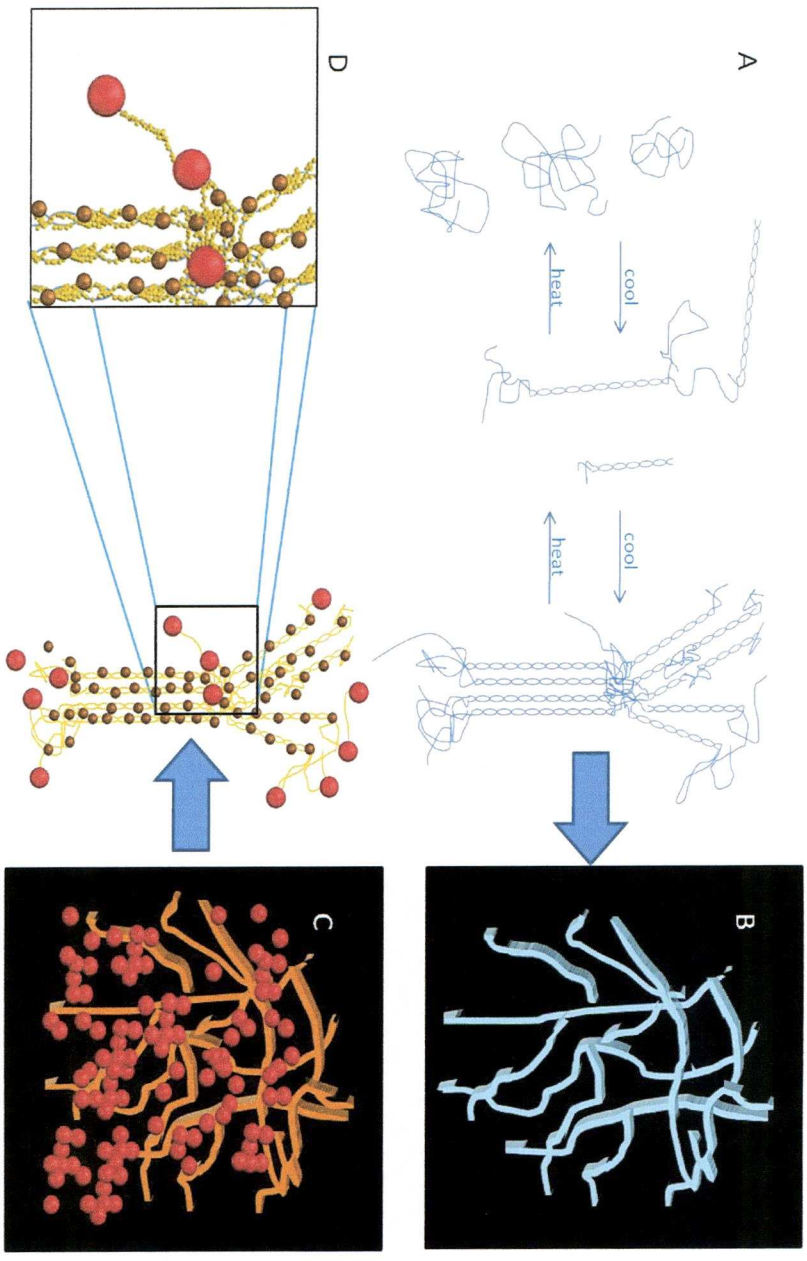

Fig 2.18 exhibits a general model of the synthesis of nanoparticles in a hydrogel. (A) displays the internal structure[65] of the network which forms at high scale a microscale (B). After soaking the gel in a metal salt solution and the reduction by sodium borohydride the gel displays large particles and an electron cloud on its network (C). This electron cloud corresponds to the presence of small particles and clusters decorating the internal helices of the network (D).

In the water phase of the gel and more particularly on the external structure of the gel, larger colloidal particles are formed. These particles dominate the XRD line broadening results and mask to some extent the presence of the much smaller clusters. The observed trend in the XRD results suggests that the proportion and size of larger colloidal particles increases with increasing concentration of metal salt in the feed solution. Figure 2.20.A confirms this suggestion. The quantity of large nanoparticles has increased dramatically as well as the average size of nanoparticles (around 30 nm). The cloud formed by the small clusters is still present (Figure 2.20.B). This increase in number and average nanoparticle size could be explained by two different approaches. Firstly, the increase of $HAuCl_4$ concentration in the gel altered the stabilization properties of the network hydrogel. This event has been already reported in different studies of carbohydrate and sugars[54-60]. The increase of $HAuCl_4$ concentration in the gel affects the pH of the system. While at low $HAuCl_4$ concentration, the nanoparticles are stabilized through –OH and $–O^-$ interactions (as a coordination complex), an increase of the $HAuCl_4$ concentration will involve the hydrolysis of the agarose molecule and an opening of their chains[60]. The degradation of the chain structure implies the alteration of the double helix system but the disappearance of the cavities and therefore of the small clusters. Moreover, the hydrolysis involves the replacement of the $–O^-$ by -OH. The abundance of the Au–OH groups makes the bonding less possible due to the weaker interaction between two –OH groups. This leads to the poor stabilization of the system and therefore the aggregations of the nanoparticles at the microscale.

The second approach suggests that the increase of gold atoms in the pores of the gel will leads to larger particles when using the same amount of stabilizing agent.

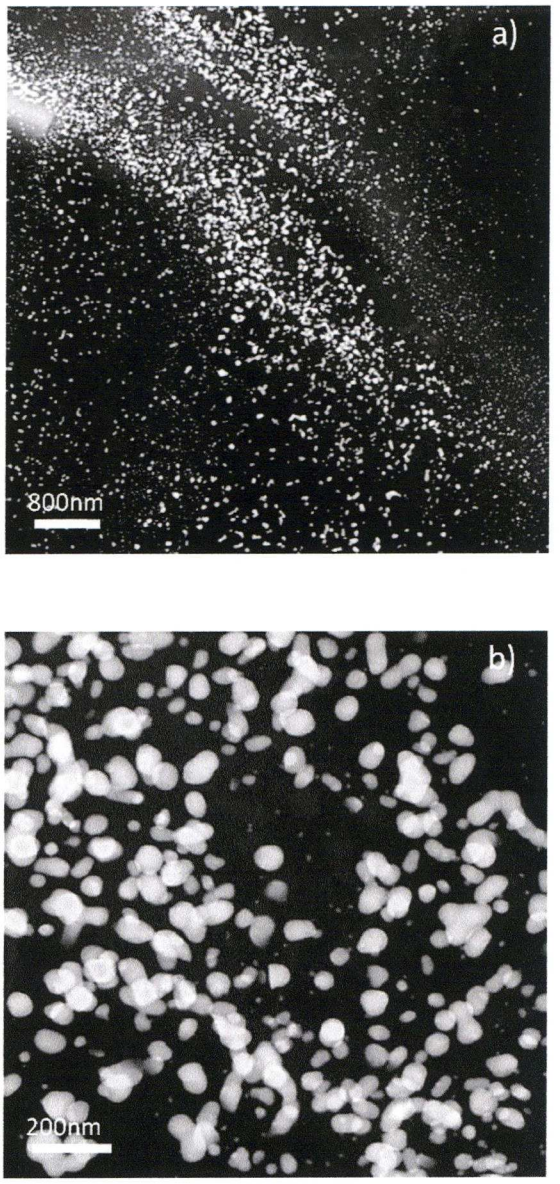

Fig 2.19 STEM image of a 60 nm epoxy embedded section of an agarose gel loaded with gold nanoparticles (500mM feed solutions). The image in (a) shows the decoration of the structure on the outside with large nanoparticles (*ca.* 30nm) and with small clusters on the inside. Image (b) corresponds to a zoom on the large nanoparticles. Aggregates can be detected in localized areas.

2.3.5 Application of the method to silver, palladium and platinum

All metal-gels were analysed by STEM, and samples were prepared following the freeze drying method. Micro dust of each metal-gel suspended in hexane solution was deposited on a carbon grid.

2.3.5.1 Silver-Gel

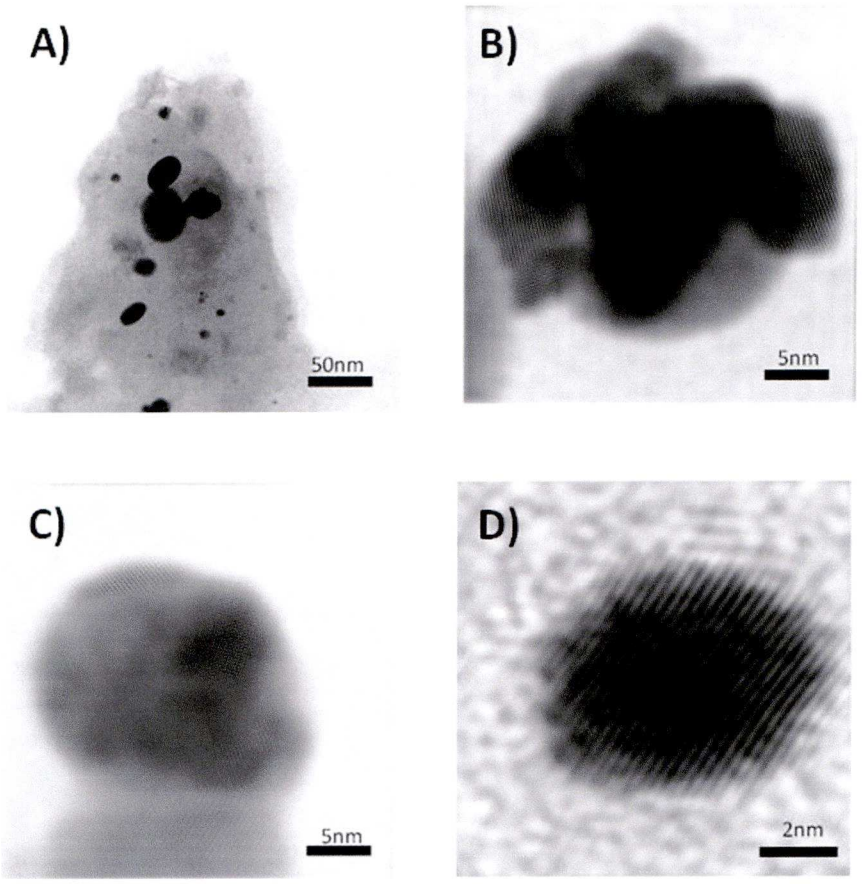

Figure 2.21 Bright field TEM pictures of a piece of agarose gel loaded with silver nanoparticles. (A) shows a dust particle made of a large electron dense cloud . This dust presents singular aggregates of silver nanoparticles (B) and few large colloids (C). Small nanoparticles are also apparent in the cloud (D).

Figure 2.21 displays the pictures of the gel loaded with silver nanoparticles. The size dispersion of the nanoparticles is similar to that presented with gold previously. The gel exhibits few aggregates of larger nanoparticles (5 to 10nm as shown in Figure 2.21B) in addition to single

colloids with sizes varying from 2 to 8nm (Figure 2.21.C and D). Unfortunately, the clusters forming the electron cloud in the gel (exhibited in Figure 2.21.A) could not be fully characterized. The investigation of the sample ("dry" gel) through MALDI shows the presence single atoms, Ag_2 and Ag_3 in the gel (example of results shown in appendix 2.7). The investigation of the wet Ag-gel should provide more information on the size of the different clusters forming this electron cloud.

2.3.5.2 Palladium-gel

Similar features can be observed when the gel is loaded with palladium as shown in Figure 2.22. In the piece of Pd-gel analysed (Figure 2.22.A), one large aggregate, few large nanoparticles and many small clusters can be visualized (Figure 2.22.B). While some nanoparticles exhibit a crystalline structure (Figure 2.22.C), others appear to be amorphous (Figure 2.22.D). Even though, the nature of their formation cannot be unequivocally established, we can confirm that this phenomenon is size dependent. We can also speculate that their existence emerged from their particular location in the network. It is probable that they were formed between aggregates formed by close-packed double helix chains. In this case, these "glassy nanoparticles" could be interpreted as aggregates of small clusters originating from the decoration of the agarose helix structures, i.e. quite literally the icing on the cake.

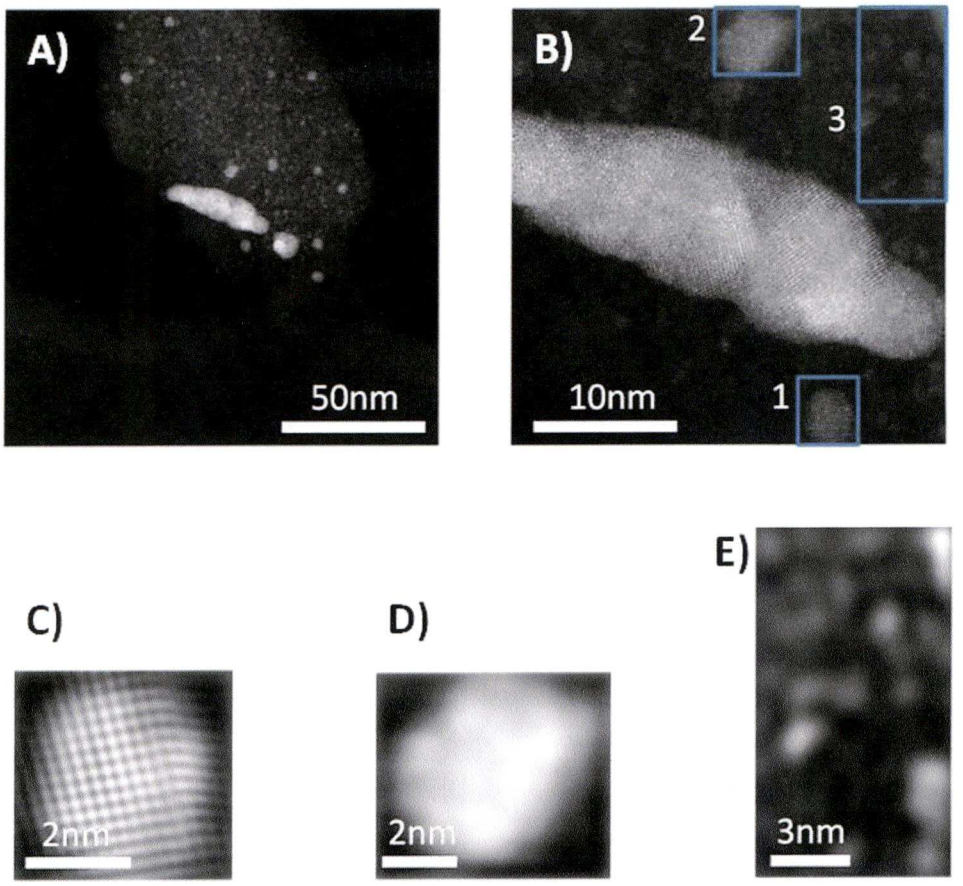

Figure 2.22 TEM pictures of agarose piece loaded with Pd nanoparticles. (A) shows a dry dust of this gel. (B) focuses on a large aggregate present in the silver loaded gel dust. (C) exhibits one many small crystalline nanoparticles present in the gel. (D) shows the existence of small amorphous nanoparticles. (E) exhibits the decoration of the network of the gel with some different size clusters.

These amorphous colloids could emanate from the strength of the interaction gel helices/clusters being superior to the electrostatic attractions which exist between metal atoms for the formation of crystalline structure. Figure 2.22.E shows the presence of small clusters in the gel.

2.3.5.3 Platinum-gel

Figure 2.23 exhibits STEM pictures obtained on the platinum-gel. Figure 2.23.A shows the piece of the gel at a large scale (microscale).

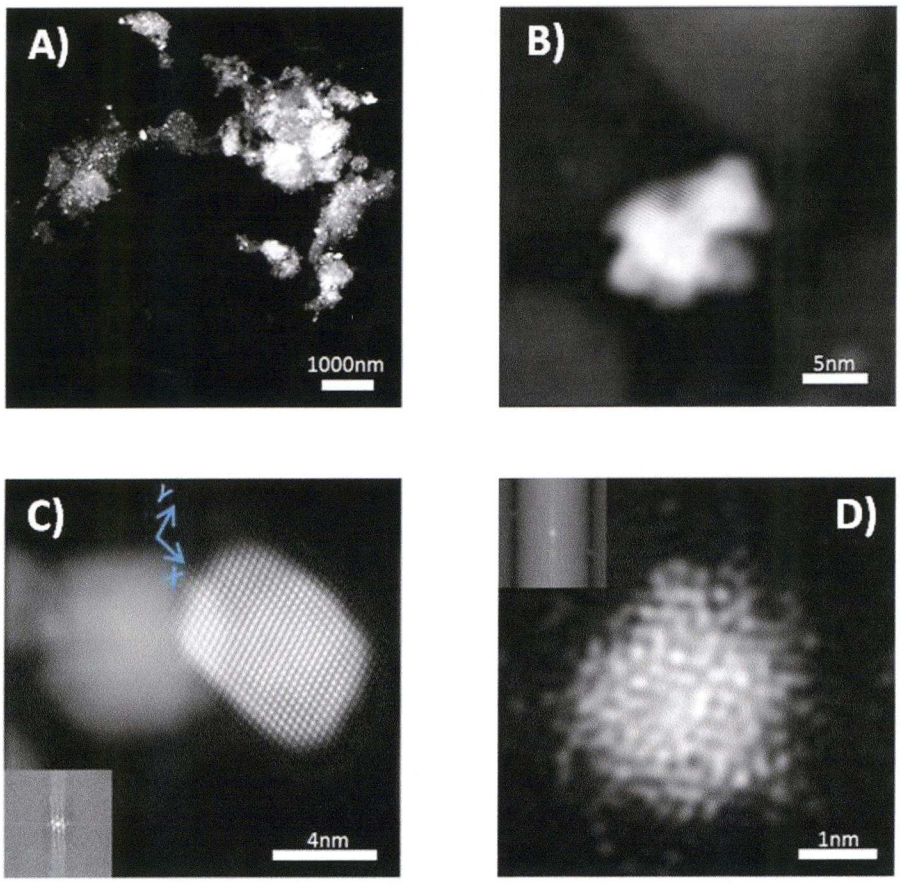

Figure 2.23 TEM pictures of agarose piece loaded with platinum nanoparticles. (A) shows the homogeneous distribution of the particles trhough the hydrogel matrix . This dense cloud contains few aggregates (B) and large amount of small crystalline nanoparticles (C) and some amorphous ones (D) the FFT in inset does not show any crystalline structure in the colloid).

The intensity of the electrons diffracted by the samples is much larger than for the other metals. Figure 2.23.B exhibits one of the many aggregates of pt nanoparticles present in the gel. Figure 2.23.C shows the atomic structure of the large nanoparticles obtained. Inter atomic distance has been measured along two different axis (X and Y on the picture). The results are summarized in table 2.1 and 2.2. The average distance between Pt atoms has been evaluated at 0.280-0.290nm and corresponds to the value expected for a Pt crystalline structure[61-63].

Finally, Figure 2.23.D shows that the Pt-gel presents also some "glassy colloids". In this case, an atomic resolution of the cluster has been obtained. The alignment of some of the atoms along different directions could correspond to the initials stages of a crystal growth. This atomic organisation cannot be only due to the interaction between the agarose molecules and the Pt atoms.

platinum (X axis)		
amount of inter atoms distance measured	length (nm)	average distance between atoms (nm)
19	5,353	0,282
21	5,982	0,285
24	6,731	0,280
22	6,171	0,281
9	2,459	0,273
9	2,549	0,283
5	1,439	0,288
6	1,709	0,285
7	1,934	0,276

Table 2.1. Summary of the average distance between atoms in the nanoparticles presented in picture 2.23.C along the X-axis.

platinum (Y axis)		
amount of inter atoms distance measured	length (nm)	average distance between atoms (nm)
5	1.47	0.294
4	1.148	0.287
11	3.187	0.290
6	1.735	0.289
7	2.039	0.291
13	3.84	0.295
8	2.323	0.290
7	1.982	0.283
10	2.873	0.287

Table 2.2. Summary of the average distance between atoms in the nanoparticles presented in picture 2.23.C along the Y-axis.

2.3.5.4 Ruthenium-gel

The analysis of the Ruthenium-gel though STEM mirrors the previous outcomes with the metals. In figure 2.24.A the Ru nanoparticles corresponding to the white specks are dispersed homogenously through the entire volume of the gel. The lower image contrast (in comparison with the other metals) is related to the lower atomic number of ruthenium. At this scale, the size of the colloids seems to be uniform except in a few localized areas where the nanoparticles appear to form aggregates as shown in Figure 2.24.B. These aggregates are formed from agglomerations of several crystals which resulted from poorly stabilized nanoparticles combining with their neighbouring particles. Figure 2.24.C shows the size of the nanoparticle dispersed in the agarose matrix. The colloid diameter corresponds to 5 nm. This nanoparticle is also surrounded by a very large amount of small clusters decorating the network. This ornamentation of the network pattern is confirmed in Figure 2.24.D, where single atoms of ruthenium are interacting with the agarose network. All these atoms are aligned in the XY plane and the difference in intensity throughout the network of gel also presumes an alignment of the atoms along the Z axis. The fast Fourrier transform on the picture shows that the system presented in Figure 2.24.D (inset) presents a crystalline structure. Many studies[64] have already reported that the ruthenium atoms in nanoparticles are organized in hexagonal lattices which are defined by:

$$a = b = 0.27nm \neq c = 0.428nm\,, \alpha = \beta = 90^o \; and \; \Upsilon = 120^o$$

Where a, b, c are the interatoms distances along the X, Y and Z axis respectively. α and β are the angles between respectively a and c and b and c. Finally, Υ correponds to the angle between a and c. In the case of the crystalline structure investigated here, the distance inter atoms along the X-axis and Y-axis (as presented in Figure 2.24.D and corresponds to a and b) are presented in the table 2.3 and 2.4. The correlation between these axis and the lattice constant a and b was determined by measuring the angle between them (120^o exactly).

Ruthenium (X axis)		
amount of inter atoms distance measured	length (nm)	average distance between atoms (nm)
9	2.701	0.300
8	2.468	0.309
9	2.72	0.302
8	2.447	0.306
6	1.814	0.302
9	2.76	0.307
9	2.76	0.307

Table 2.3. Summary of the average distance between atoms in the nanoparticles presented in picture 2.24.D along the X-axis.

Ruthenium (Y axis)		
amount of inter atoms distance measured	length (nm)	average distance between atoms (nm)
11	2.959	0.269
11	2.965	0.270
8	2.154	0.269
4	1.054	0.264
10	2.762	0.276
5	1.349	0.270
12	3.255	0.271

Table 2.4. Summary of the average distance between atoms in the nanoparticles presented in picture 2.24.D along the Y-axis.

The interatom distance "a" is 0.305nm in average while the interatom distance "b" corresponds to 0.27nm. The lattices composing the system studied can then be described:

$$a = 0.3 \neq b = 0.27nm \neq c\,, \alpha = \beta = 90^o \; and \; \Upsilon = 120^o$$

α and β values are considered to be 90^o due the perfect aligment of the atoms along the Z-axis (called tunnel effect). This crystalline structure cannot be identified as any known structure. It is extremely similar to the hexagonal structure but with an "a" value different from the one of "b".

This phenomenon is called a monoclinic distortion and corresponds to the elongation of the lattice constants that result from a number of external factors such as pressure, temperature, etc.... In this case, we believe that the elongation of the constant "*a*" is due to an epitaxial effect of the underlying agarose substrate. Indeed, Arnott *et al.*[53] reported that two strands forming the double helix of agarose can be overlapped by a translation (along the X-axis here) of 0.316nm. We could then suppose that the organisation of the atoms along the X-axis should correspond to this distance as the strands are closely packed together and so should alter the inter atoms distance. In z direction, the distance between Ru atoms should be compliant with the 0.27 nm expected from the hexagonal lattice organisation.

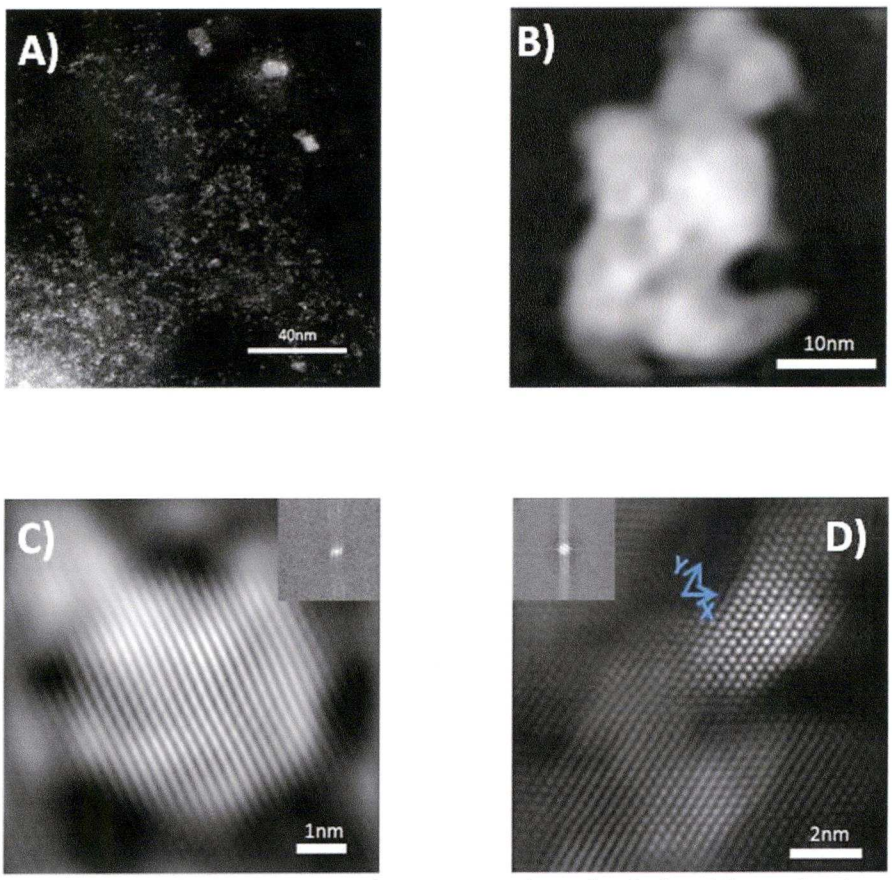

Figure 2.24 TEM pictures of agarose piece loaded with ruthenium nanoparticles. (A) shows a dust homogeneously loaded with ruthenium colloids. This dust presents few aggregates (B) and a lot of small colloids(C). (D) exhibits the decoration of the gel pattern by atoms.

Finally, the atomic layer exhibited in Figure 2.24.D exhibits an heterogeneous intensity though its surface. This is due to the differences

in Z-contrast. The intensity becomes more important when more atoms are on top of each other along the Z-axis. This means that atoms are also organized along the z-axis and their perfect overlapping (same x and y coordinates) could be related to the presence of a crystalline structure. The Z-contrast allows the determination of the number of atoms aligned along the Z-axis by quantifying the intensity on each point of the surface (as presented in section 2.2.2.4). The results are presented in appendix 2.9. The structure analysed exhibits some areas were just single atoms are present along the Z-axis. The number of atoms aligned along Z increase as we go along the Y axis, and it reaches its maximum point where 11 atoms are on top of each other. The number of atoms along Z decreases again after this point. A simulation of this three dimensional organization of the Ru atoms is presented in Figure 2.25.

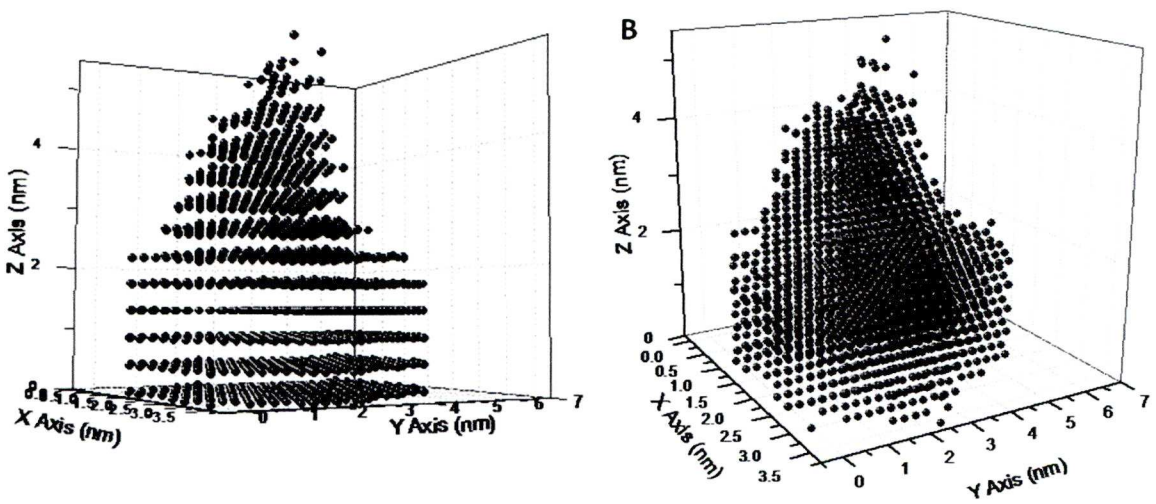

Figure 2.25. (A) Simulation of the three dimensional organization of the Ru atoms in the agarose hydrogel.(B) shows the same simulation in a different angle

The difference in number of atoms along the Z-axis could just correspond to the irregularity in the volume of the dust of Ru-gel analysed. The interesting point of this analysis was to confirm the three dimensional atomic organization of the monolayer analysed here and therefore a possible patterning of the ruthenium atoms by the gel structure.

2.4 Conclusion

The *in-situ* preparation of nanoparticles in an agarose hydrogel matrix has been demonstrated here. Experiments were carried out on five different metals all yielding similar results. Figure 2.18 exhibits a general model of this new material. Large colloids appear on the surface of the network as well as small clusters inside of the hydrogel pattern. This phenomenon stems from the nature of the network which is made of a threefold of double helix. When the pure piece of gel is soaked in the metal salt solution, the metal ions attach to the helix until saturation. The reduction of the system by $NaBH_4$ involves the formation of small cluster onto each helix. On the other hand, the heterogeneous distribution of the close-packed double helix though the volume of the gel in addition to the presence of imperfections in the double helix affect the stabilization of some clusters. The average size of these clusters is then larger (few nm). Amorphous colloids can also be detected in some localized areas. The existence of such"glassy colloids" has never been reported before.

An increase of the metal salt concentration used during the synthesis involves an increase of the average size and number of nanoparticles in the gel. This phenomenon can be explained by the saturation of the gel. Indeed, an increase of the metal ion concentration implicates the replacement of the $-O^-$ groups by –OH (hydrolysis) and an opening of the polysaccharide chains. A second approach suggests that the increase of the average gold nanoparticle size is only due to the increase in number of gold atoms in the gel pore for the same amount of stabilizing agent available. Finally, the ruthenium can be considered as a particular case. Indeed, while the other metals adopt similar decoration pattern, ruthenium is decorating the gel nanostructure with a three dimensional atomic multi-layer and the interatomic distance seems to depend on the gel structure.

References

1. D. L. Feldheim, C. A. Foss Jr, "Metal Nanoparticles Synthesis, Characterization and Applications", **2002**, Marcel Dekker, New York,(Eds.).

2. S. Link, Z. L. Wang, M. A. El-Sayed, *Journal of Physical Chemistry B* **1999**, *103*, 3529.

3. V. F. Puntes, K. M. Krishnan, A. P. Alivisatos, *Science* **2001**, *291*, 2115.

4. Y. G. Sun, Y. N. Xia, *Science* **2002**, *298*, 2176.

5. M. Grzelczak, J. Perez-Juste, P. Mulvaney, L. M. Liz-Marzan, *Chemical Society Reviews* **2008**, *37*, 1783.

6. F. Caruso. "Colloids and Colloid Assemblies", **2004**, Wiley-VCH, Weinheim (Ed.).

7. Kotov, N. A. "Nanoparticle Assemblies and Superstructures", **2005**, CRC Press, Boca Raton, (Eds.).

8. V. Subramanian, E. E. Wolf, P. V. Kamat, *Langmuir* **2003**, *19*, 469.

9. Y. Niu, R. M. Crooks, *Comptes Rendus Chimie* **2003**, *6*, 1049.

10. M. Yang, Y. Yang, Y. Liu, G. Shen, R. Yu, *Biosensors and Bioelectronics* **2006**, *21*, 1125.

11. P. Karam, L. I. Halaoui, *Analytical Chemistry* **2008**, *80*, 5441.

12. M. C. Daniel, D. Astruc, *Chemical Reviews* **2004**, *104*, 293.

13. A. C. Templeton, M. J. Hostetler, E. K. Warmoth, S. W. Chen, C. M. Hartshorn, V. M. Krishnamurthy, M. D. E. Forbes, R. W. Murray, *Journal of the American Chemical Society* **1998**, *120*, 4845.

14. G. J. Hutchings, M. Haruta, *Applied Catalysis a-General* **2005**, *291*, 2.

15. M. Haruta, *Nature* **2005**, *437*, 1098.

16. A. Corma, H. Garcia, *Chemical Society Reviews* **2008**, *37*, 2096.

17. I. Hussain, S. Graham, Z. X. Wang, B. Tan, D. C. Sherrington, S. P. Rannard, A. I. Cooper, M. Brust, *Journal of the American Chemical Society* **2005**, *127*, 16398.

18. Z. X. Wang, B. E. Tan, I. Hussain, N. Schaeffer, M. F. Wyatt, M. Brust, A. I. Cooper, *Langmuir* **2007**, *23*, 885.

19. D. Zanchet, C. M. Micheel, W. J. Parak, D. Gerion, A. P. Alivisatos, *Nano Letters* **2001**, *1*, 32.

20. D. Zanchet, C. M. Micheel, W. J. Parak, D. Gerion, S. C. Williams, A. P. Alivisatos, *Journal of Physical Chemistry B* **2002**, *106*, 11758.

21. W. J. Parak, D. Gerion, T. Pellegrino, D. Zanchet, C. Micheel, S. C. Williams, R. Boudreau, M. A. Le Gros, C. A. Larabell, A. P. Alivisatos, *Nanotechnology* **2003**, *14*, R15.

22. J. Cai, S. Kimura, M. Wada, S. Kuga, *Biomacromolecules* **2009**, *10*, 87.

23. Y. M. Mohan, J. P. Dickson, K. E. Geckeler, *Polymer International* **2007**, *56*, 175.

24. L. M. Bronstein, O. A. Platonova, A. N. Yakunin, I. M. Yanovskaya, P. M. Valetsky, A. T. Dembo, E. E. Makhaeva, A. V. Mironov, A. R. Khokhlov, *Langmuir* **1998**, *14*, 252.

25. L. M. Bronstein, O. A. Platonova, A. N. Yakunin, I. M. Yanovskaya, P. M. Valetsky, A. T. Dembo, E. S. Obolonkova, E. E. Makhaeva, A. V. Mironov, A. R. Khokhlov, *Colloids and Surfaces A: Physicochemical and Engineering Aspects* **1999**, *147*, 221.

26. D. I. Svergun, E. V. Shtykova, M. B. Kozin, V. V. Volkov, A. T. Dembo, L. M. Bronstein, O. A. Platonova, A. N. Yakunin, P. M. Valetsky, *Journal of Physical Chemistry B* **2000**, *104*, 5242.

27. K. M. Choi, K. J. Shea, *Journal of the American Chemical Society* **1994**, *116*, 9052.

28. C. S. Love, V. Chechik, D. K. Smith, K. Wilson, I. Ashworth, C. Brennan, *Chemical Communications* **2005**, 1971.

29. X. D. Wang, C. E. Egan, M. F. Zhou, K. Prince, D. R. G. Mitchell, R. A. Caruso, *Chemical Communications* **2007**, 3060.

30. L. Hughes, M. F. Wyatt, B. K. Stein, A. G. Brenton, *Analytical Chemistry* **2009**, *81*, 543.

31. R. C. Beavis, B. T. Chait, H. M. Fales, *Rapid Communications in Mass Spectrometry* **1989**, *3*, 432.

32. K. Strupat, M. Karas, F. Hillenkamp, *International Journal of Mass Spectrometry and Ion Processes* **1991**, *111*, 89.

33. R. C. Beavis, T. Chaudhary, B. T. Chait, *Organic Mass Spectrometry* **1992**, *27*, 156.

34. L. Ulmer, J. Mattay, H. G. Torres-Garcia, H. Luftmann, *European Journal of Mass Spectrometry* **2000**, *6*, 49.

35. T. D. McCarley, R. L. McCarley, P. A. Limbach, *Analytical Chemistry* **1998**, *70*, 4376.

36. A. M. Belu, J. M. DeSimone, R. W. Linton, G. W. Lange, R. M. Friedman, *Journal of the American Society for Mass Spectrometry* **1996**, *7*, 11.

37. A. Marie, S. Alves, F. Fournier, J. C. Tabet, *Analytical Chemistry* **2003**, *75*, 1294.

38. P. Nativo, I. A. Prior, M. Brust, *Acs Nano* **2008**, *2*, 1639.

39. A. G. Kanaras, F. S. Kamounah, K. Schaumburg, C. J. Kiely, M. Brust, *Chemical Communications* **2002**, 2294.

40. D. Zanchet, B. D. Hall, D. Ugarte, *Journal of Physical Chemistry B* **2000**, *104*, 11013.

41. S. I. Stoeva, B. L. V. Prasad, S. Uma, P. K. Stoimenov, V. Zaikovski, C. M. Sorensen, K. J. Klabunde, *Journal of Physical Chemistry B* **2003**, *107*, 7441.

42. Scherrer, P. (1918). "*Göttinger Nachrichten*" **98**.

43. B. L. Johansson, M. Andersson, J. Lausmaa, P. Sjovall, *Journal of Chromatography A* **2004**, *1023*, 49.

44. P. Sjovall, J. Lausmaa, B. L. Johansson, M. Andersson, *Analytical Chemistry* **2004**, *76*, 1857.

45. M. J. Kramer, I. L. Roth, *Canadian Journal of Microbiology* **1968**, *14*, 1297.

46. L. N. Waller, N. Fox, K. F. Fox, A. Fox, R. L. Price, *Journal of Microbiological Methods* **2004**, *58*, 23.

47. J. C. Love, L. A. Estroff, J. K. Kriebel, R. G. Nuzzo, G. M. Whitesides, *Chemical Reviews* **2005**, *105*, 1103.

48. N. Fishelson, I. Shkrob, O. Lev, J. Gun, A. D. Modestov, *Langmuir* **2001**, *17*, 403.

49. E. Hutter, J. H. Fendler, D. Roy, *Journal of Physical Chemistry B* **2001**, *105*, 11159.

50. J. Xu, L. H. Zhou, H. L. Liu, Y. Hu, *Journal of Experimental Nanoscience* **2006**, *1*, 103.

51. G. Y. Shen, H. Wang, G. L. Shen, R. Q. Yu, *Analytical Biochemistry* **2007**, *365*, 1.

52. J. L. Elechiguerra, J. Reyes-Gasga, M. J. Yacaman, *Journal of Materials Chemistry* **2006**, *16*, 3906.

53. S. Arnott, A. Fulmer, W. E. Scott, I. C. M. Dea, R. Moorhouse, D. A. Rees, *Journal of Molecular Biology* **1974**, *90*, 269.

54. A. V. Kabashin, M. Meunier, C. Kingston, J. H. T. Luong, *Journal of Physical Chemistry B* **2003**, *107*, 4527.

55. P. Raveendran, J. Fu, S. L. Wallen, *Journal of the American Chemical Society* **2003**, *125*, 13940.

56. H. Z. Huang, X. R. Yang, *Carbohydrate Research* **2004**, *339*, 2627.

57. J. P. Sylvestre, A. V. Kabashin, E. Sacher, M. Meunier, J. H. T. Luong, *Journal of the American Chemical Society* **2004**, *126*, 7176.

58. J. C. Liu, P. Raveendran, G. W. Qin, Y. Ikushima, *Chemical Communications* **2005**, 2972.

59. J. C. Liu, G. W. Qin, P. Raveendran, Y. Kushima, *Chemistry-a European Journal* **2006**, *12*, 2132.

60. C. M. Sun, R. J. Qu, H. Chen, C. N. Ji, C. H. Wang, Y. Z. Sun, B. H. Wang, *Carbohydrate Research* **2008**, *343*, 2595.

61. F. Atamny, D. Duff, A. Baiker, *Catalysis Letters* **1995**, *34*, 305.

62. S. Katano, E. Herceg, M. Trenary, Y. Kim, M. Kawai, *Journal of Physical Chemistry B* **2006**, *110*, 20344.

63. A. Nakahara, M. Nakamura, K. Sumitani, O. Sakata, N. Hoshi, *Langmuir* **2007**, *23*, 10879.

64. J. O. Malm, J. O. Bovin, A. K. Petford-Long, D. J. Smith, *Journal of Crystal Growth* **1988**, *89*, 165.

65. N. S. Anderson, J. W. Campbell, M. M. Harding, D. A. Rees, J. W. B. Samuel, *Journal of Molecular Biology* **1969**, *45*, 85.

Chapter 3: Characterisation of the electronic properties of the Au-gel

3.1 Introduction

Assembly of nanoparticles has been subject to many studies over the past decades[1,2]. These assemblies can be formed along one[1,3-12], two[12-16], or three dimensions[17-24] and they often exhibit interesting optical[30,31], magnetic[32,33] and electronic properties[25-29]. For instance, there has been great interest in the linear assembly of metal nanoparticles and the electronic transport characteristics of the resulting nanowire-type structures.[34,35] Likewise, electron transport through two-dimensional films of metal nanoparticles has been studied extensively[36-38], and there are several promising approaches to the development of sensing devices based on such materials[39-42]. In most studies, the assemblies can be divided in two categories: (i) template, which means that the organization of the nanoparticles is imposed or guided by the structure of their substrates or environment, or (ii) template free organization of the nanoparticles which is spontaneous and, for example, due to dipole-dipole interaction or the heterogeneous distribution of the stabilizing agents.

Here, as introduced in Chapter 2, an agarose hydrogel is used as a three dimensional scaffold for the formation gold nanoparticles. In principle, as reported in Chapter 2, the interparticle spacing in these structures could be controlled both by the metal loading applied and by the water content of the gel. Interesting electrical properties are expected close to the percolation threshold which, for sufficiently loaded gels should be adjustable by the gradual removal of water (see Figure 3.1).

This chapter presents the evolution of the electronic properties of the gel depending on the concentration of the feed solution used and on the dehydration ratio of the gel. A correlation between the results obtained and the structure of the Au-gel is proposed. Then the formation of the conductive pathways is analysed and described. Finally, the recovery of the electronic properties of the Au-gel upon rehydration is investigated and discussed.

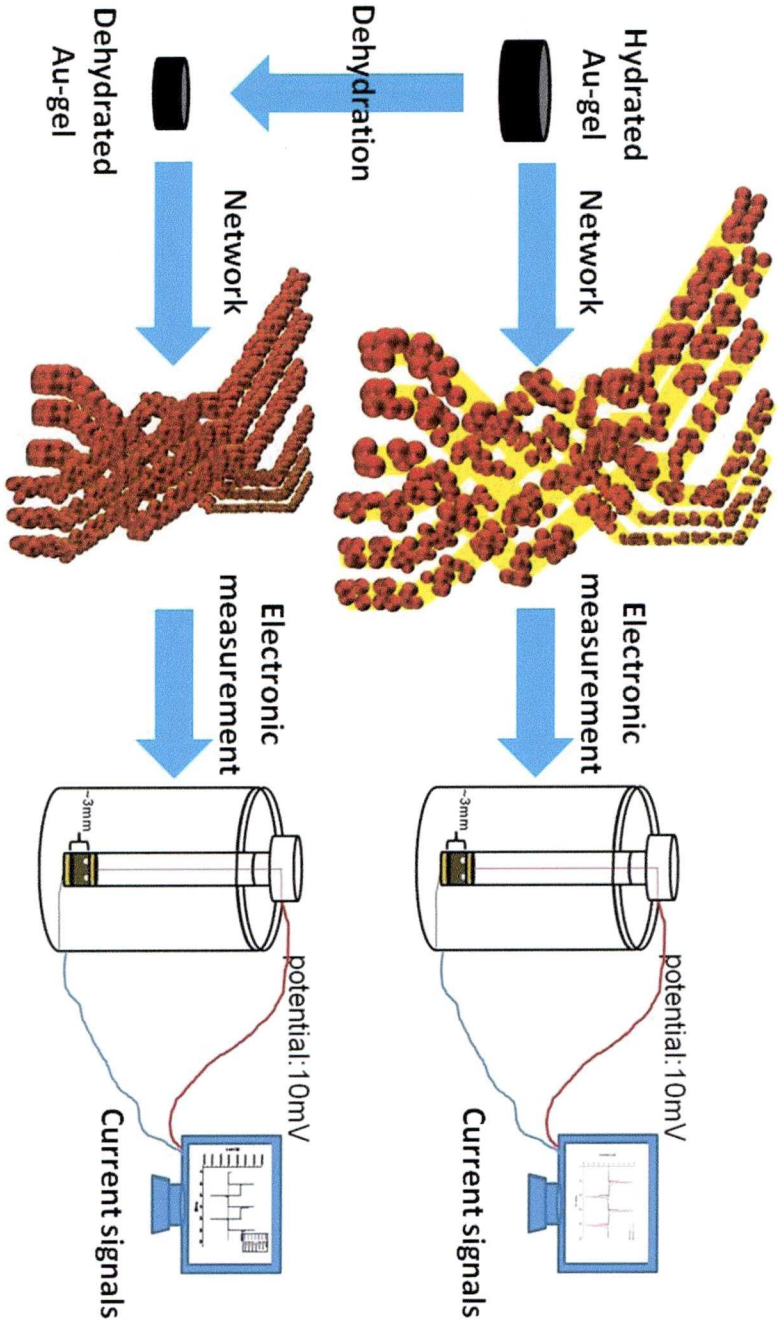

Figure 3.1 Scheme presenting the principle of the study. Basically, this cartoon shows that a transition between poor and good conductivity should occur upon dehydration of the gold loaded gel (introduced in chapter 2) due to the reduction of the interparticle distances.

3.2 Theory study of the electronic properties of the Au-gel

The theoretical approach presented here is based on three assumptions. Firstly, the aggregate are considered to be filled entirely with fibres. Secondly, the macromolecular aggregates that form the gel structure are considered of cylindrical shape. Thirdly, the coating by the GNPs is considered as uniform on the surface of the aggregates. The assumptions are presented in Figure 3.2.

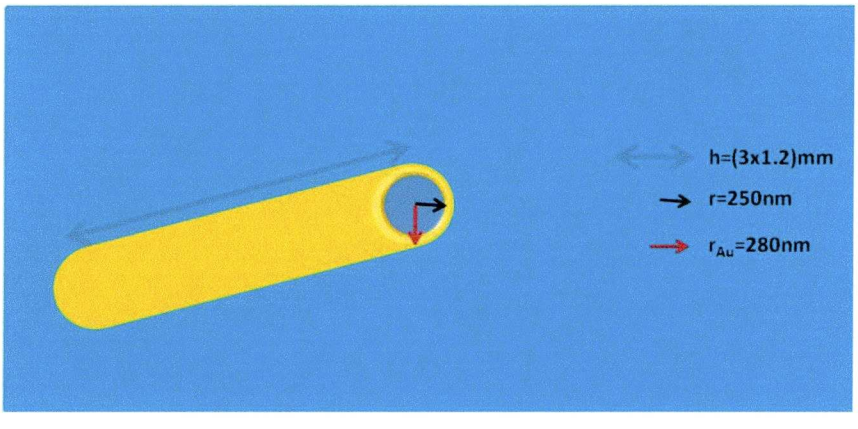

Figure 3.2 Cartoon exhibiting the homogeneous coating of the agarose aggregate's surface with GNPs.

As reported by Bulone *et al.*[43], the width of these aggregates correspond to 500nm and are composed of fibres. The volume fraction ϕ of the fibres[44] in the gel can be defined by:

$$\phi = C_{agarose}/(\rho_{dry\ agarose}\ x\ \omega_{agarose})$$

With $C_{agarose}$ being the concentration of agarose in the gel (w/v), $\rho_{dry\ agarose}$ the dry agarose density (1.64 mg/ml)[(45)] and $\omega_{agarose}$ the mass fraction of agarose in the fibres (0.625)[46].

Knowing that here the concentration of agarose is 5.4%, the volume fraction of fibres in the gel is:

$$\phi = 0.052$$

The total volume of fibres V_T in a gel of the average volume of the pieces here, i.e. $0.23cm^3$ is given by:

$$V_T = 0.052\ x\ 0.23 = 1.121x10^{-2}cm^3$$

If we assume that the aggregates of fibres also are cylindrical, the volume of each aggregate can be defined by:

$$V_{single\ aggregate} = \pi r^2 h$$

with r being the aggregate radius, and h the length of the aggregate. While the r has a value of 250nm, the h value is assumed to be similar to the thickness of the piece of gel. For the calculation, we increase the h value in comparison to the gel by 20% to account for the fact that the fibres are randomly organized and tilted in the gel:

$$V_{single\ aggregate} = \pi(250x10^{-7})^2\ x\ (0.3x1.2) = 7.07x10^{-10}cm^3$$

This means that the number of aggregates in the gel is:

$$N_{aggregates} = \frac{V_T}{V_{single\ aggregate}} = \frac{1.121x10^{-2}}{7.07x10^{-10}} = 1.59x10^7$$

If we consider a homogeneous coating of the external structure of the aggregates with GNPs of 30 nm (as the internal will be decorated with small cluster and therefore can be considered as an insulator), the volume of gold per aggregate can be expressed by:

$$V_{Au\ per\ aggregate} = \pi r_{Au}^2 h - \pi r^2 h = 1.8x10^{-10}cm^3$$ (refer to Figure 3.2 for r_{Au} value)

So the minimum mass of gold needed to achieve complete coating of the fibres in the gel is:

$$m_{Au} = \rho_{Au}\ x\ N_{aggregates} x\ V_{Au\ per\ aggregate} = 19.3x\ 1.59.10^7 x1.8x10^{-10}$$
$$= 52.37mg$$

The concentration of Au needed in the gel can then be determined as:

$$C_{gold\ in\ the\ gel} = \frac{m_{Au}}{M_{HAuCl_4} x\ V_{gel}} = \frac{52.37x10^{-3}}{393.83x\ 0.23.10^{-3}} = 578mM$$

If we correlate this value to the graph presented in Figure 2.17 in Chapter 2, the concentration of the feed solution should be:

$$C_{feed\ solution} = e^{\frac{C_{gold\ in\ gel}+153.77}{119.15}} = 466mM$$

Of course in our case this theoretical study does not take into account that we need first to saturate the nanoscale and the transition scale of the gel structure before being able to coat the external structure of the network. If that these two scales are assumed to be saturated when the gradient slope decreases dramatically, the final concentration of the feed solution could be estimated by:

$$566mM < C_{final feeding\ solution} < 666mM$$

This theorytical study is based on many of assumptions (aggregates fully filled by fibres, shape of the aggregates, etc.) and therefore the results will not be considered as one hundred percent accurate. It should be taken as an estimation of the Au(III) concentration needed to obtain percolation of a wet hydrogel.

3.3 Experimental

3.3.1 Materials

This investigation has required the use of three compounds: Hydrogen tetrachloroaurate ($HAuCl_4$) trihydrate and agarose which have been introduced in Chapter 2 and phosphorus pentoxide (P_2O_5) which has been purchased from Sigma-Aldrich.

3.3.1.1 Preparation of the samples

The samples have been prepared following the procedure presented in Chapter 2. Briefly, pieces of agarose gel were soaked in different

concentration of Au (III) feed solution for 24 hours, followed by an immersion for 24 hours in dilute solution of $NaBH_4$ (500mM).

3.3.2 Characterisation and dehydration

3.3.2.1 Electrical measurements

For the characterisation of charge transport across the gels cylindrical samples of 8.5 mm diameter were cut out from the original 3.2 mm thick wedges using a circular blade. The samples were sandwiched between two independently contacted Au foil electrodes inside a PTFE housing. To ensure good contact and reproducibility of results, a slight mechanical pressure of ca. 1.7 kPa was applied with a PTFE cylinder and a 10g weight. The current-voltage response was measured using an Autolab PGSTAT 10 potentiostat (Windsor Scientific, UK) in two electrode configuration. For electrical characterisation gels were first thoroughly dialysed to remove most ionic species from the aqueous phase. Freshly dialysed ("wet") gels were superficially dried with tissue paper and the current response to applied voltage steps of 10 mV across the gel was measured. At such small voltages no Faradayic processes occur so that all currents are either due to capacitive charging, ionic migration or electron hopping between the Au particles. Indeed, evidence for heterogeneous electron transfer between the electrodes and the gel was only found at voltages above *ca.* 400 mV. Measurements have been carried out on the gel prepared with different Au(III) concentrations and at different stage of dehydration. The dehydration of the gel has been achieved by two different methods (very slow dehydration in the refrigerator and relatively dehydrationin a dessicator in the presence of phosphorus pentoxide).

3.3.2.2 Dehydration of the gels

The first dehydration method employed in this study is the slow variant in the refrigerator. Basically, the different gels have been stored in the refrigerator for 30 days after being dialyzed. After this period of time, the gels are partially dehydrated with a loss of 40% of their original weight. The current responses obtained for the gels with different Au loading have been compared

as well as the difference of responses between each gel completed hydrated, and partially dehydrated.

The second method has involved the use of phosphorus pentoxide in order to accelerate the dehydration process. Basically, the different Au-gels have been placed in a dessicator in the presence of phosphorus pentoxide. The weight loss and the current response over time and voltage of each gel have been measured every hour.

3.3.2.3 Cell design

The cell employed in this study is presented in Figure 3.3. Basically the device is composed of two elements. The first is a cylindrical base made of silicon. The second is a probe which fits exactly into a hole of the silicon base so that the Au-gel is sandwiched between two gold electrodes. The two electrodes are attached to wires with conductive glue (silver epoxy). These two wires allow a connection between the cell measurement and the potentiostat.

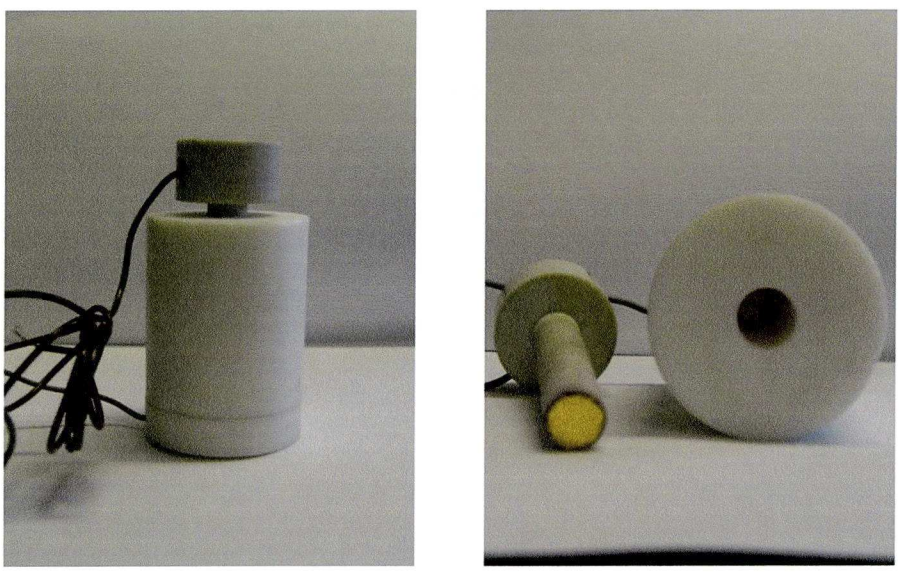

Figure 3.3 Cell measurement used in this chapter. The cell is made of silicon and the electrode are in gold .

3.3.2.4 Microscopy

Scanning Electron Microscopy (SEM): High resolution imaging of the gel morphology was performed using a Hitachi S-4800 cold Field Emission Scanning Electron Microscope (FE-SEM). The dry samples were prepared on 15 mm Hitachi M4 aluminium stubs using an adhesive high purity carbon tab. The FE-SEM measurement scale bar was calibrated using certified SIRA calibration standards. Imaging was conducted at a working distance of 8 mm and a working voltage of 3 kV using a mix of upper and lower secondary electron detectors. An Oxford Instruments 7200 EDX detector was used to conduct elemental analysis of the sample composition using 30 kV working voltage.

HAADF-STEM: The same equipment and protocol described in Chapter 2 was employed here.

3.4 Results

3.4.1 Dehydration in refrigerator

Figures 3.4.a and 3.4.b show the current responses of freshly dialysed gels with different loadings of Au nanoparticles controlled by the initial Au salt concentration of the feed solution. Simply by looking at the current response curves a clear trend is observed showing increasing capacitance and decreasing conductivity with increasing metal loading, except for the highest metal loading which shows a slight increase in conductivity. While the decrease in conductivity appears counterintuitive at first sight, it simply indicates that electron transport via the metal content of the gel is negligible at most but the highest metal loading. Indeed before percolation, the inter particle distance is too large for any electron hopping. At very low concentration the dielectric constant of the material is higher than the pure gel so the conductivity appears lower. The metal inclusions, however, appear to contribute significantly to the capacitance of the material thereby lowering the electric field inside the gel. Once capacitive charging is complete, the remaining conductivity is due to ionic migration. This in turn depends on the

local electric field which explains the observed decrease in conductivity with increasing metal nanoparticle loading.

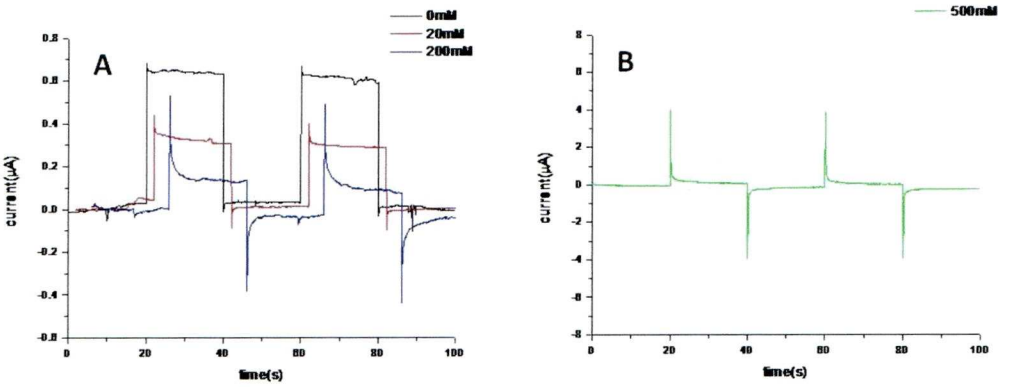

g
ure 3.4 (A) Comparison of the current responses over time between a pure piece of agarose gel hydrated and two hydrated Au-gel with different concentrations of feeding solution(20mM and 200mM). (B) shows the currents response over time of the other wet Au-gel with high concentration of feeding solution (500mM).

A different picture arises when the gels after dialysis are partially dehydrated ("dry"). Here, this was achieved simply by ageing them under controlled conditions in a refrigerator. The results are shown in Figure 3.5.a and 3.5.b. Again from looking at the current response curves, the capacitance still increases with increasing metal loading, but the conductivity now remains approximately constant at a value about ten times lower than that of the unloaded "wet" gel.

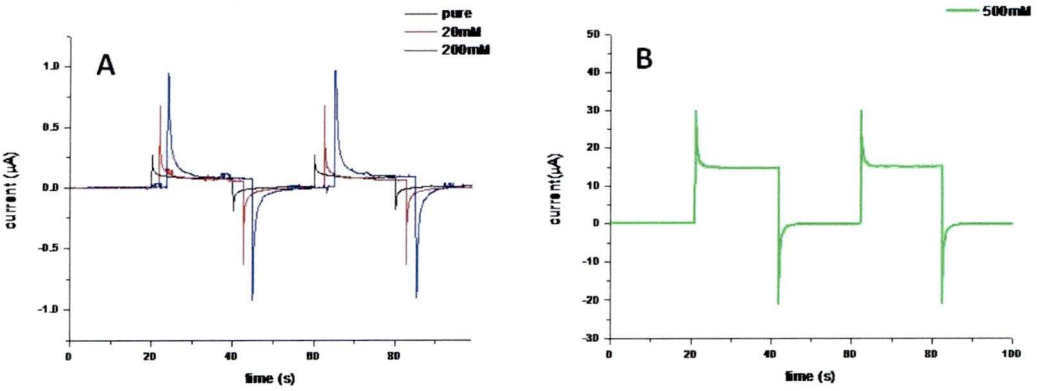

3.5 (A) Comparison of the current responses over time between the gels presented in Figure 3.4.A but partially dehydrated. (B) shows the current signal of the gel presented Figure 3.3.b but also partially dehydrated.

This suggests that in the "dry" material ion migration is impeded by the denser polymeric network. The conductivity remains constant at these low values up to a certain point, when it suddenly increases steeply by two orders of magnitude at a metal loading that we interpret as the percolation threshold, *i.e.* the appearance of the first conductive path across the gel via metal nanoparticles in contact with each other (Figure 3.6.a). This does not imply that the mechanism of conduction is metallic, since there will still be boundaries between the particles that may act as small insulating gaps but it means that the inter particle distance is small enough to allow charge transport through electron hopping. In addition to the much higher conductivity observed, the currents measured at this point exhibit strictly ohmic behaviour as demonstrated by successively increasing the values of the voltage steps (Figure 3.6.b)

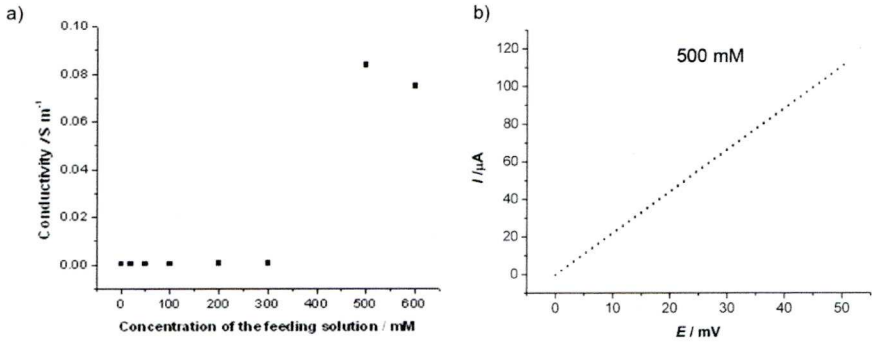

Figure 3.6 a) Conductivity of the dry gel as a function of the concentration of the feed solution used. b) Ohmic behaviour of dried gel with percolation.

For the purpose of gaining quantitative understanding of the charge transport behaviour observed in the present work, it is convenient to model the gel with the simple equivalent circuit (Figure 3.7) for a leaking capacitor shown in Figures 3.4 and 3.5. The current response to a voltage step is then given by:

$$i = \frac{U}{R_2} + \frac{U}{R_1} e^{\frac{-t}{R_1 C}}$$

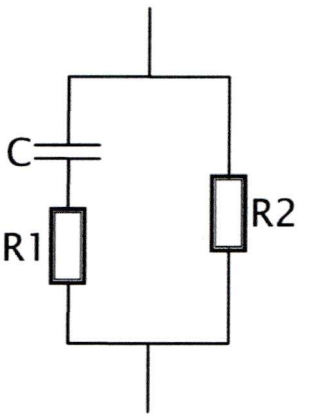

Figure 3.6. Equivalent electronic circuit of the gel with or without gold. The current answers provided by such electronic circuits are fitting the current answer of the gels studied in this chapter.

It is now possible to determine R_1, R_2 and C simply by fitting the experimental voltage step data using the previous equation. The results for all samples are summarized in Table 3.1 and support the above qualitative discussion of the current-voltage behaviour observed. Note, that the ohmic conductance, G, of the gels now equals $1/R_2$. The fitting of the voltage steps is presented in appendix (Appendices 3.1 and 3.2).

Concentration (mM)	Resistance				Capacitance	
	Dry		Wet		Dry	Wet
	R1/kΩ	R2/kΩ	R1/kΩ	R2/kΩ	C/μF	
0	53.466	131.235	188.457	13.366	12.2	2.45
20	16.04	144.358	80.199	33.262	20	11
200	10.445	90.223	25.778	75.978	105	21
500	0.662	0.69	2.485	20.623	872	58.1

Table 3.1 Table summarizing the values of R1, R2 and C obtained for the hydrated and partially dehydrated gels with different concentrations of feed solution.

3.4.2 Correlation of gel structure and charge transport properties

In this section, we correlate the evolution of the electronic behaviour of the gel upon the increase of the gold concentration determined in the section above with their respective network structures (decoration with GNPs) as presented in Chapter 2.

Knowing that R1 and C are in series, we suppose that they correspond to the internal structure of the network. In this case, R1 relates to ionic migration through the gel, and C to the small nanoparticles located on the surface of the agarose fibres made close packed double helix and separated with small clusters. Indeed, a capacitor can be defined as two conductors separated by an insulator: the larger the insulator the lower the capacitance value of the system. R2 is assumed to be related to the presence of larger nanoparticles decorating the surface of the fibre aggregates (microscale network structure).

For the hydrated gel, the R2 values do not show any dependency to the amount of gold present in the gel. This means, as reported before, that the electron transport through the large nanoparticles is negligible due to the significant interparticle distance. On the other hand, R1 and C values seem to be strongly dependent of the concentration of feed solution employed. First, the decoration of the internal structure with small gold cluster increases the dielectric constant of the medium[47] and therefore the electromagnetic permittivity of the gel. This is confirmed by the decrease of the value R1 between the 0 and 20mM gels. In addition, the presence of small nanoparticles on the surface of the fibres involves an increase of the capacitance value of the system as they are separated by insulating gaps (small clusters). As explained in Chapter 2, an increase of the gold concentration in the gel results in the saturation of its internal structure as well as a hydrolysis of the agarose molecules composing it and therefore a degradation of the nanoscale pattern of the polymer (opening chains of molecules which are here the stabilizing agents). These two phenomena are rationalized with an increase of the average size of the clusters/small particles and by a reduction of the inter-cluster/interparticle distances. They are associated to a decrease of the R1 value and to an enhancement of the C value.

When the gels are dried, distances between particles at the nanoscale and microscale are reduced. Consequently, the R1 and R2 values decrease and the C value increases. It is important to point out that the difference of R1, R2 and C values between the 400mM and 500mM systems is considerable. This represents the percolation point of the composite and is defined by electrons hopping between the nanoparticles and therefore the appearance of a conductive path through the gel. The presence of high R and C values simultaneously can be explained by the random organisation of the gel structure and consequently the heterogeneous decoration of the pattern with the gold nanoparticles.

The data presented in this section of the chapter confirm the possible tunability of the electronic properties of the Au-gel using a dehydration approach. The next step of the study was to analyse the dependency of the electronic properties of the different Au-gels relative to the dehydration ratio.

3.4.3 Chemical dehydration

3.4.3.1 Evaluation of R2

Figure 3.8.a shows a three dimensional graph of the results obtained. The x axis represent the weight loss of the gel upon dehydration ($\%_w$), the Y axis corresponds to the concentration (mM) of the feed solution used to prepare the gel and the Z axis represents the conductance of the gels ($\frac{1}{R_2}$). Firstly, this graph shows the existence of a dynamic percolation point as the gel exhibits a high conductance value at different concentrations and weight loss. This dynamic percolation point is located between 440 and 500mM. It seems to have a higher conductance value at 460mM than at 500mM. This may be due the fact that the measurements were taken every hour and therefore the true maximum conductance value of the percolation point may in fact lie between two measured data points. While the system percolates just once at 440 and 460mM, it appears to percolate three times at higher concentration value (500mM) and seems to be dependent of the dehydration ratio of the gel. After percolation, the system loses its high conductivity again. This indicates that the percolation is only temporary, fragile, and reversible.

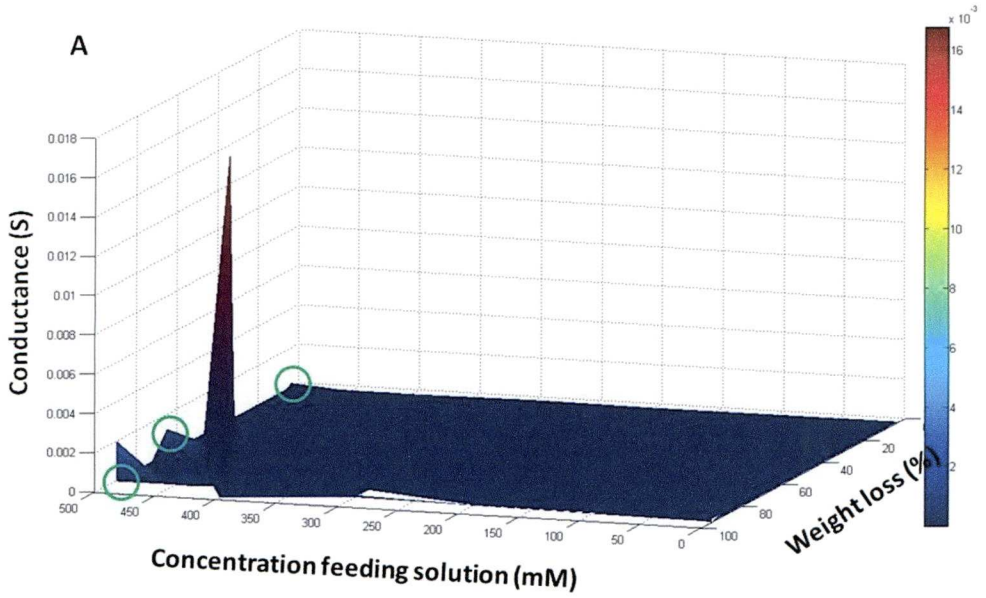

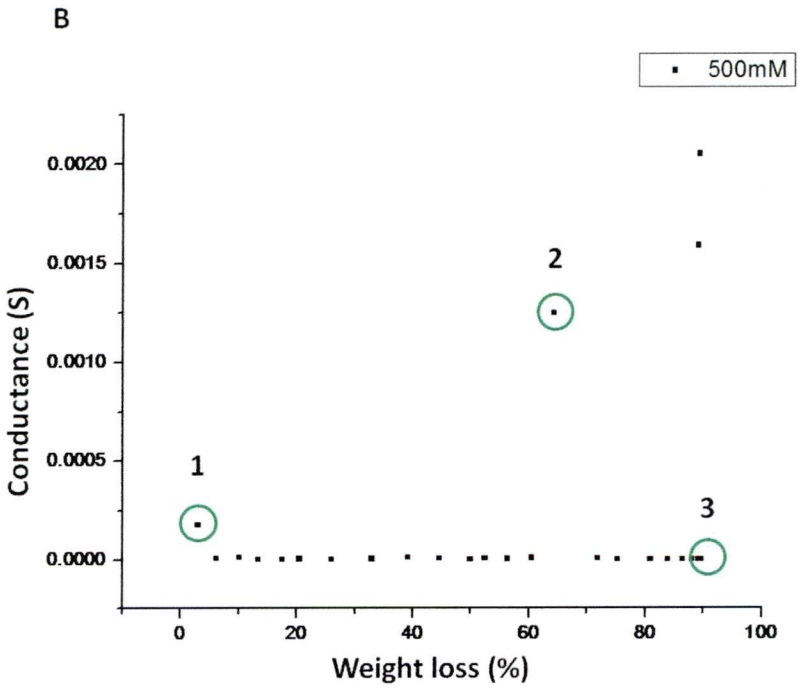

3FigureFigure 3.8 (A) three dimensional graph representation the evolution of the conductance of the Au-gel as a function of the concentration of the feed solution used and the dehydration ratio. (B) Evolution of the conductance value of the 500 mM Au-gel as a function of the dehydration ratio of the gel. The points 1, 2, 3 represents the points at which the 500mM Au-gel has been characterised via HAADF-STEM.

This phenomenon can be either due to the breaking of the gel structure upon fast dehydration or the Brownian motion of the nanoparticles combined with the three dimensional dewetting of the gel. The breaking of the gel structure would alter the electron hopping between the nanoparticles by increasing the distance between them and a stronger dehydration of the gel would reduce again the interparticle distance and consequently allow the electrons to flow through the nanoparticles. This would be characterised by a significant enhancement of the conductance value of the composite.

On the other hand, if this phenomenon is due to the Brownian motion of the nanoparticles and the dewetting of the gel, the lack of conductance between two successive percolation points would be explained by the appearance of insulating gaps at the original location of the nanoparticles which have moved away to form aggregates. In this case, the next percolation point would be reached when the gel structure has shrunk enough to reduce the size of these insulating gaps and to allow once more electron hopping between the nanoparticles aggregates. Figure 3.8.b tends to corroborate this hypothesis. For the 500 mM Au-gel, the lowest conductance value was obtained at highest weight loss (see values in the in the appendix 3.3). This figure exhibits also an increase of the conductance value between the different percolation points along the Y axis. This can be explained by the reduction of the general interparticle distance and consequently an increase of the number of nanoparticles available transport the charge.

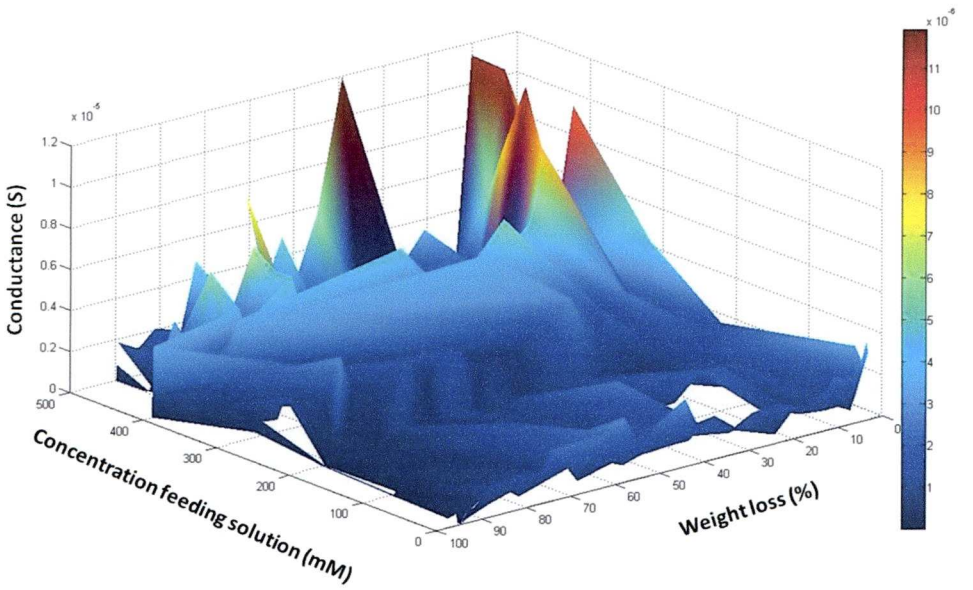

Figure 3.9 Expansion of the three dimensional graph presented in Figure 3.8.a to the low conductance values.

The very high conductance values at the percolation points make the presentation of the other values impossible on the scale of Figure 3.8.a. Therefore a second three dimensional graph which focuses on low values is shown in Figure 3.9. This graph also indicates fluctuation in conductance that may be due to rearrangement by a Brownian motion of the nanoparticles. At low concentrations of feed solution, the conductance value does not seem to have any dependency on the dehydration ratio of the gel. This indicates that the level of decoration of the microscale structure of the gel by large nanoparticles is poor. The shrinkage of the gel reduces the interparticle distance but not enough to allow electron hopping between them. As the concentration of the soaking solution is increased, the conductance values increase and conductive pathways seem to appear. These pathways appear to be strongly affected by the dehydration of the gel. From 200mM to 500mM, the conductance values evolve in wave form as a function of the dehydration ratio of the gel. The existence of these "minor" percolation points emanates from the appearance of small conductive pathway through the structure. This electronic state vanishes when some nanoparticles migrate to other locations (aggregates). The next "minor" percolation point is then reached when the

shrinkage of the gel (reduction on gel structure length) covers the distance travelled though by the nanoparticles.

In order to confirm the Brownian motion of the nanoparticles, the 500mM Au-gel has been investigated through scanning electron microscopy at different steps of the dehydration process (corresponding to the circles in Figure 3.8.b). The results are presented in the next session of the chapter.

3.4.3.2 Role of Brownian motion and electrophoretic mobility

Figure 3.10 shows a STEM picture of the 500mM Au-gel at different levels of dehydration. Figure 3.9.a and b correspond to the structure of the gel fully hydrated (a dust of the sample was deposited on the carbon grid). The first picture shows that the nanoparticles synthesized in the gel present originally different shapes such as spheres, rods and triangles much like the sweets found in the box of "Quality Street". This means that the wet gel is not percolating. On the other hand, Figure 3.10.b which corresponds to a STEM picture taken on another area of the same gel, exhibits the presence of nanoparticles aggregate in the composite. The shape of these aggregates suggests that the gel pattern acts as a scaffold for their formation. The presence of these nanoporous gold structure provides a conductive pathway trough the gel as proved by the conductance value presented in Figure 3.8.b (circle1). Figure 3.10.c and d show the STEM picture obtained on the gel at the second percolation point (circle 2 in Figure 3.8.b). The first picture clearly indicates the reduction of the distance between the "QS" nanoparticles. Most of them have already aggregated with each other. These new aggregates are still separated by some single nanoparticles decorating the microscale gel structure. These single nanoparticles facilitate the electron hopping between the aggregates and consequently the conductance value is enhanced in comparison with the previous percolating point. Figure 3.10.d shows that the aggregates are still using the gel network as a template even though they appear to be larger than the aggregates presented in the Figure 3.10.b. Finally, Figures 3.10.e and f exhibit the STEM pictures obtained on the totally shrunk gel. The first one shows that most of the large nanoparticles have percolated. They appear to form a perfect replica of the gel network structure. On the other hand, the picture presented in Figure 3.10.f reveals that

these aggregates, formed by the large nanoparticles, are not homogeneously distributed through the matrix. Some parts of the gel network are no longer covered by large particles and exhibit a row surface. However the structure of the gel can still be visualized through STEM. This indicates that the internal structure of the network is decorated by small gold cluster. This phenomenon is mainly due to the dewetting of the gel. All the large nanoparticles which decorated "homogeneously" the structure of the wet hydrogel have percolated with their neighbouring NPs upon dehydration. This has involved the formation of aggregates which are heterogeneously distributed through the matrix. After total dehydration, the inter-aggregate distance is maximum and electron hopping is no longer possible between them. Consequently, the gel can be considered as an insulator and so present a poor capacitance value (circle 3 in Figure 3.8.b).

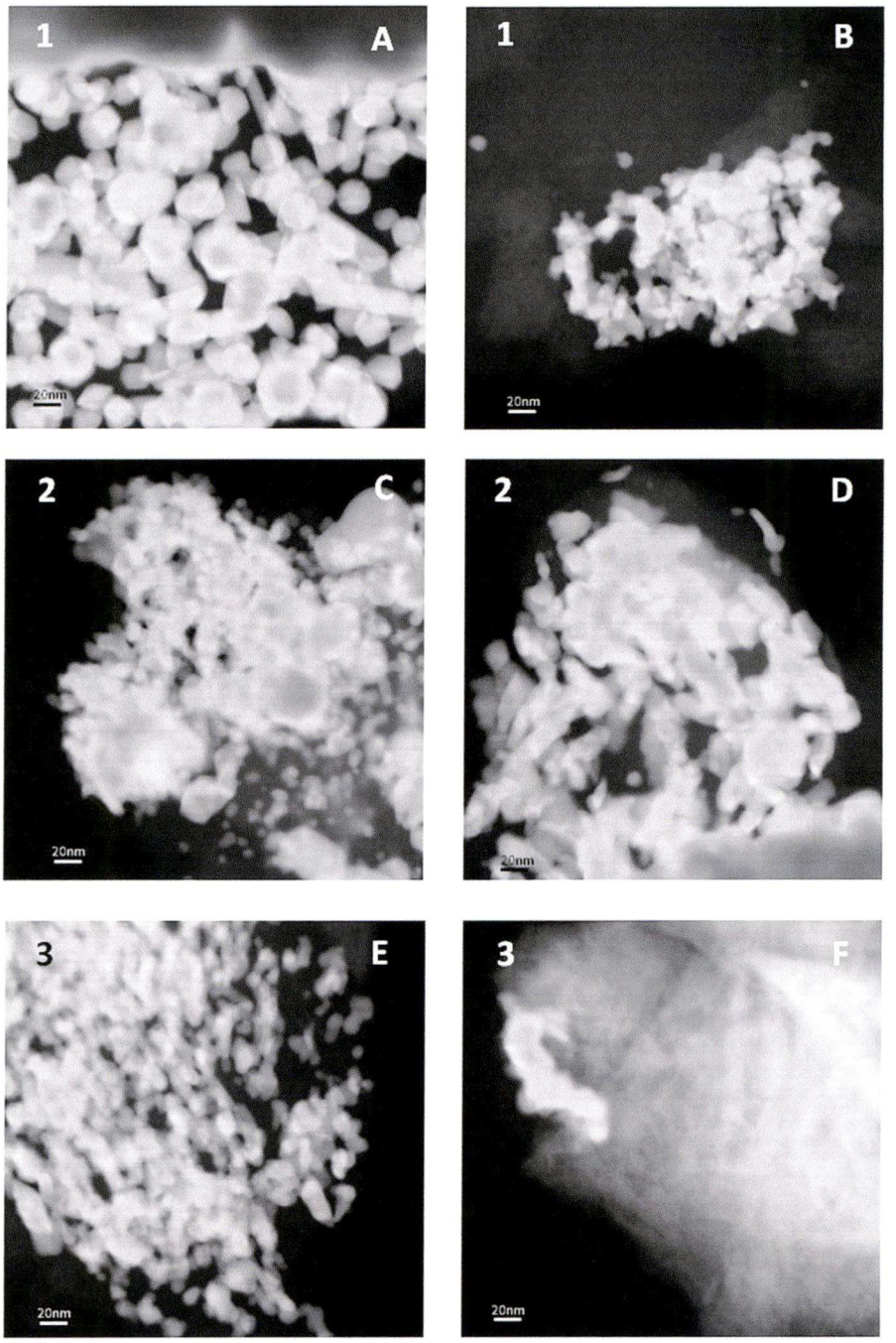

Figure 3.10 (A) and (B) show HAADF-STEMS picture obtained from the hydrated 500mM Au-gel in two different areas. (C) and (D) show HAADF-STEM pictures of the same gels upon partial dehydration. They correspond to the structure of the gel at the second percolation points (circle 2 in Figure 3.8.b). (E) and (F) correspond to the HAADF-STEM pictures of the same gel after complete dehydration. Aggregates of large nanoparticles can be detected heterogeneously distributed in the gel.

3.4.3.3 Concentration requirement for percolation of hydrated Au-gel

The concentration of the feed solution was increased until the pH of the solution caused the destruction of the gel. This limitation corresponds to 600mM. Figure 3.11.a compares the current answers obtained for the Au-gels over time for different concentrations of feeding solution when 10mV is applied to the gel samples.

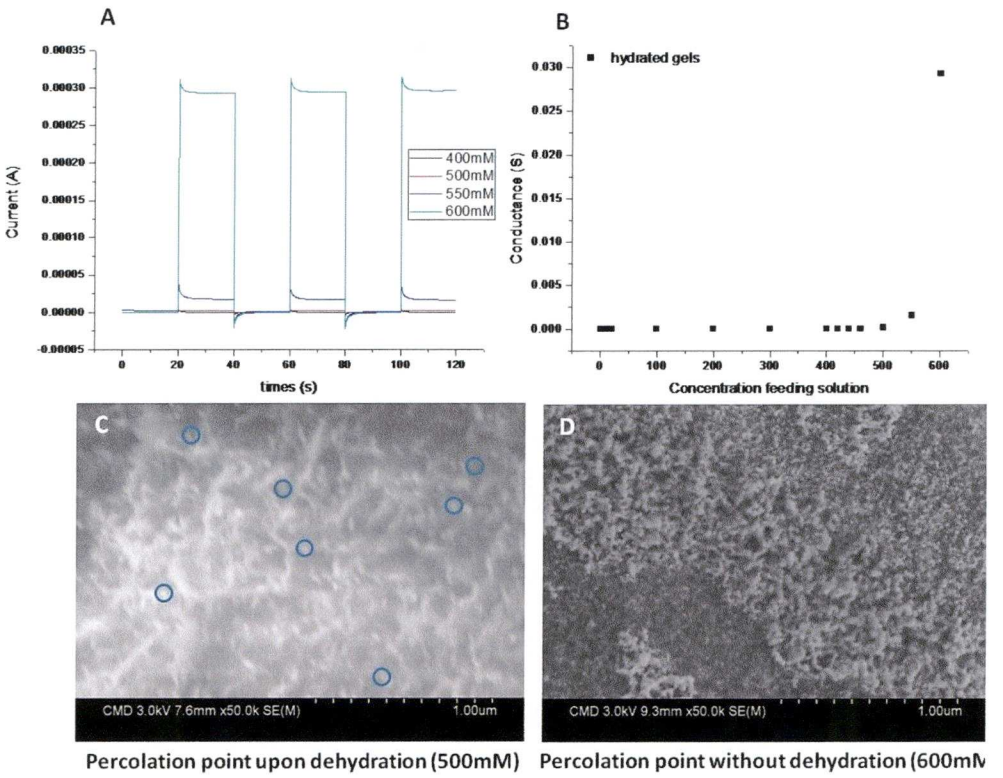

Figure 3.11 (A) compares the current responses obtained for the hydrated Au-gel with different concentration of feed solution. (B) presents the evolution of the conductance value (determined by analysis of the signals presented in (A)) as a function of the concentration of feed solution employed. (C) shows the SEM image of the 500mM au-gel at the third percolation point. Aggregates of nanoparticles can be visualized as well as single nanoparticles (some of them are circled in blue), (D) shows a SEM image of the 600mM au-gel completely hydrated. Polydispersed nanoparticles (in size) can be visualized but no aggregates can be detected.

Figure 3.11.a shows that the current response is significantly higher at 600mM than at lower concentrations. The evolution of the conductance of the hydrated Au-gel as a function of the concentration of the feed solution has been plotted in Figure 3.11.b. The conductance is enhanced by 2.10^3times between 400mM and 600mM. The system seems to percolate when a feeding solution with a concentration of 500-550mM is employed. This range of concentration matches the value proposed in the theoretical study in section 3.2. This means that at this range of concentration, the interparticle distance is small enough to transport the charge from one electrode to the other by electron hopping between the nanoparticles. Figure 3.11.c shows a SEM picture of the 500mM Au-gel at the third percolation point. The picture exhibits that the system is composed of aggregates which are decorating the gel pattern and of single particles (some of them are circled in blue here). As explained previously, it is believed that the conductive pathways are obtained through the Brownian motion of the singles nanoparticles and by migration in the electric field. Indeed, when the nanoparticles move between two aggregates they allow charge transport between them by forming "bridges" for electron hopping. The blurry aspect of the picture is due to the charging of the gel through the electron beam which means that the system is not saturated with large nanoparticles. This also suggests that the percolation is reached due to the motion of the nanoparticles. On the other hand, the system appears to be different for 600mM hydrated Au-gel (Figure 3.11.d). First of all, the 600mM Au-gel does not exhibit any aggregates. This means that the agarose possesses strong stabilizing properties. Secondly, the quality of the picture is extremely good. This means that there is no charging effect on the surface of the sample and therefore that the gel pattern is saturated by the nanoparticles. The total saturation of the gel network with large nanoparticles also explains the high conductance value obtained as the composite offers a larger amount of conductive pathways for the charge transport between the two electrodes.

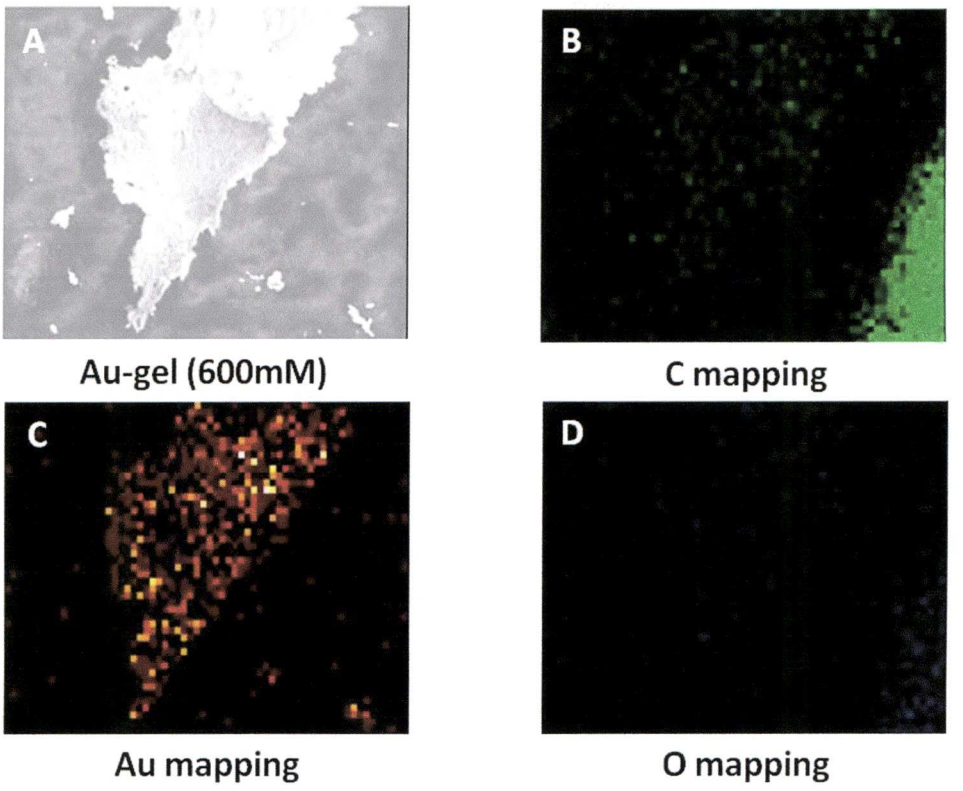

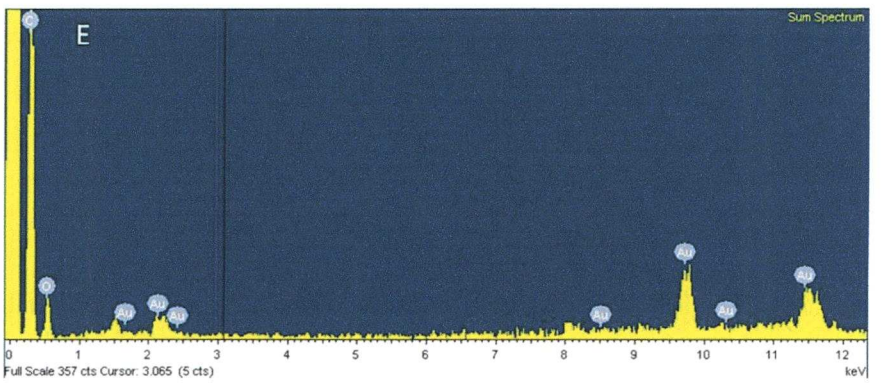

Figure 3.12 (A) shows an SEM image of a piece of hydrated 600mM Au-gel. (B), (C) and (D) correspond to the C, Au and O mapping, respectively, on the gel surface. (E) shows the EDX spectrum of the Au-gel analysed.

Our SEM investigation of the 600 mM hydrated Au-included elemental mapping of its surface by EDX (equipping the SEM). Figure 3.12 summarizes the results obtained on this gel. Figure 3.12.a shows the sample of the Au-gel and Figure 3.12.b, c and d show the respective mapping of C, Au and O, respectively, on the surface of the composite. As expected from the chemical composition of the agarose monomer ($C_{24}H_{38}O_{18}$), carbon is present homogeneously through the entire surface of the gel (Figure 3.12.b) and oxygen can also be detected (Figure 3.12.d). Importantly, the Au mapping of

the piece of gel confirms the homogeneous decoration of the structure with gold nanoparticles. The higher quality of the Au mapping in comparison to carbon and oxygen is due to the much higher density of gold (Figure 3.12.c). These qualitative measurements are still extremely valuable in this study as they give a visual confirmation of the decoration of the gel by the GNPs.

3.4.3.5 Reversibility of the electronic properties of the gel

The final part of the investigation of the Au-gels focused on the recovery of the electronic properties of the totally dehydrated gels by rehydration. Indeed, if the Au-gels are rehydrated, the nanoparticles should become mobile again and could act as bridges between the aggregates to create pathways for charge transport between the two electrodes. Figure 3.13 summarized the results obtained. Figure 3.13.a displays the amount of weight lost by each Au-gel corresponding to the total dehydration. As expected, the weight loss decreases as the concentration of Au in the gel increases. Indeed, after a complete dehydration, the gel is only composed of agarose and GNPs. Therefore the weight loss corresponds to:

$$Weight\ loss\ (\%) = 100 - (\frac{m_{Au} + m_{dry\ agarose}}{m_{hydrated\ Au-gel}})x100$$

On the other side, the analysis of the weight recovered is also of interest. Indeed, Figure 3.13.b shows that the amount of weight recovered from the au-gel (in comparison to its original weight), after immersion in water for 24 hours, decreases as the concentration of the feed solution used to initially prepare the gel increases. This means that the aggregates of gold nanoparticles alter the rehydration of the fibres they are coating by blocking the diffusion of the water into the close packed agarose double helix system. Figure 3.13.c shows the current answer for the rehydrated 500mM Au-gel. The signal shows a recovery of some conductive pathways. The conductance of this rehydrated system is:

$$G = 3.7.10^{-4}S$$

Of course this value cannot be compared to the value obtained previously on the same gel during the first dehydration (80% weight loss). The system does not present the same pattern after rehydration as most of the nanoparticles have aggregated irreversibly under the total dehydration of the matrix and have formed aggregates which are coating the network. Indeed, the distance between particles is so reduced under dehydration that the particles aggregate. Moreover, the GNPs surface facing the water phase is not protected by any ligands; this facilitates the appearance of aggregation. Under rehydration of the gel, the distance between the aggregates increases but the particles stay aggregated (because it is not reversible). An even larger conductance value than the one found above was obtained by a second dehydration of the gel for one hours (corresponding to a weight loss of 87% and presented in Figure 3.13.D).

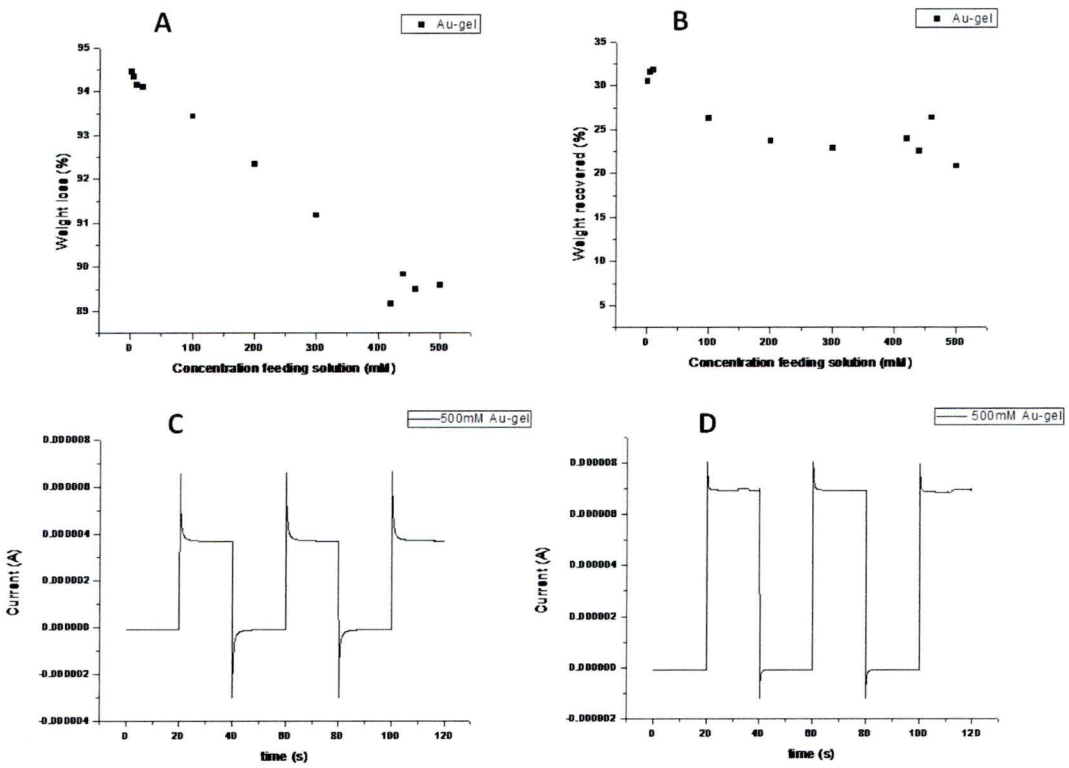

Figure 3.13 (A) Weight loss (%) for the different Au-gel after their complete dehydration as a function of the concentration of feed solution used. (B) presents a plot of the weight recovered by the different Au-gels after an immersion of 24 hours in water vs. the concentration of the feed solution employed to prepare the different Au-gels. (C) shows the currents response of the 500mM rehydrated Au-gel when a voltage of 10 mV is applied. (D) shows that current response can be enhanced when this Au-gel is dehydrated again (corresponding to 87% weight loss).

3.5 Conclusions

In this chapter, the electronic properties of the Au- gel have been characterised at different Au loadings and upon dehydration. The dehydration of the gels has been accomplished via two methods: spontaneous (placing the samples in the refrigerator) and chemical (in the presence of the phosphorus pentoxide). While the first method has validated the concept of enhancing the electronic properties of the gel by dehydration of the matrix and offered a modelling of the new composite with an equivalent circuit, the second method has offered a better understanding of the charge transport mechanism through the different Au-gel. This second method has pointed out the presence of dynamic percolation points. The location of these points depends on the concentration of the feed solution employed as well as the dehydration ratio of the gel. Several percolation points can be reached for the same concentration depending at different steps of the dehydration. These events are mainly due to the Brownian motion of the single nanoparticles through the volume of the gel combined to the three dimensional dewetting of the gel. When these single nanoparticles are localized between two aggregates they allow the passage of the charge between them by electron hopping. The charge transport phenomenon is slightly different when the concentration of feeding solution is high enough to allow the percolation of the hydrated Au-gel. The passage of the charge through the composite does not involves any motion of the nanoparticles. Finally, recovery of the percolation point can be obtained for a shrunk Au-gel by rehydration of the gel with water. The correlation between the conductance value obtained after the first dehydration and after rehydration for the same Au-gel (presenting the same volume and the same amount of water) cannot be done as the gel presents two completely different conductive patterns in the two cases.

References

1.J. A. Dahl, B. L. S. Maddux, J. E. Hutchison, *Chemical Reviews* **2007**, *107*, 2228.

2. F. Westerlund, T. Bjornholm, *Current Opinion in Colloid & Interface Science* **2009**, *14*, 126.

3. S. Lin, M. Li, E. Dujardin, C. Girard, S. Mann, *Advanced Materials* **2005**, *17*, 2553.

4. S. Pruneanu, L. Olenic, S. A. F. Al-Said, G. Borodi, A. Houlton, B. R. Horrocks, *Journal of Materials Science* **2010**, *45*, 3151.

5. M. H. Wang, Y. J. Li, Z. X. Xie, C. Liu, E. S. Yeung, *Materials Chemistry and Physics* **2010**, *119*, 153.

6. M. Fukao, A. Sugawara, A. Shimojima, W. Fan, M. A. Arunagirinathan, M. Tsapatsis, T. Okubo, *Journal of the American Chemical Society* **2009**, *131*, 16344.

7. C. J. Murphy, A. M. Gole, S. E. Hunyadi, C. J. Orendorff, *Inorganic Chemistry* **2006**, *45*, 7544.

8. S. Si, A. Kotal, T. K. Mandal, *Journal of Physical Chemistry C* **2007**, *111*, 1248.

9. S. Srivastava, N. A. Kotov, *Soft Matter* **2009**, *5*, 1146;
10. V. Maheshwari, J. Kane, R. F. Saraf, *Advanced Materials* **2008**, *20*, 284.

11. Y. X. Zhang, H. C. Zeng, *Journal of Physical Chemistry B* **2006**, *110*, 16812.

12. T. Hassenkam, K. Norgaard, L. Iversen, C. J. Kiely, M. Brust, T. Bjornholm, *Advanced Materials* **2002**, *14*, 1126.

13. J. Sharma, R. Chhabra, A. Cheng, J. Brownell, Y. Liu, H. Yan, *Science* **2009**, *323*, 112.

14. S. T. Liu, T. Zhu, R. S. Hu, Z. F. Liu, *Physical Chemistry Chemical Physics* **2002**, *4*, 6059.

15. M. Kanehara, E. Kodzuka, T. Teranishi, *Journal of the American Chemical Society* **2006**, *128*, 13084.

16. Z. Shen, M. Yamada, M. Miyake, *Journal of the American Chemical Society* **2007**, *129*, 14271.

17. M. M. Maye, S. C. Chun, L. Han, D. Rabinovich, C. J. Zhong, *Journal of the American Chemical Society* **2002**, *124*, 4958.

18. H. Y. Huang, W. F. Chen, P. L. Kuo, *Journal of Physical Chemistry B* **2005**, *109*, 24288.

19. J. Vignolle, T. D. Tilley, *Chemical Communications* **2009**, 7230.

20. I. A. Zucchi, C. E. Hoppe, M. J. Galante, R. J. J. Williams, M. A. Lopez-Quintela, L. Matejka, M. Slouf, J. Plestil, *Macromolecules* **2008**, *41*, 4895.

21. N. Khanduja, S. Selvarasah, C. L. Chen, M. R. Dokmeci, X. G. Xiong, P. Makaram, A. Busnaina, *Applied Physics Letters* **2007**, *90*.

22. S. Si, T. K. Mandal, *Langmuir* **2007**, *23*, 190.

23. H. F. Zhang, I. Hussain, M. Brust, M. F. Butler, S. P. Rannard, A. I. Cooper, *Nature Materials* **2005**, *4*, 787.

24. F. A. Aldaye, H. F. Sleiman, *Angewandte Chemie-International Edition* **2006**, *45*, 2204.

25. A. S. Nair, K. Kimura, *Physical Chemistry Chemical Physics* **2009**, *11*, 9346.

26. B. Abeles, P. Sheng, M. D. Coutts, Y. Arie, *Advances in Physics* **1975**, *24*, 407.

27. M. Brust, D. Bethell, D. J. Schiffrin, C. J. Kiely, *Advanced Materials* **1995**, *7*, 795.

28. N. Krasteva, I. Besnard, B. Guse, R. E. Bauer, K. Mullen, A. Yasuda, T. Vossmeyer, *Nano Letters* **2002**, *2*, 551.

29. G. Schmid, U. Simon, *Chemical Communications* **2005**, 697.

30. T. Wang, R. B. Zheng, X. G. Hu, L. X. Zhang, S. J. Dong, *Journal of Physical Chemistry B* **2006**, *110*, 14179.

31. T. Shimada, K. Imura, M. K. Hossain, H. Okamoto, M. Kitajima, *Journal of Physical Chemistry C* **2008**, *112*, 4033.

32. A. Mamedov, J. Ostrander, F. Aliev, N. A. Kotov, *Langmuir* **2000**, *16*, 3941.

33. H. T. Yang, C. M. Shen, Y. K. Su, T. Z. Yang, H. J. Gao, Y. G. Wang, *Applied Physics Letters* **2003**, *82*, 4729.

34. T. Z. Yang, C. M. Shen, Z. Li, H. R. Zhang, C. W. Xiao, S. T. Chen, Z. C. Xu, D. X. Shi, J. Q. Li, H. J. Gao, *Journal of Physical Chemistry B* **2005**, *109*, 23233.

35. T. Hassenkam, K. Moth-Poulsen, N. Stuhr-Hansen, K. Norgaard, M. S. Kabir, T. Bjornholm, *Nano Letters* **2004**, *4*, 19.

36. M. Brust, D. Bethell, C. J. Kiely, D. J. Schiffrin, *Langmuir* **1998**, *14*, 5425.

37. N. Fishelson, I. Shkrob, O. Lev, J. Gun, A. D. Modestov, *Langmuir* **2001**, *17*, 403.

38. J. B. Pelka, M. Brust, P. Gierlowski, W. Paszkowicz, N. Schell, *Applied Physics Letters* **2006**, *89*.

39. H. Wohltjen, A. W. Snow, *Analytical Chemistry* **1998**, *70*, 2856.

40. Q. Y. Cai, E. T. Zellers, *Analytical Chemistry* **2002**, *74*, 3533.

41. W. H. Steinecker, M. P. Rowe, E. T. Zellers, *Analytical Chemistry* **2007**, *79*, 4977.

42. Y. Joseph, I. Besnard, M. Rosenberger, B. Guse, H. G. Nothofer, J. M. Wessels, U. Wild, A. Knop-Gericke, D. S. Su, R. Schlogl, A. Yasuda, T. Vossmeyer, *Journal of Physical Chemistry B* **2003**, *107*, 7406.

43. D. Bulone, D. Giacomazza, V. Martorana, J. Newman, P. L. San Biagio, *Physical Review E* **2004**, *69*.

44. A. Pluen, P. A. Netti, R. K. Jain, D. A. Berk, *Biophysical Journal* **1999**, *77*, 542.

45. T. C. Laurent, *Biochimica Et Biophysica Acta* **1967**, *136*, 199.

46. E. M. Johnson, D. A. Berk, R. K. Jain, W. M. Deen, *Biophysical Journal* **1995**, *68*, 1561.

47. S. Bhattacharya, D. Gangopadhyay, N. Chanda, S. A. Grant, Y. S. Liu, P. R. Sharp, R. Bashir, K. Gangopadhyay, S. Gangopadhyay, *Sensor Letters* **2008**, *6*, 778.

Chapter 4: SERS

For any information on the SERS spectra please contact

Dr. Ramon Alvarez-Puebla

Departamento de Quimica Fisica and Unidad Asociada CSIC, Universidade de Vigo, 36310 Vigo, Spain,

E-mail: ramon.alavarez@uvigo.es

4.1 Introduction

As reported in all the previous chapters, nanoparticles can find applications in many different areas such as photonics, medical imaging, drug delivery, catalysis, electronic devices, and detection via surface-enhanced spectroscopies[1-3] and research is still carried out extensively on these topics. For instance, the development of new composites made of nanoparticles and their use as surface-enhanced Raman scattering (SERS) substrates is presently an important field of research[4-6]. These interests have been motivated by the extraordinary analytical potential of SERS[7-15] combined with a possible optimization of the restricted experimental conditions (affinity requirements between the molecule with the gold or silver surface[16], generation of hotspots by the substrate[17-22] and oxidation of the substrate surface). Currently, a vast effort has been made to resolve these drawbacks by the use of nanostructured materials[23-25], substrates containing highly efficient hotspots[34,35,37,38] or by decorating gold and silver surfaces with molecular systems for the trapping of analytes[16,26-33]. Unfortunately, just few systems[71] present molecular trapping, recyclable properties and a possible formation of hotspots on their respective surfaces at the same time.

In this chapter, the use of a piece of agarose gel loaded with silver nanoparticles (Ag-gel) as a SERS substrate is investigated. The principle is illustrated in Figure 4.1. The formation of hotspots upon the dehydration of the composite is demonstrated by the SERS detection of 1-naphtalenethiol. 1-naphtalenethiol presents a thiol group which can bind covalently on the surface of the silver nanoparticles (extremely stable bonding) and therefore can be located in the electromagnetic field emanating from the particles under the laser beam. The molecule trapping properties of the Ag-gel are then presented through the detection of dichlorodiphenyl-trichloroethane (DDT) molecules which has never been reported before. Finally the reversibility of this new material is explored with the analysis of three different analytes: crystal violet (CV, cationic molecule), 2-naphtoic acid (anionic molecule) and DDT (neutral molecule).

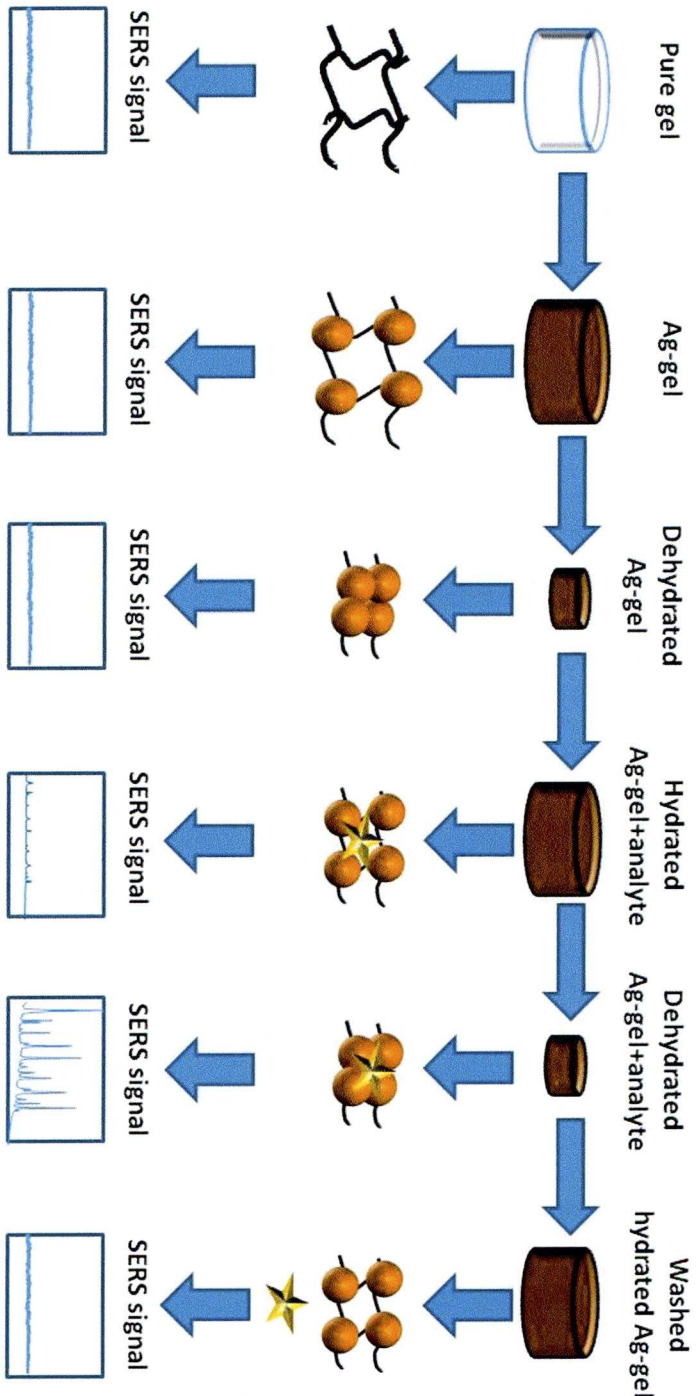

Figure 4.1 Scheme presenting the unique aspect of the Ag-gel used in this study.

4.2 Surface Enhanced Raman Scattering (SERS)

Surface Enhanced Raman Spectroscopy is a technique that uses the surface of a rough metal substrate (usually Ag or Au) or nanoparticles to increase the Raman signal of the molecule studied by a factor of 10^5 to 10^{14} depending on the values of different parameters such as the wavelength, the polarisation, the nanostructure of the substrate and the nature of the metal used.

Although some disagreements appear in the literature, the nature of this enhancement is considered to be mainly electromagnetic[39] and can additionally be associated to a chemical mechanism[40]. The nature of the signal enhancement can be explained by the fact that the Raman intensity is the product of the incident electric field strength and the derivative of the polarisability. The theory behind the electromagnetic and the chemical mechanisms is outlined in what follows.

4.2.1 Electromagnetic mechanism

As reported by Moskovits *et al.* [41] a radiated field is produced by the metal nanoparticle on its surface under the incident field from the laser irradiation. These two fields are related by the following equation:

$$E_S = gE_0$$

Where E_0 is the incident field strength, E_s the field radiated by the nanoparticles and g the average enhancement of the field on the surface of the nanoparticles. If a molecule is now adsorbed to the surface of the nanoparticles it will be excited by E_s field, and the intensity of the Raman scattered light coming from the molecule can be expressed by:

$$E_R \, \alpha \, \alpha_R E_S \, \alpha \, \alpha_R g E_o$$

with α_R as a combination of Raman tensor. E_R can be enhanced by a factor g` if the metal nanoparticles scatter light at the Raman shifted wavelength.

Knowing that the SERS intensity is proportional to the square modulus of E_{sers} the following relationship can be expressed:

$$I_{SERS} \alpha |\alpha_R|^2 |gg`|^2 I_0$$

Where I_{sers} is the intensity of the surface enhanced Raman signal scattered by the molecule and I_0 the intensity of the incident field. The general SERS enhancement is then defined as the ratio between the Raman scattered intensity in the presence nanoparticles with the signal intensity obtained without any enhancement and can be described as:

$$G = \left|\frac{\alpha_R}{\alpha_{R_0}}\right| |gg`|^2$$

With α_{Ro} as the Raman polarisability of the isolated molecule. If we take the example of a silver nanoparticle at 400nm the factor g is around 30. The general SERS enhancement will therefore be:

$$G = |30|^4 = 8.1x10^5$$

assuming that the polarisability of the molecule in the presence of the nanoparticle remains unchanged.

This physical effect shows the importance of using metal nanoparticles as substrates for the detection of molecules by Raman spectroscopy. Figure 4.2 illustrates this principle. To optimize the enhancement of the signal the influence of different parameters such as the nature of the metal, the size, shape, the nature of the nanostructure and the orientation of the E vector should be taken into consideration. Their impact will be treated in the following sections.

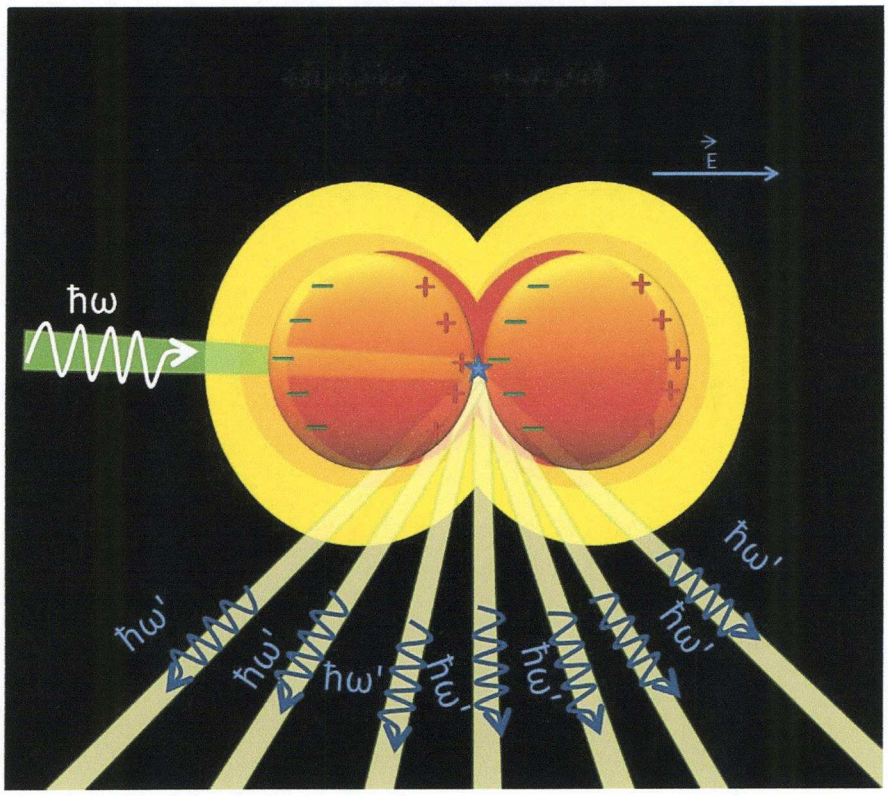

Figure 4.2 Illustration of the SERS principle (not to scale). The incident light is in green while the light scattered by the molecules (represented by a star) after the enhancement of the field provided by the aggregate of the nanoparticles is shown in yellow.

4.2.1.1 The nature of the metal

The different metals used for SERS are the coinage and alkali metals[41] because they have plasmon resonances in the visible range (due to their singly occupied s-orbital). Another advantage of using these metals can be explained by the dielectric function:

$$\alpha = \frac{R^3(\varepsilon_b \omega^2 - \omega_p^2) + i\omega\gamma\varepsilon_b}{[(\varepsilon_b + 3)\omega^2 - \omega_p^2] + i\omega\gamma(\varepsilon_b + 3)}$$

where R is the radius of the metal nanoparticles, ε_b the contribution of the interband transition to the dielectric function, ω_p the metal Plasmon resonance and γ the electronic-scattering state which is inversely proportional to the DC conductivity of the metal used. The imaginary part of this function represents the loss of material at the frequency employed. This value is very small for coinage and alkali metals at their resonance frequency therefore their resonances are much sharper and more intense. The preference for using silver rather than gold or copper stems from the same reason. The ε_b value of copper is larger than gold which in turn is larger than the value of silver. Knowing that the width of the resonance is defined by:

$$\gamma(\varepsilon_b + 3)$$

The resonance of copper is larger that of gold and both are larger that of silver. Consequently the SERS enhancement increases in this order.

4.2.1.2 Nanoparticle size

An ideal substrate should be composed of silver nanoparticles with an average size between 5 and 100nm. Indeed, if the average size of the particles is within the laser wavelength range or above, the striking of their surfaces by the incident laser beam will result in the appearance of high-order multipoles which are non radiative. Consequently the Raman scattering is poor.

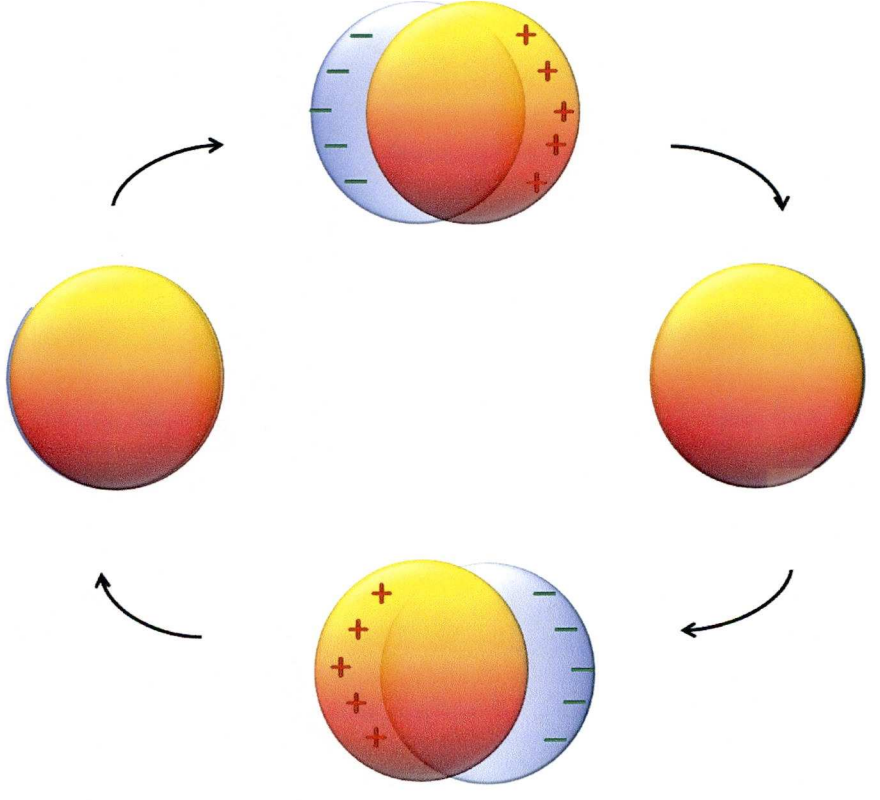

Figure 4.3 Representation of the surface plasmon resonance. The gray areas correspond to the electronic cloud surrounding the particle.

The inefficiency of nanoparticles under 5nm in enhancing the Raman signal can be explained by the gradual loss of the surface plasmon resonance with decreasing size . When an external electromagnetic field interacts with a small metallic sphere an oscillating dipole is formed on the

surface of the nanoparticle. A force E_{dep} is then created to depolarize this anisotropic charge density. The opposition of these two forces involves an oscillation of the electronic shell around the particle (see Figure 4.3 above). When the wavelength of this oscillation is resonant with the wavelength of the induced light, the small nanoparticle absorbs it and this phenomenon, called surface plasmon resonance can be detected by spectroscopy.

When the size of the metal nanoparticles decreases, the intensity of the SPR also decreases as the electronic scattering process at the particle surface diminishes. The effective conductivity of the nanoparticles is dropping as well as the SERS efficiency of the substrate. For nanoparticles under 2nm the pseudo bulk description involved in the definition of the SPR no longer applies. The energy levels are discontinuous in contrast to the bulk. The small colloid should instead be considered as a quantum object with the appearance of discrete energy states in which the electronic energy between the quantum level δ is defined by:

$$\delta = \frac{3E_F}{2\,zN_A} > k_B T$$

where $E_{F\,is}$ the Fermi level and z the total number of valence electrons. This expression is very important in order to describe the conductance properties of the nanoparticles. If $\delta < k_B T$, the nanoparticles will behave as an insulator and as a conductor if $\delta > k_B T$.

4.2.1.3 The effect of particle shape

The strength of the Raman signal using surface enhancement is also dependent on the shape of the nanoparticles which form the nanostructured substrate. As explained previously the SERS efficiency is affected by the overlapping of the SPR of the substrate and the laser wavelength used. Changing the shape of the nanoparticles induces a change in the SPR localisation and results in the possibility of obtaining multiple LSPRs. The choice of the shape should first be related to the laser wavelengths available.

Earlier, the massive influence of the plasmon band width on the SERS intensity was described. For nanoparticles of different shapes that are composed of the same metal, the width of the plasmon band is different. Dong *et al.*[42]reported that for gold nanoparticles the results are:

$$I_{sers}dogbone > I_{sers}Nanorod(ratio3.3) > I_{sers}cube > Iserstetrapods >$$

$$I_{sers}Nanorod(ratio2.4) > I_{sers}Spheres$$

These results are in agreement with the discussion of El-Sayed and co-workers who stipulated that greater Raman scattering is obtained for a molecule on Au{110} than on Au{111}.This phenomenon can be explained by the fact that Au{110} has higher surface energy[43]. These results are confirmed by Ray and co-workers[44] who shown that for Ag:

$$I_{sers}nanoprism > I_{sers}Sphere > I_{sers}nanorod$$

The mismatch between the results with gold and silver in the case of nanorod can be explained by the fact that Ag nanorods expose only {111} and {100} plates. The difference between spherical nanoparticles and prisms can be justified by the rich optical properties of the prisms and the roughness of their surfacesA computational simulation of the enhancement of the local field near silver particles with different shapes confirmed the previous statement[45] (Figure 4.4). It is extremely important to point out that this simulation is done under conditions where the induced field is parallel to longest dimension of the nanoparticles.

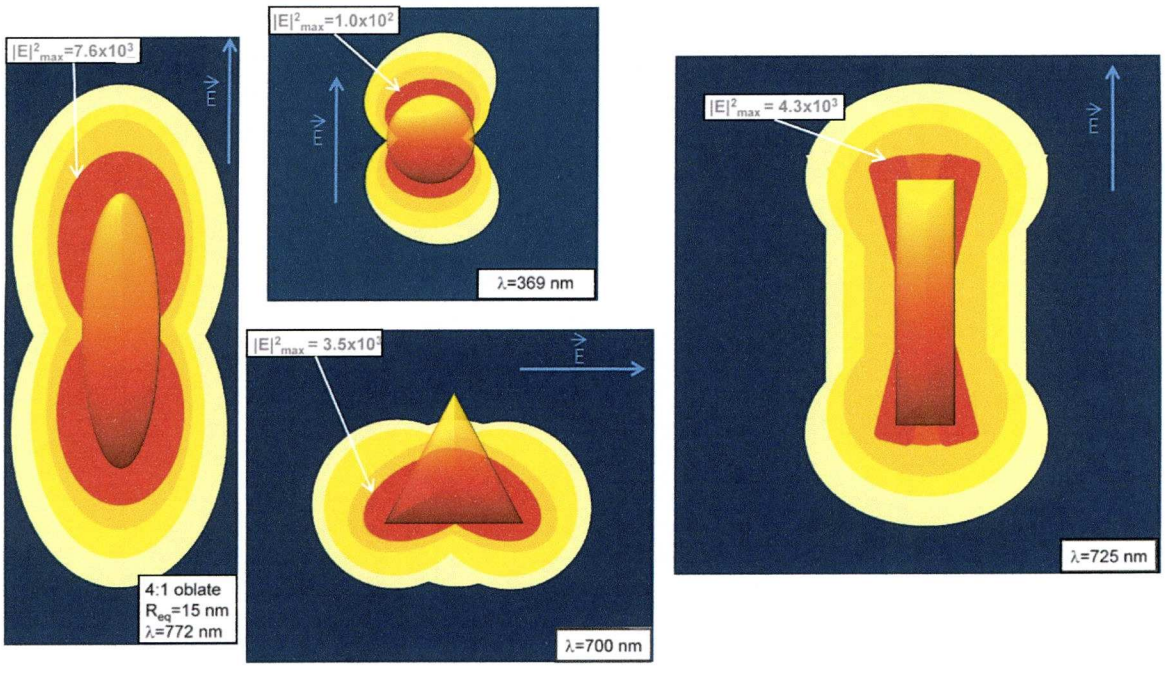

Figure 4.4 Contours of the local field near silver particles at specified wavelength. Showing values of the peak field E^2 (reproduction from ref. 45)

4.2.1.4 Influence of the angle of the incident light with respect to the nanoparticles

The angle of the incident polarized light can have a huge impact on the detection of SERS. Figure 4.5 is a simple illustration of the incident polarized light on the nanoparticles with two different angles. In the first example, the molecule is localized in the gap between the two nanoparticles and the E-vector is parallel to the axis of the two colloids. The smaller the gap between the two nanoparticles, the larger the capacitive field sensed by the molecule will be and the larger the dipole induced in each nano-object due to the effect of a combined field between the laser light and the field of the neighbouring particle. These effects disappear completely if the light is polarised with the E-vector perpendicular to the axis of the nanoparticles even if the molecule is present in the gap between them. The molecule will not "feel" the charges induced by the nanoparticles (Figure 4.5 illustration 2) and there will be no

location of field enhancement due to the proximity of the two nanoparticles.

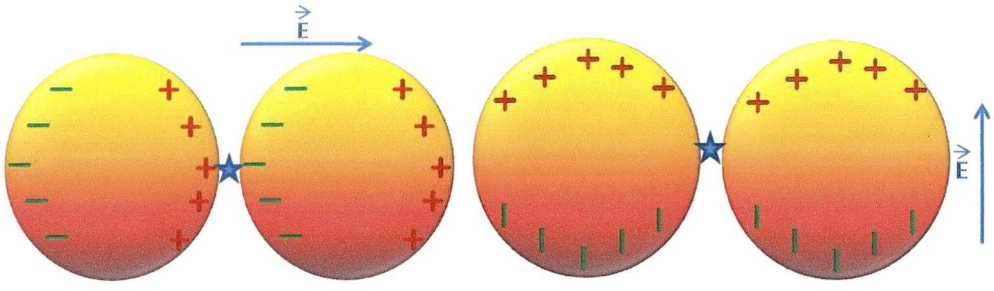

Figure 4.5 The two different polarisations of light (S and P).

4.2.1.5 Importance of the aggregates

Based on the previous explanations, the effect of the presence of aggregates in SERS substrates can be clearly understood. The analysis of a local dimer in the aggregate will show an enhancement of the total field in the gap between the two nanoparticles due to the appearance of a retarded field coming from the other particles. This field comes in addition to the local dimer field. Moreover, while the polarization of an isolated dimer is anisotropic (strong dependence on the axis of the dimer) it becomes much more isotropic in the presence of an aggregate (the electromagnetic coupling between the different nanoparticles being entangled). The presence of any anisotropy in an aggregate of several nanoparticles comes from the presence of a dominating dimer. The Surface Plasmon Band of an aggregate will also be much broader than that of a dimer and contribute to the aggregation dependence of the SERS intensity.

4.2.1.6 Distance between nanoparticles in aggregates and location of the molecule

To understand and localize the perfect position of the molecule in the substrate the situation need to be described with an electrostatic model[46]. If nanoparticles are considering as conducting spheres and the field as electrostatic we can clearly see that the potential drop will be situated in the

gap between the two nanoparticles. In order to optimize the SERS detection of a molecule it should be situated in this interparticle region. Based on Kall *et al.*[46] calculations the ideal gap between two nanoparticles should be around 1nm. As the interparticle distance increases, the SERS effect on the molecule studied will decrease. Schatz *et al.* claim 2nm[70].

4.2.1.7 Concentration of the molecule studied

The concentration of the molecule analysed via SERS plays an important role for the signal intensity. Even if a linear relationship between the concentration of the molecule and the SERS enhancement could be expected experiments have shown that their relationship is more complicated. At low concentration, the SERS enhancement will increase until it reaches a maximum point at a specific concentration (dependent on the molecule studied). Then, the enhancement decreases dramatically and stabilises at a particular value where the concentration no longer influences it[44].

At low concentration, the adsorbate coverage on the surface of the metal nanoparticles is very low too (presence in submonolayer)[47]. The scattering coming from this layer is very weak and so is the SERS response. An increase in concentration causes an increase in the SERS signal until a monolayer of adsorbate is formed. At higher concentration the adsorbate forms multilayers and so the SERS intensity of the signal decreases again.

4.2.2 Chemical enhancement mechanism

The theory described earlier attributes the enhancement of Raman scattering to an electromagnetic mechanism. But this physical approach of the problem cannot be the only explanation to the huge enhancement provided by SERS as any specific adsorbate detection differs under the same condition and with nearly identical polarisability. This difference has been quantified and can span two orders of magnitude. This phenomenon can be related to the presence of a chemical enhancement. The mechanism appears to be due to the creation of a new electronic state arising from chemisorption which provides a resonant state for Raman scattering[48]. This

event occurs at the Fermi level of the metallic substrate which lies in the middle of the HOMO-LUMO gap of the adsorbates i.e. the Raman scattering analyte. Charge Transfer is now possible from the HOMO of the molecule to the Fermi Level of the substrate at half the energy of the adsorbates HOMO-LUMO excitation (Figure 4.6), which is commonly in the UV-visible range and therefore accessible.

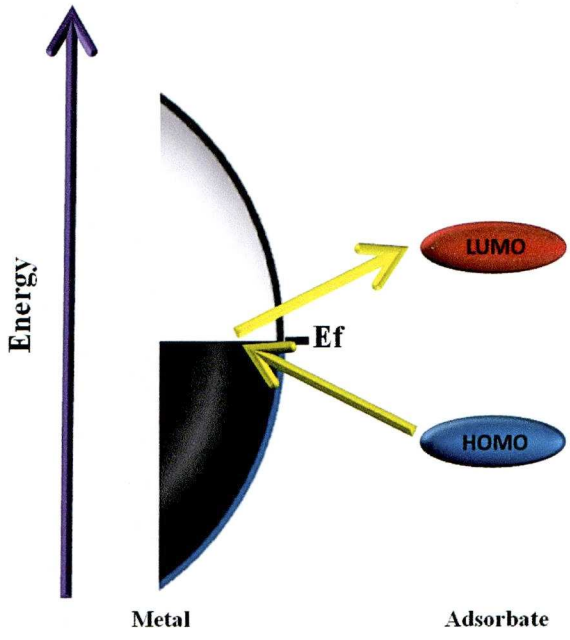

Figure 4.6 Chemical enhancement principle: symmetry between the HOMO-LUMO of the molecule and the Fermi level of the nanoparticle.

A good understanding of the SERS mechanisms helps to interpret the results obtained in any Raman study. It is also needed to optimize the experimental conditions in term of the substrate properties and laser wavelength.

4.3 Experimental

4.3.1 Materials

Please refer to the section 2.2.1 in chapter 2 (page 34) for a description of the material used to prepare the SERS substrate. 1-naphtalenethiol (1NAT: $C_{10}H_8S$) was purchased in Acros Organics. Dicholoro-diphenyl-trichloroethane (DDT: $C_{14}H_9Cl_5$), crystal violet (CV: $C_{25}H_{30}ClN_3$), and 2-naphtoic acid ($C_{10}H_7CO_2H$) were obtained from Sigma Adrich.

4.3.2 Methods

4.3.2.1 Sample preparation

The SERS substrate has been obtained by soaking a pure piece of agarose gel ($0.23cm^3$) in a 3 ml aqueous solution of $AgNO_3$ (concentration: 500mM) for 24 hours. The loaded gel was then immersed in a 3ml aqueous solution of $NaBH_4$ (concentration: 500mM) also for 24hrs. Finally, the Ag-gel obtained was dialysed in milli-Q water for 48 hours[36].

4.3.2.2 Characterisation

The Ag-gel substrate was characterized by X-ray powder diffraction, UV-visible spectroscopy, and TEM. The Ag-gel was embedded in epoxy resin for characterization by TEM. The SERS properties of the Ag-gel were then characterized via Raman spectroscopy.

Raman spectroscopy: the inelastically scattered radiation was collected with a Renishaw Invia Reflex system equipped with Peltier charge-coupled device (CCD) detectors and a Leica confocal microscope. The spectrograph uses high resolution gratings with additional band-pass filter optics. Samples were excited with four different laser lines at 532 (Nd:Yag), 633 (He-Ne), 785 and 830 nm (diode). The corresponding laser line was focused onto the sample in backscattering geometry using a 50× objective (n. a. 0.75) providing scattering areas of ca. 1 μm^2. The SERS optical activity of the Ag-gel composites was tested with 1NAT, a well-studied non-resonant SERS probe (no overlapping between the different

laser wavelengths with the maximum absorbance of the molecule). Samples were prepared by immersing the polymer into 1NAT 10^{-5} M aqueous solution for two hours. SERS spectra were collected on the wet and dried gel with each of the laser lines. Optical enhancing homogeneity of the Ag-gel was studied by using the Renishaw StreamLine accessory with the 785 nm laser line. For DDT, the analysis was carried out by immersing the Ag-gel in aqueous DDT solutions of different concentration (between 10^{-4} and 10^{-8} M) prepared from DDT 10^{-3} M stock solution in ethanol for two hours. After drying, the surfaces were studied with the 785 nm laser line. Reversibility upon analyte charge was studied by immersing the Ag loaded agarose gel, either in CV 10^{-6} M (cationic probe), NCOOH 10^{-5} M (anionic probe) or DDT 10-^{5} M (neutral probe) for 2 hours. Samples were then studied with either 633 or 785 nm laser lines and immersed in a washing 1% sodium citrate aqueous solution for 2 hours, CV and NCOOH, and a ethanol:water (1:1) mixture. This process was repeated three times for each sample to ensure reproducibility

4.4 Results and Discussion

4.4.1 Characterisation of the Ag-gel

The preparation of the Ag loaded agarose gel is reported in section 4.3.2.2. Briefly, two size ranges of nanoparticles are observed. At low concentration of $AgNO_3$ in the feeding solution, large colloids with an average size of 8nm are dispersed in the water phase and small clusters from 0 to 5 nm decorate the network of the matrix. The increase in concentration of the metal salt in the sample resulted in an average size enhancement of the large colloids as shown in chapter 2. The structural model and behaviour for agarose gels loaded with in situ prepared gold nanoparticles is also applicable to silver loaded gels. The characterisation of the 500mM sample by TEM (Fig4.7.A) exhibits the common behaviour of silver and gold. Here, the larger particles as well as aggregates thereof are resolved as irregularly shaped black specks, while the electron dense coating of the gel network appears as a homogeneous gray cloud. Using a higher concentration of silver nitrate with the same concentration of

reducing agent in this synthesis results in an enlargement of average size as well as an amplification of size polydispersity for the nanoparticles obtained. Even though the TEM instrument used to characterise the nanoparticle sizes in the high loading sample is not suitable to analyse precisely the nature of the electron cloud coating the pattern of the hydrogel, the Super STEM results displayed in chapter 2 and the MALDI performed on the sample at low concentration reinforce the hypothesis of the presence of small clusters on the network.

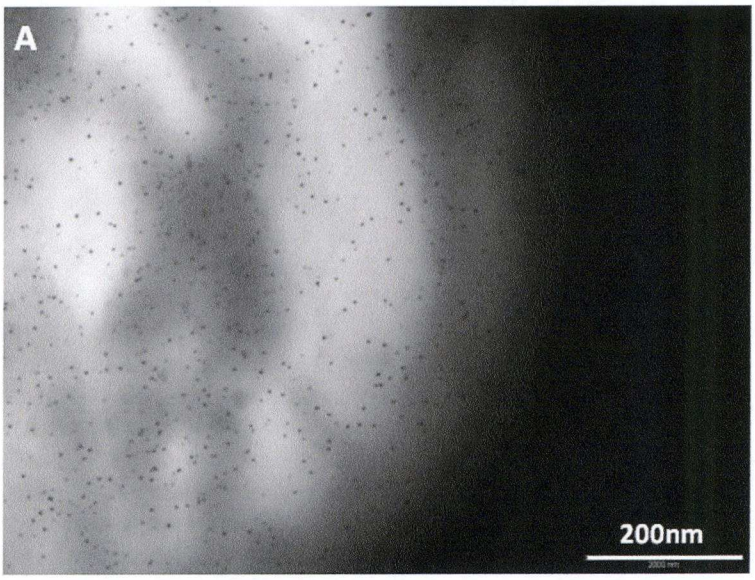

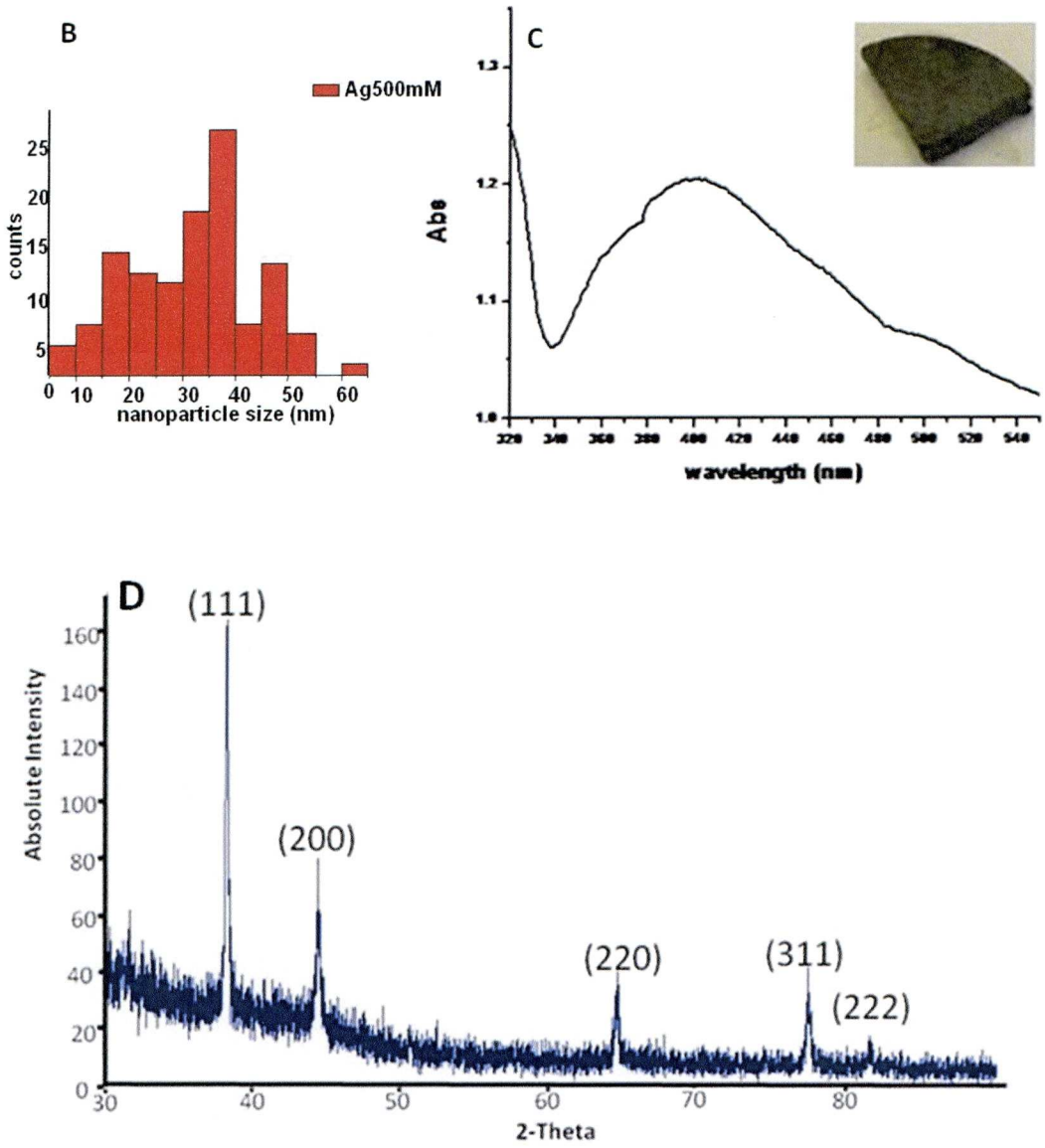

Figure 4.7 (A) TEM image of a cross section of agarose loaded with silver nanoparticles. (B) shows the size distribution of the silver nanoparticles inside the gel. (C) exhibits the uv-vis spectrum of silver nanoparticles decorating the network of the agarose hydogel (inset shows an optical picture of the bulk polymer). (D) presents the X-Ray pattern of the Ag-Agarose gel

The determination of the size of the small clusters was not investigated as the work here focuses particularly on the potential interest of using Ag-gel loaded with large nanoparticles as a substrate for SERS. The nanoparticles exhibited on the TEM picture were measured using AnalySIS software (Soft Imaging Systems). One hundred nanoparticles were measured in order to quantify their size dispersity. The result is shown in Figure 4.7.B Inset. The average size is estimated as 35nm with wide dispersion from 5 to 55nm. The suggested model (presented in section 4.1) is further supported by XRD (Figure 4.7.D), which clearly shows the presence of fcc Ag nanoparticles, the approximate average size of which can be estimated as 33 nm by Scherrer line broadening analysis.[37] The analysis of the general appearance of the gel and its uv-vis signal confirm the previous statement. Figure 4.7.C inset shows the gel after the synthesis of silver nanoparticles in situ. The surfaces appear to be dark brown when the inside reveals a combination of yellow and dark brown. These optical properties reflect the presence of a high concentration of small and spherical silver particles. Figure 4.7.C represents the uv-vis signal of a cross section of the Ag-gel. The SPR is around 420nm which is consistent with the presence of silver nanoparticles. The broad absorption band can be explained by the polydispersity in size of the colloids obtained and the blue-shifted part by the matrix. This could be due to scattering by the gel network, which scales as λ^{-4} and would enhance the total extinction at low wavelengths. It is important to report that the blue shift could be also explained by the inconsistency in shape of silver colloids. As reported by Pinto *et al.*[49] nanorods and triangles can be present in solution when the synthesis of homogeneous spherical silver nanoparticles was attempted. Similar phenomenon could therefore take place in the Ag-gel presented here. In any case, this new Ag-gel composite should present extremely good properties as a substrate for SERS applications.

4.4.2 SERS

The agarose gel loaded with silver nanoparticles was analysed without analyte using four different wavelengths, 532, 633, 785 and 830nm. Figure 4.8 shows the signals obtained at each excitation wavelength. The outcome of these experiments confirms the interest of using this material as a substrate for SERS. This is due to the low cross section of polysaccharides[69]. The spectra obtained revealed the absence of vibrations in a very large Raman shift window. In comparison the introduction of a low

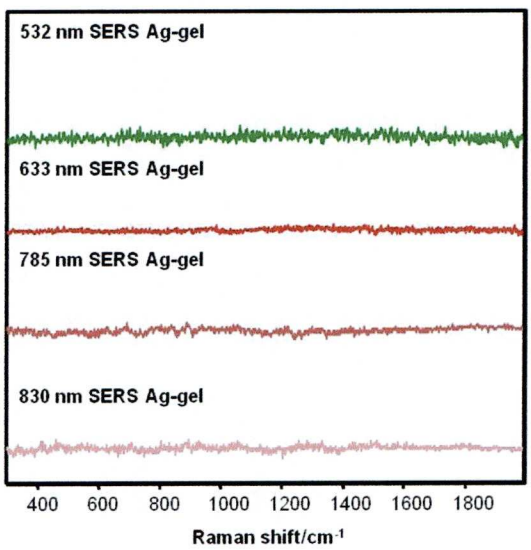

Figure 4.8: SERS spectra of the dry Ag-Agarose gel without analyte at 4 different excitation wavelengths (532, 633, 785, 830nm)

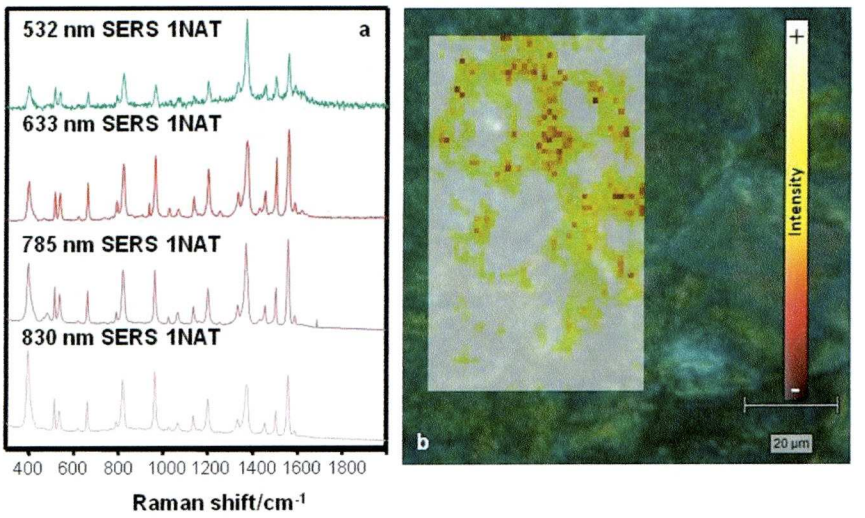

Figure 4.9: (a) SERS spectra of the same dry gel with 1-Napthtalenethiol. (b) StreamLine map of the Ag-Agarose gel with 1-Naphtalenethiol (785) composed by 2639 spectra with spatial resolution of ca. 1µm^2

concentrated solution of 1-NAT gives SERS spectra at all the different wavelengths (Figure 4.9.a).The sample presents ring stretching (1553, 1503, and 1368 cm-1), CH bending (1197 cm-1), ring breathing (968 and 822 cm-1), ring deformation (792, 664, 539, and 517cm-1), and CS stretching (389 cm-1), regardless of the laser line used and even using very low laser power at the sample (~1 µW). These vibrations corroborate the calculated vibrational wavenumber obtained by Alvarez-Puebla and al[50]. SERS mapping of the surface of the gel was performed in order to determine the location of the aggregate enhancing the signal (Figure 4.9.b). The picture confirms that the large silver nanoparticles decorating the hydrogel network are the origin of this phenomenon. The mapping also reveals heterogeneity of the SERS enhancing ability of the silver loading in the surface even though its main part provides a maximum intensity.

4.4.3 Hot Spots

In order to optimize the detection of 1NAT all measurements were carried out on a dried gel. The key role of the drying process is to allow the formation of silver aggregates upon shrinkage of the gel structure which promote interactions between the different electromagnetic fields of the nanoparticles by reducing the distance between them and hence can result in the generation of so-called "hot spots" in some localized areas. The nature of these is well-known and emanates from the interactions of the electromagnetic fields between aggregates of nanoparticles in the substrate, which enhance fields of other neighbouring aggregates: this creates a localized area where the field is extremely intense and is thus ideal for the detection of Raman active molecules even at a low concentration. For a demonstration of this concept of dynamic hot spots, SERS spectra of 1NAT in Ag-gel were acquired using all four available excitation laser lines, both before and after dehydration. Figure 4.10 shows the substantial increase of the signal in all cases. The enhancement factor goes from 10 (green line) up to 10^2 (near Infra Red) as the laser energy decreases (the enhancement factor has been calculated by comparing the peak with the highest intensity from each family of signals). Also the wet gel seems to yield the most clearly defined spectrum when the substrate is excited at 633nm. These experiments show the remarkable property of hotspot formation via the shrinkage of the substrate but also suggest the possibility of trapping molecules that do not adsorb to silver surfaces or nanoparticles inside the supporting gel.

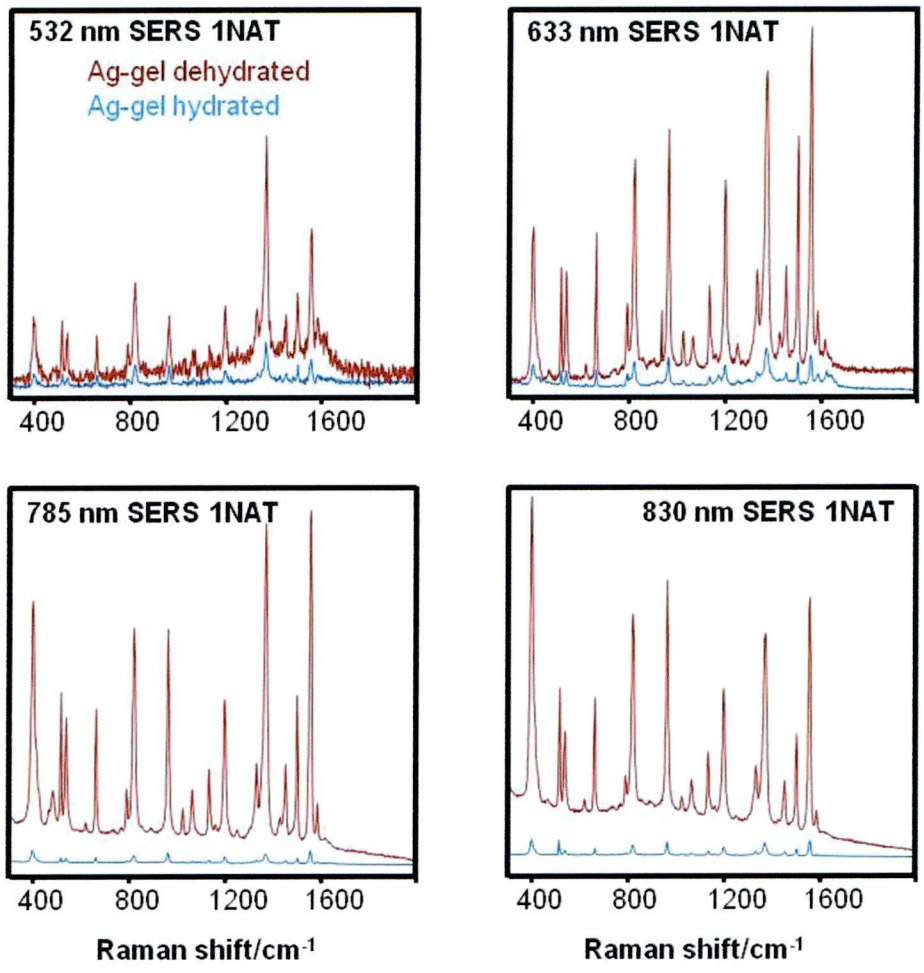

Figure 4.10 SERS spectra of 1-Naphtalenethiol in Ag-gel. The blue signals correspond to the measurements on the wet gel and the red signals to the measurements on the air-dried gel. The sample was analysed at 4 different excitation wavelengths (532, 633, 785 and 830nm)

4.4.4 Molecule-trapping

The trapping efficiency of Ag-Agar was tested using a small and well-known contaminant[51], DDT. This molecule discovered in 1874, was widely employed as a pesticide and against the spread of malaria before being banned for use in 1972 in the United States followed by Europe in 1980's for its carcinogenic effects. It has been classified by the EPA (Environmental Protection Agency) as a "probable" human carcinogen. Epidemological studies show that DDT can cause cancer of the liver, pancreas, breast and could be a source of leukaemia, lymphoma and testicular cancer[52-57]. As any organochlorine compounds it can be linked to

diabetes[58] and can also cause neurological problems[59], asthma and a drop of fertility in male subjects[60]. The SERS spectrum of this has not been reported before due to its poor absorption properties on metallic surfaces, especially for gold and silver. Nevertheless, by immersing dry Ag-gels in aqueous DDT solutions of various concentrations (10^{-4}-10^{-8}M) and subsequently shrinking the gel by dehydration, it has been possible to obtain a well resolved Raman-enhanced vibrational pattern of the target molecule (Figure 4.11). The spectrum was found to be fully reproducible and is characterized by the ring stretchings (1491, 1467, 1451, and 1428 cm^{-1}), aliphatic CC stretching (1297 cm^{-1}), CH bending (1091 cm^{-1}), ring breathing (1001 cm^{-1}), ring deformation (935 cm^{-1}), CH twisting (899 and 848 cm^{-1}), CH wagging (745 cm^{-1}), and CCl stretchings (685 and 554 cm^{-1}). The vibrational pattern of DDT could be unequivocally recognized, even for concentrations down to the micromolar regime[61]. Although this may not seem an extremely high sensitivity compared to other analytical techniques,[62-64] it should be taken into account that SERS spectra can be acquired in very short times and with basically no need for prior sample treatment.

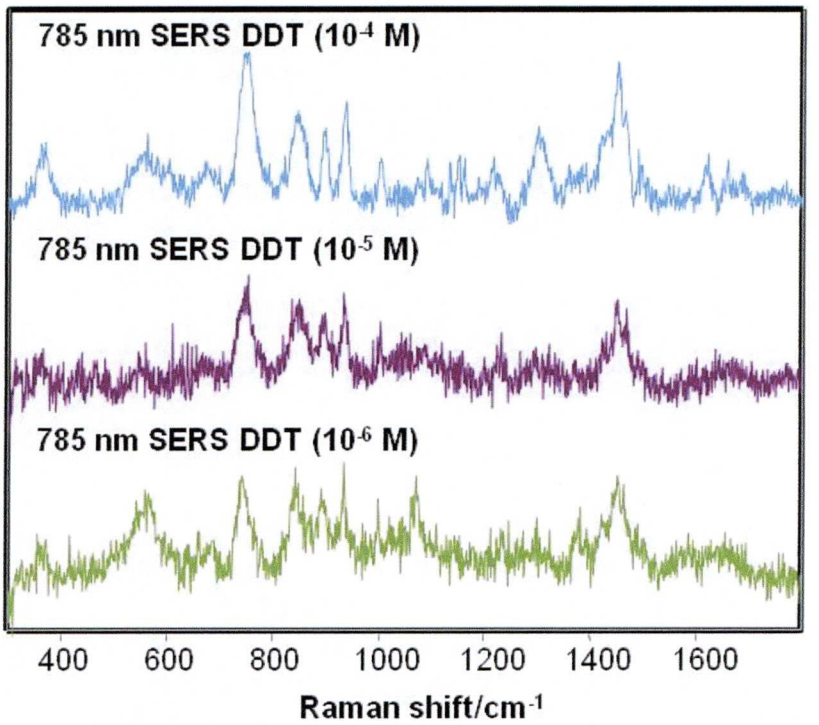

Figure 4.11 SERS spectra of DDT at 3 different concentrations after trapping into the Ag-Agarose gel by immersion and dehydration.

4.4.5 Reversibility

Finally, knowing that the agarose hydrogel can shrink at room temperature and swell upon immersion in aqueous solutions and that this process can be repeated as long as the gel is not damaged the reversibility of the loading of the Ag-gels with analyte was studied for a variety of molecular probes. Figure 4.12 shows the results for a cation (crystal violet, CV), an anion (2-naphthoic acid, NCOOH), and a neutral molecular species, DDT. In all cases, the gel was first immersed in the solution containing the corresponding analyte, characterized by SERS, then immersed in an aqueous washing solution of 1 $\%_w$ sodium citrate, and the SERS spectra were measured again. This process was repeated three times to ensure the full reusability of this sensor platform.

Remarkably, for each of these different analytes, the characteristic vibrational patterns could be clearly identified when the analyte was present but were completely removed upon washing.

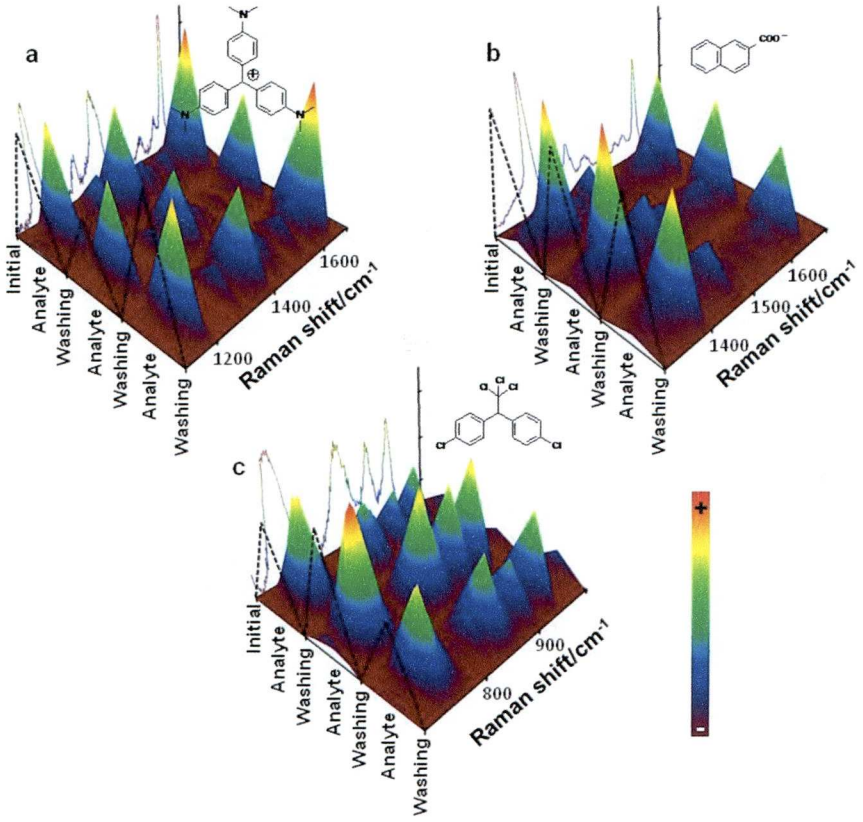

Figure 4.12 Reversible SERS behaviour of Ag-Agar gel after immersion the polymer in solutions containing (A) crystal violet 10^{-6}M, (B) 2-naphtoic acid 10^{-5}M, and (C) dichloro-diphenyl-thichloroethane 10^{-5}M. Crystal violet and 2-naphtoic acid were washed with 1% sodium citrate solution water solution and dichloro-diphenyl-thichloroethane with a mixture of water-ethanol (1:1)

To ensure that the effect is not an artefact due to the occasional measurement of hot spots, extended mapping was carried out on the blank polymer, after addition of the analyte and after washing (Figure 4.13).

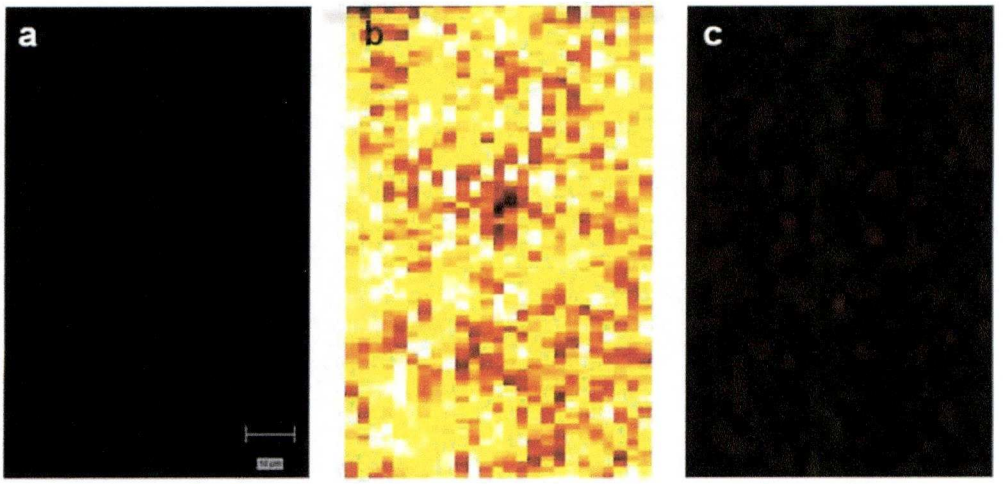

Figure 4.13 SERS maps of the Ag-Agar gel before (a) and after (b) crystal violet addition, as well as after washing with 1% trisodium citrate in water (c).

For charged species, it is very likely that sodium and citrate ions compete for the retention sites of the analyte on the nanoparticles, thus displacing it because of their much higher concentration and thereby cleaning the sensor. When the analyte was again in contact with the gel, it was retained, giving rise to signals of similar intensity. In the case of DDT, although the same washing process was followed, it was observed that the low affinity of this molecule toward metallic surfaces makes the citrate solution unnecessary, rendering the sensor ready for reutilization after simply washing with water. These results further demonstrate the trapping properties of the gel, together with its reversibility for a wide variety of substances with different chemical properties, within a material that is capable of generating dynamic hot spots with extremely high enhancing activity, which is comparable to that of aggregated silver colloids.

4.5 Conclusions

As shown in chapter 2 the synthesis of silver nanoparticles in agarose gel can be achieved following the essentially same procedure that is used for gold. They follow a similar pattern inside the agarose gel matrix. At low metal salt concentration, with the gel matrix playing the role of the template, the metal decorates the inside and the surface of the threefold helix. This leads to different size clusters upon $NaBH_4$ reduction. The clusters flanked by the helices are extremely small (just a few atoms) while the colloids stabilised on the surface of the network are much bigger (4-5nm) as presented in chapter 2. The increase in concentration results in an increase in the nanoparticle size notably for the one decorating the exterior of the hydrogel pattern. When the concentration of the metal salt in the hydrogel is high enough, these big nanoparticles come closer to each other (reduction of the interparticle distance due to an increase in diameter) and some of them collapse to form small aggregates.

Since one of the key points of this study was to focus on creating the best substrate for the SERS detection of different molecules, a highly loaded Ag-gel was used in all experiments. The XRD results gave an average nanoparticle size of 33nm, while the TEM pictures showed a wide size distribution. The small clusters are still present in the gel and form the cloudy effect on the TEM pictures. These nanoparticles are mostly spherical according to the XRD spectrum even though the previous chapter have shown a "Quality Street" shape distribution on localised areas (see section 3.4.3.2 in chapter 3). The dehydration of the gel results in an increase in number and size of the aggregates and a homogeny of their presence through the entire surface of the gel. The polarisation of the laser with the gel does not influence in any case the intensity of the signal received. The in-situ formation of the metal nanoparticles provides a three dimensional decoration of the network. After shrinkage, the aggregates formed can be described as an assembly of dimers having different axis orientation. This anisotropy gives a more intense and homogenous

enhancement of the field through the entire surface of the substrate. The influence of the interparticle distance is unknown due to the same reason explained earlier, however, the SERS mapping performed shows the presence of a large number of hotspots homogeneously dispersed on the surface of the gel. The map suggests that the average distance between two particles should be 1nm or less by correlation with the general SERS theory described before (section 4.2.1.6). This assumption can be confirmed if we correlate the HAADF-STEM pictures of the Au-agar gel presented in chapter 2 with the Ag-agar employed in this study. The shrinkage of the gel reduces the interparticle distances. In localized areas, neighbouring particles cannot be described as entities anymore as they form aggregates on the surface of the gel network. In this chapter the hydrogel is dehydrated and the molecule studied is trapped inside. The first shrinkage of the gel is performed to allow the integration of a maximum amount of analyte during the immersion process. The second dehydration allows the trapping of the molecule between nanoparticles forming aggregates. This material provides ideal conditions to detect molecules via SERS.

The distance of the molecule with nanoparticles is a major parameter in the enhancement factor value on the Raman signal. While the enhancement factor goes down as $G=[r/(r+d)]^{10}$for a monolayer of molecules with a distance, d, between the nanoparticles of a radius "r" and the molecules, this issue is even more important in a single molecule case with $G=[r/(r+d)]^{12}$. The justifications of the influence of this parameter for the two molecules studied in this chapter are different. For 1NAT the molecules can be chemisorbed onto the surface of the silver nanoparticles. The nature of the signal enhancement can be electromagnetic and chemical. The combination of both explains the good detection of this molecule with our substrate. The interest of using DDT in this study was to highlight the remarkable properties of the gel as a substrate for the enhancement of the Raman signal without any chemisorption of the molecules onto its surface. The improvement of the signal intensity of

DDT is purely based on electromagnetic mechanisms. Even though the average distance between each DDT molecule with nanoparticles has not been determined, all molecules are surrounded by aggregates resulting in the apparition of hotspots hence giving a homogeneous and good detection of DDT through the entire surface of the substrate. These hotspots also affect the impact of the concentration of the molecules present in the gel as just few molecules can provide a SERS signal when chemisorption onto the surface of the particles is possible. The lack of chemical enhancement in this system is responsible for some limitations in the SERS detection of DDT, even though an identifiable pattern was obtained for a concentration down to 10^{-6}M without any particular effort made in placing the molecule in hot areas.

The analysis of the results obtained show cases the outstanding properties of metal loaded gels for ultrasensitive SERS detection. They provide all the features for a high enhancement of the signal intensity under normal experimental conditions. The swelling property of the hydrogel facilitates the incorporation of the desired molecule onto its surface for examination through Raman spectroscopy. The experiments carried out on the dehydrated gel in comparison with the "wet" gel in the presence of 1NAT also exhibit a significant enhancement of the SERS pattern. This observation can be easily explained considering that the electromagnetic coupling between two or more metallic nanoparticles has been consistently reported to redshift the corresponding LSPR,[65] so that the overlap between LSPR and laser line is improved for longer wavelength excitations. This results in an increase of the enhancement of the SERS signal when excited using lower energy lasers, as predicted by overlap, in a fashion similar to that of surface-enhanced Raman excitation spectroscopy[66-68]. Finally the reversibility of the Ag-gel was studied and demonstrated for a variety of molecular probes giving for each of them high intensity SERS signals after each washing. This washing process was completed using a sodium citrate solution for the anion (crystal violet) and the cation (2-naphtoic acid) and water for DDT.

References

1. C. Daniel, D. Astruc, *Chemical Reviews* **2004**, *104*, 293.

2. S. K. Ghosh, T. Pal, *Chemical Reviews* **2007**, *107*, 4797.

3. M. E. Stewart, C. R. Anderton, L. B. Thompson, J. Maria, S. K. Gray, J. A. Rogers, R. G. Nuzzo, *Chemical Reviews* **2008**, *108*, 494.

4. A. D. Strickland, C. A. Batt, *Analytical Chemistry* **2009**, *81*, 2895.

5. M. Spuch-Calvar, L. Rodriguez-Lorenzo, M. P. Morales, R. A. Alvarez-Puebla, L. M. Liz-Marzan, *Journal of Physical Chemistry C* **2009**, *113*, 3373.

6. Y. S. Huh, A. J. Lowe, A. D. Strickland, C. A. Batt, D. Erickson, *Journal of the American Chemical Society* **2009**, *131*, 2208.

7. K. Kneipp, H. Kneipp, I. Itzkan, R. R. Dasari, M. S. Feld, *Chemical Reviews* **1999**, *99*, 2957.

8. L. Rodriguez-Lorenzo, R. A. Alvarez-Puebla, I. Pastoriza-Santos, S. Mazzucco, O. Stephan, M. Kociak, L. M. Liz-Marzan, F. J. G. de Abajo, *Journal of the American Chemical Society* **2009**, *131*, 4616.

9. J. A. Dieringer, K. L. Wustholz, D. J. Masiello, J. P. Camden, S. L. Kleinman, G. C. Schatz, R. P. Van Duyne, *Journal of the American Chemical Society* **2009**, *131*, 849.

10. P. G. Etchegoin, P. D. Lacharmoise, E. C. Le Ru, *Analytical Chemistry* **2009**, *81*, 682.

11. S. E. J. Bell, J. N. Mackle, N. M. S. Sirimuthu, *Analyst* **2005**, *130*, 545.

12. S. E. J. Bell, N. M. S. Sirimuthu, *Analyst* **2004**, *129*, 1032.

13. S. E. J. Bell, N. M. S. Sirimuthu, *Journal of the American Chemical Society* **2006**, *128*, 15580.

14. S. E. J. Bell, N. M. S. Sirimuthu, *Chemical Society Reviews* **2008**, *37*, 1012.

15. S. E. J. Bell, S. J. Spence, *Analyst* **2001**, *126*, 1.

16. R. A. Alvarez-Puebla, E. Arceo, P. J. G. Goulet, J. J. Garrido, R. F. Aroca, *Journal of Physical Chemistry B* **2005**, *109*, 3787.

17. L. Brus, *Accounts of Chemical Research* **2008**, *41*, 1742.

18. J. P. Camden, J. A. Dieringer, Y. M. Wang, D. J. Masiello, L. D. Marks, G. C. Schatz, R. P. Van Duyne, *Journal of the American Chemical Society* **2008**, *130*, 12616.

19. G. Braun, I. Pavel, A. R. Morrill, D. S. Seferos, G. C. Bazan, N. O. Reich, M. Moskovits, *Journal of the American Chemical Society* **2007**, *129*, 7760.

20. F. Svedberg, Z. P. Li, H. X. Xu, M. Kall, *Nano Letters* **2006**, *6*, 2639.

21. E. C. Le Ru, E. Blackie, M. Meyer, P. G. Etchegoin, *Journal of Physical Chemistry C* **2007**, *111*, 13794.

22. D. R. Ward, N. K. Grady, C. S. Levin, N. J. Halas, Y. P. Wu, P. Nordlander, D. Natelson, *Nano Letters* **2007**, *7*, 1396.

23. I. Pastoriza-Santos, A. Sanchez-Iglesias, B. Rodriguez-Gonzalez, L. M. Liz-Marzan, *Small* **2009**, *5*, 440.

24. J. R. Anema, A. G. Brolo, P. Marthandam, R. Gordon, *Journal of Physical Chemistry C* **2008**, *112*, 17051.

25. A. Kudelski, *Langmuir* **2003**, *19*, 3805.

26. R. A. Alvarez-Puebla, R. F. Aroca, *Analytical Chemistry* **2009**, *81*, 2280.

27. S. Tan, M. Erol, S. Sukhishvili, H. Du, *Langmuir* **2008**, *24*, 4765.

28. L. Guerrini, J. V. Garcia-Ramos, C. Domingo, S. Sanchez-Cortes, *Langmuir* **2006**, *22*, 10924.

29. L. Guerrini, J. V. Garcia-Ramos, C. Domingo, S. Sanchez-Cortes, *Analytical Chemistry* **2009**, *81*, 1418.

30. L. Guerrini, J. V. Garcia-Ramos, C. Domingo, S. Sanchez-Cortes, *Analytical Chemistry* **2009**, *81*, 953.

31. K. C. Bantz, C. L. Haynes, *Vibrational Spectroscopy* **2009**, *50*, 29.

32. R. A. Alvarez-Puebla, R. Contreras-Caceres, I. Pastoriza-Santos, J. Perez-Juste, L. M. Liz-Marzan, *Angewandte Chemie-International Edition* **2009**, *48*, 138.

33. S. Abalde-Cela, S. Ho, B. Rodriguez-Gonzalez, M. A. Correa-Duarte, R. A. Alvarez-Puebla, L. M. Liz-Marzan, N. A. Kotov, *Angewandte Chemie-International Edition* **2009**, *48*, 5326.

34. F. Le, D. W. Brandl, Y. A. Urzhumov, H. Wang, J. Kundu, N. J. Halas, J. Aizpurua, P. Nordlander, *Acs Nano* **2008**, *2*, 707.

35. J. Kneipp, X. T. Li, M. Sherwood, U. Panne, H. Kneipp, M. I. Stockman, K. Kneipp, *Analytical Chemistry* **2008**, *80*, 4247.

36. E. Faoucher, P. Nativo, K. Black, J. B. Claridge, M. Gass, S. Romani, A. L. Bleloch, M. Brust, *Chemical Communications* **2009**, 6661.

37. Y. K. Park, S. H. Yoo, S. Park, *Langmuir* **2008**, *24*, 4370.

38. S. J. Lee, A. R. Morrill, M. Moskovits, *Journal of the American Chemical Society* **2006**, *128*, 2200.

39. D. L. Jeanmaire, R. P. Van Duyne, *Journal of Electroanalytical Chemistry* **1977**, *84*, 1.

40. M. G. Albrecht, J. A. Creighton, *Journal of the American Chemical Society* **1977**, *99*, 5215.

41. M. Moskovits, in *Surface-Enhanced Raman Scattering: Physics and Applications, Vol. 103*, Springer-Verlag Berlin, Berlin, **2006**, pp. 1.

42. X. G. Hu, T. Wang, L. Wang, S. J. Dong, *Journal of Physical Chemistry C* **2007**, *111*, 6962.

43. B. Nikoobakht, M. A. El-Sayed, *Journal of Physical Chemistry A* **2003**, *107*, 3372.

44. V. S. Tiwari, T. Oleg, G. K. Darbha, W. Hardy, J. P. Singh, P. C. Ray, Chemical Physics Letters 2007, 446, 77.
45. G. C. Schatz, M. A. Young, R. P. Van Duyne, in Surface-Enhanced Raman Scattering: Physics and Applications, Vol. 103, Springer-Verlag Berlin, Berlin, 2006, pp. 19.

46. H. X. Xu, M. Kall, in Surface-Enhanced Raman Scattering: Physics and Applications, Vol. 103, Springer-Verlag Berlin, Berlin, 2006, pp. 87.

47. W. B. Lacy, L. G. Olson, J. M. Harris, *Analytical Chemistry* **1999**, *71*, 2564.

48. A. Campion, P. Kambhampati, *Chemical Society Reviews* **1998**, *27*, 241.

49. V. V. Pinto, M. J. Ferreira, R. Silva, H. A. Santos, F. Silva, C. M. Pereira, *Colloids and Surfaces a-Physicochemical and Engineering Aspects* **2010**, *364*, 19.

50. R. A. Alvarez-Puebla, D. S. Dos Santos, R. F. Aroca, *Analyst* **2004**, *129*, 1251.

51. V. Turusov, V. Rakitsky, L. Tomatis, *Environmental Health Perspectives* **2002**, *110*, 125.

52. M. P. Longnecker, W. J. Rogan, G. Lucier, *Annual Review of Public Health* **1997**, *18*, 211.

53. U. G. Ahlborg, L. Lipworth, L. Titusernstoff, C. C. Hsieh, A. Hanberg, J. Baron, D. Trichopoulos, H. O. Adami, *Critical Reviews in Toxicology* **1995**, *25*, 463.

54. D. H. Garabrant, J. Held, B. Langholz, J. M. Peters, T. M. Mack, *Journal of the National Cancer Institute* **1992**, *84*, 764.

55. S. M. Snedeker, *Environmental Health Perspectives* **2001**, *109*, 35.

56. D. Baris, S. H. Zahm, K. P. Cantor, A. Blair, *Occupational and Environmental Medicine* **1998**, *55*, 522.

57. A. Ekbom, A. WicklundGlynn, H. O. Adami, *Lancet* **1996**, *347*, 553.

58. C. J. Everett, I. L. Frithsen, V. A. Diaz, R. J. Koopman, W. M. Simpson, A. G. Mainous, *Environmental Research* **2007**, *103*, 413.

59. L. Hardell, G. Lindstrom, B. Van Bavel, *Environmental Research* **2002**, *88*, 141.

60. M. A. Dalvie, J. E. Myers, M. L. Thompson, T. G. Robins, S. Dyer, J. Riebow, J. Molekwa, M. Jeebhay, R. Millar, P. Kruger, *Environmental Research* **2004**, *96*, 1.

61. P. Aldeanueva-Potel, E. Faoucher, R. A. Alvarez-Puebla, L. M. Liz-Marzan, M. Brust, *Analytical Chemistry* **2009**, *81*, 9233.

62. A. L. Graham, C. A. Carlson, P. L. Edmiston, *Analytical Chemistry* **2002**, *74*, 458.

63. M. Alvarez, A. Calle, J. Tamayo, L. M. Lechuga, A. Abad, A. Montoya, *Biosensors & Bioelectronics* **2003**, *18*, 649.

64. M. M. Frias, A. G. Frenich, J. L. M. Vidal, M. M. Sanchez, F. Olea, N. Olea, *Journal of Chromatography B* **2001**, *760*, 1.

65. P. K. Jain, W. Y. Huang, M. A. El-Sayed, *Nano Letters* **2007**, *7*, 2080.

66. R. A. Alvarez-Puebla, D. J. Ross, G. A. Nazri, R. F. Aroca, *Langmuir* **2005**, *21*, 10504.

67. C. L. Haynes, R. P. Van Duyne, *Journal of Physical Chemistry B* **2003**, *107*, 7426.

68. A. D. McFarland, M. A. Young, J. A. Dieringer, R. P. Van Duyne, *Journal of Physical Chemistry B* **2005**, *109*, 11279.

69. R. F. Aroca, Surface Enhanced Vibrational Spectroscopy; Wiley: New York, **2006**.

70. E. Hao, G. C. Schatz, *Journal of Chemical Physics* **2004**, *120*, 357.

71. S. E. J. Bell, S. J. Spence, *Analyst* **2001**, *126*, 1.

Chapter 5: Analysis of functionalised GNPs by SERS

5.1 Introduction

In the last two decades gold nanoparticles (GNPs) have been intensively studied due to the tunability of their optical[1], electronic and self assembly[2-4] properties. In addition, the ease of functionalising them and their low toxicity made them interesting for biological application[5-7] and more precisely for cancer cell detection[8-9]. The functionalization of GNPs can be obtained in four different ways: (i) direct synthesis in the presence of a functional thiol[10-18], (ii) ligand exchange[19-26], (iii) post–synthetic modification of the pendant functionalities by an interfacial reaction[27-30] and (iv) coupling biomolecules through non-specific electrostatic interactions[31]. In the following study the functionalization of GNPs with one drug, daunorubicin, has been studied. The reason for the choice of this molecule is due to its anti cancer activity. While the functionalization of the GNPs with daunorubicin (DNR) has been achieved by first making a thiol derivative of the DNR by reaction with a NHS-ester, the second molecule thioguanine, possessing its own thiol group, is able to attach directly to the GNP. The full characterization of each coating has been achieved by UV-vis, scanning electron microscopy, fluorescence spectrometry (DNR) and elemental analysis. In parallel, a second characterisation of the two structures has been carried out via Raman spectroscopy by trapping the functionalized NPs in the Ag-gel substrate presented before. This sandwich method should enable the detection of the drug molecule located on the surface of the GNPs[32].

5.2 Sandwich Structure

In surface enhanced Raman scattering, a sandwich structure corresponds to a system in which the analyte molecule is trapped between two or more particles. Most of the time, the particles sandwiching this molecule are from different natures. The interests of using such kind of structures are a facilitation of the hotspot formation and a larger wavelength range cover by the LSPR of the system[33-42].

As shown in Figure 5.1, the decoration of the network with large silver nanoparticles (SNPs) in addition to the shrinkage of the gel should result in an enhancement of the Raman signal of the analyte. The dehydration of the gel should involve a homogeneous generation of hotspots on the hydrogel pattern as well as reduce the distance between the molecules or particles studied and the SNPs. Moreover, if the system investigated is composed of gold nanoparticles the shrinkage of the substrate should involve aggregation of the GNPs with SNPs and so enhance the Raman signal at 630nm. In addition, it was shown in the first part of this chapter that a molecule studied in the Ag-gel should present a larger enhancement at 630nm than at 514nm due to the LSPR of the substrate. The combination of the two effects should provide very interesting results at this excitation wavelength.

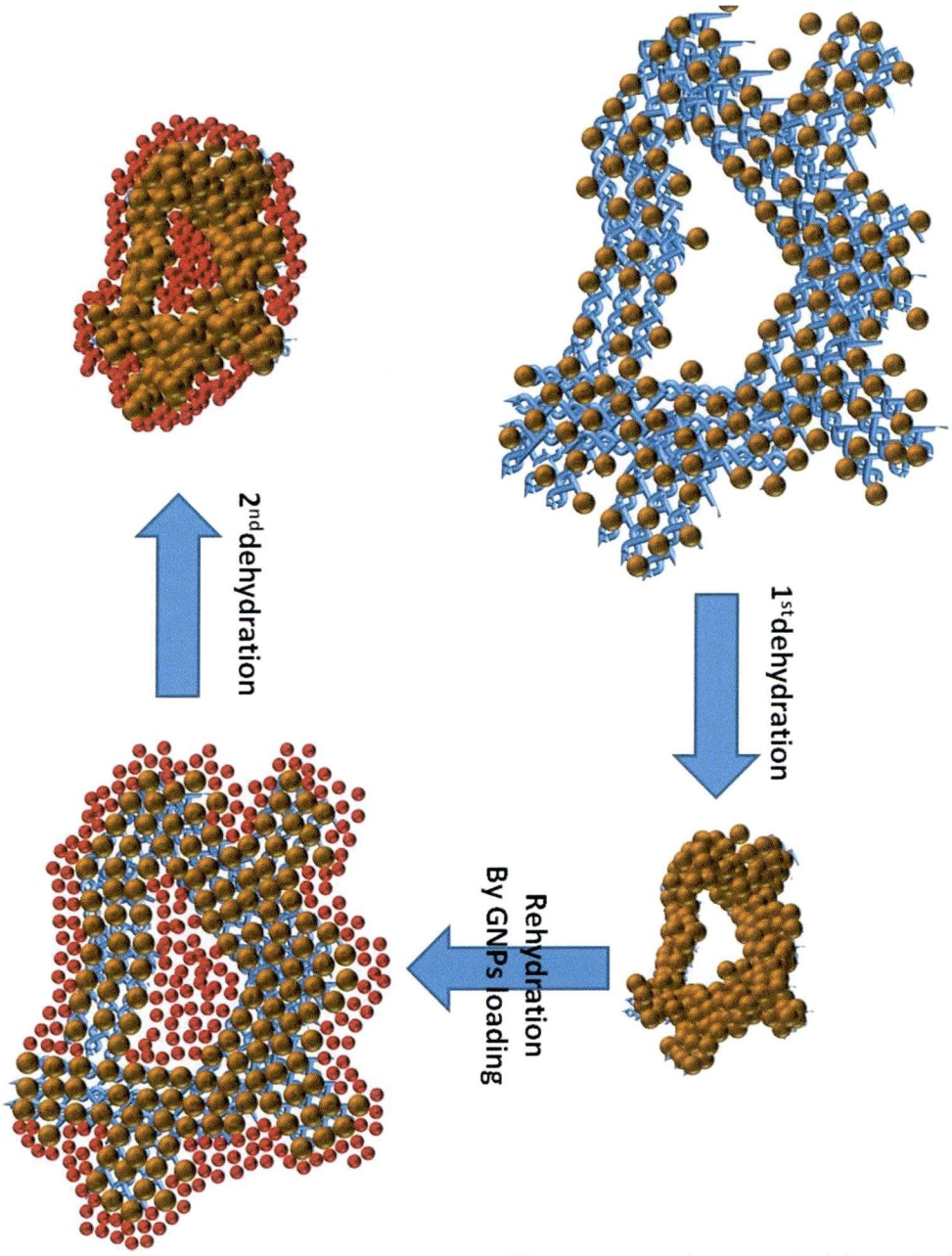

Figure 5.1 Cartoon presenting the different steps of the sandwich method used to detect the GNPs coating. The Ag-gel is first dehydrated in order to remove the water from the gel. The composite is then rehydrated by immersion in an aqueous solution of GNPs. Finally, the gel is dehydrated a second time to reduce the distance between SNPs-GNPs and to allow the formation of hotspots in the system.

5.3 Experimental

5.3.1 Materials

PEG-NHS (HS-C11-EG6-OCH2-COONHS) was purchased from Prochimia and daunorubicin (daunomycin hydrochloride: $C_{27}H_{29}NO_{10} \cdot HCl$) was purchased from Sigma Aldrich. All chemicals were used as received. In all experiments water deionised with a Milli-Q plus 185 system was used.

5.3.2Methods

5.3.2.1 Sample preparation

The Ag-gel produced for the previous Raman study was recycled here (Figure 5.1). Briefly, after three dialyses of the gel for 24 hours in Milli-Q water in order to remove the presence all the sodium borohydride, the substrate is shrunk at room temperature (natural dehydration). Following its dehydration, the hydrogel is then immersed into the solution of analyte for 2 hours. The soaking of the gel in the sample solution studied involves its rehydration and, therefore, the incorporation of the analyte molecules. A second shrinkage of the substrate involves trapping the analyte in the hydrogel.

5.3.2.2 Gold nanoparticles

Citrate-stabilised gold nanoparticles were prepared according to the Turkevich-Frens procedure[43]. Briefly, 0.06 g of $HAuCl_4.3H_2O$ was dissolved in 150 ml of water and heated to near boiling temperature. To this was added a hot (ca. 60°C) aqueous trisodium citrate solution (20ml, 50 mM), and the mixture was refluxed for 40 min. It was subsequently allowed to cool to room temperature, stirred overnight and filtered before use (0.45 μm, Millipore filter). The ruby red solution was characterised by UV-vis spectroscopy. This route provides fairly uniform, charge-stabilised nanoparticles, easily amenable to further functionalisation. Giersig and Mulvaney demonstrated that citrate-capped gold nanoparticles can be converted into thiol-protected particles simply by the addition of thiols[46].

This property was exploited for the preparation of PEG-NHSDNR nanoparticles.

5.3.3.3 Functionalisation of the Gold Nanoparticles

Citrate-stabilised gold nanoparticles were functionalised with two different anti cancer drugs. The goal of these studies is to attach a maximum number of drug molecules onto the surface of the nanoparticles in order to increase the efficiency of possible future cancer treatments via these solutions. Two different methods have been employed to attach the DNR onto the nanoparticle surface. The first one (Figure 5.2.A) was made via EDC coupling between PEG-COOH and NH2 molecule of the drug following Susumu *et al.*study[44].This method provided around 100 DNR molecules per particle. To increase the number of DNR molecules per particle a second approach, expected to be more efficient, was employed using PEG-NHS ester (Figure 5.2.B) and the number of linkages between the PNHS-DNR and the nanoparticles achieved through this process was carefully quantified by fluorescence.

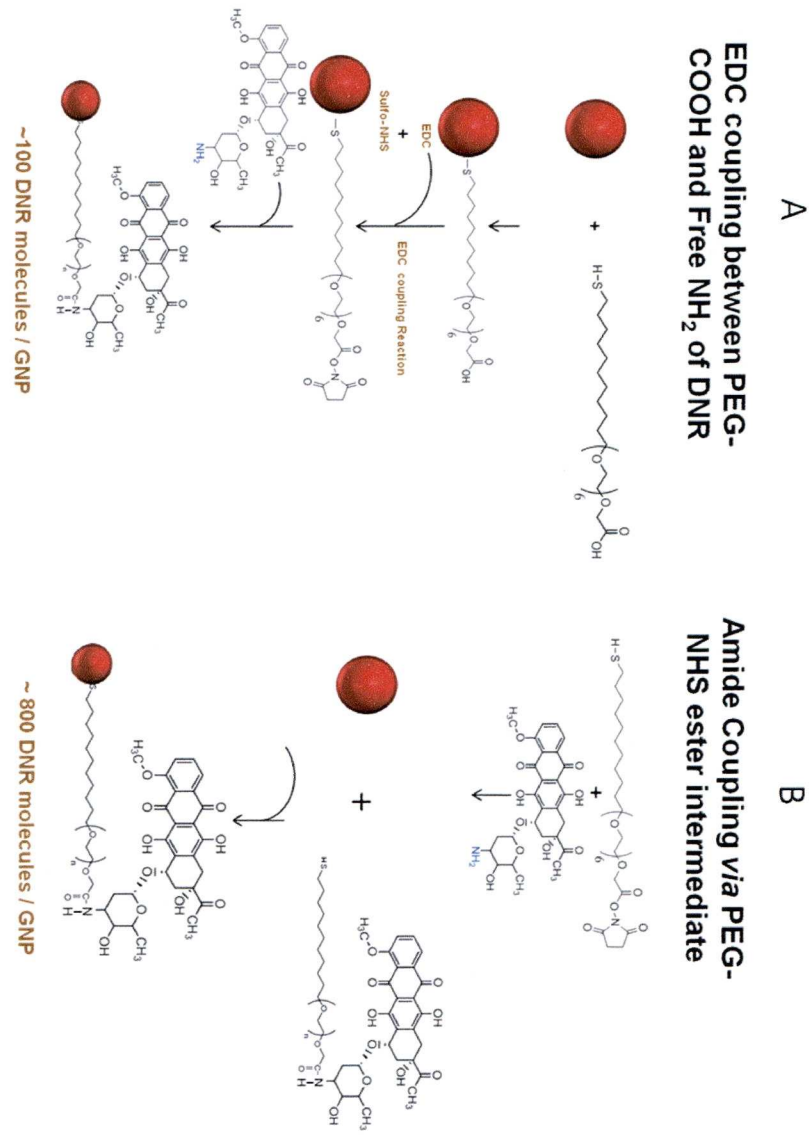

Figure 5.2 Presentation of two methods employed for the functionalisation of the GNPs. This chapter focuses on the second method (method B) as it provides a larger number of DNR molecules per nanoparticle.

5.3.3.4 Characterisation of the system

UV-vis and SEM measurements were carried out with the same instrumentation described in preceding chapters.

Fluorescence measurements were performed using a PerkinElmer LS 55 Fluorescence Spectrometer.

Elemental analysis was carried out using an ICP-AES (spectro model CIROS-CCD).

Raman spectroscopy: to validate the Surface enhanced Raman effect, Raman spectra were recorded both with an Argon (514.5nm) and He–Ne (633nm) laser. The spectra were acquired using a Jobin-Yvon LabRam HR consisting of a confocal microscope coupled to a single grating spectrometer equipped with a notch filter and a CCD camera detector. All spectra were recorded in a backscattering geometry. Five cycles of signal acquisition were performed per sample with an acquisition time of 30s per cycle. The laser power was 15mW output for the Ar ion laser (514nm) and 6mW for He-Ne (633nm). The influence of the acquisition time on the SERS/SERRS signals of our molecules was analysed at 532 nm using a RSI 2001 model for Raman System Inc (maximum power of 25mW).

Thioguanine and daunorubicin molecules have been analysed following the same process. The free molecules in solution have been characterised at 514nm and 633nm in the Ag-gel substrate providing the SERS and/or SERRS spectra of the drugs. The enhancement of the signal should offer the complete vibration bands of the molecules studied. GNPs coated with the drugs are then investigated in an Ag-gel and pure gel at 514nm and 633nm.

5.3.3.5 Quantification of the number of DNR or thioguanine per nanoparticles

The number of DNR molecules attached to the GNP surface has been determined by the interpretation of the UV-vis spectra (presented later in Figure 5.5) and on the analysis of the fluorescent measurements achieved on GNP solutions with different concentrations.

Firstly, the citrate nanoparticle diameter was determined using the method of Haiss *et al*[49]:

$$d = e^{\frac{B_1 * A_{SPR}}{A_{450} - B_2}}$$

Where B_1=3, B_2=2.2, A_{spr} represents the absorbance of the plasmon resonance peak, A_{450} is the absorbance at 450nm and d the diameter of the nanoparticles analysed. Taking the values of A_{spr} and A_{450} from Figure 5.5.A the nanoparticles' diameter is estimated at 13nm (with an average deviation of 11% following the discussion in the paper). Haiss' study also correlates the diameter of the nanoparticles with the molar decadic extinction coefficient (ε) at λ=450 nm. This value was integrated into the Beer-Lambert Law at 450nm:

$$A_{450} = \varepsilon_{450} * C * l$$

With l the width of the cuvette (value: 1) provides the molar concentration of the nanoparticle solution in moles and, therefore the amount of gold nanoparticles present in the solution. The loading of drug molecules per particle obtained by the use of the PEG-NHS ester was then efficiently quantified exploiting the fluorescent nature of the drug[45]. Indeed, the intensity of the DNR fluorescence spectrum (Figure 5.3) can be correlated to the concentration of the solution by a linear regression.

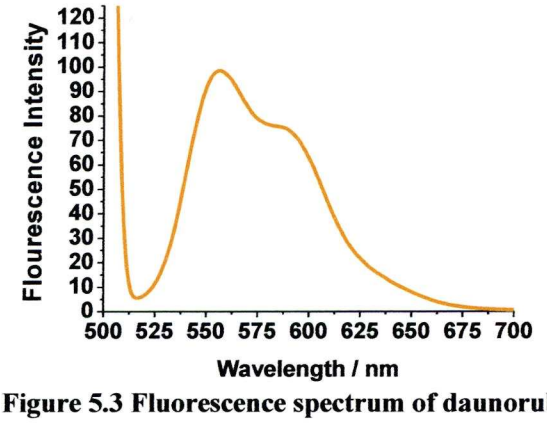

Figure 5.3 Fluorescence spectrum of daunorubicin

Fluorescence of dyes in the vicinity of a metallic surface is quenched[47]. For this reason, no fluorescence is obtained for DNR molecules as long as they are attached to the nanoparticles. The introduction of dithiothreitol (DTT), to the nanoparticle solutions liberates the DNR molecules by ligand exchange, and fluorescence appears. The correlation between the fluorescence intensity in the solution after addition of DTT with the linear

regression graph of fluorescence intensity vs. concentration provides the number of DNR molecules present in the solution.

These results have been compared to the evaluation of the number of DNR attached to the surface of each nanoparticle carried out using ICP-AES.

ICP-AES measurements were also performed to determine the number of thioguanine attached to the surface of each GNP.

5.4 Results and discussion

5.4.1 Characterisation of the GNPs

The synthesis of the nanoparticles has been developed and carried out by Samia Saleemi. Figure 5.4 presents the UV-vis spectra of the GNPs before and after functionalisation of their surfaces. It reveals a significant shift of the plasmon band from 520 nm to 530 nm, which can be attributed to the change in the refractive index induced by the altered ligand shell.

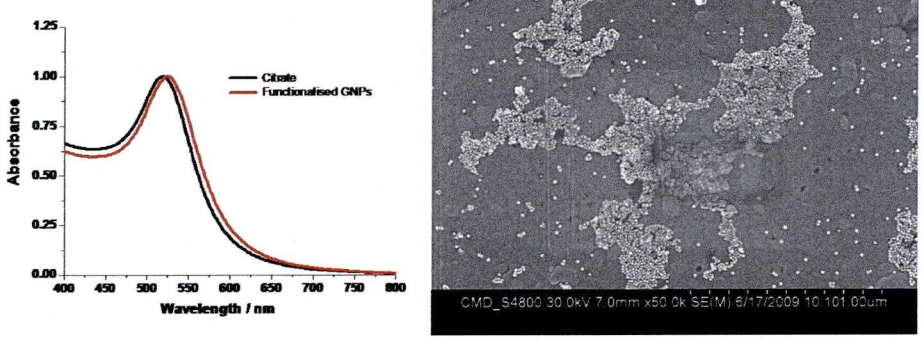

Figure 5.4 On the left side are the UV-visible spectra of the GNPs before and after functionalisation. On the right side is a SEM picture of the GNPs (average size of 10nm). These results have been provided by Samia Saleemi

Figure 5.5 exhibits also a SEM picture of these nanoparticles. The average diameter can be estimated at 10-11nm.

5.4.2 Quantification of the number of DNR molecules per nanoparticles

5.4.2.1 UV-vis and Fluorescence measurements

The Fluorescence spectroscopy has also been performed by Samia Saleemi. The number of DNR drug molecules per nanoparticle has been estimated at 800 when the method B was used (Figure 5.2).

5.4.2.2 ICP-AES measurements

To obtain a value for the total number of ligands per gold nanoparticles, the ratio between sulfur and gold was determined by ICP-AES. From these values, the amount of PNHS per nanoparticle can be established and so the ratio between the number of DNR molecules per PNHS. By considering the size of the nanoparticles to be 10nm (as they appear with SEM) we can stipulate that:

$$10nm\ GNP = 30870\ atoms \text{ (unpublished in house information)}$$

Knowing that the AES results are:

$$S: 1.372ppm;\ M_w = 32.065\ g.mol^{-1};\ C = 4.28.10^{-5}M$$

$$Au: 122.175ppm;\ M_w = 196.97\ g.mol^{-1};\ C = 6.28.10^{-4}M$$

So:

$$Amount\ of\ {}^{ligands}/_{NP} = \frac{4.28.10^{-5}M * 30870}{6.2.10^{-4}M} = 2130\ molecules$$

It means that each nanoparticle is coated with 1330 PNHS and 800 PNHS-DNR molecules.

The amount of PNHS per particle characterized for PHNS-DNR nanoparticles was verified by analysing the coating of PNHS onto gold nanoparticles via elemental analysis. The results are:

$$S: 7.491ppm;\ M_w = 32.065g.mol^{-1}; C = 2.34.10^{-4}M$$

$$Au: 659.65ppm;\ M_w = 196.97g.mol^{-1}; C = 3.35.10^{-3}M$$

So:

$$Amount\ of\ {}^{ligands}/_{NP} = \frac{2.34.10^{-4} * 30870}{3.35.10^{-3}} = 2153\ molecules$$

The results are in excellent agreement with those discussed above and show that the value of approximately 2000-2200 ligands per particle is robust.

5.4.3 Ligand-shell analysis by Raman spectroscopy

5.4.3.1 Optical properties of DNR molecules

The investigation of the molecular absorbance has been achieved by UV-vis and is shown in Figure 5.5. The absorbance spectrum of DNR exhibits a band at 520nm. This means that below an excitation wavelength of 514nm and 532nm SERRS signals should be obtained

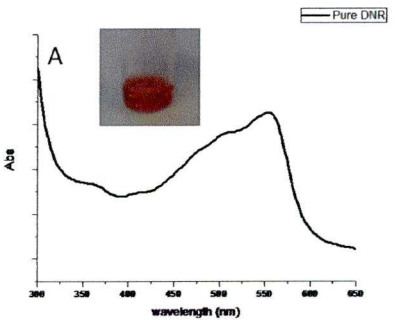

Figure 5.5 UV-visible spectrum of danorubicin with a maximum absorbance at 550nm.

5.4.4.2 Raman investigation of Daunorubicin

First, the shrunk Ag-gel was soaked in a 2.10^{-6} M solution of daunorubicin. After a second shrinkage of the gel to trap the molecules Raman spectra were recorded at the surface of the Ag-gel at 514nm (200-2200cm^{-1} range). Figure 5.6.A shows the SERRS spectrum obtained.

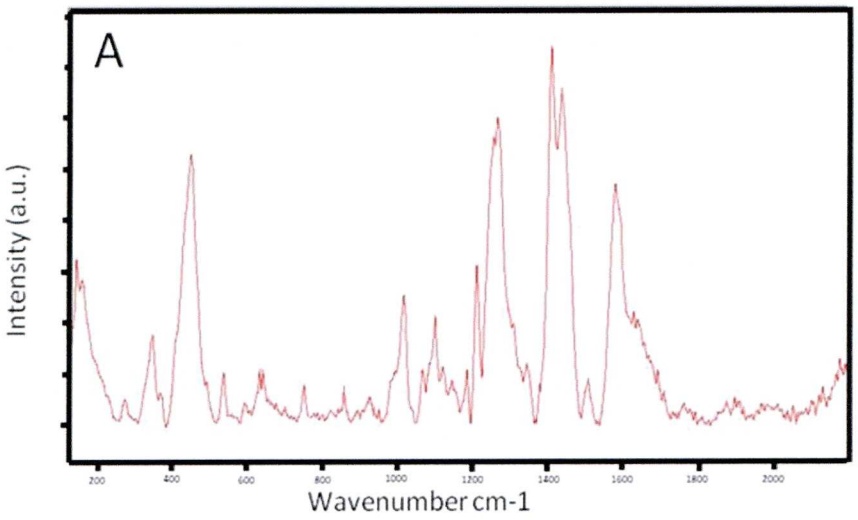

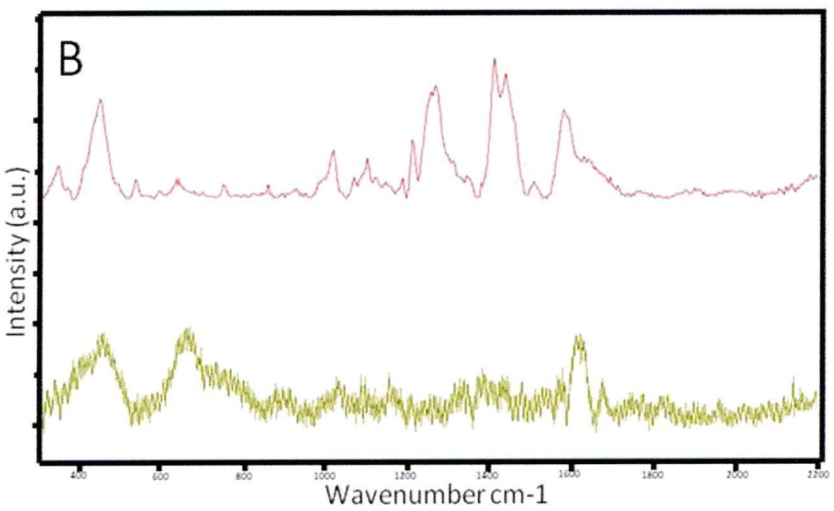

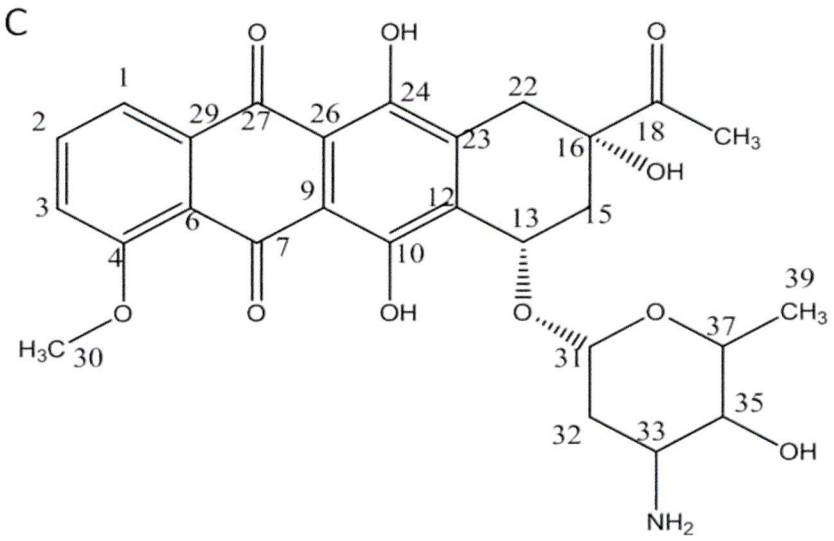

Figure 5.6 (A) SERRS signal of daunorubicin in the Ag-gel at 514nm excitation wavelength (2.10^{-6}M). (B) SERRS signal of free daunorubicin at 514nm compared to SERS signal of the same solution at 633nm. (C) Daunorubicin structure with each C-atom in the molecule numbered

High intensity peaks can be detected at 341, 446, 1210, 1246, 1266, 1408, 1435 and 1575 cm^{-1}. In addition, secondary peaks at 1008, 1101,1500,1624cm^{-1} and minor peaks at 534, 590, 634, 743, 843, 928, 1061, 1117, 1141, 1173, 1306, 1342cm^{-1} can be also detected. By comparison with the study by Das *et al.*[48] with reference to Figure 5.6.C each peak can be attributed to a precise vibration. 341cm^{-1} corresponds to ring bending, $C^{21/12}$-O-H wagging, C^{20}-H_2 wagging; 446 cm^{-1} to ring bending (phenyl group), C^{39}-H wagging, $C^{28/8}$=O bending; 534cm^{-1} to C^{24}-OH wagging, C^{31}-O-C^{13} wagging; 590 and 635cm^{-1} to C^{9}-C^{10}-O wagging, C^{15}-C^{16}-C^{18} wagging; 743cm^{-1} to ring (C-H) bending, $C^{31/35}$-H wagging, C^{39}-H_3 wagging; 843cm^{-1} to out of plane ring; 928 cm^{-1} to CO-H bending, C^{20}-H, O^{28}....H-O^{25} bending; 1008cm^{-1} to C^{20}-H_2 (aliphatic), C=O bending, C^{16}-OH bending, C^{16}-C^{18}-C^{22} bending; 1061cm^{-1} to C-C=O bending, C^{16}-OH bending, C^{13}-H bending, C^{16}-C^{22}bending; 1101cm^{-1} to stretching ring, $C^{22/32}$-H_2 wagging, $C^{16/35}$-OH stretching, C^{39}-H_3 wagging; 1117 cm^{-1} Ring breathing, C^{16}-C^{18}-O, C^{30}-H_3 bending; 1141cm^{-1} to ring, C-H (aromatic), C^{30}-H_3; 1173 and 1210cm^{-1} to OH...O bending, ring, out of plane C^{20}-H_2,

C^{11}-OH bending, N-H_2; 1246cm^{-1} to C^{32}-H_2, $C^{33/35/37}$-H, O^{36}-H, C-O^{38}-C; 1266cm^{-1} to O^{10}-H...O^{8} bending, N-H_2 bending, C^{16}-O-H bending, C-$H_{1/2or3}$ bending; 1306 and 1342cm^{-1} to O-H....O bending, ring, $C^{22/15}$-H_2, C^{16}-OH bending, C^{13}-H; 1408cm^{-1} to ring (phenyl) stretching, O-H, $C^{22/20/15}$-H_2, $C^{13/31/33/37}$-H bending, C^{32}-H_2 bending; 1435cm^{-1} to ring-O, ring=O, $C^{22/20/15}$-H_2 bending, $C^{13/31/33/37}$-H bending, C^{32}-H_2 bending; 1500cm^{-1} to $C^{20/22}$-H_2 bending, $CO^{11/25}$-H bending; 1575cm^{-1} to ring, ring (phenyl) and finally 1624cm^{-1} to ring. All these vibrations are characteristic of daunorubicin. This experiment demonstrates the strong surface enhancement properties of the Ag-gel. The same substrate was then analysed under a 633nm excitation wavelength. Figure 5.6.B displays the spectrum acquired in comparison to the spectrum obtained at 514nm. The resulting intensity of the signal (633nm) is weaker than the one presented before (514nm) and most of the vibrational bands have disappeared even though the first part of the chapter referred to an increase of the signal enhancement as the laser energy was decreased. This phenomenon can be easily explained by the UV-vis spectrum of the DNR presented earlier. Under the 514nm excitation wavelength the system displays a SERRS signal while the signal obtained at 633nm is a SERS signal. The overlapping of the DNR absorption band with the laser wavelength enhance further the peaks corresponding to the C-C stretching (1408, 1435, 1575 and 1624cm^{-1}) and the peaks at low wavelengths.

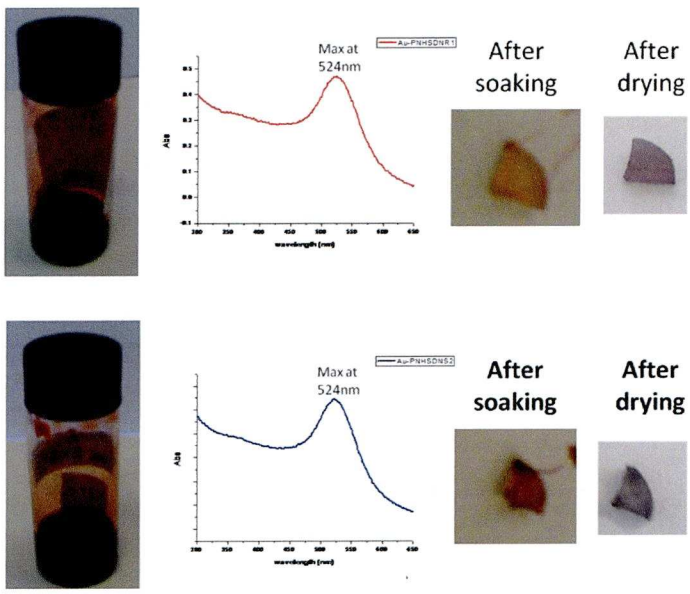

Figure 5.7 (Top) shows the UV-vis spectrum of the GNPs in solution ($2.13.10^{-7}$M) and on the right the gel loaded with these GNPs before and after dehydation. (Bottom) shows the same analysis obtained with a higher concentration of GNPs in the sample solution ($6.76.10^{-7}$M)

With the SERRS/SERS detection of the drug having been validated, the second part of the Raman study focussed on the recognition of the shell coating the GNPs. Two systems were set up and compared at each excitation wavelength. The first was an Ag-gel containing the GNPs in its water phase and the second is a pure gel containing the GNPs also in its water phase. At first sight the systems could be considered as quite similar but the shrinkage of the pure gel is different from the same gel decorated with silver nanoparticles. When the Ag-gel loses 90% percent of its volume upon dehydration the pure gel loses 95%. The rehydration process is also different. While the Ag-gel recovers 17% of its volume the pure gel recovers more than 30%. This means that when the same concentration of GNPs in incorporated in both gel, the distance inter GNPs will be smaller in the pure gel that in the Ag-gel. This could have a massive impact on the measurement at 633nm. Fig 5.7.A and B display the UV-vis spectra of two different concentrations of GNPs before and after the shrinkage of the gel.

When the pure gel was soaked in a 213nM aqueous solution of 10nm gold nanoparticles and subsequently shrunk, the colour of the gel changed from red to violet. This means that the interparticle distance is reduced due to the dehydration of the substrate. This involves a shift in the surface plasmon resonance of the system which becomes larger when the concentration of gold nanoparticle solution is increased as shown in Figure 5.7.B (concentration of GNPs: 653nm). The colour of the gel after dehydration in this case is purple-blue. Although the UV-vis measurements on the shrunken gel did not provide any relevant data on the absorption bands we can assume that their surface plasmon resonance correspond to 600 and 700nm respectively (shift to longer wavelengths).

For simplicity, the different samples studied with different experimental conditions are denoted by the abbreviations showed in table 5.1

Molecule analysed	Substrate	GNP concentration (nM)	name of the sample
DNR	Ag-gel	653	DNR1
		213	DNR2
	pure gel	653	PUREDNR1
		213	PUREDNR2

Table 5.1 Nomenclature of the samples presented in this chapter

The next Figures (5.8.A, B, and C) display the Raman spectra of the different systems. Figure 5.8.A exhibits the spectra of DNR1 in comparison to the PUREDNR1 at a 514nm excitation wavelength.

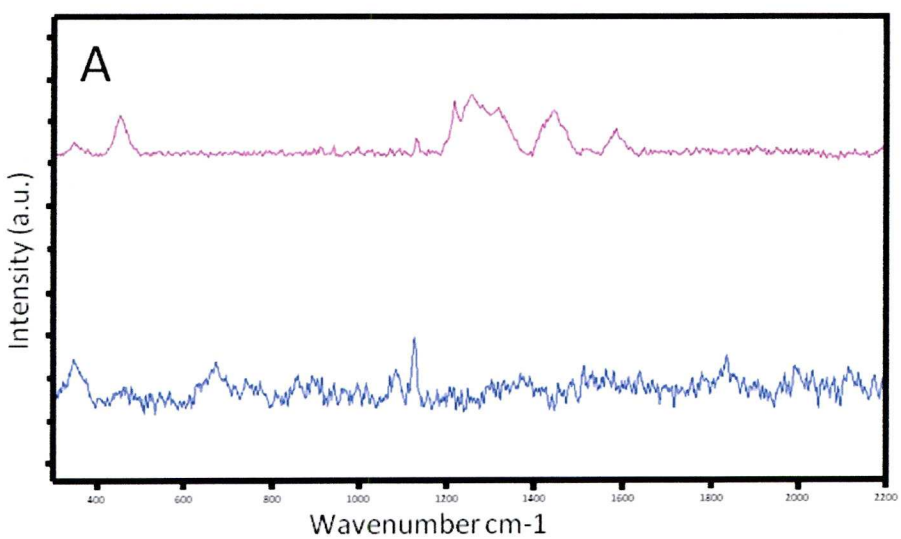

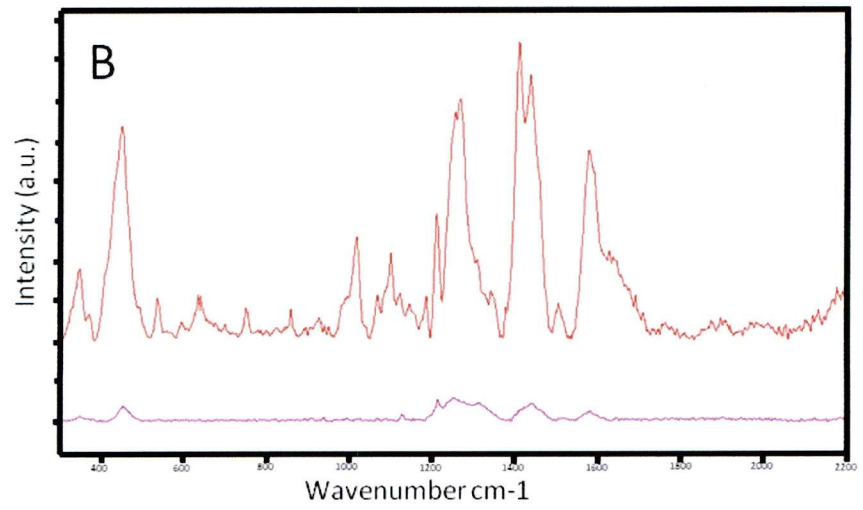

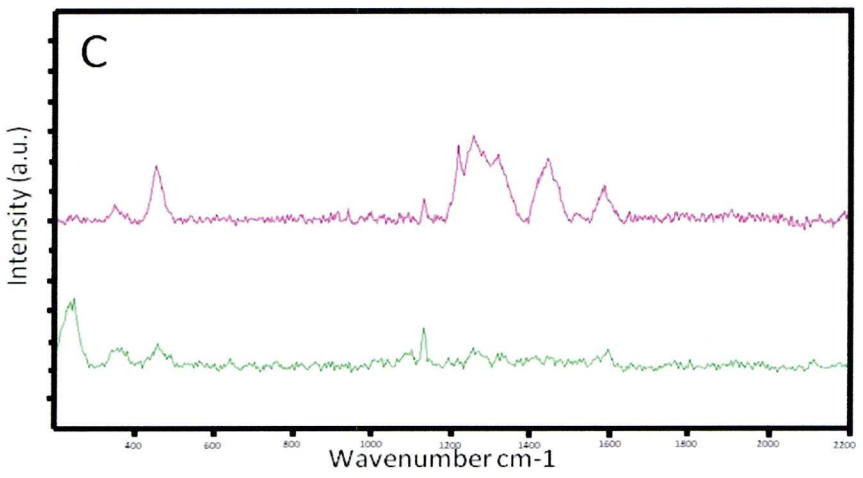

Figure 5.8 (A) Raman spectra obtained with the DNR1 (pink) and the pure1 (blue) at 514nm excitation wavelength. (B) Spectrum obtained on a free DNR solution (red) compared to the DNR1 (pink) at 514nm. (C) Spectrum obtained on DNR1 (pink) and DNR2 (green) at 514nm.

The presence of silver particles surrounding the GNPs enhanced the signal and more specifically peaks at 352, 449, 1126, 1213, 1251, 1276, 1412, 1425, 1439, 1508, 1574 and 1581 cm^{-1}. All these peaks are related to the vibrations (stretching, breathing and bending) of the rings which composed daunorubicin molecules. For PUREDNR1, the signal obtained was very poor and just one peak could be detected (1126cm^{-1}). This comparison showed the importance of the silver particles within the sandwich structure. Figure 5.8.B compares the SERRS signal obtained on a pure solution of

DNR in a in Ag-gel (concentration 2.10^{-6}M) to the SERRS signal acquired with DNR1 (concentration of DNR: $653x10^{-9}x800=5.22.10^{-4}$M). Despite a concentration of DNR molecules 200 times larger the SERRS signal obtained with DNR1 is extremely weak compared to the SERRS signal of a pure solution of DNR in an Ag-gel. Several explanations are possible for this phenomenon. Firstly, when the Ag-gel is soaked in a pure solution of DNR the molecules interact directly with the surface of the silver nanoparticles (by its amine group). Moreover, the swelling upon the loading of the molecule solution results in an increase of the interparticle distance. The molecules can diffuse between the particles and be trapped between them under the second dehydration of the gel. This means that the molecules are situated where the hotspots are formed. On the other hand, when the molecules form the GNP shell, the diffusion of the system between the silver nanoparticles is clearly affected by the size of the GNP themselves (10nm diameter). The GNPs can only interact with the silver aggregates on their surfaces. Secondly, assuming the diameter of each silver nanoparticles to be 33nm (referred to the TEM picture displayed in the first part of this chapter) and the diameter of the GNPs as 10nm with a shell thickness of 3.2nm (the length of the PNHS-DNR structure was evaluated at 3.28nm using SPARTAN software), it is clearly evident that just a fraction of the GNPs shell will be localised in the electromagnetic field emanated from the resonance of the silver nanoparticles. Figure 5.9 illustrates these problems.

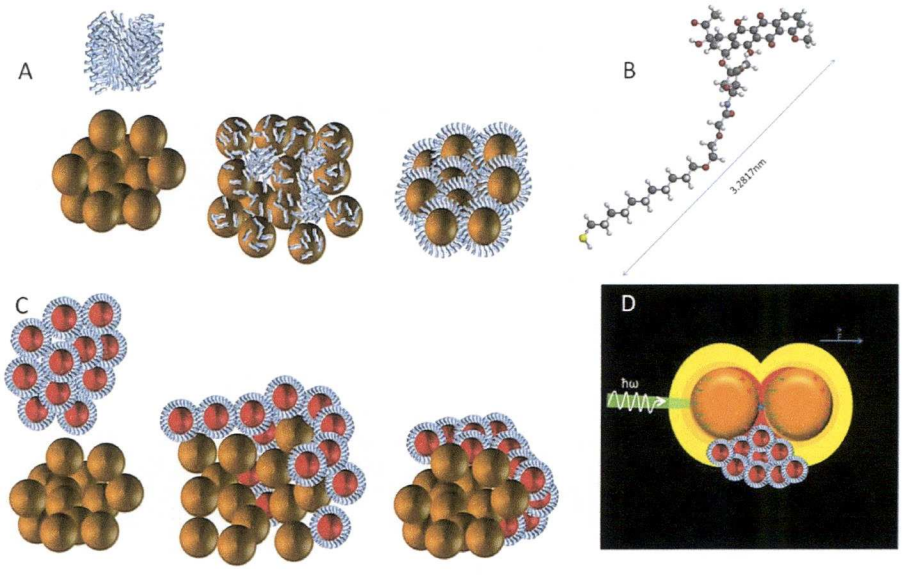

Figure 5.9 (A) Cartoon displaying the coating with the free DNR molecules of the SNP surface and the diffusion of these molecules inside the hotspots. (B) shows the PNHS-DNR ligand structure and its length (3.28nm). (C) shows that the problem is different when the DNR molecules are coating the GNPs. The DNR molecules cannot interact with the entire surface of the SNPs and even less diffused inside the hotspots. Finally (D) is a cartoon exhibiting the maximum ratio of DNR molecules which can interact with the SNPs when they coat the GNPs.

So if the GNPs were saturating the Ag-gel pores, just a third of GNPS present outside the GNPs aggregates would be interacting with the silver nanoparticles. This issue should disappear with the increase of the laser excitation wavelength as the GNPs should be in resonance as well as the silver aggregates. Finally, Figure 5.8.C shows a comparison of DNR1 and DNR2. As the GNP concentration decreases in the gel, the intensity of the SERRS spectra also decreases. The intensity of the SERS signal decreases following the expression $(a/r)^{12}$, where a is the radius of the silver particle and r is the distance of the observed point to the centre of the silver particle In our case, the decrease of the GNP concentration in the gel increase the SNP-GNP distance and so reduces the possible signal of the molecules forming the GNP shell.

In fact it is possible to give an estimation of the concentration of GNP solution needed in order to obtain a maximum signal. We know that

94.6%$_w$ of the hydrogel is water. Knowing the density of agarose and water we can say that:

$$\rho_{aga} = 0.9 \; and \; \rho_{water} = 1$$

$$\%_{V\,aga} = \frac{\frac{5.4}{9}}{\frac{5.4}{9} + 94.6} = 6 \; and \; \%_{V\,water} = \frac{94.6}{\frac{5.4}{9} + 94.6} = 94$$

Knowing that each piece of wet gel used here had a volume 0.23cm^3:

$$Volume_{water\ per\ piece\ of\ wet\ gel} = \frac{0.23.10^{-6}\ x\ 94}{100} = 2.162x10^{-7}m^3$$

Considering that the decoration of the gel network with silver nanoparticles follows the same pattern to that of gold (see page 70 in section 2.3.5.1 in Chapter 2) and considering that when the gel is shrunk and rehydrated the final volume of the gel corresponds to only 21% of the starting volume, we can say that the maximum volume of GNPs than can be contained in the gel is:

$$Volume_{GNPs} = 0.21\ x\ 2.162x10^{-7} = 4.54x10^{-8}m^3$$

Moreover, the complete dehydration of the gel involves a loss of 90% of the gel volume. So the optimum volume of GNPs necessary to optimize the SERRS detection is:

$$Volume_{GNPs\ after\ dehydration} = 0.1\ x\ 2.162x10^{-7} = 2.162x10^{-8}m^3$$

Finally we know the volume of 1GNP coated with DNR:

$$d_{GNP\ coated} = 10 + 2x3.28 = 16.56nm$$

$$Volume_{1\ GNP\ coated\ with\ DNR} = \frac{4}{3}x\ \pi\ x\ r^3 = 2.378\ x\ 10^{-24}m^3$$

So we need:

$$Amount\ of\ GNPs = \frac{2.162x10^{-8}}{2.378x10^{-24}} = 9.092x10^{15}$$

This amount of particles should be present in a volume of $4.54x10^{-8}m^3$ (equivalent to $5.54x10^{-5}dm^3$). So the concentration of GNPs needed at the beginning of the experiment is:

$$C_{GNPS} = \frac{9.092x10^{15}}{4.54.10^{-5}\ x\ 6.022141x10^{23}} = 3.33x10^{-4}M$$

This is 500 times more concentrated than in DNR1. It is, of course, impossible to consider the execution of this kind of experiment as it would take a long time to provide such a high concentration of nanoparticles. The other alternative would be to dramatically decrease the pore size of the gel by increasing the concentration of agarose in the hydrogel. DNR1and DNR2 were also characterised at 633nm. Figure 5.10 displays the signals obtained. Figure 5.10.A and B reveal that the signal is enhanced at 633nm in comparison to the signals acquired at 514nm in both systems. Peaks at 365, 464, 1215, 1248, 1268, 1307, 1337, 1410, 1431, 1567, 1625 cm^{-1} are enhanced in DNR1 and correspond to the vibrations described before for the Figure 5.8. Several new vibrational bands (1471, 1514, 1552, 1663 and $1712cm^{-1}$) detected here did not appear in the previous signals. They correspond respectively to ring, C^{30}-H_3 bending; $C^{20/22}$-H_2 bending, $CO^{11/25}$-H bending; ring (phenyl); stretching ring, CO^{25}-H bending and finally N-H bending.

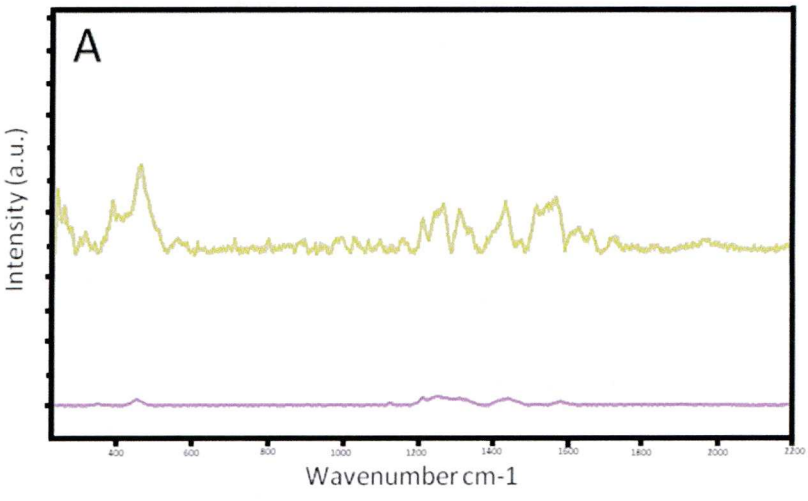
A
Intensity (a.u.)
400
600
800
1000
1200
1400
1600
1800
2000
2200
Wavenumber cm-1

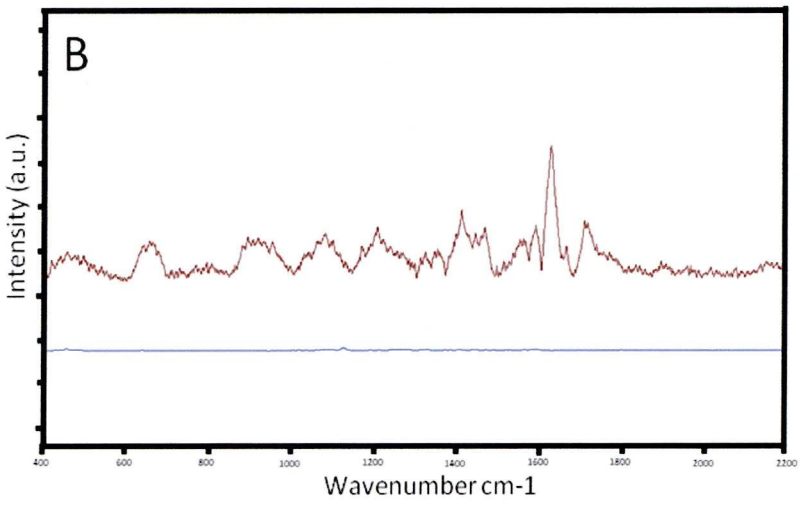
B
Intensity (a.u.)
400
600
800
1000
1200
1400
1600
1800
2000
2200
Wavenumber cm-1

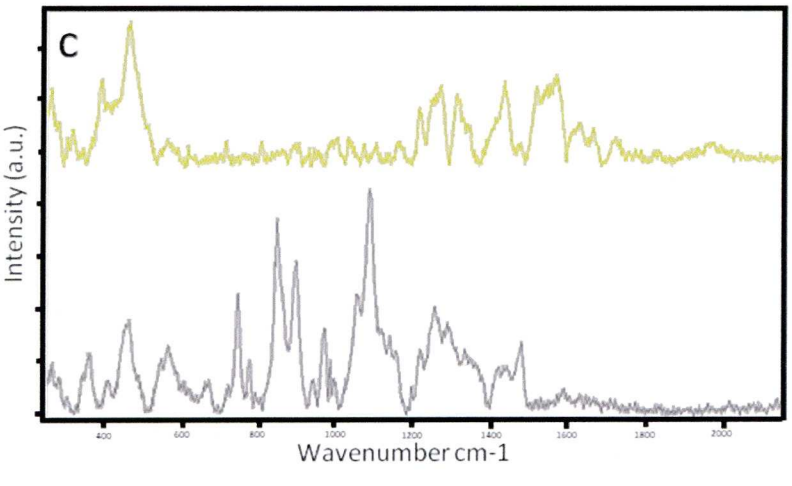
C
Intensity (a.u.)
400
600
800
1000
1200
1400
1600
1800
2000
Wavenumber cm-1

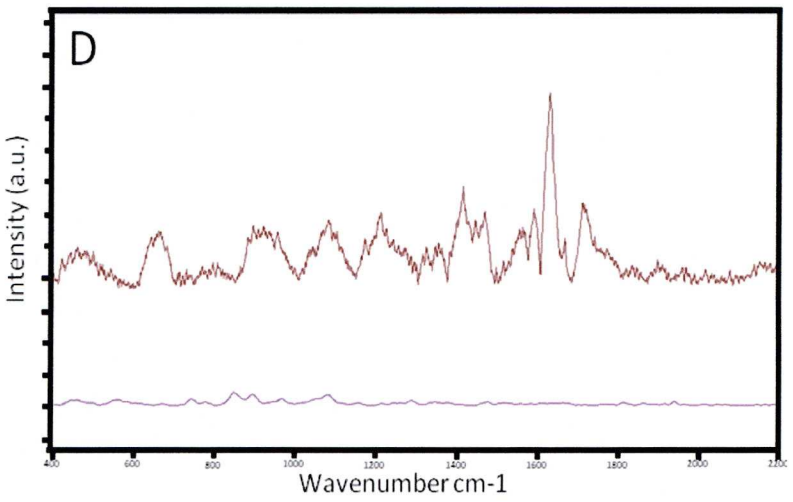

Figure 5.10 (A) shows a comparison between the Raman spectrum of DNR1 obtained under 514nm (pink) and 633nm (kaki) excitation wavelengths. (B) displays the same characterisation on DNR2 (633nm in brown and 514nm in blue). (C) compares DNR1 (kaki) with PUREDNR1 (grey) at 633nm excitation wavelength. Finally (D) compares DNR2 (brown) and PUREDNR2 (violet) at 633nm.

For DNR2, peaks are well enhanced at 1408,1439, 1460, 1560, 1626, 1661, 1705cm^{-1} and some can be detected at 647, 1067, 1163 and 1201cm^{-1}. Their vibrational association have been described in previous analyses. The strongest vibration is situated at 1626 cm^{-1} and corresponds to the rings. The absence of strong peaks in both cases between 440 to 1200cm^{-1} can be related to the absence of the daunorubicin molecular resonance under a a 633nm excitation wavelength. At this laser energy, the signals obtained are no longer SERRS but SERS. The enhancement of the signal takes its origin from the overlapping between the LSPR of the Ag-substrate with the laser wavelength. The signals of DNR1 and DNR2 were then compared to the signals of PUREDNR1 and PUREDNR2 acquired with the same excitation wavelength. While PUREDNR1 provides a more complete detection of the shell coatings than DNR1 (Figure 5.10.C) DNR2 obtained a better detection than PUREDNR2 (Figure 5.10.D). In the pure gel, the laser interacts immediately with the surface of the GNPs. In addition, if the SPR of the GNPs overlaps the wavelength excitation, the electromagnetic field around the GNPS will be enhanced and so the detection of the molecules attached onto their surface. If the SPR of the GNPs structure does not

overlap the excitation wavelength, the electromagnetic field will not be enhanced and so it will be more difficult to detect molecules attached onto the surface of the GNPs. When a silver nanoparticle structure is surrounded by the GNP system, the laser interacts with the surface of the silver nanoparticles. The electromagnetic field will be extremely enhanced at their surfaces and diminishes as a function of surface distance. The last two explanations provide insight into the behaviour of our two systems. The "large distance" between the GNPs and SNPs (in SERS measurement) results in a decrease of the DNR detection in the sandwich structure.

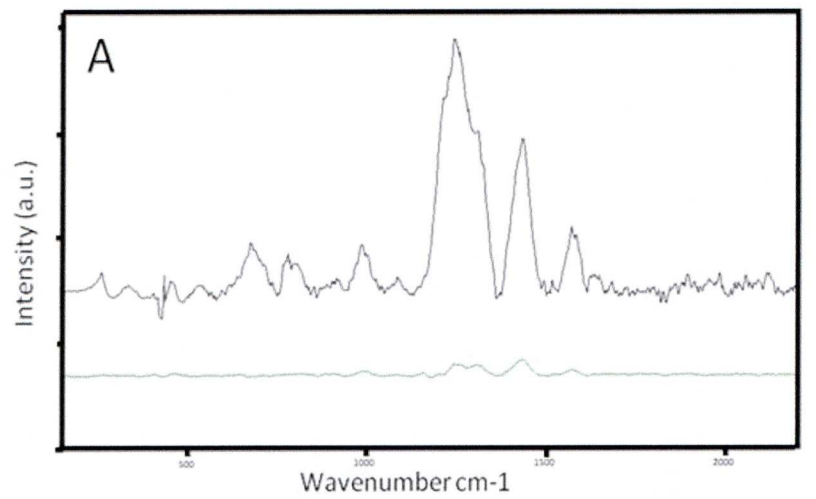

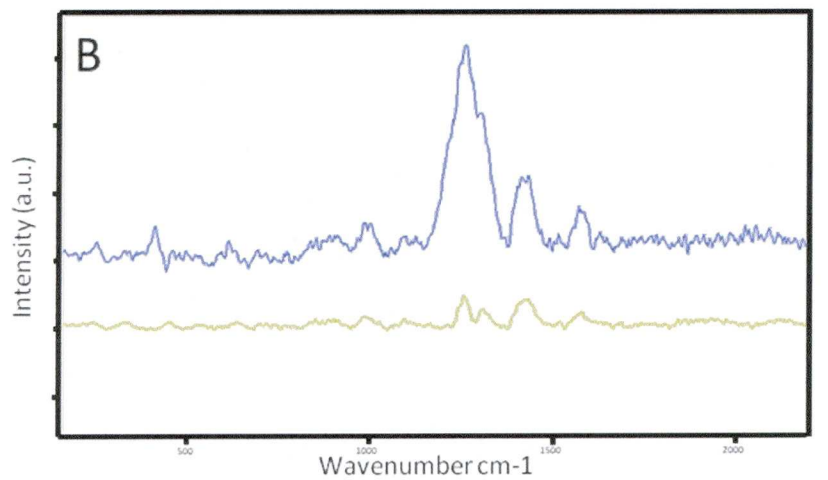

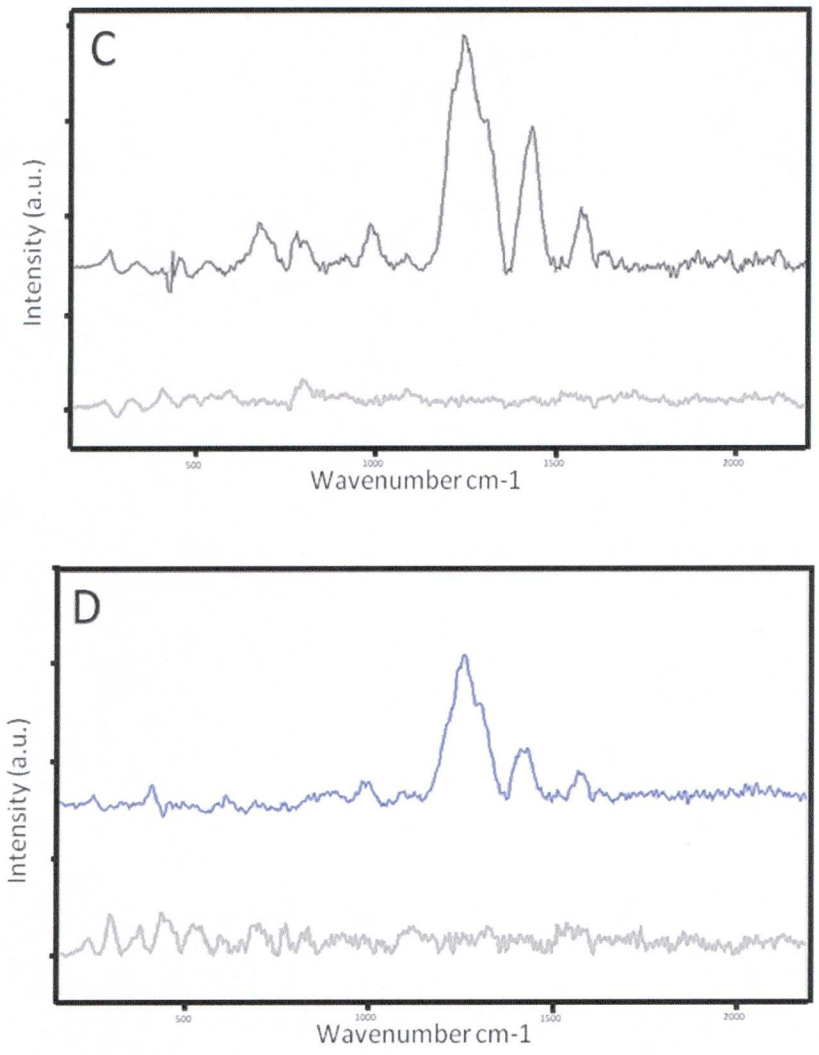

Figure 5.11 (A) exhibits the spectra obtained on DNR1 at 532nm after 60s (green) and 480s (black) acquisition time. (B) shows the same characterisation on DNR2 (60s in kaki and 480s in blue). Figure C compares the DNR1 (black) and PUREDNR1 (grey) signals obtained at 532nm after 480s acquisition time. Finally, (D) represents the same characterisation than in Figure C but obtained with DNR2 (blue) and PUREDNR2 (grey).

Finally, analysis of DNR1, DNR2 and PUREDNR1and PUREDNR2 with different acquisition times was completed at 535nm. The results are shown in Figure 5.11.Vibrational peaks of the DNR can be detected in both systems in the Ag-gel with 60s and 480s acquisition times. Obviously, better signals are obtained with longer acquisition times (Figure 5.11.A and B). An increase in GNP concentration gives a higher intensity signal and a better detection of the DNR (see explanation on the SNP-GNP distance mentioned above). Peaks at 343, 451, 533, 678, 775,801,852, 909, 986,

1079, 1208, 1244, 1300, 1429 and 1574cm^{-1} appear with the most enhanced bands being related to the vibration of the rings. These signals perfectly match the signal acquired with the solution of pure DNR presented in Figure 5.6.A. On the other hand, PUREDNR1 and PUREDNR2 provide signals with no particular enhancement. In these series of experiments the peaks are very broad due to burning of the sample (distance between the laser and substrate is too small).

5.5 Conclusions

To conclude, this study shows that the trapping of GNPs in silver gel allows the detection of the molecules coating the surface of the GNPs. At 633nm, the presence of the silver "cage" around the GNPs enhanced the electromagnetic fields thus augmenting the vibration intensity of the molecules formed around the GNPs. These molecules are also detected at 514nm levels with their signal greatly enhanced due the presence of localized surface plasmon resonance in the silver substrate. The intensity of the signal could be further enhanced if the SNP-GNP distance can be reduced. This could be achieved by an increase of the GNPs concentration in the gel by the decrease of the pore size of the gel. Knowing that to obtain a maximum enhancement of the signal the molecule should be between 0 and 1 nm from the surface of the gold the system can clearly be optimized. Moreover, the saturation of the pore should result in the formation of hotspots homogeneously through the entire surface and in addition to the chemisorption of the molecule on the surface of the GNPs the signal should be extremely enhanced.

The detection of the GNPs can also be achieved by using a pure gel if the concentration of GNPs is high enough. The signal obtained can be even better than with the sandwich method due to the better hydration properties of the gel although no detection can be obtained at high energy excitation.

To summarize, the sandwich method provides an enhancement of the signal with all excitation wavelengths used while the pure gel can provide a better SERS signal of the molecules coating the GNP shell with the correct concentration and the right excitation. If we consider that the concentration

of GNPs generally used in most experiments are no more than few nM, the use of an Ag-gel as a SERS substrate could provide a fast detection of the molecules functionalising the GNPs while the use of a pure piece of gel would not offer any interesting SERS features.

References

1. S. Eustis, M. A. El-Sayed, *Chemical Society Reviews* **2006**, *35*, 209.

2. D. I. Gittins, A. S. Susha, B. Schoeler, F. Caruso, *Advanced Materials* **2002**, *14*, 508.

3. M. Brust, M. Walker, D. Bethell, D. J. Schiffrin, R. Whyman, *Journal of the Chemical Society-Chemical Communications* **1994**, 801.

4. V. Sharma, K. Park, M. Srinivasarao, *Materials Science & Engineering R-Reports* **2009**, *65*, 1.

5. N. T. K. Thanh, L. A. W. Green, *Nano Today* **2010**, *5*, 213.

6. D. A. Giljohann, D. S. Seferos, W. L. Daniel, M. D. Massich, P. C. Patel, C. A. Mirkin, *Angewandte Chemie-International Edition* **2010**, *49*, 3280.

7. E. Boisselier, D. Astruc, *Chemical Society Reviews* **2009**, *38*, 1759.

8. I. H. El-Sayed, X. H. Huang, M. A. El-Sayed, *Nano Letters* **2005**, *5*, 829.

9. J. F. Hainfeld, D. N. Slatkin, H. M. Smilowitz, *Physics in Medicine and Biology* **2004**, *49*, N309.

10. A. G. Kanaras, F. S. Kamounah, K. Schaumburg, C. J. Kiely, M. Brust, *Chemical Communications* **2002**, 2294.

11. S. H. Chen, K. Kimura, *Langmuir* **1999**, *15*, 1075.

12. M. Brust, J. Fink, D. Bethell, D. J. Schiffrin, C. Kiely, *Journal of the Chemical Society-Chemical Communications* **1995**, 1655.

13. T. G. Schaaff, G. Knight, M. N. Shafigullin, R. F. Borkman, R. L. Whetten, *Journal of Physical Chemistry B* **1998**, *102*, 10643.

14. S. W. Chen, R. W. Murray, *Langmuir* **1999**, *15*, 682.

15. A. C. Templeton, S. W. Chen, S. M. Gross, R. W. Murray, *Langmuir* **1999**, *15*, 66.

16. P. A. Buining, B. M. Humbel, A. P. Philipse, A. J. Verkleij, *Langmuir* **1997**, *13*, 3921.

17. W. P. Wuelfing, S. M. Gross, D. T. Miles, R. W. Murray, *Journal of the American Chemical Society* **1998**, *120*, 12696.

18. G. H. Woehrle, L. O. Brown, J. E. Hutchison, *Journal of the American Chemical Society* **2005**, *127*, 2172.

19. D. I. Gittins, F. Caruso, *Chemphyschem* **2002**, *3*, 110.

20. D. Shenoy, W. Fu, J. Li, C. Crasto, G. Jones, C. DiMarzio, S. Sridhar, M. Amiji, *International Journal of Nanomedicine* **2006**, *1*, 51.

21. M. J. Hostetler, A. C. Templeton, R. W. Murray, *Langmuir* **1999**, *15*, 3782.

22. L. O. Brown, J. E. Hutchison, *Journal of Physical Chemistry B* **2001**, *105*, 8911.

23. M. G. Warner, S. M. Reed, J. E. Hutchison, *Chemistry of Materials* **2000**, *12*, 3316.

24. M. G. Warner, J. E. Hutchison, *Nature Materials* **2003**, *2*, 272.

25. R. Levy, N. T. K. Thanh, R. C. Doty, I. Hussain, R. J. Nichols, D. J. Schiffrin, M. Brust, D. G. Fernig, *Journal of the American Chemical Society* **2004**, *126*, 10076.

26. Q. Dai, J. G. Worden, J. Trullinger, Q. Huo, *Journal of the American Chemical Society* **2005**, *127*, 8008.

27. K. Kamata, Y. Lu, Y. N. Xia, *Journal of the American Chemical Society* **2003**, *125*, 2384.

28. A. C. Templeton, M. J. Hostetler, E. K. Warmoth, S. W. Chen, C. M. Hartshorn, V. M. Krishnamurthy, M. D. E. Forbes, R. W. Murray, *Journal of the American Chemical Society* **1998**, *120*, 4845.

29. A. H. Latham, M. E. Williams, *Langmuir* **2006**, *22*, 4319.

30. B. L. V. Prasad, S. K. Arumugarn, T. Bala, M. Sastry, *Langmuir* **2005**, *21*, 822.

31. C. D. Keating, K. M. Kovaleski, M. J. Natan, *Journal of Physical Chemistry B* **1998**, *102*, 9404.

32. F. McKenzie, K. Faulds, D. Graham, *Nanoscale* **2010**, *2*, 78.

33. H. Acharya, J. Sung, B. H. Sohn, D. H. Kim, K. Tamada, C. Park, *Chemistry of Materials* **2009**, *21*, 4248.

34. E. Cortes, N. G. Tognalli, A. Fainstein, M. E. Vela, R. C. Salvarezza, *Physical Chemistry Chemical Physics* **2009**, *11*, 7469.

35. R. Gunawidjaja, E. Kharlampieva, I. Choi, V. V. Tsukruk, *Small* **2009**, *5*, 2460.

36. Y. C. Liu, *Electrochemistry Communications* **2005**, *7*, 1071.

37. L. H. Lu, A. Eychmuller, A. Kobayashi, Y. Hirano, K. Yoshida, Y. Kikkawa, K. Tawa, Y. Ozaki, *Langmuir* **2006**, *22*, 2605.

38. T. Y. Olson, A. M. Schwartzberg, C. A. Orme, C. E. Talley, B. O'Connell, J. Z. Zhang, *Journal of Physical Chemistry C* **2008**, *112*, 6319.

39. C. J. Orendorff, A. Gole, T. K. Sau, C. J. Murphy, *Analytical Chemistry* **2005**, *77*, 3261.

40. M. Rycenga, K. K. Hou, C. M. Cobley, A. G. Schwartz, P. H. C. Camargo, Y. N. Xia, *Physical Chemistry Chemical Physics* **2009**, *11*, 5903.

41. S. P. Xu, B. Zhao, W. Q. Xu, Y. G. Fan, *Colloids and Surfaces a-Physicochemical and Engineering Aspects* **2005**, *257-58*, 313.

42. Y. A. Yang, A. M. Bittner, K. Kern, *Journal of Solid State Electrochemistry* **2007**, *11*, 150.

43. J. Turkevich, P. C. Stevenson, J. Hillier, *Discussions of the Faraday Society* **1951**, 55.

44. K. Susumu, H. T. Uyeda, I. L. Medintz, T. Pons, J. B. Delehanty, H. Mattoussi, *Journal of the American Chemical Society* **2007**, *129*, 13987.

45. M. T. Htun, *Journal of Luminescence* **2009**, *129*, 344.

46. M. Giersig, P. Mulvaney, *Langmuir* **1993**, *9*, 3408.

47. P. Anger, P. Bharadwaj, L. Novotny, *Physical Review Letters* **2006**, *96*.

48. G. Das, A. Nicastri, M. L. Coluccio, F. Gentile, P. Candeloro, G. Cojoc, C. Liberale, F. De Angelis, E. Di Fabrizio, *Microscopy Research and Technique* **2010**, *73*, 991.

49. W. Haiss, N. T. K. Thanh, J. Aveyard, D. G. Fernig, *Analytical Chemistry* **2007**, *79*, 4215.

Chapter 6: conclusions, improvements, and perspectives

6.1 Conclusions

In the second chapter, we describe the in-situ synthesis of network-forming metal nanoparticles in agarose hydrogels. This was achieved by the immersion of a pure piece of the gel in a metal salt solution followed by immersion in a solution of a reducing agent (500mM solution of $NaBH_4$). Clusters and atomic layers of metal were obtained and stabilized through interactions with the hydrogel network. In the case of gold, the nanoparticle/cluster size was fully characterized by the use of different techniques. While the investigation by X-ray diffraction has provided the average size of the large nanoparticles, mass spectrometry (MALDI-TOFMS) has evidenced the existence of much smaller clusters and atoms inside the gel matrix. These results have been confirmed by electron microscopy. In dark field mode, the gel shows a decoration of its internal network (nanoscale) by small clusters, and by large nanoparticles on its external structure (microscale). The decoration of the network involves the appearance of amorphous metal colloids. These colloids are called "glassy colloids" and are located on the surface of agarose fibre aggregates. These fibres are composed of close packed double helical agarose molecules. We have also shown that an increase in concentration of metal ions in the hydrogel results in an increase of the average size of the larger nanoparticles. This can be explained by the hydrolysis and the opening of agarose chains under a decrease of the pH of the system. –OH groups replace $–O^-$ and cavities between the double helix chains of agarose disappear. The clusters and the nanoparticles, at their respective scales, become unstable and aggregate with their neighbours. This, however, is one possible explanation. The observed results may also be due to a larger availability of metal in the gel. Most of the other metals lead to the same nanocoating pattern. Only Ru-gel provides a slightly different decoration pattern. While the Ru-gel forms few aggregates, the gel exhibits a three dimensional atomic multilayer organisation at the nanoscale. The interatomic distance in the crystalline structure appears to be template by the spacing between the agarose strands and the configuration of the agarose double helix.

The third chapter describes a study of the electronic properties of the Au-gel. The evolution of these electronic properties has been investigated under the influence of two key factors: (i) the concentration of metals ions present in the gel which affect the number and average size of the nanoparticles obtained and (ii) the amount of water present in the hydrogel after dehydration, which should impinge on the average interparticle distance and therefore facilitate the charge transport through the composite. When the gel is "wet" an increase of gold nanoparticle loading results in a decrease of its conductivity and an increase of its capacitance. The small clusters decorating the gel structure act as insulators while large nanoparticles are conductors. The diminution of the conductivity can therefore be explained by the increase in the number of small clusters related to the increase of the concentration of metals ions in the gel (until saturation of the nanoscale gel structure). On the other hand, the evolution of the capacitance corresponds to the increase in the number and average size of the large nanoparticles and therefore to the decrease of the distance separating them. Here, the large NPs are analogous to the conducting regions of the capacitor while the small cluster regions represent the insulating layer.

The investigation of the composite under dehydration shows dramatic changes in the electronic properties of the system. While the evolution of the capacitance value follows the same pattern as in the wet gel, the conductance is also increasing significantly. The conductivity of the system is also influenced by the reduction of the interparticle distance and the coexistence of these two phenomena is explained by the heterogeneity in the surface decoration and consequently in the presence of percolating point. A second and deeper analysis of the electronic properties of the system upon chemical dehydration shows that the existence of these percolation points corresponds to a counterbalance between the Brownian motion of the nanoparticles and the dewetting of the gel. The total shrinkage of the gel leads to a spectacular decrease of the conductivity due to the formation of aggregates which are separated by greater distances than the original single NPs present in the "wet" gel. A partial recovery of the conductivity can be obtained with the rehydration of the gel. This recovery cannot be total as many of the aggregates formed during the dehydration process will remain.

If the concentration of Au(III) used is above this percolation point/area, conductivity is obtained without any dehydration.

Finally, the fourth and fifth chapters focus on the use of this new material as a recyclable substrate for SERS detection.

In the fourth chapter, the Ag-gel (using a 500mM feed solution) is used as a substrate for SERS of naphtalenethiol. In addition, a large enhancement of the SERS signal of the molecule can be obtained by the shrinkage of the substrate after the loading of the analyte. This enhancement is related to the formation of dynamic hotspots on the surface of the substrate upon dehydration. The trapping property of the substrate was then investigated. For the first time, DDT molecules, which cannot interact with the surface of the SNPs and therefore have never been studied by SERS, can be detected even at low concentration using this new substrate. The molecules are trapped in the pore of the Ag-gel. The reversibility of the system was finally demonstrated with three different molecules: (i) crystal violet (cationic), (ii) 2-naphtoic acid (anionic) and (iii) DDT. In the case of the ionic charged compounds the system was washed with a citrate solution and for DDT just with water. In each case, after the washing process, the SERS signal completely disappears. The experiments were repeated three times and perfect reproducibility of the SERS signal was obtained in each case.

In the fifth chapter, the same substrate and technique was used for the analysis of the molecule coating GNPs. The results show that the presence of SNPs enhances the detection of the molecules at higher laser energy (532nm) due the LSPR of the composite shrunk. On the other hand, at lower energy (633nm), the use of the Ag-gel as a substrate provides moderate results in comparison with the use of a pure piece of gel. If the concentration of GNPs is high enough, the SERS signal can be actually better in a pure piece of gel. The shrinkage of the gel involves a diminution of the interparticle distance and some of the LSPR of the GNPs system overlap the excitation wavelength of the laser used. Additionally, the molecules are chemisorbed onto the surface of the GNPs and therefore are located in the strongly enhanced electromagnetic fields emanating from the GNPs "aggregates" after excitation. In comparison, when the sandwich

method is used, the laser beam strikes the silver nanoparticles and therefore the enhancement of the electromagnetic field is located around the GNPs. Consequently, the quality of the molecule detection will be dependent of the distance between the molecule and the SNPs. In contrast, if the concentration of GNPs is low enough to not provide any LSPR which can overlap with the excitation wavelength of the laser, the Ag-gel provides a better detection of the molecule as the silver substrate presents some LSPR at 633nm.

All studies reported here exhibit the interesting physical and chemical properties of this new class of composites and their potential use for applications in different fields such as biosensing and SERS detection.

6.2 Improvements

The general interpretations given at the end of each chapter obviously rely on the results obtained but also on some assumptions. On one hand, these assumptions can provide a better understanding of the different system studied by deducing some of their behaviour and/or characteristics which have not been determined through the different methods of characterization On the other hand, these assumptions, true to the definition of the word, are very often suggestive and cannot be as reliable as experimental data. Additionally, investigations always have a scope for improvements. In this section of the chapter, we present the different characterization techniques required to provide a better understanding of the general study and propose general improvements of the different characterizations already used.

In Chapter 2, the nanoparticles could be characterized via UV-visible spectroscopy by using the reflectance instead of the transmission mode. The use of the UV-vis in transmission mode results in the presence of a very large background on the resulting spectra, this occurs because the spectra are based more on the presence of the agarose (which will transmit the light). The use of the same instrument in reflection mode should decrease the agarose effect on the spectra and plasmon bands corresponding to the existence of nanoparticles should be seen. The same optimization could be applied to the X-ray diffraction investigation of the gels. The concentration

of metal in the gel could also be optimized. For example, the Au-gel could be completely dissolved in a diluted solution of hydrochloric acid. The amount of gold in the solution could be then determined by elemental analysis. Additionally, MALDI measurements should be carried out in a pure piece of agarose. These measurements would allow a better understanding of the polymeric series detected with our samples and should provide some indications of the interaction between the metal particles and the matrix structure. Finally, the assumption of the degradation of the gels under the increase of Au(III) concentration in the gel could be analysed by FTIR. Indeed, the opening of the agarose chains should be identifiable by the appearance of characteristic peaks due to carboxylic acid, C=O and –OH (increase in intensity)[2].

For Chapter 3, just few improvements have been identified. If obtaining conductivity at a lower Au (III) concentration becomes the primary objective of the study, then the use of another reducing agent can be beneficial. Agarose, which can act as a stabilizing and reducing agent, is an attractive option. At low Au (III) concentration, larger nanoparticles and therefore lower interparticle distance can be obtained than with BH_4. This would also allow a better preservation of the network structure and therefore a better alignment of the particles. In addition, the irreversible aggregation of the nanoparticles upon dehydration of the hydrogel could be prevented by the addition of PEG-OH in the polymer prior to shrinkage. This should provide a better recovery of the electronic properties of the percolating gel after rehydration.

The improvements of the study presented in Chapter 4 should all be based on the acquisition of quantitative data. Indeed, it would be interesting to quantify enhancement of the signal intensity obtained due to the formation of hotpots. Additionally, a study of the possibility to quantify the different concentrations of molecules (presenting no interaction with the SNPs) trapped in the gel in relation to their SERS signal intensity would be really very interesting. A change in the shape of the nanoparticles[4-5], could also improve the detection of molecules through trapping by amplifying their SERS signal intensity.

Finally the improvements of the study presented in Chapter 5 should be focussed on decreasing the distance between the SNPs and the GNPs present in the system. This should permit the appearance of hotspots made of GNPs and SNPs and trap the molecule chemisorbed on the surface of the NPs in these hotspots. Therefore the molecule detection should be optimized. The addition of hexanedithiol in the system could facilitate the formation of these hotspots. Of course, some of the HDT molecules will bind SNPs to SNPs and GNPs to GNPs but some GNPs should still interact with the SNPs.

All these improvements could result in a better understanding of the system and an optimization of the applications presented in this thesis.

6.3 Future work

Future works should focus on the reduction of the nanoparticle size dispersion and the application of such type of new composite in catalysis and SERS detection of molecule.

The decrease of the size dispersion of the nanoparticles can be obtained by changing different conditions of the synthesis. Indeed, a decrease of the Au(III) concentration in addition to a shorter immersion time of the gel in the metal salt solution and a decrease of the experimental temperature dramatically affects the size of the nanoparticles obtained. Figure 6.1 shows the Au-gel obtained by a soaking in 0.2mM Au(III) feeding solution for 30min at 4C followed by a reduction in BH_4 (500mM) for 30min. The gel displays a yellow-light brown colour. This means that the particles synthesized in the gel are below 3nm.

Figure 6.1 Au-gel obtained with a low gold concentration of feeding solution and a short immersion time.

The sample should be investigated using different techniques such as electron microscopy, x-ray diffraction and UV-visible in order to confirm the the optical evaluation presented above.

This composite could also be a good substrate for catalysis. Mixing a solution of titanium oxide (TiO_2) (1%w) ,agarose powder (5,4%w) and 10ml water then heating for 30 min at 100°C followed by subsequent cooling down until complete gelation of the sample produces a composite (see figure 6.2). This composite is expected to present a nanocoating of the hydrogel network by TiO_2. The hybrid gel is then soaked in an Au (III) solution (0.2mM) for 30min followed by an immersion in a solution of $NaBH_4$ for 1hour. We expect that this step will allow the formation of GNPs on the TiO_2 nanoporous structure obtained with the previous step and therefore be catalytically active[1,3]. Figure 6.3 shows the material obtained.

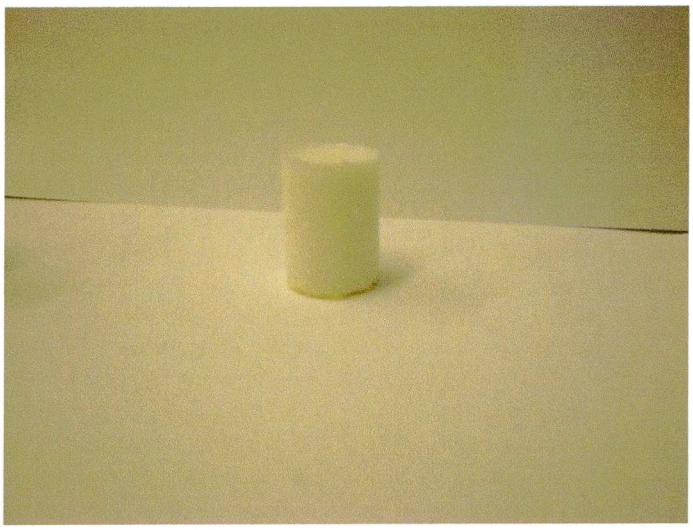

Figure 6.2 Composite of TiO_2/Agarose obtained by mixing the TiO_2 with agarose powder.

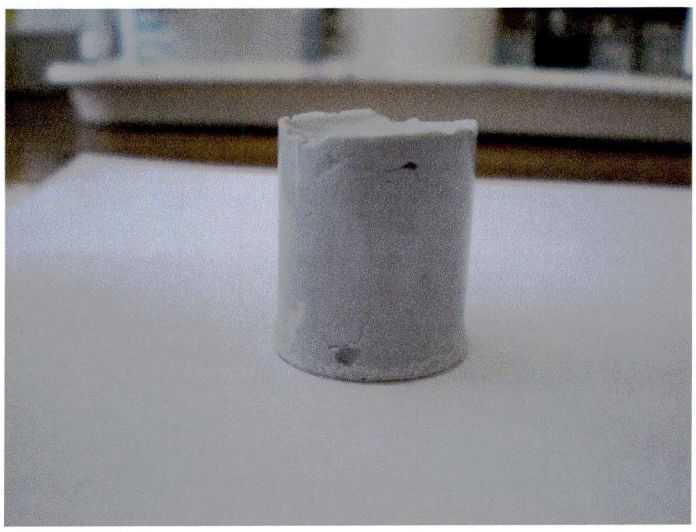

Figure 6.3 Composite of TiO_2-Au-gel obtained by soaking the TiO_2/agarose gel in a gold feeding solution reduced with aqueous NaBH4 solution.

References

1. D. G. Shchukin, J. H. Schattka, M. Antonietti, R. A. Caruso, *Journal of Physical Chemistry B* **2003**, *107*, 952.

2. C. M. Sun, R. J. Qu, H. Chen, C. N. Ji, C. H. Wang, Y. Z. Sun, B. H. Wang, *Carbohydrate Research* **2008**, *343*, 2595.

3. X. D. Wang, D. R. G. Mitchell, K. Prince, A. J. Atanacio, R. A. Caruso, *Chemistry of Materials* **2008**, *20*, 3917.

4. N. Pazos-Perez, S. Barbosa, L. Rodriguez-Lorenzo, P. Aldeanueva-Potel, J. Perez-Juste, I. Pastoriza-Santos, R. A. Alvarez-Puebla, L. M. Liz-Marzan, *Journal of Physical Chemistry Letters* **2010**, *1*, 24.

5. L. Rodriguez-Lorenzo, R. A. Alvarez-Puebla, F. J. G. de Abajo, L. M. Liz-Marzan, *Journal of Physical Chemistry C* **2010**, *114*, 7336.

Appendix

Appendix

Appendix chapter 2

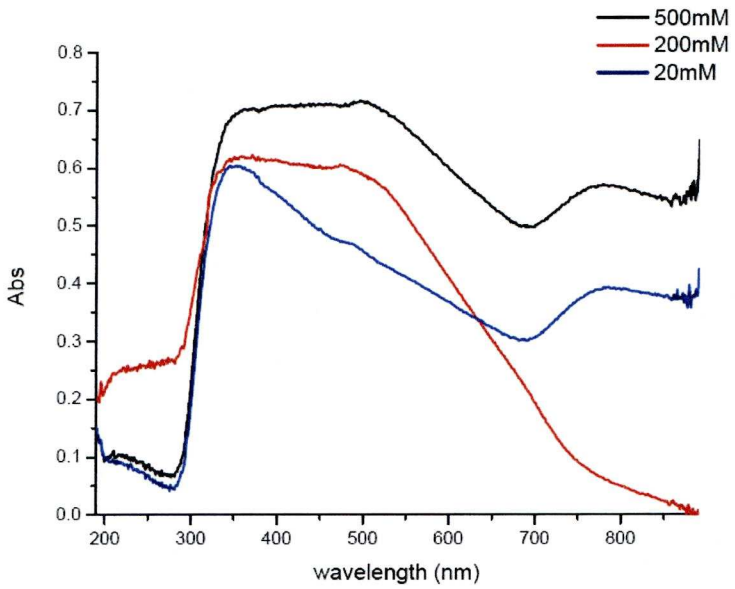

Appendix 2.1. UV-vis spectra of gels containing Au nanoparticles obtained with different concentration of feed solution. Note the appearance of a small plasmon band above 500 nm indicating the presence of particles larger than about 3 nm.

(A)

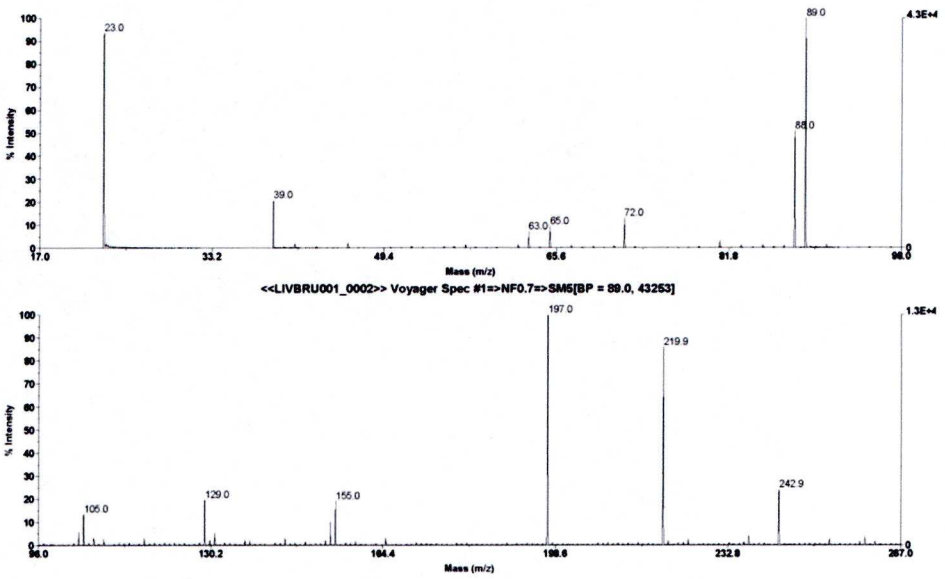

(B)

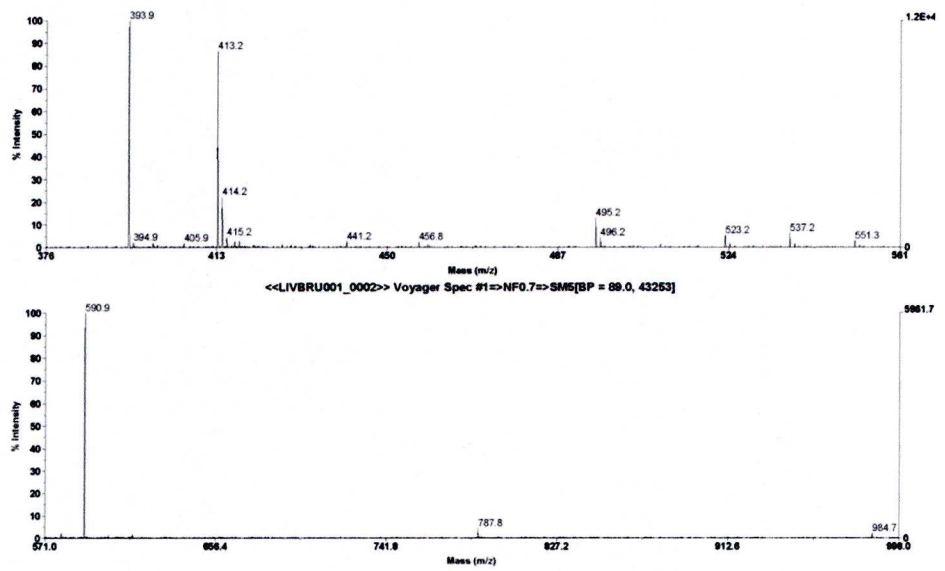

Appendix 2.2 (A) and (B): positive ion solvent-free MALDI-TOFMS spectra for Au-gel in LDI mode and showing the presence of Au_1, Au_2 and Au_3 inside the hydrogel matrix

(A)

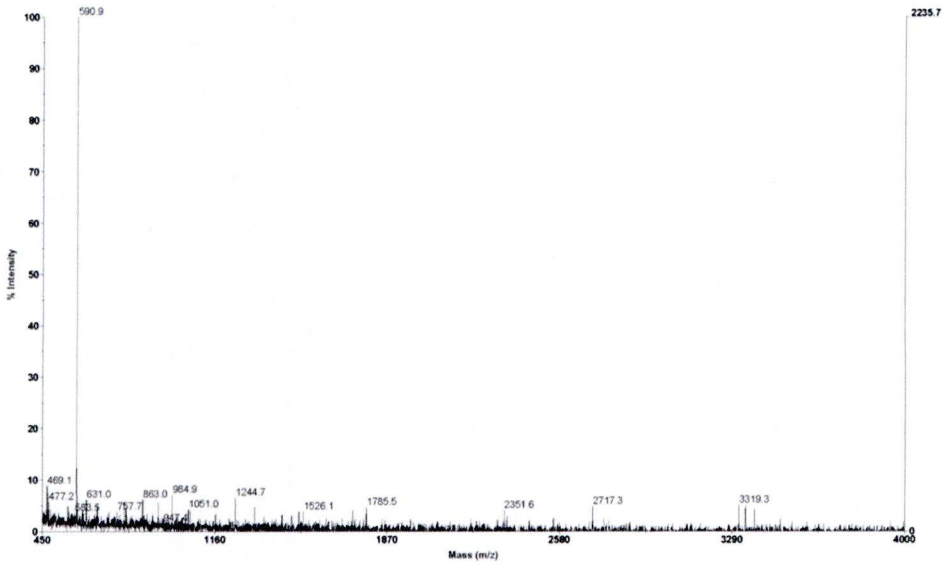

(B)

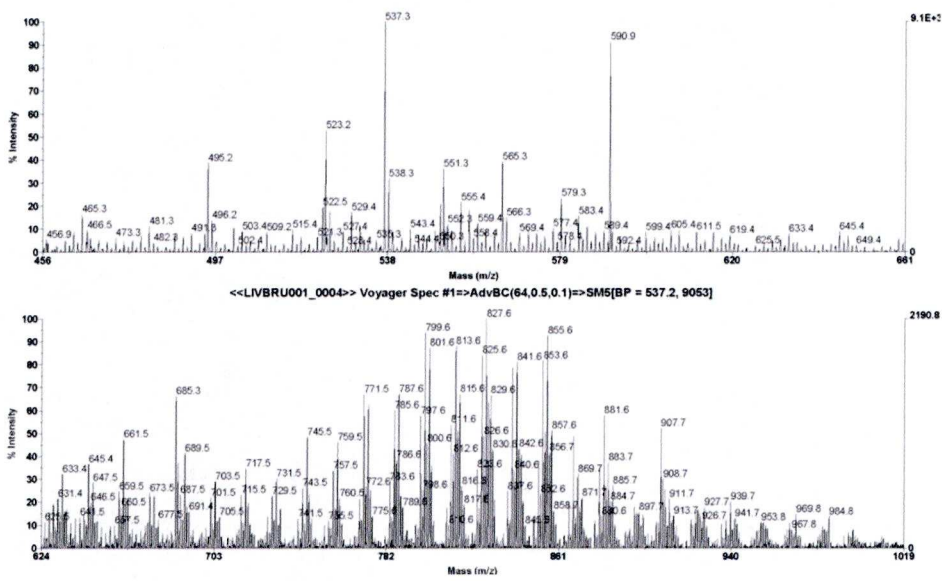

Appendix 2.3. (A) negative ion solvent-free MALDI-TOFMS for Au-gel with SA matrix and (B) positive ion solvent-free MALDI-TOFMS spectrum for Au-gel with DHB matrix both showing the presence of Au_3. DHB exhibits also higher range clusters and polymeric series.

(A)

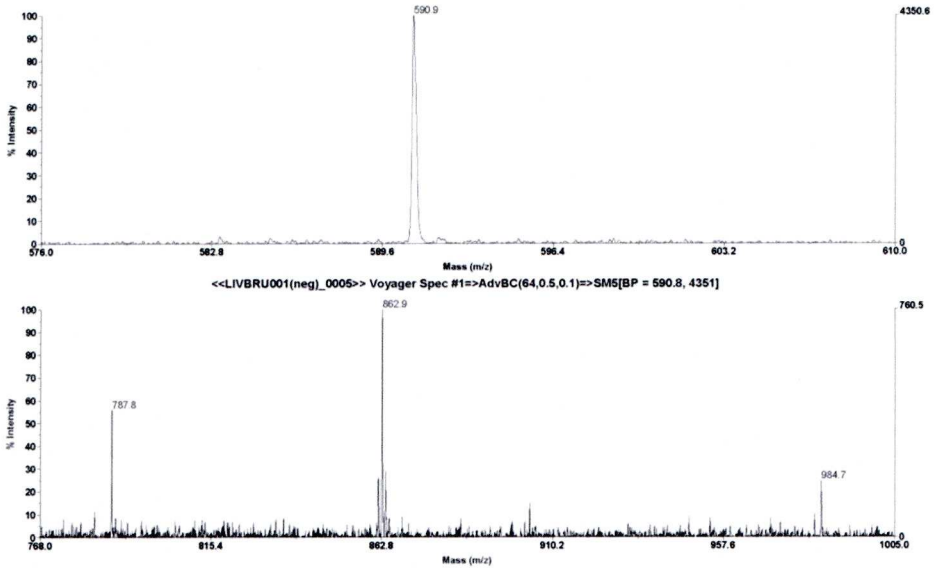

(B)

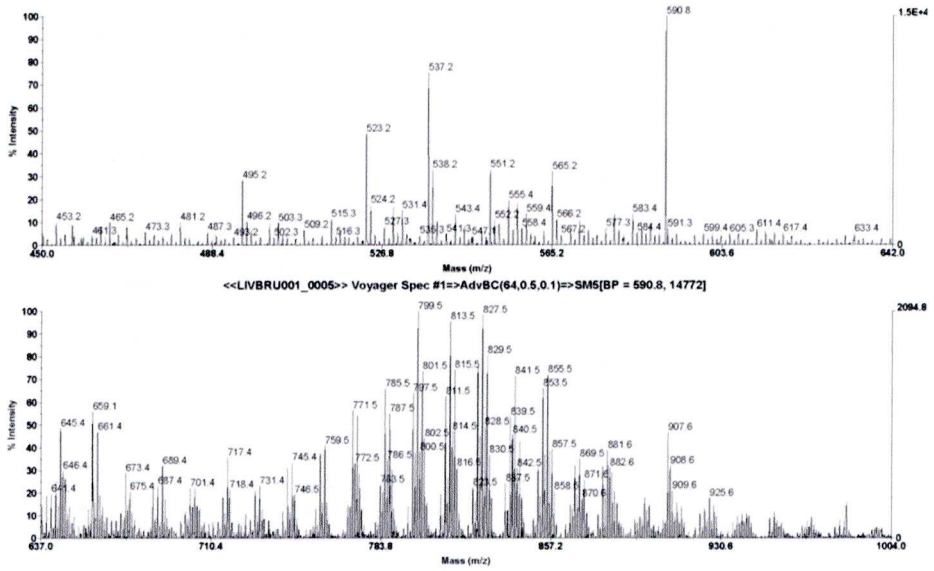

Appendix 2.4 (A) negative ion solvent-free MALDI-TOFMS spectrum for Au-gel with CHCA matrix and (B) positive ion solvent-free MALDI-TOFMS spectrum for Au-gel with CHCA matrix both showing the presence of Au_3 and higher range clusters as well as polymeric series.

(A)

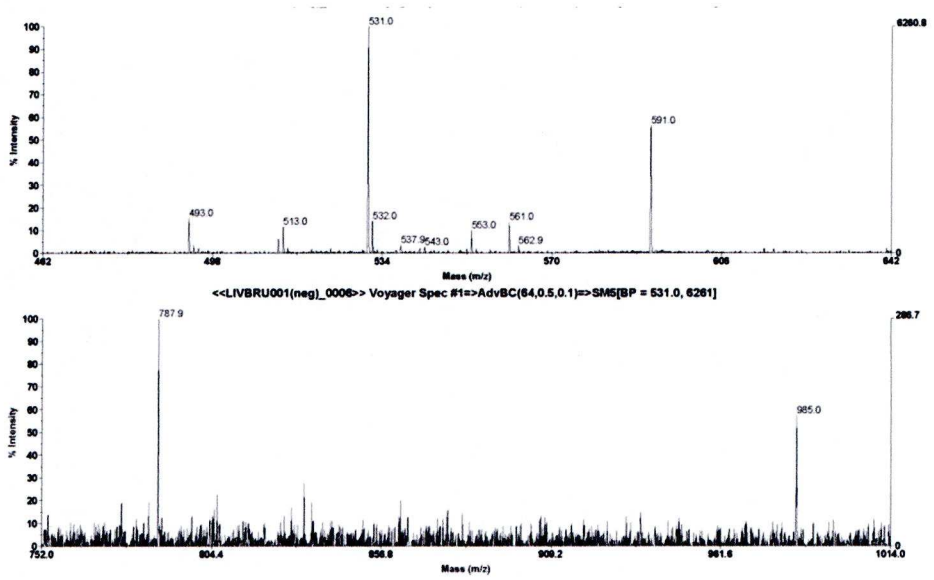
531.0
6280.9
591.0
493.0
513.0
532.0
537.9
543.0
553.0
561.0
562.9
% Intensity
Mass (m/z)
<<LIVBRU001(neg)_0006>> Voyager Spec #1=>AdvBC(64,0.5,0.1)=>SM5[BP = 531.0, 6281]
787.9
286.7
985.0
752.0
804.4
856.8
909.2
961.6
1014.0

(B)

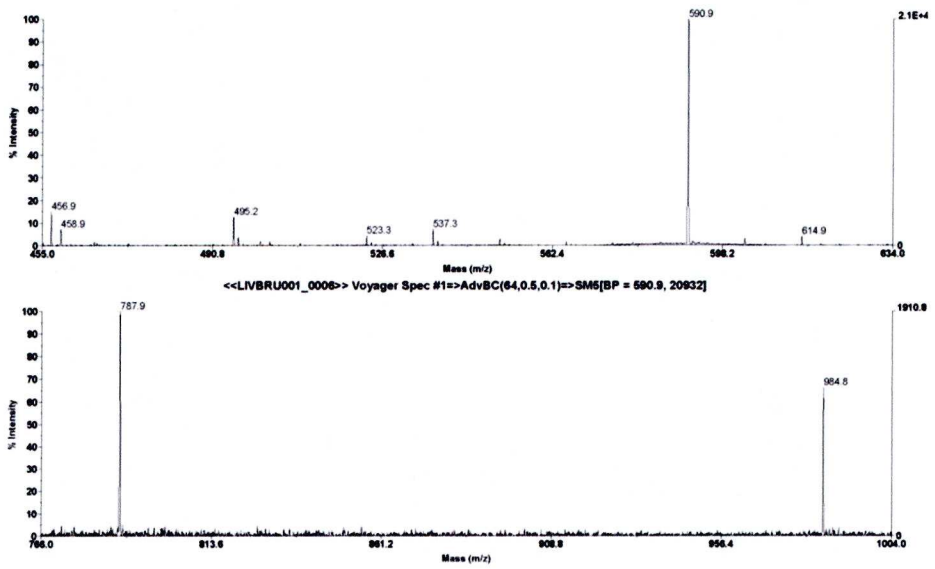
590.9
2.1E+4
456.9
458.9
495.2
523.3
537.3
614.9
% Intensity
Mass (m/z)
<<LIVBRU001_0006>> Voyager Spec #1=>AdvBC(64,0.5,0.1)=>SM5[BP = 590.9, 20932]
787.9
1910.9
984.8
766.0
813.6
861.2
908.8
956.4
1004.0

(C)

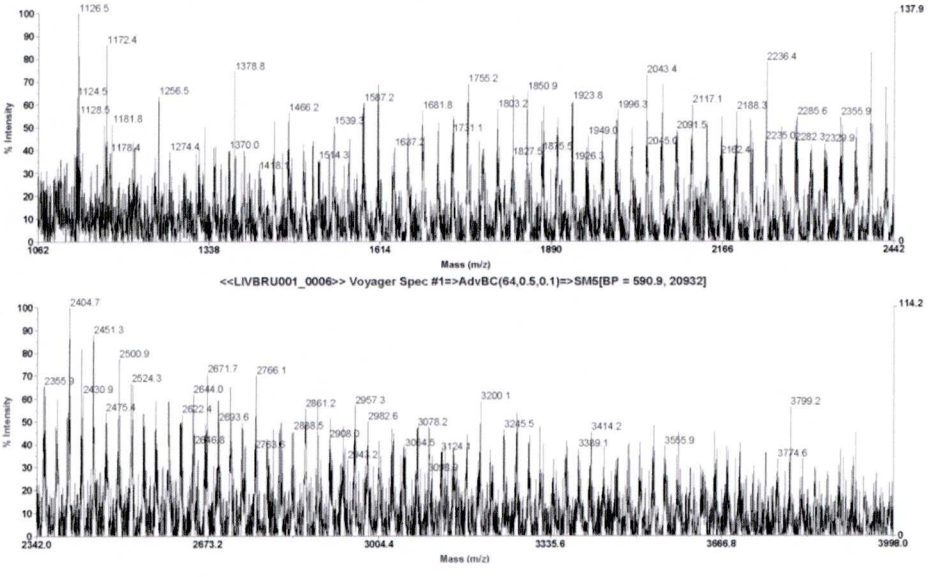

Appendix 2.5. (A) negative ion solvent-free MALDI-TOFMS spectrum for Au-gel with PFBA matrix, (B) positive ion solvent-free MALDI-TOFMS spectrum for Au-gel with PFBA both showing the presence of Au_3, Au_4 and Au_5 clusters. (C) is a positive ion solvent-free MALDI-TOFMS spectrum for Au-gel with PFBA matrix which exhibits polymeric series.

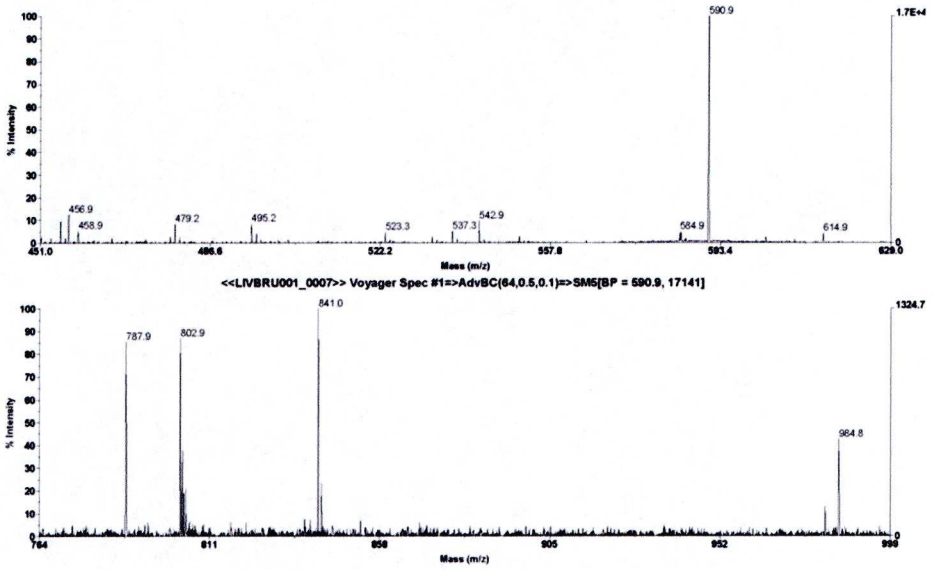

Appendix 2.6 positive ion solvent-free MALDI-TOFMS spectrum for Au-gel with PCFA matrix which exhibits Au_3, Au_4 and Au_5 clusters.

(A)

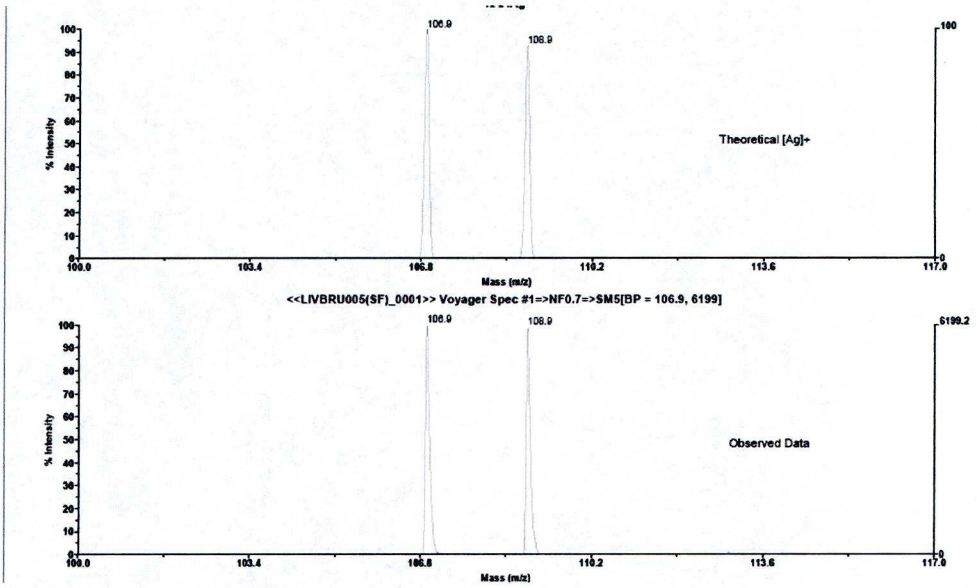
106.9
108.9
Theoretical [Ag]+
% Intensity
Mass (m/z)
<<LIVBRU005(SF)_0001>> Voyager Spec #1=>NF0.7=>SM5[BP = 106.9, 6199]
106.9
108.9
6199.2
Observed Data
% Intensity
Mass (m/z)

(B)

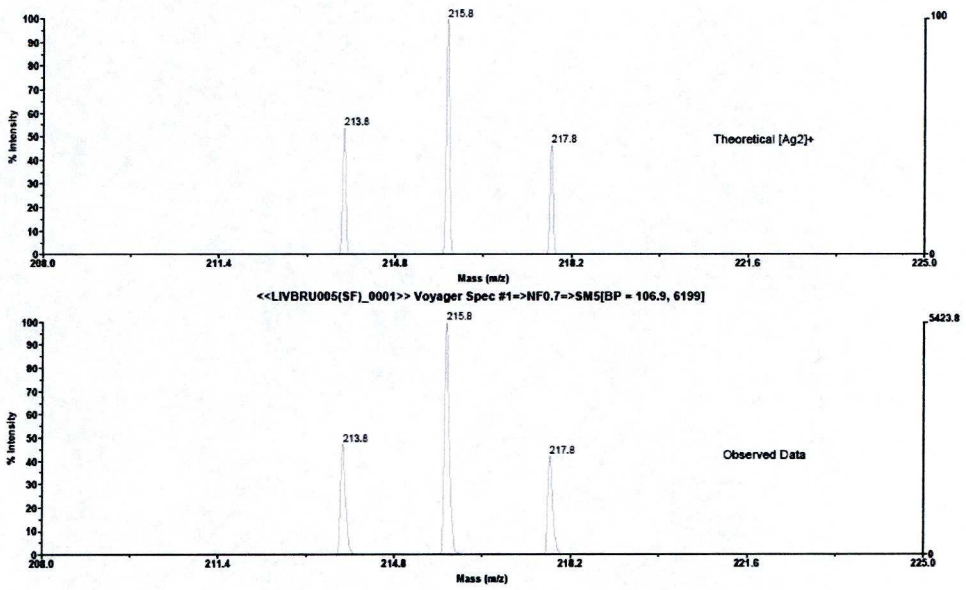
215.8
213.8
217.8
Theoretical [Ag2]+
% Intensity
Mass (m/z)
<<LIVBRU005(SF)_0001>> Voyager Spec #1=>NF0.7=>SM5[BP = 106.9, 6199]
215.8
5423.8
213.8
217.8
Observed Data
% Intensity
Mass (m/z)

(C)

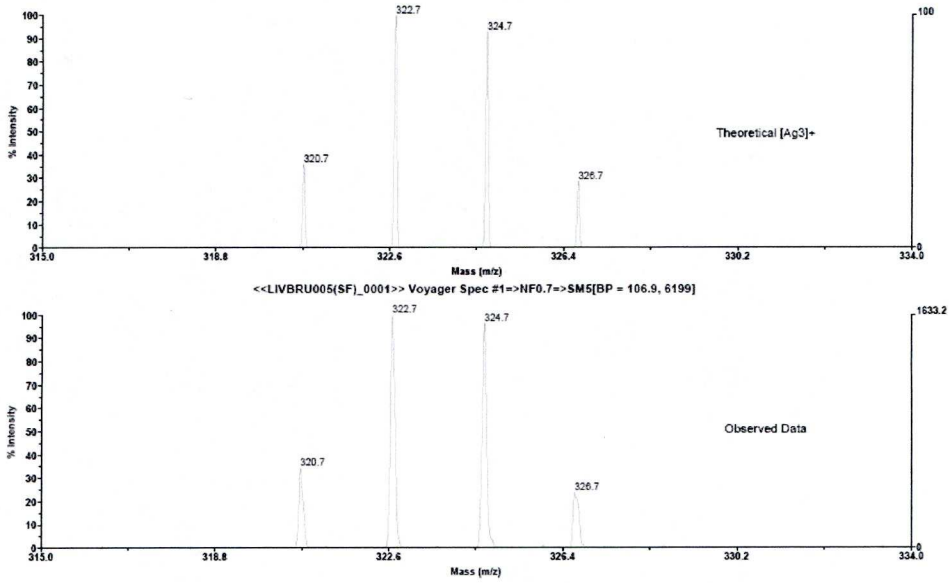

Appendix 2.7 Positive ion solvent-free MALDI-TOFMS spectra for Au-gel in LDI mode and showing the presence of Ag_1(figure A), Ag_2(figure B) and Ag_3 (figure C) inside the hydrogel matrix. Each of the figure shows a perfect match between the results obtained and the results expected from the theory.

Appendix 2.8 STEM picture of the monolayer of ruthenium atoms presented in the chapter 2 as figure 2.23D. Atoms present on the surface of the monolayer have been assigned a number and the number of atoms aligned along the Z-axis in each of these "spots" have been determined. The results are presented in appendix 2.9.

Appendix 2.9 Table summarizing the number of atoms along Z-axis

	label	Intensity Atoms	Intensity Bkground	Bkg Correct Int	1 atom	# atoms
1	a1	3.02E+08	1.26E+08	1.76E+08	3.01E+07	6
2	a2	3.24E+08	1.26E+08	1.98E+08	3.01E+07	7
3	a3	3.26E+08	1.26E+08	2.01E+08	3.01E+07	7
4	a4	3.01E+08	1.26E+08	1.76E+08	3.01E+07	6
5	a5	2.94E+08	1.26E+08	1.68E+08	3.01E+07	6
6	a6	2.92E+08	1.26E+08	1.66E+08	3.01E+07	6
7	a7	2.93E+08	1.26E+08	1.67E+08	3.01E+07	6
8	a8	3.28E+08	1.26E+08	2.02E+08	3.01E+07	7
9	a9	3.14E+08	1.26E+08	1.88E+08	3.01E+07	6
10	a10	3.26E+08	1.26E+08	2.00E+08	3.01E+07	7
11	a11	3.23E+08	1.26E+08	1.97E+08	3.01E+07	7
12	a12	3.11E+08	1.26E+08	1.85E+08	3.01E+07	6
13	a13	3.02E+08	1.26E+08	1.76E+08	3.01E+07	6
14	a14	2.98E+08	1.26E+08	1.73E+08	3.01E+07	6
15	a15	3.57E+08	1.26E+08	2.31E+08	3.01E+07	8
16	a16	3.44E+08	1.26E+08	2.19E+08	3.01E+07	7
17	a17	3.44E+08	1.26E+08	2.19E+08	3.01E+07	7
18	a18	3.23E+08	1.26E+08	1.97E+08	3.01E+07	7
19	a19	3.08E+08	1.26E+08	1.82E+08	3.01E+07	6
20	a20	3.26E+08	1.26E+08	2.01E+08	3.01E+07	7
21	a21	2.88E+08	1.26E+08	1.62E+08	3.01E+07	5
22	a22	2.58E+08	1.26E+08	1.33E+08	3.01E+07	4
23	a23	2.74E+08	1.26E+08	1.48E+08	3.01E+07	5
24	a24	3.00E+08	1.26E+08	1.74E+08	3.01E+07	6
25	a25	3.31E+08	1.26E+08	2.05E+08	3.01E+07	7
26	a26	3.48E+08	1.26E+08	2.23E+08	3.01E+07	7
27	a27	3.72E+08	1.26E+08	2.46E+08	3.01E+07	8
28	a28	3.98E+08	1.26E+08	2.73E+08	3.01E+07	9
29	a29	4.01E+08	1.26E+08	2.75E+08	3.01E+07	9
30	a30	3.67E+08	1.26E+08	2.41E+08	3.01E+07	8
31	a31	3.92E+08	1.26E+08	2.66E+08	3.01E+07	9
32	a32	4.18E+08	1.26E+08	2.92E+08	3.01E+07	10
33	a33	4.15E+08	1.26E+08	2.89E+08	3.01E+07	10
34	a34	4.23E+08	1.26E+08	2.97E+08	3.01E+07	10
35	a35	3.55E+08	1.26E+08	2.29E+08	3.01E+07	8
36	a36	3.41E+08	1.26E+08	2.15E+08	3.01E+07	7
37	a37	3.00E+08	1.26E+08	1.75E+08	3.01E+07	6
38	a38	2.38E+08	1.26E+08	1.12E+08	3.01E+07	4
39	a39	2.91E+08	1.26E+08	1.65E+08	3.01E+07	5
40	a40	3.56E+08	1.26E+08	2.30E+08	3.01E+07	8
41	a41	4.36E+08	1.26E+08	3.10E+08	3.01E+07	10
42	a42	3.96E+08	1.26E+08	2.70E+08	3.01E+07	9
43	a43	4.52E+08	1.26E+08	3.26E+08	3.01E+07	11
44	a44	4.51E+08	1.26E+08	3.25E+08	3.01E+07	11
45	a45	4.49E+08	1.26E+08	3.23E+08	3.01E+07	11

46	a46	4.44E+08	1.26E+08	3.18E+08	3.01E+07	11
47	a47	4.23E+08	1.26E+08	2.97E+08	3.01E+07	10
48	a48	4.25E+08	1.26E+08	2.99E+08	3.01E+07	10
49	a49	4.27E+08	1.26E+08	3.02E+08	3.01E+07	10
50	a50	4.61E+08	1.26E+08	3.35E+08	3.01E+07	11
51	a51	4.36E+08	1.26E+08	3.10E+08	3.01E+07	10
52	a52	4.51E+08	1.26E+08	3.25E+08	3.01E+07	11
53	a53	3.85E+08	1.26E+08	2.59E+08	3.01E+07	9
54	a54	3.36E+08	1.26E+08	2.11E+08	3.01E+07	7
55	a55	2.87E+08	1.26E+08	1.61E+08	3.01E+07	5
56	a56	2.51E+08	1.26E+08	1.26E+08	3.01E+07	4
57	a57	3.03E+08	1.26E+08	1.77E+08	3.01E+07	6
58	a58	4.37E+08	1.26E+08	3.11E+08	3.01E+07	10
59	a59	4.15E+08	1.26E+08	2.90E+08	3.01E+07	10
60	a60	4.80E+08	1.26E+08	3.54E+08	3.01E+07	12
61	a61	4.56E+08	1.26E+08	3.30E+08	3.01E+07	11
62	a62	4.38E+08	1.26E+08	3.13E+08	3.01E+07	10
63	a63	4.20E+08	1.26E+08	2.94E+08	3.01E+07	10
64	a64	4.22E+08	1.26E+08	2.96E+08	3.01E+07	10
65	a65	3.86E+08	1.26E+08	2.60E+08	3.01E+07	9
66	a66	4.23E+08	1.26E+08	2.97E+08	3.01E+07	10
67	a67	4.36E+08	1.26E+08	3.10E+08	3.01E+07	10
68	a68	4.70E+08	1.26E+08	3.44E+08	3.01E+07	11
69	a69	5.17E+08	1.26E+08	3.91E+08	3.01E+07	13
70	a70	5.12E+08	1.26E+08	3.86E+08	3.01E+07	13
71	a71	5.43E+08	1.26E+08	4.18E+08	3.01E+07	14
72	a72	4.77E+08	1.26E+08	3.51E+08	3.01E+07	12
73	a73	5.14E+08	1.26E+08	3.88E+08	3.01E+07	13
74	a74	3.79E+08	1.26E+08	2.53E+08	3.01E+07	8
75	a75	2.49E+08	1.26E+08	1.23E+08	3.01E+07	4
76	a76	3.25E+08	1.26E+08	1.99E+08	3.01E+07	7
77	a77	4.24E+08	1.26E+08	2.99E+08	3.01E+07	10
78	a78	4.80E+08	1.26E+08	3.54E+08	3.01E+07	12
79	a79	4.73E+08	1.26E+08	3.48E+08	3.01E+07	12
80	a80	5.20E+08	1.26E+08	3.95E+08	3.01E+07	13
81	a81	5.02E+08	1.26E+08	3.76E+08	3.01E+07	13
82	a82	4.65E+08	1.26E+08	3.39E+08	3.01E+07	11
83	a83	4.36E+08	1.26E+08	3.10E+08	3.01E+07	10
84	a84	4.26E+08	1.26E+08	3.00E+08	3.01E+07	10
85	a85	4.37E+08	1.26E+08	3.11E+08	3.01E+07	10
86	a86	3.42E+08	1.26E+08	2.16E+08	3.01E+07	7
87	a87	3.13E+08	1.26E+08	1.87E+08	3.01E+07	6
88	a88	3.61E+08	1.26E+08	2.35E+08	3.01E+07	8
89	a89	3.95E+08	1.26E+08	2.69E+08	3.01E+07	9
90	a90	4.54E+08	1.26E+08	3.28E+08	3.01E+07	11
91	a91	4.50E+08	1.26E+08	3.24E+08	3.01E+07	11
92	a92	4.57E+08	1.26E+08	3.32E+08	3.01E+07	11
93	a93	4.54E+08	1.26E+08	3.29E+08	3.01E+07	11
94	a94	4.73E+08	1.26E+08	3.47E+08	3.01E+07	12
95	a95	4.91E+08	1.26E+08	3.65E+08	3.01E+07	12

96	a96	4.72E+08	1.26E+08	3.46E+08	3.01E+07	11
97	a97	3.98E+08	1.26E+08	2.72E+08	3.01E+07	9
98	a98	3.38E+08	1.26E+08	2.12E+08	3.01E+07	7
99	a99	3.43E+08	1.26E+08	2.17E+08	3.01E+07	7
100	b1	4.40E+08	1.26E+08	3.14E+08	3.01E+07	10
101	b2	4.96E+08	1.26E+08	3.70E+08	3.01E+07	12
102	b3	4.87E+08	1.26E+08	3.61E+08	3.01E+07	12
103	b4	4.70E+08	1.26E+08	3.44E+08	3.01E+07	11
104	b5	4.70E+08	1.26E+08	3.44E+08	3.01E+07	11
105	b6	4.71E+08	1.26E+08	3.46E+08	3.01E+07	11
106	b7	4.70E+08	1.26E+08	3.44E+08	3.01E+07	11
107	b8	3.90E+08	1.26E+08	2.64E+08	3.01E+07	9
108	b9	3.30E+08	1.26E+08	2.04E+08	3.01E+07	7
109	b10	3.71E+08	1.26E+08	2.45E+08	3.01E+07	8
110	b11	4.32E+08	1.26E+08	3.06E+08	3.01E+07	10
111	b12	4.24E+08	1.26E+08	2.98E+08	3.01E+07	10
112	b13	4.38E+08	1.26E+08	3.12E+08	3.01E+07	10
113	b14	4.46E+08	1.26E+08	3.20E+08	3.01E+07	11
114	b15	4.49E+08	1.26E+08	3.23E+08	3.01E+07	11
115	b16	4.77E+08	1.26E+08	3.52E+08	3.01E+07	12
116	b17	4.81E+08	1.26E+08	3.55E+08	3.01E+07	12
117	b18	5.01E+08	1.26E+08	3.75E+08	3.01E+07	12
118	b19	4.17E+08	1.26E+08	2.92E+08	3.01E+07	10
119	b20	3.15E+08	1.26E+08	1.89E+08	3.01E+07	6
120	b21	3.32E+08	1.26E+08	2.06E+08	3.01E+07	7
121	b22	4.51E+08	1.26E+08	3.25E+08	3.01E+07	11
122	b23	4.12E+08	1.26E+08	2.86E+08	3.01E+07	10
123	b24	4.15E+08	1.26E+08	2.89E+08	3.01E+07	10
124	b25	4.22E+08	1.26E+08	2.97E+08	3.01E+07	10
125	b26	4.44E+08	1.26E+08	3.18E+08	3.01E+07	11
126	b27	4.02E+08	1.26E+08	2.76E+08	3.01E+07	9
127	b28	4.11E+08	1.26E+08	2.85E+08	3.01E+07	9
128	b29	3.56E+08	1.26E+08	2.30E+08	3.01E+07	8
129	b30	3.21E+08	1.26E+08	1.96E+08	3.01E+07	6
130	b31	3.23E+08	1.26E+08	1.97E+08	3.01E+07	7
131	b32	3.30E+08	1.26E+08	2.05E+08	3.01E+07	7
132	b33	3.98E+08	1.26E+08	2.73E+08	3.01E+07	9
133	b34	3.80E+08	1.26E+08	2.54E+08	3.01E+07	8
134	b35	4.08E+08	1.26E+08	2.82E+08	3.01E+07	9
135	b36	3.80E+08	1.26E+08	2.54E+08	3.01E+07	8
136	b37	3.44E+08	1.26E+08	2.19E+08	3.01E+07	7
137	b38	2.71E+08	1.26E+08	1.45E+08	3.01E+07	5
138	b39	2.12E+08	1.26E+08	8.65E+07	3.01E+07	3
139	b40	3.01E+08	1.26E+08	1.75E+08	3.01E+07	6
140	b41	3.62E+08	1.26E+08	2.36E+08	3.01E+07	8
141	b42	4.14E+08	1.26E+08	2.88E+08	3.01E+07	10
142	b43	3.80E+08	1.26E+08	2.55E+08	3.01E+07	8
143	b44	3.74E+08	1.26E+08	2.48E+08	3.01E+07	8
144	b45	3.49E+08	1.26E+08	2.24E+08	3.01E+07	7
145	b46	3.26E+08	1.26E+08	2.01E+08	3.01E+07	7

146	b47	3.13E+08	1.26E+08	1.88E+08	3.01E+07	6
147	b48	3.01E+08	1.26E+08	1.75E+08	3.01E+07	6
148	b49	2.84E+08	1.26E+08	1.58E+08	3.01E+07	5
149	b50	3.24E+08	1.26E+08	1.98E+08	3.01E+07	7
150	b51	3.03E+08	1.26E+08	1.77E+08	3.01E+07	6
151	b52	2.91E+08	1.26E+08	1.66E+08	3.01E+07	5
152	b53	3.46E+08	1.26E+08	2.20E+08	3.01E+07	7
153	b54	3.13E+08	1.26E+08	1.87E+08	3.01E+07	6
154	b55	2.64E+08	1.26E+08	1.39E+08	3.01E+07	5
155	b56	2.53E+08	1.26E+08	1.27E+08	3.01E+07	4
156	b57	2.59E+08	1.26E+08	1.33E+08	3.01E+07	4
157	b58	2.41E+08	1.26E+08	1.15E+08	3.01E+07	4
158	b59	2.71E+08	1.26E+08	1.45E+08	3.01E+07	5
159	b60	2.71E+08	1.26E+08	1.45E+08	3.01E+07	5
160	b61	2.81E+08	1.26E+08	1.55E+08	3.01E+07	5
161	b62	2.94E+08	1.26E+08	1.68E+08	3.01E+07	6
162	b63	2.80E+08	1.26E+08	1.55E+08	3.01E+07	5
163	b64	2.57E+08	1.26E+08	1.32E+08	3.01E+07	4
164	b65	2.31E+08	1.26E+08	1.05E+08	3.01E+07	4
165	b66	2.48E+08	1.26E+08	1.22E+08	3.01E+07	4
166	b67	1.76E+08	1.26E+08	5.02E+07	3.01E+07	2
167	b68	1.65E+08	1.26E+08	3.96E+07	3.01E+07	1
168	b69	1.62E+08	1.26E+08	3.59E+07	3.01E+07	1
169	b70	1.91E+08	1.26E+08	6.51E+07	3.01E+07	2
170	b71	1.79E+08	1.26E+08	5.29E+07	3.01E+07	2
171	b72	1.79E+08	1.26E+08	5.27E+07	3.01E+07	2
172	b73	1.73E+08	1.26E+08	4.67E+07	3.01E+07	2
173	b74	1.59E+08	1.26E+08	3.33E+07	3.01E+07	1
174	b75	1.84E+08	1.26E+08	5.85E+07	3.01E+07	2
175	b76	1.66E+08	1.26E+08	4.02E+07	3.01E+07	1
176	b77	1.82E+08	1.26E+08	5.60E+07	3.01E+07	2
177	b78	1.63E+08	1.26E+08	3.72E+07	3.01E+07	1
178	b79	1.75E+08	1.26E+08	4.88E+07	3.01E+07	2
179	b80	1.68E+08	1.26E+08	4.24E+07	3.01E+07	1
180	b81	1.57E+08	1.26E+08	3.16E+07	3.01E+07	1
181	b82	1.82E+08	1.26E+08	5.63E+07	3.01E+07	2
182	b83	1.74E+08	1.26E+08	4.84E+07	3.01E+07	2
183	b84	1.56E+08	1.26E+08	3.01E+07	3.01E+07	1
184	b85	1.70E+08	1.26E+08	4.46E+07	3.01E+07	1
185	b86	1.67E+08	1.26E+08	4.16E+07	3.01E+07	1
186	b87	1.79E+08	1.26E+08	5.29E+07	3.01E+07	2
187	b88	1.71E+08	1.26E+08	4.49E+07	3.01E+07	1
188	b89	1.63E+08	1.26E+08	3.72E+07	3.01E+07	1
189	b90	1.63E+08	1.26E+08	3.75E+07	3.01E+07	1
190	b91	1.56E+08	1.26E+08	3.05E+07	3.01E+07	1
191	b92	2.00E+08	1.26E+08	7.40E+07	3.01E+07	2
192	b93	1.97E+08	1.26E+08	7.11E+07	3.01E+07	2
193	b94	1.89E+08	1.26E+08	6.34E+07	3.01E+07	2
194	b95	1.81E+08	1.26E+08	5.56E+07	3.01E+07	2
195	b96	1.81E+08	1.26E+08	5.56E+07	3.01E+07	2

196	b97	1.77E+08	1.26E+08	5.11E+07	3.01E+07	2
197	b98	1.78E+08	1.26E+08	5.17E+07	3.01E+07	2
198	c1	1.77E+08	1.26E+08	5.13E+07	3.01E+07	2
199	c2	1.83E+08	1.26E+08	5.69E+07	3.01E+07	2
200	c3	1.72E+08	1.26E+08	4.62E+07	3.01E+07	2
201	c4	1.83E+08	1.26E+08	5.70E+07	3.01E+07	2
202	c5	1.77E+08	1.26E+08	5.10E+07	3.01E+07	2
203	c6	1.73E+08	1.26E+08	4.67E+07	3.01E+07	2
204	c7	1.89E+08	1.26E+08	6.37E+07	3.01E+07	2
205	c8	2.76E+08	1.26E+08	1.50E+08	3.01E+07	5
206	c9	2.91E+08	1.26E+08	1.65E+08	3.01E+07	5
207	c10	3.05E+08	1.26E+08	1.79E+08	3.01E+07	6
208	c11	2.80E+08	1.26E+08	1.54E+08	3.01E+07	5
209	c12	3.19E+08	1.26E+08	1.93E+08	3.01E+07	6
210	c13	3.12E+08	1.26E+08	1.86E+08	3.01E+07	6
211	c14	2.75E+08	1.26E+08	1.49E+08	3.01E+07	5
212	c15	2.73E+08	1.26E+08	1.47E+08	3.01E+07	5
213	c16	2.89E+08	1.26E+08	1.63E+08	3.01E+07	5
214	c17	2.79E+08	1.26E+08	1.53E+08	3.01E+07	5
215	c18	2.80E+08	1.26E+08	1.54E+08	3.01E+07	5
216	c19	2.78E+08	1.26E+08	1.52E+08	3.01E+07	5
217	c20	2.51E+08	1.26E+08	1.25E+08	3.01E+07	4
218	c21	2.47E+08	1.26E+08	1.21E+08	3.01E+07	4
219	c22	2.37E+08	1.26E+08	1.11E+08	3.01E+07	4
220	c23	2.44E+08	1.26E+08	1.18E+08	3.01E+07	4
221	c24	2.57E+08	1.26E+08	1.31E+08	3.01E+07	4
222	c25	2.71E+08	1.26E+08	1.45E+08	3.01E+07	5
223	c26	2.79E+08	1.26E+08	1.53E+08	3.01E+07	5
224	c27	2.99E+08	1.26E+08	1.73E+08	3.01E+07	6
225	c28	2.74E+08	1.26E+08	1.49E+08	3.01E+07	5
226	c29	2.77E+08	1.26E+08	1.51E+08	3.01E+07	5
227	c30	2.54E+08	1.26E+08	1.28E+08	3.01E+07	4
228	c31	2.42E+08	1.26E+08	1.16E+08	3.01E+07	4
229	c32	2.36E+08	1.26E+08	1.10E+08	3.01E+07	4
230	c33	2.29E+08	1.26E+08	1.04E+08	3.01E+07	3
231	c34	2.09E+08	1.26E+08	8.31E+07	3.01E+07	3
232	c35	2.00E+08	1.26E+08	7.37E+07	3.01E+07	2

Appendix chapter 3

3.1. Current-voltage response and Fitting of the transient current part of the signal obtained with "wet" Au nanoparticle-loaded gels. Red curves are fits and black curves are measurements. Note that the fitting was obtained by the determination of τ from the graphs. An exponential fitting has been used by setting the y_0 as 0 and including τ in the exponential coefficient in the following equation: $y=y_0+Ae^{(-t/\tau)}$

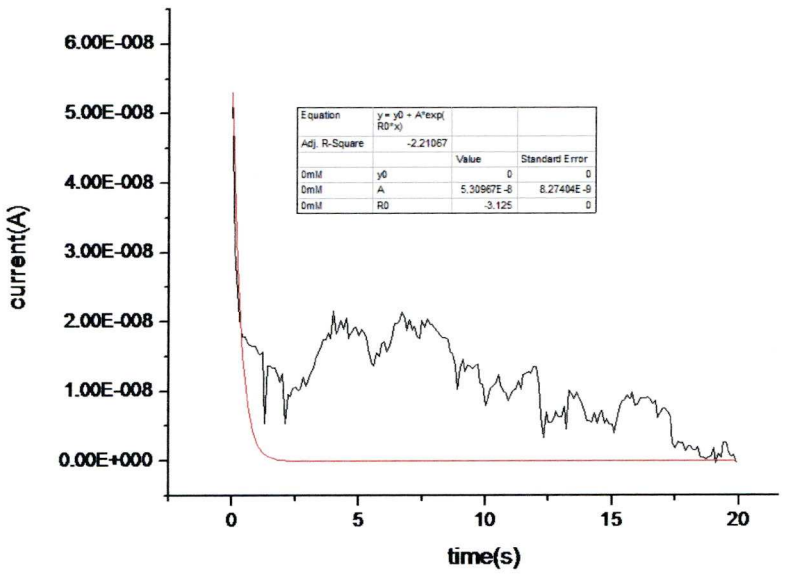

Appendix 3.1.1. Current-voltage response and Fitting of the transient current part of the signal on the pure"wet" gel (absence of nanoparticles).

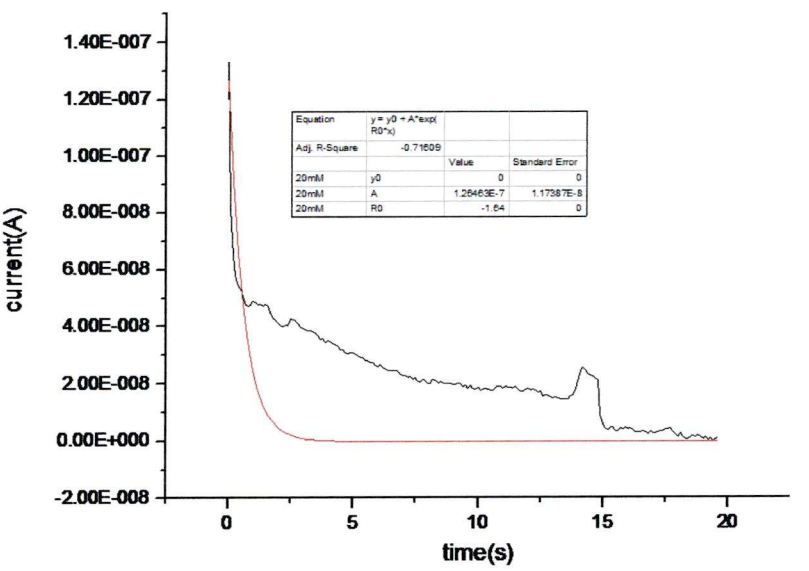

Appendix 3.1.2. Current-voltage response and Fitting of the transient current part of the signal on the "wet" gel (20mM $HAuCl_4$ feed solution).

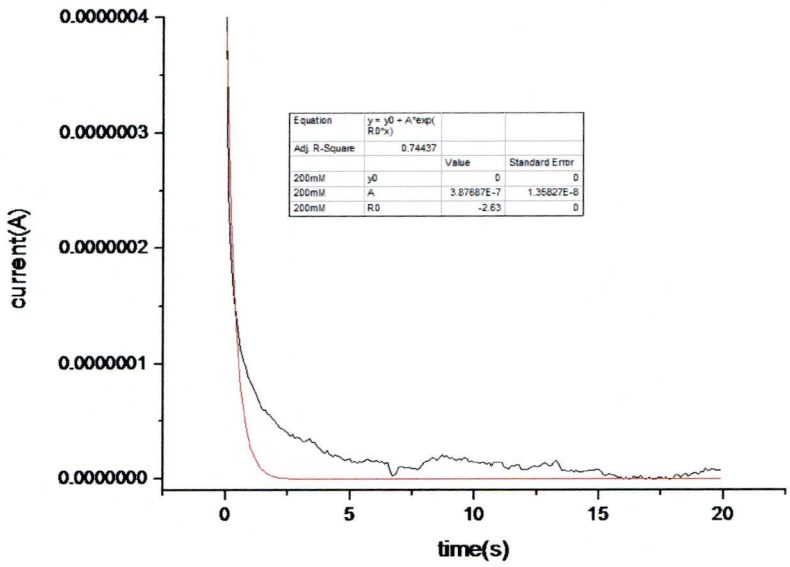

Appendix 3.1.3. Current-voltage response and Fitting of the transient current part of the signal on the "wet" gel (200mM $HAuCl_4$ feed solution).

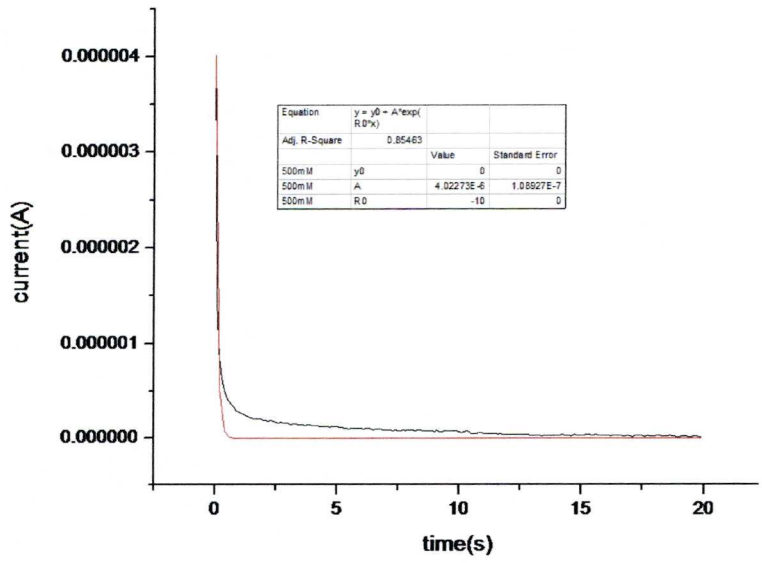

Appendix 3.1.4. Current-voltage response and Fitting of the transient current part of the signal on the "wet" gel (500mM $HAuCl_4$ feed solution).

3.2. Current-voltage response and Fitting of the transient current part of the signal on "dry" gels immersed in feed solutions of $HAuCl_4$. Note that the fitting of the "dry" gels is better than that of the "wet" ones,

except for higher metal loadings. We attribute this to the Ohmic behaviour that is only fully justified in "dry" gels and highly loaded wet ones. The simplified model of a leaking capacitor is not adequate to describe the behaviour of the wet gels with low metal loading, where conduction occurs only by ionic migration. While the transient part can still be described well, the fits fail to describe the non-Ohmic currents.

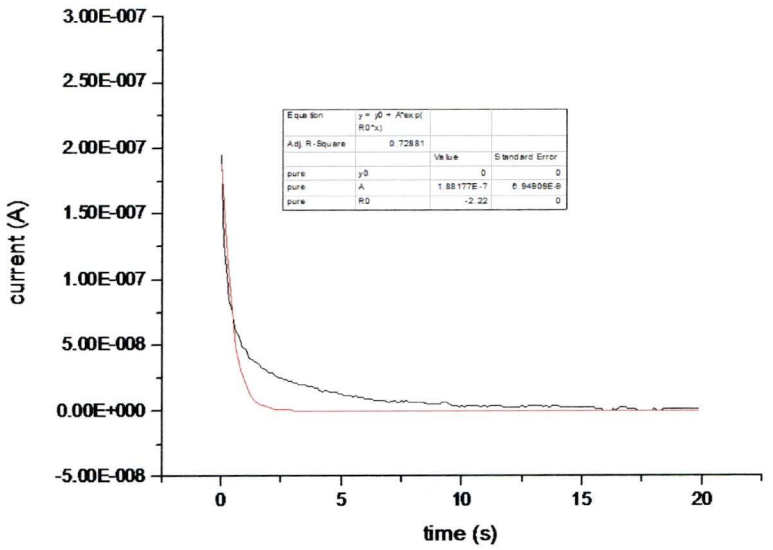

Appendix 3.2.1. Current-voltage response and Fitting of the transient current part of the signal on the pure"dry" gel (absence of nanoparticles).

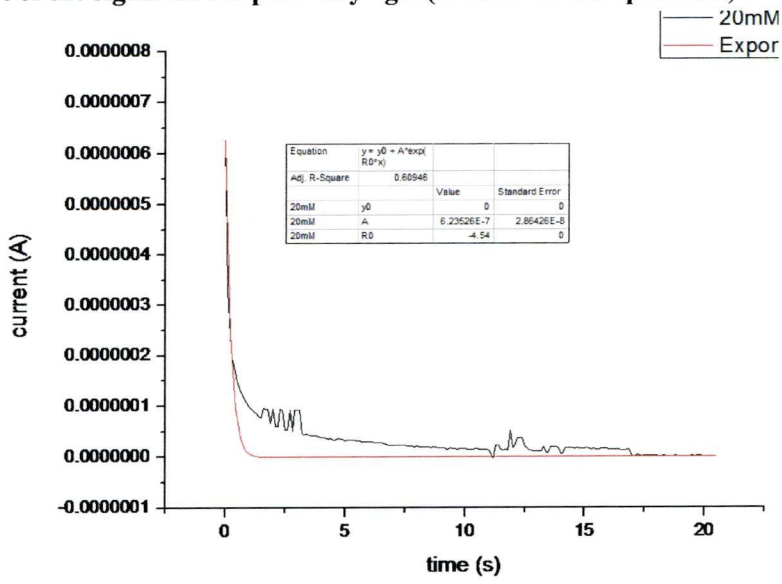

Appendix 3.2.2. Current-voltage response and Fitting of the transient current part of the signal on the "dry" gel (20mM $HAuCl_4$ feed solution).

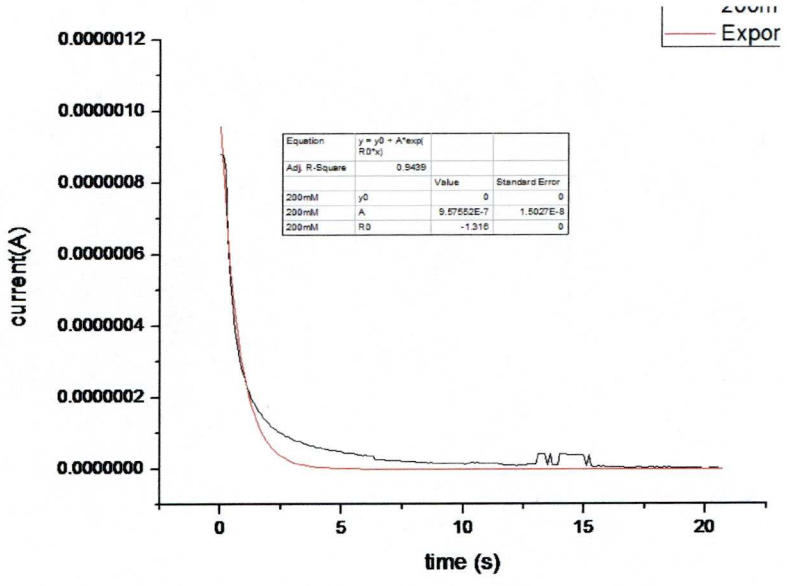

Appendix 3.2.3. Current-voltage response and Fitting of the transient current part of the signal on the "dry" gel (200mM $HAuCl_4$ feed solution).

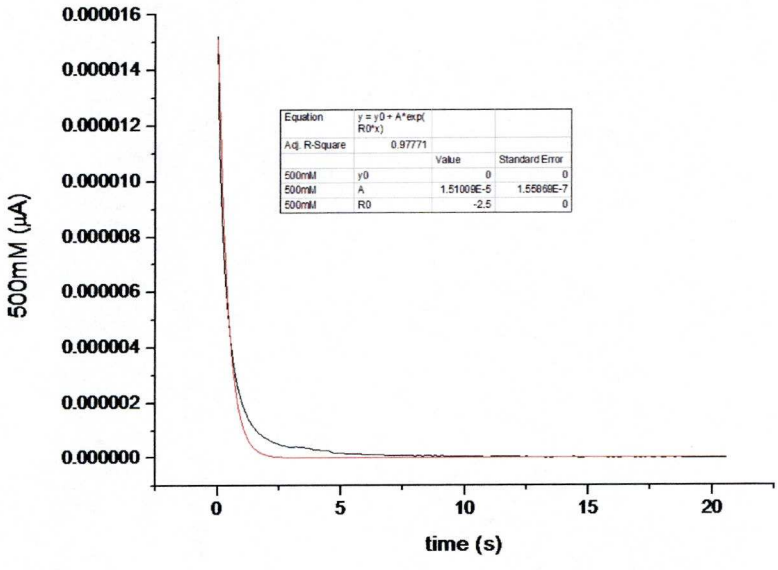

Appendix 3.2.4. Current-voltage response and Fitting of the transient current part of the signal on the "dry" gel (500mM $HAuCl_4$ feed solution).

Appendix 3.3 Summary of the R2 and therefore the conductance value obtained for each Au-gel upon dehydration

	R2 value												
Dehydration time (hours)	1mM	5mM	10mM	20mM	100mM	200mM	300mM	400mM	420mM	440mM	460mM	500mM
0	3.24E-08	3.65E-08	2.71E-08	3.30E-08	2.73E-08	2.03E-08	4.59E-08	9.90E-08	4.58E-08	2.60E-08	7.51E-08	1.79E-06
1	2.20E-08	1.09E-08	4.57E-09	1.42E-08	2.67E-08	1.75E-08	1.46E-08	2.92E-08	1.26E-08	1.13E-08	1.12E-07	6.22E-08
2	2.43E-08	1.47E-08	7.87E-09	1.05E-08	1.27E-08	1.30E-08	2.61E-08	8.32E-08	1.10E-07	8.07E-08	5.31E-08	1.14E-07
3	1.47E-08	1.81E-08	7.66E-09	9.33E-09	1.71E-08	9.92E-09	1.45E-08	4.88E-08	1.82E-08	8.74E-09	1.16E-08	1.49E-08
4	1.14E-08	1.28E-08	1.01E-08	6.70E-09	8.85E-09	6.43E-09	2.15E-08	4.02E-08	2.76E-08	1.40E-08	2.00E-08	1.81E-08
5	1.34E-08	1.37E-08	1.09E-08	8.65E-09	2.05E-08	8.54E-09	1.68E-08	5.28E-08	2.38E-08	1.08E-08	2.40E-08	3.47E-08
6	4.22E-09	1.80E-08	1.06E-08	1.19E-08	2.13E-08	1.14E-08	2.97E-08	3.74E-08	2.10E-08	1.44E-08	1.75E-08	1.90E-08
8	1.13E-08	1.67E-08	1.02E-08	8.66E-08	9.63E-09	1.01E-08	1.97E-08	3.43E-08	2.90E-08	1.19E-08	6.44E-09	3.28E-08
10	1.28E-08	9.85E-09	1.08E-08	1.08E-08	8.55E-09	7.43E-09	8.24E-09	3.67E-08	4.69E-08	2.95E-08	8.62E-09	1.19E-07
12	1.50E-08	1.22E-08	1.88E-08	1.39E-08	2.73E-08	1.04E-08	9.00E-09	7.35E-09	8.91E-09	1.07E-08	4.57E-09	5.63E-08
14	2.34E-08	3.15E-08	1.37E-08	1.26E-08	1.63E-08	6.44E-09	8.65E-09	4.73E-09	7.99E-09	5.69E-09	5.87E-09	2.30E-08
16	1.10E-08	1.10E-08	9.87E-09	1.78E-08	1.03E-08	8.22E-09	9.76E-09	7.56E-09	2.05E-08	9.76E-09	5.45E-09	4.91E-08
17	8.30E-09	1.78E-08	1.99E-08	1.06E-08	8.87E-09	1.18E-08	1.80E-08	2.67E-09	2.96E-08	8.16E-09	7.67E-09	2.68E-08
18	1.24E-08	1.72E-08	2.14E-08	1.40E-08	1.42E-08	6.69E-09	1.74E-08	7.69E-09	1.03E-08	1.28E-08	9.42E-09	7.40E-08
19	6.26E-09	1.14E-08	8.87E-09	1.09E-08	9.15E-09	7.98E-09	7.44E-09	7.24E-09	4.71E-08	4.69E-08	6.73E-09	1.25E-05
20	2.52E-08	2.45E-08	2.95E-08	2.56E-08	2.04E-08	1.05E-08	1.83E-08	1.49E-08	5.38E-07	6.18E-08	2.44E-08	4.83E-08
21	1.03E-08	1.43E-08	2.15E-08	1.50E-08	1.37E-08	5.33E-09	1.21E-08	1.36E-08	1.47E-08	2.22E-08	1.89E-08	1.40E-08
22	6.17E-09	1.30E-08	1.18E-08	1.02E-08	8.37E-09	5.08E-09	1.11E-08	3.45E-08	3.73E-08	5.72E-09	2.04E-08	
23	1.14E-08	1.67E-08	1.91E-08	1.07E-08	7.34E-09	4.00E-09	7.93E-09	4.67E-10	7.20E-09	5.48E-08	8.43E-09	1.41E-08
24	9.09E-09	1.06E-08	1.28E-08	9.46E-09	6.16E-09	4.07E-09	8.65E-09	8.96E-09	1.67E-04	6.26E-09	1.31E-08	1.09E-08
25	4.34E-09	1.12E-08	1.25E-08	1.01E-08	5.85E-09	2.40E-09	2.88E-08	1.04E-08	8.18E-09	2.50E-08	6.57E-09	1.68E-08
26	5.42E-09	1.02E-08	1.31E-08	7.19E-09	1.98E-09	7.52E-09	1.08E-08	6.32E-09	3.52E-08	9.96E-10	1.82E-08	
27	9.56E-10	6.83E-09	1.35E-08	1.13E-08	4.24E-09	4.89E-10	1.07E-08	1.01E-08	3.44E-09	5.40E-09	1.15E-10	1.59E-05
28	4.09E-11	1.15E-08	1.57E-08	6.86E-09	3.47E-09	2.05E-11	1.03E-08	1.75E-10	1.68E-09	2.69E-09	2.17E-10	1.13E-09
29		7.68E-09	1.28E-08	4.14E-09	1.59E-09	7.15E-11	1.59E-08	1.16E-09	1.01E-10	3.83E-10	1.95E-11	2.05E-05
30	6.19E-12	5.94E-09	9.04E-09	2.43E-09	1.61E+10		6.02E-09	1.39E-09	2.20E-12	4.07E-06	3.01E-11	5.59E-12
31	7.61E-13	2.02E-09	6.64E-09	2.75E-09	2.92E-11	4.79E-11	6.76E-09	9.03E-09	5.21E-12	5.38E-06	6.13E-11	7.50E-09
33	1.58E-12	5.14E-12	6.92E-09	3.86E-11	9.06E-12	1.13E-12	2.51E-09	9.16E-11	2.53E-12	6.72E-12	1.89E-12	1.47E-12

	Conductance value (S)												
Dehydration time (hours)	1mM	5mM	10mM	20mM	100mM	200mM	300mM	400mM	420mM	440mM	460mM	500mM
0	3.24E-06	3.65E-06	2.71E-06	3.30E-06	2.73E-06	2.03E-06	4.59E-06	9.90E-06	4.58E-06	2.60E-06	7.51E-06	1.79E-04
1	2.20E-06	1.09E-06	4.57E-07	1.42E-06	2.67E-06	1.75E-06	1.46E-06	2.92E-06	1.26E-06	1.13E-06	1.12E-05	6.22E-06
2	2.43E-06	1.47E-06	7.87E-07	1.05E-06	1.27E-06	1.30E-06	2.61E-06	8.32E-06	1.10E-05	8.07E-06	5.31E-06	1.14E-05
3	1.47E-06	1.81E-06	7.66E-07	9.33E-07	1.71E-06	9.92E-07	1.45E-06	4.88E-06	1.82E-06	8.74E-07	1.16E-06	1.49E-06
4	1.14E-06	1.28E-06	1.01E-06	6.70E-07	8.85E-07	6.43E-07	2.15E-06	4.02E-06	2.76E-06	1.40E-06	2.00E-06	1.81E-06
5	1.34E-06	1.37E-06	1.09E-06	8.65E-07	2.05E-06	8.54E-07	1.68E-06	5.28E-06	2.38E-06	1.08E-06	2.40E-06	3.47E-06
6	4.22E-07	1.80E-06	1.06E-06	1.19E-06	2.13E-06	1.14E-06	2.97E-06	3.74E-06	2.10E-06	1.44E-06	1.75E-06	1.90E-06
8	1.13E-06	1.67E-06	1.02E-06	8.66E-06	9.63E-07	1.01E-06	1.97E-06	3.43E-06	2.90E-06	1.19E-06	6.44E-07	3.28E-06
10	1.28E-06	9.85E-07	1.08E-06	1.08E-06	8.55E-07	7.43E-07	8.24E-07	3.67E-06	4.69E-06	2.95E-06	8.62E-07	1.19E-05
12	1.50E-06	1.22E-06	1.88E-06	1.39E-06	2.73E-06	1.04E-06	9.00E-07	7.35E-07	8.91E-07	1.07E-06	4.57E-07	5.63E-06
14	2.34E-06	3.15E-06	1.37E-06	1.26E-06	1.63E-06	6.44E-07	8.65E-07	4.73E-07	7.99E-07	5.69E-07	5.87E-07	2.30E-06
16	1.10E-06	1.10E-06	9.87E-07	1.78E-06	1.03E-06	8.22E-07	9.76E-07	7.56E-07	2.05E-06	9.76E-07	5.45E-07	4.91E-06
17	8.30E-07	1.78E-06	1.99E-06	1.06E-06	8.87E-07	1.18E-06	1.80E-06	2.67E-07	2.96E-06	8.16E-07	7.67E-07	2.68E-06
18	1.24E-06	1.72E-06	2.14E-06	1.40E-06	1.42E-06	6.69E-07	1.74E-06	7.69E-07	1.03E-06	1.28E-06	9.42E-07	7.40E-06
19	6.26E-07	1.14E-06	8.87E-07	1.09E-06	9.15E-07	7.98E-07	7.44E-07	7.24E-07	4.71E-06	4.69E-06	6.73E-07	1.25E-03
20	2.52E-06	2.45E-06	2.95E-06	2.56E-06	2.04E-06	1.05E-06	1.83E-06	1.49E-06	5.38E-05	6.18E-06	2.44E-06	4.83E-06
21	1.03E-06	1.43E-06	2.15E-06	1.50E-06	1.37E-06	5.33E-07	1.21E-06	1.36E-06	1.47E-06	2.22E-06	1.89E-06	1.40E-06
22	6.17E-07	1.30E-06	1.18E-06	1.02E-06	8.37E-07	5.08E-07	1.11E-06	3.45E-06	3.73E-06	3.72E-06	5.72E-07	2.04E-06
23	1.14E-06	1.67E-06	1.91E-06	1.07E-06	7.34E-07	4.00E-07	7.93E-07	4.67E-08	7.20E-07	5.48E-06	8.43E-07	1.41E-06
24	9.09E-07	1.06E-06	1.28E-06	9.46E-07	6.16E-07	4.07E-07	8.65E-07	8.96E-07	1.67E-02	6.26E-07	1.31E-06	1.09E-06
25	4.34E-07	1.12E-06	1.25E-06	1.01E-06	5.85E-07	2.40E-07	2.88E-06	1.04E-06	8.18E-07	2.50E-06	6.57E-07	1.68E-06
26	5.42E-07	1.02E-06	1.31E-06	7.19E-07	7.13E-07	1.98E-07	7.52E-07	1.08E-06	6.32E-07	3.52E-06	9.96E-08	1.82E-06
27	9.56E-08	6.83E-07	1.35E-06	1.13E-06	4.24E-07	4.89E-08	1.07E-06	1.01E-06	3.44E-07	5.40E-07	1.15E-08	1.59E-03
28	4.09E-09	1.15E-06	1.57E-06	6.86E-07	3.47E-07	2.05E-09	1.03E-06	1.75E-08	1.68E-07	2.69E-07	2.17E-08	1.13E-07
29	#DIV/0!	7.68E-07	1.28E-06	4.14E-07	1.59E-07	7.15E-09	1.59E-06	1.16E-07	1.01E-08	3.83E-08	1.95E-09	2.05E-03
30	6.19E-10	5.94E-07	9.04E-07	2.43E-07		#DIV/0!	6.02E-07	1.39E-07	2.20E-10	4.07E-04	3.01E-09	5.59E-10
31	7.61E-11	2.02E-07	6.64E-07	2.75E-07	2.92E-09	4.79E-09	6.76E-07	9.03E-07	5.21E-10	5.38E-04	6.13E-09	7.50E-07
33	1.58E-10	5.14E-10	6.92E-07	3.86E-09	9.06E-10	1.13E-10	2.51E-07	9.16E-09	2.53E-10	6.72E-10	1.89E-10	1.47E-10

In situ preparation of network forming gold nanoparticles in agarose hydrogels†

Erwan Faoucher,[a] Paola Nativo,[a] Kate Black,[b] John B. Claridge,[a] Mhairi Gass,[c] Simon Romani,[b] Andrew L. Bleloch[b] and Mathias Brust*[a]

Received (in Cambridge, UK) 31st July 2009, Accepted 8th September 2009
First published as an Advance Article on the web 24th September 2009
DOI: 10.1039/b915787e

Gold nanoparticles are obtained by reduction of a Au(III) precursor within an agarose hydrogel where they form percolating networks upon partial dehydration and shrinkage of the gel.

Tremendous advances have been made in metal nanoparticle synthesis over the past two decades. Detailed protocols for the control of the key parameters, particle composition, size and shape are now widely available.[1–5] As the field gains maturity, more attention is being paid to nanoparticles as components of functional composites for applied purposes.[6–8] Stability, longevity and controlled interaction with other components are thus important secondary parameters. These can be addressed by tailoring the interface between the particles and their environment usually by the choice of ligand molecules, often thiols.[9,10] However, for applications that rely on the chemical accessibility of the metal surface, alternative strategies have to be found. Current developments in catalysis by Au nanoparticles illustrate this problem.[11–13] Catalyst nanoparticles are commonly generated *in situ* by reduction of a Au(III) precursor adsorbed to the support material.[13] Here we describe a conceptually similar approach where a gold salt is reduced inside an agarose hydrogel. This yields a composite material with an hierarchical organisation of gold nanoparticles the size of which is related to the position they occupy, within the gel structure. While reports on the entrapment of pre-prepared metal nanoparticles in gels are common[14–17] less attention has been paid to the use of gels as the actual reaction medium.[18–21] Cai *et al.* prepared Ag, Au and Pt nanoparticles in cellulose hydrogels,[18] and Mohan *et al.* prepared Ag nanoparticles in a hydrogel and obtained a material with antibacterial properties.[19] In our new method an agarose gel is first loaded with Au salt by immersion for 24 h in an aqueous solution of hydrogen tetrachloroaurate followed by a transfer of the Au loaded gel to a 500 mM aqueous solution of sodium borohydride where immediate reduction of the Au(III) complex to Au(0) takes place manifested by a colour change from yellow to black (see Scheme in ESI†). To confirm the presence of Au nanoparticles, the sample was analysed by X-ray powder diffraction (XRD) and electron microscopy. The XRD data (see ESI†) clearly indicate the presence of fcc Au nanocrystals. The approximate size of the particles as estimated by line broadening analysis using the Scherrer equation[22] increases with increasing Au loading. The absence of narrow peaks rules out the formation of bulk Au, which, at the salt concentrations used, would be the only product, if the reaction had been carried out in aqueous solution in the absence of stabilising agents. Given the well-known limitations of XRD line broadening analysis a careful electron microscopic analysis is essential to obtain a reasonable insight into the sizes, morphologies and three-dimensional organisation of the particles obtained. This forms the basis for suggesting a structural model for the nanoparticle-loaded gel. In Fig. 1a–c electron microscopic images of a gel containing Au nanoparticles prepared using a 20 mM hydrogen tetrachloroaurate feed solution are shown. The images in Fig. 1a and b were obtained by scanning transmission electron microscopy (STEM) in dark field mode of a 60 nm thin section of the

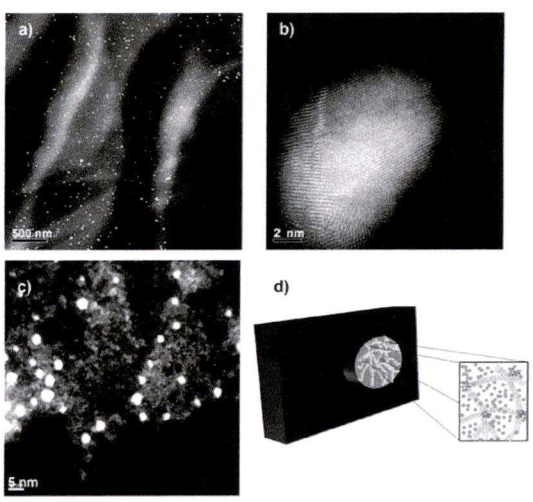

Fig. 1 STEM image of a 60 nm epoxy embedded section of an agarose gel loaded with gold nanoparticles showing the agarose network structure coated with gold clusters (a) and a single gold nanoparticle dispersed within the water phase of the gel (b). HAADF-STEM image of the freeze-dried agarose gel decorated with gold clusters (c) and schematic illustration of a simplified structural model of the composite (d). The concentration of the gold feed solution was 20 mM in all cases

[a] *Centre for Nanoscale Science, Department of Chemistry, University of Liverpool, Crown Street, Liverpool, UK L69 7ZD. E-mail: mbrust@liv.ac.uk; Fax: +44 (0)151 794 3554; Tel: +44 (0)151 794 3555*
[b] *Department of Engineering, Derby Building, University of Liverpool, Brownlow Hill, Liverpool, UK L69 3GH. E-mail: a.l.bleloch@liv.ac.uk; Fax: +44 (0)151 794 4701; Tel: +44 (0)151 794 4703*
[c] *Daresbury Laboratories, Super-STEM, Keckwick Lane, Daresbury, UK WA4 4AD. E-mail: m.h.gass@liv.ac.uk; Tel: +44 (0)1925 864 905*

† Electronic supplementary information (ESI) available: Details of the materials used and synthesis of Au Nps, XRD, TEM, STEM and current–time response for wet and dry gel. See DOI: 10.1039/b915787e

This journal is © The Royal Society of Chemistry 2009

gel embedded in standard epoxy resin used routinely for biological samples. In Fig. 1a the agarose network of the gel is clearly visible as an electron dense (light) cloud that suggests the presence of Au atoms or clusters decorating the polymeric framework. In addition, *ca.* 8 nm Au particles appear as bright spots on the surface of the network and to a lesser degree also free in the water-phase of the gel. A high resolution image of a representative particle is shown in Fig. 1b exhibiting a multiply twinned structure commonly observed in Au nanoparticles of this size.[23] To confirm our hypothesis that the polymeric framework of the gel is decorated by Au atoms and/or small clusters, a freeze-dried sample of the gel was inspected by high angle annular dark field scanning transmission electron microscopy HAADF-STEM. The result shown in Fig. 1c reveals the presence of Au clusters in the range of 0.5 to 4 nm plus electron dense material not resolved as particulate matter. This observation is consistent with a decoration of the agarose framework by Au atoms and clusters. The smallest discernible clusters are Au_{13} (see enlarged image in ESI†).[24–26] From the extensively studied structure of agarose gel[27] and the present electron microscopic analysis the following structural model is proposed for the composite material. As illustrated in Fig. 1d (for an enlarged image see ESI†) the gel is composed of interwoven helices of agarose polymer strands stabilised by water pockets in the helical cavities. It is suggested that upon reduction of metal ions in the gel very small clusters (large dots) and atoms form and lodge in these cavities thereby decorating the gel framework. The upper limit of particle size appears to be *ca.* 5 nm (small dots). In the water-phase of the gel, larger particles are formed and appear to remain dispersed within the water cells. These particles dominate the XRD line broadening results and mask to some extent the presence of the much smaller clusters. The observed trend in the XRD results suggests that the proportion and size of larger colloidal particles in the water-phase increases with increasing concentration of metal salt in the feed solution. This is confirmed by electron microscopy of samples with a higher metal loading (see ESI†). There has been a lot of interest in self-organisation of metal nanoparticles and in electronic transport through the resulting line, film or network structures.[28–32] Several promising approaches to the development of sensing devices based on such materials have been suggested.[33–36] In a gel, three-dimensional networks of nanoparticles are readily obtained, and the interparticle spacing may be controllable. Interesting electrical properties are expected, in particular, close to the percolation threshold. For charge transport measurement our gels were first thoroughly dialysed to remove most ionic species from the aqueous phase and then cut into discs of 8.5 mm diameter and 3.2 mm thickness. Freshly prepared ("wet") samples were superficially dried with tissue paper and the current response to applied voltage steps from 0 to 10 mV across the gel was measured using the setup depicted in Fig. 2a. This procedure was repeated with partially dehydrated ("dry") gels obtained by removal of an amount of water corresponding to 40% of their original weight. The current–time curves (see ESI†) corresponding to the potential steps were interpreted using the simple equivalent circuit of a leaking capacitor shown in Fig. 2b with the ohmic resistance of the system, R_2, the

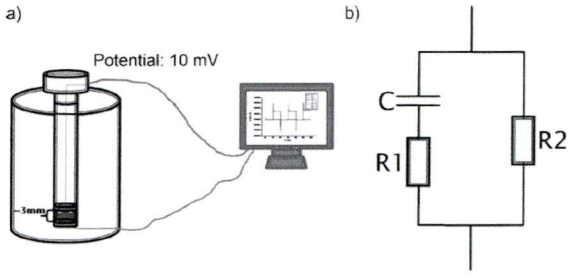

Fig. 2 Schematic illustration of the device used to measure charge transport across discs of agarose gel between two flat gold foil electrodes (a) and equivalent circuit used to fit the experimental results (b).

capacitance, C, and the transient charging resistance, R_1, which becomes approximately equal to R_2 above the percolation threshold, *i.e.* the appearance of the first conductive path across the gel *via* metal nanoparticles in contact with each other. The current response to a voltage step is then given by

$$i = \frac{U}{R_2} + \frac{U}{R_1} e^{\frac{-t}{R_1 C}} \quad (1)$$

It is now possible to determine R_1, R_2 and C by fitting the experimental voltage step data using eqn (1) (see ESI† for the fitted voltage steps). The results are summarized in Table 1. While the initial increase in resistance (R_2) with increasing gold loading in "wet" samples appears counterintuitive, it simply indicates that here the electron transport *via* the metal content of the gel is negligible at most but the highest metal loading. As the metal inclusions contribute significantly to the capacitance (C) of the material their presence lowers the electric field inside the gel and thus decreases the conductance that stems from ionic migration. A different picture arises for dry samples. Now, the resistivity (R_2) remains approximately constant at a value about ten times higher than that of the unloaded "wet" gel, while the capacitance (C) still increases with increasing metal loading. This suggests that in the "dry" material ion migration is impeded by the denser polymeric network. The conductivity remains constant at these low values up to a certain point, when it suddenly increases steeply by two orders of magnitude at a gold loading that we interpret as the percolation threshold (Fig. 3a). This does not implythat the mechanism of conduction is metallic, since there will still be boundaries between the particles that may act as small insulating gaps. In addition to the much higher conductivity observed, the currents measured at this point exhibit strictly ohmic behaviour as demonstrated by successively increasing

Table 1 Summary of resistance and capacitance values of "wet" and "dry" gels obtained from gels exposed to Au feed solutions of different concentration

	Resistance				Capacitance	
	Dry		Wet		Dry	Wet
Concentration/mM	R_1/kΩ	R_2/kΩ	R_1/kΩ	R_2/kΩ	C/μF	
0	53.466	131.235	188.457	13.366	12.2	2.45
20	16.04	144.358	80.199	33.262	20	11
200	10.445	90.223	25.778	75.978	105	21
500	0.662	0.69	2.485	20.623	872	58.1
600	0.827	0.77	1.007	53.466	1170	1334

This journal is © The Royal Society of Chemistry 2009

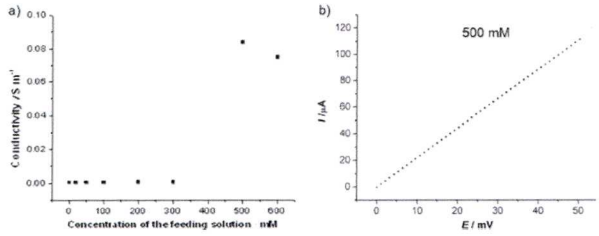

Fig. 3 Conductivity of Au loaded gel *vs.* concentration of feed solution used. Note the transition to a percolated system between 300 and 500 mM (a). Experimental current–voltage behaviour above the percolation threshold demonstrating ohmic properties (b).

the values of the voltage steps (Fig. 3b). Whether the current flows predominantly through the larger particles formed in the water-phase or the small clusters decorating the polymer framework cannot be decided based on the data presently available. Temperature dependent studies are needed to evaluate activation energies for electron hopping processes from which the size of the metal structures involved could be estimated.[37,38] In conclusion, we have demonstrated a facile new method for the preparation of gold nanoparticles using a hydrogel as a reaction medium and stabilising matrix. The resultant composite material has been characterised by HAADF-STEM and XRD. Initial work towards understanding electronic transport through the gels has been presented and a simple model has been used to fit the experimental data. Owing to their tunable charge transport properties the materials prepared show promise for the development of sensors. While the present study has focussed strongly on Au nanoparticles, preliminary work shows that Pt, Pd and Ru nanoparticle-loaded gels are also readily obtained by analogous procedures (see ESI† for TEM and XRD) suggesting applications in catalysis. A study focussing on controllable Raman enhancement in gels loaded with Ag nanoparticles prepared by the method described here has been completed.[39]

Financial support *via* an EPSRC quota award of a PhD studentship (EF) and by the Marie Curie R&T Network PATTERNS (PN) is gratefully acknowledged. The authors wish to thank Charles Clavering for assistance with the electronic characterisation of samples, John Bacsa for assistance with XRD measurements, Laurence Duchesne for the freeze drying of samples and Paul Chalker for helpful discussions.

Notes and references

1 *Metal Nanoparticles Synthesis, Characterization, and Applications*, ed. D. L. Feldheim, C. A. Foss Jr., Marcel Dekker, New York, 2002.
2 S. Link, Z. L. Wang and M. A. El-Sayed, *J. Phys. Chem. B*, 1999, **103**, 3529–3533.
3 V. F. Puntes, K. M. Krishnan and A. P. Alivisatos, *Science*, 2001, **291**, 2115–2117.
4 Y. G. Sun and Y. N. Xia, *Science*, 2002, **298**, 2176–2179.
5 M. Grzelczak, J. Perez-Juste, P. Mulvaney and L. M. Liz-Marzan, *Chem. Soc. Rev.*, 2008, **37**, 1783–1791.
6 *Colloids and Colloid Assemblies*, ed. F. Caruso, Wiley-VCH, Weinheim, 2004.
7 *Nanoparticle Assemblies and Superstructures*, ed. N. A. Kotov, CRC Press, Boca Raton, 2005.
8 V. Subramanian, E. E. Wolf and P. V. Kamat, *Langmuir*, 2003, **19**, 469–474.
9 M.-C. Daniel and D. Astruc, *Chem. Rev.*, 2004, **104**, 293–346.
10 A. C. Templeton, M. J. Hostetler, E. K. Warmoth, S. Chen, C. M. Hartshorn, V. M. Krishnamurthy, M. D. E. Forbes and R. W. Murray, *J. Am. Chem. Soc.*, 1998, **120**, 4845–4849.
11 G. J. Hutchings and M. Haruta, *Appl. Catal., A*, 2005, **291**, 2–5.
12 M. Haruta, *Nature*, 2005, **437**, 1098–1099.
13 A. Corma and H. Garcia, *Chem. Soc. Rev.*, 2008, **37**, 2096–2126.
14 X. Wang, E. C. Egan, M. Zhou, K. Prince, D. R. G. Mitchell and R. A. Caruso, *Chem. Commun.*, 2007, 3060–3062.
15 D. Zanchet, C. M. Micheel, W. J. Parak, D. Gerion and A. P. Alivisatos, *Nano Lett.*, 2001, **1**, 32–35.
16 D. Zanchet, C. M. Micheel, W. J. Parak, D. Gerion, S. C. Williams and A. P. Alivisatos, *J. Phys. Chem. B*, 2002, **106**, 11758–11763.
17 W. J. Parak, D. Gerion, T. Pellegrino, D. Zanchet, C. Micheel, S. C. Williams, R. Boudreau, M. A. Le Gros, C. A. Larabell and A. P. Alivisatos, *Nanotechnology*, 2003, **14**, R15–R27.
18 J. Cai, S. Kimura, M. Wada and S. Kuga, *Biomacromolecules*, 2009, **10**, 87–94.
19 Y. M. Mohan, K. Lee, T. Premkumar and K. E. Geckeler, *Polymer*, 2007, **48**, 158–164.
20 K. C. Moon and K. J. Shea, *J. Am. Chem. Soc.*, 1994, **116**, 9052–9060.
21 C. S. Love, V. Chechik, D. K. Smith, K. Wilson, I. Ashworth and C. Brennan, *Chem. Commun.*, 2005, 1971–1973.
22 P. Scherrer, *Nach. Ges. Wiss. Goettingen, Math. Phys. Kl.*, 1918, **2**, 98.
23 J. L. Elechiguerra, J. Reyes-Gasga and M. J. Yacaman, *J. Mater. Chem.*, 2006, **16**, 3906–3919.
24 J. M. Abad, I. E. Sendroiu, M. Gass, A. Bleloch, A. J. Mills and D. J. Schiffrin, *J. Am Chem. Soc.*, 2007, **129**, 12932–12933.
25 K. J. Nobusada, *Phys. Chem. B*, 2004, **108**, 11904–11908.
26 L. D. Menard, H. Xu, S.-P. Gao, R. D. Twesten, A. S. Harper, Y. Song, G. Wang, A. D. Douglas, J. C. Yang, A. I. Frenkel, R. W. Murray and R. G. Nuzzo, *J. Phys. Chem. B*, 2006, **110**, 14564–14573.
27 S. Arnott, A. Fulmer, W. E. Scott, I. C. M. Dea, R. Moorhouse and D. A. Rees, *J. Mol. Biol.*, 1974, **90**, 269–284.
28 T. Hassenkam, K. Norgaard, L. Iverson, C. J. Kiely, M. Brust and T. Bjornholm, *Adv. Mater.*, 2002, **14**, 1126–1130.
29 T. Hassenkam, K. Moth-Poulsen, N. Stuhr-Hansen, K. Nørgaard, M. S. Kabir and T. Bjørnholm, *Nano Lett.*, 2004, **4**, 19–22.
30 M. Brust, D. Bethell, C. J. Kiely and D. J. Schiffrin, *Langmuir*, 1998, **14**, 5425–5429.
31 N. Fishelson, I. Shkrob, O. Lev, J. Gun and A. D. Modestov, *Langmuir*, 2001, **17**, 403–412.
32 J. B. Pelka, M. Brust, P. Gierlowski, W. Paszkowicz and N. Schell, *Appl. Phys. Lett.*, 2006, **89**, 063110.
33 H. Wohltjen and A. W. Snow, *Anal. Chem.*, 1998, **70**, 2856–2859.
34 Q.-Y. Cai and E. T. Zellers, *Anal. Chem.*, 2002, **74**, 3533–3539.
35 S. H. Steinecker, M. P. Rowe and E. T. Zellers, *Anal. Chem.*, 2007, **79**, 4977–4986.
36 Y. Joseph, A. Peić, X. Chen, J. Michl, T. Vossmeyer and A. Yasuda, *J. Phys. Chem. C*, 2007, **111**, 12855–12859.
37 M. Brust, D. Bethell, D. J. Schiffrin and C. J. Kiely, *Adv. Mater.*, 1995, **7**, 795–797.
38 B. Abeles, P. Sheng, M. D. Coutts and Y. Arie, *Adv. Phys.*, 1975, **24**, 407–461.
39 P. Aldeanueva-Potel, E. Faoucher, R. A. Alvarez-Puebla, L. M. Liz-Marzan and M. Brust, *Anal. Chem.*, 2009, DOI: 10.1021/ac901333p.

Anal. Chem. **2009**, *81*, 9233–9238

Recyclable Molecular Trapping and SERS Detection in Silver-Loaded Agarose Gels with Dynamic Hot Spots

Paula Aldeanueva-Potel,[†] Erwan Faoucher,[‡] Ramón A. Alvarez-Puebla,*[,†] Luis M. Liz-Marzán,[†] and Mathias Brust[‡]

Departamento de Química Física and Unidad Asociada CSIC, Universidade de Vigo, 36310 Vigo, Spain, Centre for Nanoscale Science, and Department of Chemistry, University of Liverpool, Crown Street, Liverpool L697ZD, United Kingdom

We describe the design and fabrication of composite agarose gels, highly loaded with silver nanoparticles. Because the gel can collapse upon drying and recover when rehydrated, it can be foreseen as an excellent mechanical molecular trap that additionally gives rise to dynamic hot spots as the network volume decreases and the silver particles get close to each other, thereby generating the high electromagnetic fields that are needed for ultradetection. Additionally, as silver nanoparticles are physically trapped inside the polymer network, analytes can be washed out by dialysis when immersed in a washing solution, so that recycling can be achieved. Finally, the use of SERS for ultradetection of dichlorodiphenyl-trichloroethane (DDT) is reported for the first time, demonstrating the ability of this novel nanocomposite material to reversibly sequester nonconventional SERS analytes.

Development of nanostructured colloids and surfaces with the ability to support localized surface plasmon resonances (LSPR) is turning into a hot field in materials research because of their wide application in different areas such as photonics, medical imaging, drug delivery, catalysis, and ultrasensitive detection via surface-enhanced spectroscopies.[1−3] In the particular case of the latter, and especially in the case of the surface-enhanced Raman scattering (SERS) spectroscopy,[4] the engineering of such optically active materials into advanced assembled composites that will add functionality to the final sensor devices is a key issue.[5−7] Besides the extraordinary analytical potential of SERS,[8−16] which encompasses the ability for ultrarapid and ultrasensitive detection, down to the single-molecule, while providing all the structural and chemical information of the analyte under study, several shortcomings are still to be resolved. First, at present, SERS cannot be considered as a general analytical technique since registration of enhanced spectra with sufficient quality is basically restricted to molecules carrying functional groups that have sufficient affinity for silver or gold surfaces, which are the most common plasmonic nanostructures.[4,17] Second, the intensity of the SERS signal measured for a given analyte strongly relies on the generation of a high density of so-called hot spots (specific sites where the electric field is largely enhanced)[18−23] on the sensor element. Third, due to the intrinsic nature of the analyte−nanoparticle interactions, most SERS substrates are single-use which hampers their integration in online devices for repetitive, real time monitoring. Currently, a vast effort is being devoted to resolve these drawbacks. For example, extension of the molecular families that may be analyzed has been achieved by using copper nanostruc-

* Author to whom correspondence should be addressed. E-mail: ramon.alvarez@uvigo.es.

[†] Universidade de Vigo.

[‡] University of Liverpool.

(1) Daniel, M.-C.; Astruc, D. *Chem. Rev.* **2004**, *104*, 293–346.
(2) Ghosh, S. K.; Pal, T. *Chem. Rev.* **2007**, *107*, 4797–4862.
(3) Stewart, M. E.; Anderton, C. R.; Thompson, L. B.; Maria, J.; Gray, S. K.; Rogers, J. A.; Nuzzo, R. G. *Chem. Rev.* **2008**, *108*, 494–521.
(4) Aroca, R. F. *Surface Enhanced Vibrational Spectroscopy*; Wiley: New York, 2006.
(5) Strickland, A. D.; Batt, C. A. *Anal. Chem.* **2009**, *81*, 2895–2903.
(6) Spuch-Calvar, M.; Rodriguez-Lorenzo, L.; Morales, M. P.; Alvarez-Puebla, R. A.; Liz-Marzan, L. M. *J. Phys. Chem. C* **2009**, *113*, 3373–3377.
(7) Huh, Y. S.; Lowe, A. J.; Strickland, A. D.; Batt, C. A.; Erickson, D. *J. Am. Chem. Soc.* **2009**, *131*, 2208–2213.
(8) Kneipp, K.; Kneipp, H.; Itzkan, I.; Dasari, R. R.; Feld, M. S. *Chem. Rev.* **1999**, *99*, 2957–2976.
(9) Rodriguez-Lorenzo, L.; Alvarez-Puebla, R. A.; Pastoriza-Santos, I.; Mazzucco, S.; Stephan, O.; Kociak, M.; Liz-Marzan, L. M.; Garcia de Abajo, F. J. *J. Am. Chem. Soc.* **2009**, *131*, 4616–4618.
(10) Dieringer, J. A.; Wustholz, K. L.; Masiello, D. J.; Camden, J. P.; Kleinman, S. L.; Schatz, G. C.; Van Duyne, R. P. *J. Am. Chem. Soc.* **2009**, *131*, 849–854.
(11) Etchegoin, P. G.; Lacharmoise, P. D.; Le Ru, E. C. *Anal. Chem.* **2009**, *81*, 682–688.
(12) Bell, S. E. J.; Mackle, J. N.; Sirimuthu, N. M. S. *Analyst* **2005**, *130*, 545–549.
(13) Bell, S. E. J.; Sirimuthu, N. M. S. *Analyst* **2004**, *129*, 1032–1036.
(14) Bell, S. E. J.; Sirimuthu, N. M. S. *J. Am. Chem. Soc.* **2006**, *128*, 15580–15581.
(15) Bell, S. E. J.; Sirimuthu, N. M. S. *Chem. Soc. Rev.* **2008**, *37*, 1012–1024.
(16) Bell, S. E. J.; Spence, S. J. *Analyst* **2001**, *126*, 1–3.
(17) Alvarez-Puebla, R. A.; Arceo, E.; Goulet, P. J. G.; Garrido, J. J.; Aroca, R. F. *J. Phys. Chem. B* **2005**, *109*, 3787–3792.
(18) Brus, L. *Acc. Chem. Res.* **2008**, *41*, 1742–1749.
(19) Camden, J. P.; Dieringer, J. A.; Wang, Y.; Masiello, D. J.; Marks, L. D.; Schatz, G. C.; Van Duyne, R. P. *J. Am. Chem. Soc.* **2008**, *130*, 12616–12617.
(20) Braun, G.; Pavel, I.; Morrill, A. R.; Seferos, D. S.; Bazan, G. C.; Reich, N. O.; Moskovits, M. *J. Am. Chem. Soc.* **2007**, *129*, 7760–7761.
(21) Svedberg, F.; Li, Z.; Xu, H.; Kall, M. *Nano Lett.* **2006**, *6*, 2639–2641.
(22) Le Ru, E. C.; Blackie, E.; Meyer, M.; Etchegoin, P. G. *J. Phys. Chem. C* **2007**, *111*, 13794–13803.
(23) Ward, D. R.; Grady, N. K.; Levin, C. S.; Halas, N. J.; Wu, Y.; Nordlander, P.; Natelson, D. *Nano Lett.* **2007**, *7*, 1396–1400.

10.1021/ac901333p CCC: $40.75 © 2009 American Chemical Society
Published on Web 10/19/2009

tured materials,[24−26] or by decorating the gold or silver surfaces with molecular systems that are capable of electrostatically,[17,27,28] chemically,[29−32] or mechanically[33,34] trapping analytes that are usually hard to retain. However, nanostructures of first-row metals are unstable and show a strong tendency toward rapid oxidation at open atmosphere or in aqueous solution, thereby losing their plasmonic properties. Regarding surface functionalization, most of the current approaches only partially resolve the problem for certain types of molecules and in most cases the trapping interaction is very strong and thus prevents multiple usage. In the same line, many sensor substrates containing highly efficient hot spots have been recently developed.[35−39] However, again, these substrates can only be used once and may not be able to retain complex molecular systems. In addition, most approaches rely on micro- or nanosized composites, thereby complicating integration within real life devices.

We describe in this paper the design and fabrication of composite agarose gels, densely loaded with silver nanoparticles. Because the gel can collapse upon drying and recover when rehydrated, it can be foreseen as an excellent mechanical molecular trap that additionally gives rise to dynamic hot spots as the network volume decreases and the silver particles get close to each other, thereby generating the huge electromagnetic fields that are needed for ultradetection. Additionally, as silver nanoparticles are physically trapped inside the polymer network, analytes can be washed out by dialysis when immersed in a cleaning solution, so that recycling can be achieved. On the other hand, the bulk dimensions of these composites allow straightforward integration into macro-, micro-, and nanosensor devices. The optical and mechanical trapping properties, as well as the recyclable nature of these systems, were characterized with a number of analytes including thiolated, cationic, anionic, and molecular analytes. Finally, the use of SERS for ultradetection of dichlorodiphenyl-trichloroethane (DDT), an ubiquitous environmental pollutant,[40] which is usually related to diabetes, asthma, neuropsychological, and psychiatric symptoms and classified as Group 2B carcinogen by the International Agency for Research on Cancer,[41,42] is reported for first time. This demonstrates the ability of this novel nanocomposite material to reversibly sequester nonconventional SERS analytes, such as organochlorine pesticides.

EXPERIMENTAL METHODS

Unless otherwise stated chemicals were purchased from Sigma Aldrich. Sodium borohydride ($NaBH_4$) was obtained from BDH, and agarose (molecular grade) from Bioline. All chemicals were used as received. Milli-Q plus 185 water was used in all experiments.

Synthesis of the Silver-Loaded Agarose Gels (Ag-Agar). A general protocol for the preparation of metal−nanoparticle-loaded agarose hydrogels is presented elsewhere.[37] Briefly, agarose hydrogels (5.4%w) were prepared by dissolving 285 mg of agarose in 5 mL of water at 90 °C in a glass vial of 20 mm inner diameter followed by sonication until all gas bubbles were removed and storage for at least 1 h at 4 °C. The vial was then carefully destroyed with a small metal hammer (caution!) to isolate the resultant hydrogel, which was rinsed with water and cut with a razor blade into discs of ca. 3.2 mm thickness. For the preparation of silver nanoparticles, a wedge-shaped quarter of an agarose hydrogel disk was immersed in 3 mL of a 500 mM feed solution of $AgNO_3$ for 24 h. The hydrogels were then removed from the feed solution, quickly rinsed with water, and immediately transferred to 3 mL of a freshly prepared 500 mM solution of sodium borohydride. After 24 h, the Ag-loaded gels were removed from the sodium borohydride solution and dialyzed in ca. 50 mL of water for 48 h, replacing the water every 12 h. The gels were stored in closed vials under water.

X-ray Powder Diffraction (XRD). Data were collected on a Stoe STADI P diffractometer using Cu $K\alpha_1$ radiation in transmission foil geometry. Measurements were carried out on ca. 1 mm slices of gel cut with a razor blade. They were held in place between acetate films to prevent shrinkage of the sample by the beam due to dehydration.

UV−Visible Spectroscopy. Solid-state spectra were recorded with a Perkin-Elmer Lambda 650 S UV/vis spectrometer equipped with a Labsphere integrating sphere over the spectral range 190−900 nm (6.53−1.38 eV) using $BaSO_4$ reflectance standards. Samples were prepared by compressing a small piece of gel between two glass slides. A sample of unloaded gel was used as a reference.

Transmission Electron Microscopy (TEM). Before the gels were embedded in epoxy resin, they were dehydrated in a graded series of ethanol solutions (30, 60, 70, 90, and 100%v) for 30 min at each concentration and then infiltrated by a graded series of epoxy resin in absolute ethanol (proportion of resin was 1/4, 1/2, and 3/4 of the total volume) each step for 1 h. After being embedded in the pure resin, it was polymerized at 60 °C for one week. This unusually slow step was necessary to avoid irreversible sticking of the sample to the diamond blade during the subsequent cutting process. Ultrathin sections (60 nm) were cut using a LKB

(24) Pastoriza-Santos, I.; Sánchez-Iglesias, A.; Rodríguez-González, B.; Liz-Marzán, L. M. *Small* **2009**, *5*, 440–443.
(25) Anema, J. R.; Brolo, A. G.; Marthandam, P.; Gordon, R. *J. Phys. Chem. C* **2008**, *112*, 17051–17055.
(26) Kudelski, A. *Langmuir* **2003**, *19*, 3805–3813.
(27) Alvarez-Puebla, R. A.; Aroca, R. F. *Anal. Chem.* **2009**, *81*, 2280–2285.
(28) Tan, S.; Erol, M.; Sukhishvili, S.; Du, H. *Langmuir* **2008**, *24*, 4765–4771.
(29) Guerrini, L.; Garcia-Ramos, J. V.; Domingo, C.; Sanchez-Cortes, S. *Langmuir* **2006**, *22*, 10924–10926.
(30) Guerrini, L.; Garcia-Ramos, J. V.; Domingo, C. n.; Sanchez-Cortes, S. *Anal. Chem.* **2009**, *81*, 953–960.
(31) Guerrini, L.; Garcia-Ramos, J. V.; Domingo, C. n.; Sanchez-Cortes, S. *Anal. Chem.* **2009**, *81*, 1418–1425.
(32) Bantz, K. C.; Haynes, C. L. *Vib. Spectrosc.* **2009**, *50*, 29–35.
(33) Alvarez-Puebla, R. A.; Contreras-Caceres, R.; Pastoriza-Santos, I.; Perez-Juste, J.; Liz-Marzan, L. M. *Angew. Chem., Int. Ed.* **2009**, *48*, 138–143.
(34) Abalde-Cela, S.; Ho, S.; Rodríguez-González, B.; Correa-Duarte, Miguel, A.; Álvarez-Puebla, Ramón, A.; Liz-Marzán, Luis, M.; Kotov, Nicholas, A. *Angew. Chem., Int. Ed.* **2009**, *48*, 5326–5329.
(35) Le, F.; Brandl, D. W.; Urzhumov, Y. A.; Wang, H.; Kundu, J.; Halas, N. J.; Aizpurua, J.; Nordlander, P. *ACS Nano* **2008**, *2*, 707–718.
(36) Kneipp, J.; Li, X.; Sherwood, M.; Panne, U.; Kneipp, H.; Stockman, M. I.; Kneipp, K. *Anal. Chem.* **2008**, *80*, 4247–4251.
(37) Faoucher, E.; Nativo, P.; Black, K.; Claridge, J. B.; Gass, M.; Romani, S.; Bleloch, A. L.; Brust, M. *Chem. Commun.*, in press, DOI: 10.1039/B915787E.
(38) Park, Y.-K.; Yoo, S.-H.; Park, S. *Langmuir* **2008**, *24*, 4370–4375.
(39) Lee, S. J.; Morrill, A. R.; Moskovits, M. *J. Am. Chem. Soc.* **2006**, *128*, 2200–2201.
(40) Turusov, V.; Rakitsky, V.; Tomatis, L. *Environ. Health Perspect.* **2002**, *110*, 125–128.
(41) Ahlborg, U. G.; Lipworth, L.; Titus-Ernstoff, L.; Hsieh, C. C.; Hanberg, A.; Baron, J.; Trichopoulos, D.; Adami, H. O. *Crit. Rev. Toxicol.* **1995**, *25*, 463–531.
(42) Longnecker, M. P.; Rogan, W. J.; Lucier, G. *Annu. Rev. Public Health* **1997**, *18*, 211–244.

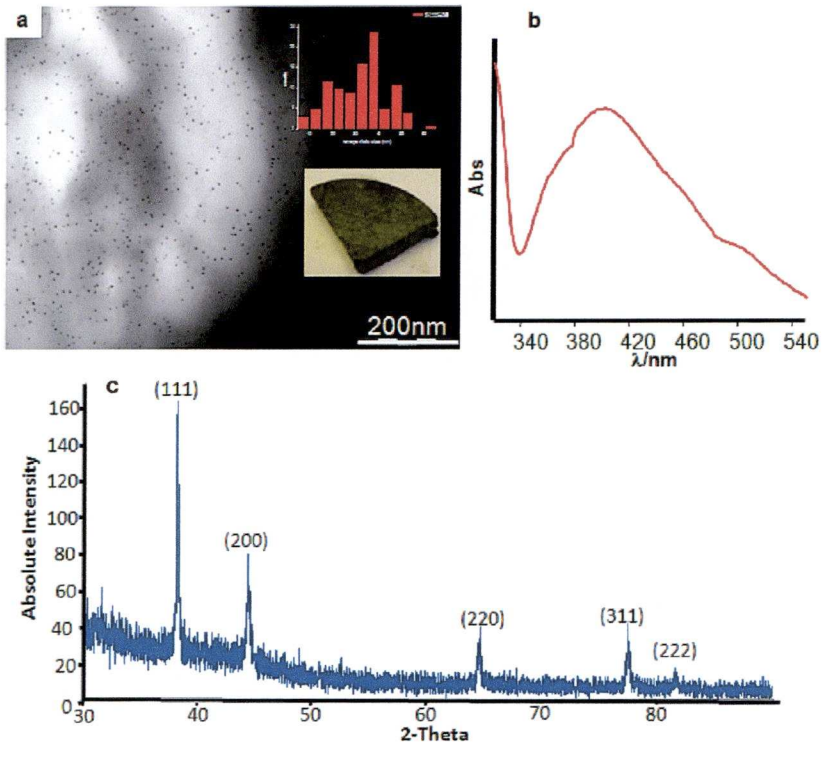

Figure 1. (A) Cross-sectional TEM image of the Ag-Agar gel (inset shows an optical picture of the bulk polymer). (B) UV−vis spectrum and (C) X-ray diffraction pattern of the Ag-Agar gel.

ultramicrotome. The sections were placed on a carbon-coated copper grid and dried at room temperature. TEM images were obtained using a 120 kV FEI technai Spirit TEM.

SERS. The inelastic scattered radiation was collected with a Renishaw Invia Reflex system equipped with Peltier charge-coupled device (CCD) detectors and a Leica confocal microscope. The spectrograph uses high resolution gratings with additional band-pass filter optics. Samples were excited with four different laser lines at 532 (Nd:Yag), 633 (He−Ne), and 785 and 830 nm (diode). The corresponding laser line was focused onto the sample in backscattering geometry using a 50× objective (n.a. 0.75) providing scattering areas of ca. 1 μm^2.

The SERS optical activity of the Ag-Agar composites was tested with 1-naphthalenethiol (1NAT, Acros Organics), a well-studied nonresonant SERS probe. Samples were prepared by immersing the polymer into 1NAT 10^{-5} M aqueous solution for 2 h. SERS spectra were collected on the wet and dried gel with each of the laser lines. Optical enhancing homogeneity of the Ag-Agar was studied by using the Renishaw StreamLine accessory with the 785 nm laser line.

For dichlorodiphenyl-trichloroethane (DDT), the analysis was carried out by immersing the Ag-Agar in DDT aqueous solutions of different concentration (between 10^{-4} and 10^{-8} M) prepared from DDT 10^{-3} M stock solution in ethanol for 2 h. After being dried, the surfaces were studied with the 785 nm laser line.

Reversibility as a function of the analyte charge was studied by immersing the Ag-loaded agarose gel, either in crystal violet 10^{-6} M (CV, cationic probe), 2-naphthoic acid 10^{-5} M (NCOOH, anionic probe), or DDT 10^{-5} M (neutral probe) for 2 h. Samples were then studied with either 633 or 785 nm laser lines and immersed in a washing 1% citrate aqueous solution for 2 h, CV and NCOOH, and an ethanol:water (1:1) mixture. This process was repeated three times for each sample to ensure reproducibility.

RESULTS AND DISCUSSION

A general structural model for agarose gels loaded with in situ prepared metal nanoparticles based on high resolution imaging is presented in detail elsewhere.[37] In summary, metal nanoparticles of two size ranges are usually obtained: (i) large, 8 to 60 nm, particles dispersed in the water phase of the gel, and (ii) small, 0−5 nm, clusters and nanoparticles decorating the gel's polymeric framework. This is also the case for Ag as shown in the TEM image of a section of the loaded gel in Figure 1a. Here, the larger particles as well as aggregates thereof are resolved as irregularly shaped black specks, while the electron dense coating of the gel network with small clusters appears as a homogeneous gray cloud. More highly resolved electron microscopy images are difficult to obtain with the combination of material and sample preparation technique chosen here and are not subject of the present study. The suggested model is further supported by XRD (Figure 1b), which clearly shows the presence of *fcc* Ag nanoparticles, the approximate average size of which can be estimated as 33 nm by Scherrer line broadening analysis.[38] The material appears yellow to dark brown depending on thickness, which is consistent with the presence of Ag nanoparticles with a plasmon absorption band around 420 nm. The UV−vis spectrum shown in Figure 1c is in agreement with this observation, although the plasmon band is unusually broad and slightly blue-shifted. This could be due to scattering by the gel network, which scales as λ^{-4} and would enhance the total extinction at low wavelengths.

Consistent with the low SERS cross-section of polysaccharides,[4] the background SERS spectra of the dry, unloaded (with no

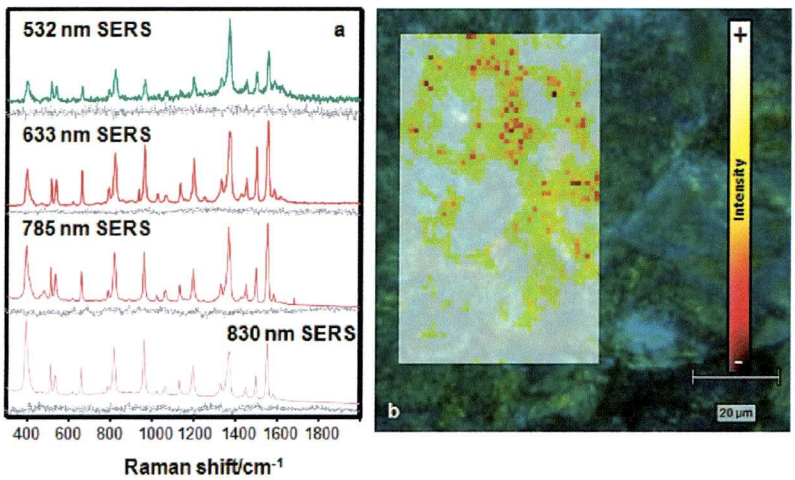

Figure 2. (A) SERS spectra of the dry Ag-Agar gel with 1NAT (colored spectra) and without the analyte (gray spectra). (B) StreamLine map of the Ag-Agar gel with 1NAT (785 nm) composed of 2639 spectra with spatial resolution of ca. 1 μm^2.

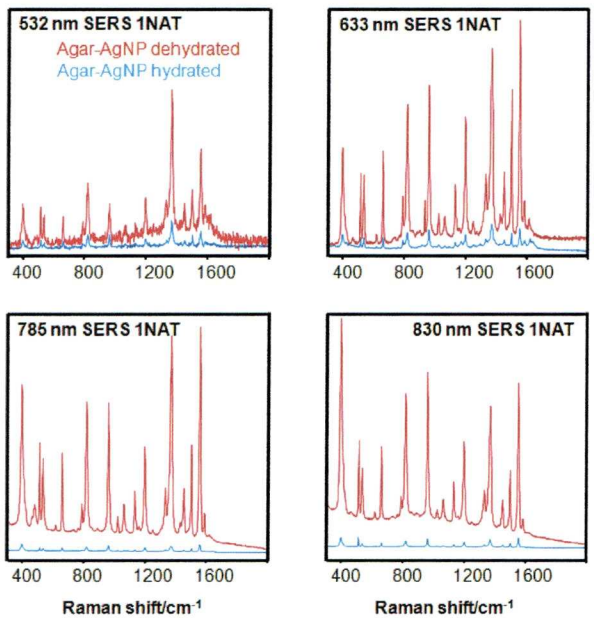

Figure 3. SERS spectra of 1NAT in Ag-Agar before and after air-drying the gel for different excitation laser lines (532, 633, 785, and 830 nm).

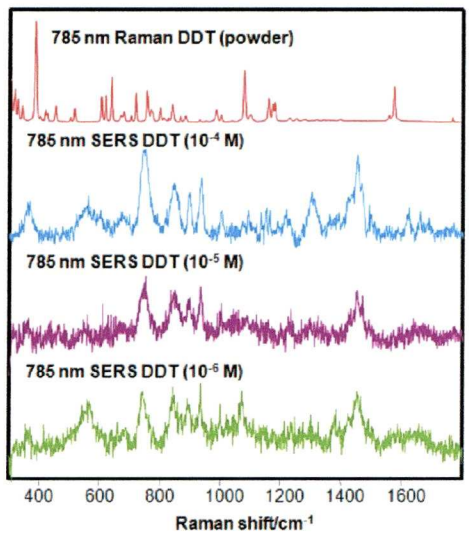

Figure 4. Bulk Raman and SERS spectra of DDT after trapping it into the Ag-Agar gel by immersion and dehydration.

analyte) Ag-Agar gels (gray lines in Figure 2A) present a very clean spectral window from the visible (532 nm) to the near-IR (830 nm). In contrast, upon immersion of the gel in an aqueous solution of 1-naphtalenethiol (1NAT) and subsequent air-drying, the SERS spectra (colored lines in Figure 2A) show well-defined bands with high intensity, which are characteristic of 1NAT: ring stretching (1553, 1503, and 1368 cm^{-1}), CH bending (1197 cm^{-1}), ring breathing (968 and 822 cm^{-1}), ring deformation (792, 664, 539, and 517 cm^{-1}), and CS stretching (389 cm^{-1}),[43] regardless of the laser line used and even using very low laser power at the sample (~1 μW). SERS mapping (Figure 2B) clearly shows that the SERS enhancing ability of the Ag-loaded gel is homogeneous through the entire surface, which reveals that this is an extremely clean and efficient substrate for SERS, allowing ultrasensitive detection in a wide spectral window of excitation wavelengths (from the green to the near-IR). The high intensity provided by these materials is related to the generation of a high density of hot spots when the gel collapses upon dehydration. The consequent volume reduction of the material (ca. 12-fold, as compared with its hydrated form) drives the embedded colloidal silver nanoparticles close to each other, thus promoting the interaction between their respective electromagnetic fields and therefore further increasing the enhanced Raman signal.

For demonstration of this concept of dynamic hot spots, SERS spectra of 1NAT in Ag-Agar were acquired using all available excitation laser lines, both before and after dehydration. Figure 3 shows the substantial increase of the signal in all cases, though in a more pronounced manner as the laser energy is decreased (toward the IR), ranging from barely 10-fold in the case of the green line (532 nm) to over 100 fold in the case of the NIR lines (785 and 830 nm). This observation can be easily explained considering that the electromagnetic coupling between two or more metallic nanoparticles has been consistently reported to red-shift the corresponding LSPR,[44] so that the overlap between LSPR

(43) Alvarez-Puebla, R. A.; Dos Santos, D. S., Jr.; Aroca, R. F. *Analyst* **2004**, *129*, 1251–1256.

(44) Jain, P. K.; Huang, W.; El-Sayed, M. A. *Nano Lett.* **2007**, *7*, 2080–2088.

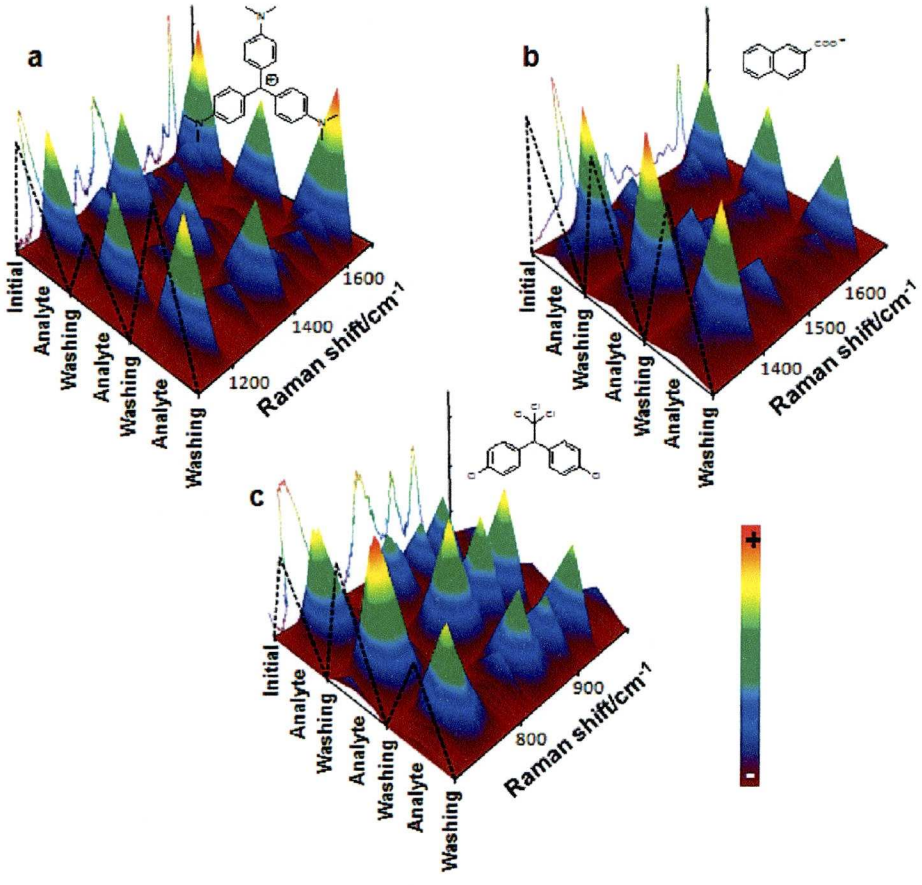

Figure 5. Reversible SERS behavior of Ag-Agar gel after immersing the polymer into solutions containing (a) crystal violet 10^{-6} M, (b) 2-naphthoic acid 10^{-5} M, and (c) DDT 10^{-5} M, after washing with 1% citrate aqueous solution, CV and NCOOH, and water-ethanol mixture (1:1), DDT.

and laser line is improved for longer wavelength excitations. This results in an increase of the enhancement of the SERS signal when excited using lower energy lasers, as predicted by the electromagnetic mechanism because of the better laser–plasmon overlap, in a fashion similar to that of surface-enhanced Raman excitation spectroscopy.[45–47]

The clear advantages of this new system, i.e., its superior optical enhancing properties together with the reversible dehydration and rehydration ability, for dynamic generation of optical hot spots and molecular trapping, were demonstrated through a series of experiments. The trapping efficiency of Ag-Agar was tested using a small and relevant contaminant, the organochlorine DDT. The SERS spectrum of this widespread pesticide has not been reported so far, because it cannot be adsorbed onto metallic surfaces in general, and on silver or gold in particular. Nevertheless, by immersing Ag-Agar gels in DDT aqueous solutions of various concentrations (10^{-4}–10^{-8} M) and subsequently collapsing the gel by dehydration, it has been possible to obtain a well resolved Raman-enhanced vibrational pattern of the target molecule (Figure 4). The spectrum was found to be fully reproducible and is characterized by the ring stretchings (1491, 1467, 1451, and 1428 cm^{-1}), aliphatic CC stretching (1297 cm^{-1}), CH bending (1091 cm^{-1}), ring breathing (1001 cm^{-1}), ring deformation (935 cm^{-1}), CH twisting (899 and 848 cm^{-1}), CH wagging (745 cm^{-1}), and CCl stretchings (685 and 554 cm^{-1}). Notably, the vibrational pattern of DDT could be unequivocally recognized, even for concentrations down to the micromolar regime. Although this may not seem an extremely high sensitivity, as compared with other analytical techniques,[48–50] it should be taken into account that SERS spectra can be acquired in very short times and with basically no need for prior sample treatment.

Finally, the reversibility of the Ag-Agar gels was studied for a variety of molecular probes. Figure 5 shows the results for a cation (crystal violet, CV), an anion (2-naphthoic acid, NCOOH), and a neutral molecular species, DDT. In all cases, the gel was first immersed in the solution containing the corresponding analyte, characterized by SERS, and immersed in a washing aqueous solution of 1 wt % sodium citrate, and the SERS spectra were measured again. This process was repeated three times to ensure the full reusability of this sensor platform.

Remarkably, for each of these different analytes, the characteristic vibrational patterns could be clearly identified when the analyte was present but were completely removed upon washing.

(45) Alvarez-Puebla, R. A.; Ross, D. J.; Nazri, G.-A.; Aroca, R. F. *Langmuir* **2005**, *21*, 10504–10508.
(46) Haynes, C. L.; Van Duyne, R. P. *J. Phys. Chem. B* **2003**, *107*, 7426–7433.
(47) McFarland, A. D.; Young, M. A.; Dieringer, J. A.; Van Duyne, R. P. *J. Phys. Chem. B* **2005**, *109*, 11279–11285.
(48) Graham, A. L.; Carlson, C. A.; Edmiston, P. L. *Anal. Chem.* **2002**, *74*, 458–467.
(49) Alvarez, M.; Calle, A.; Tamayo, J.; Lechuga, L. M.; Abad, A.; Montoya, A. *Biosens. Bioelectron.* **2003**, *18*, 649–653.
(50) Moreno Frias, M.; Garrido Frenich, A.; Martinez Vidal, J. L.; Mateu Sanchez, M.; Olea, F.; Olea, N. *J. Chromatogr. B: Anal. Technol. Biomed. Sci. Appl.* **2001**, *760*, 1–15.

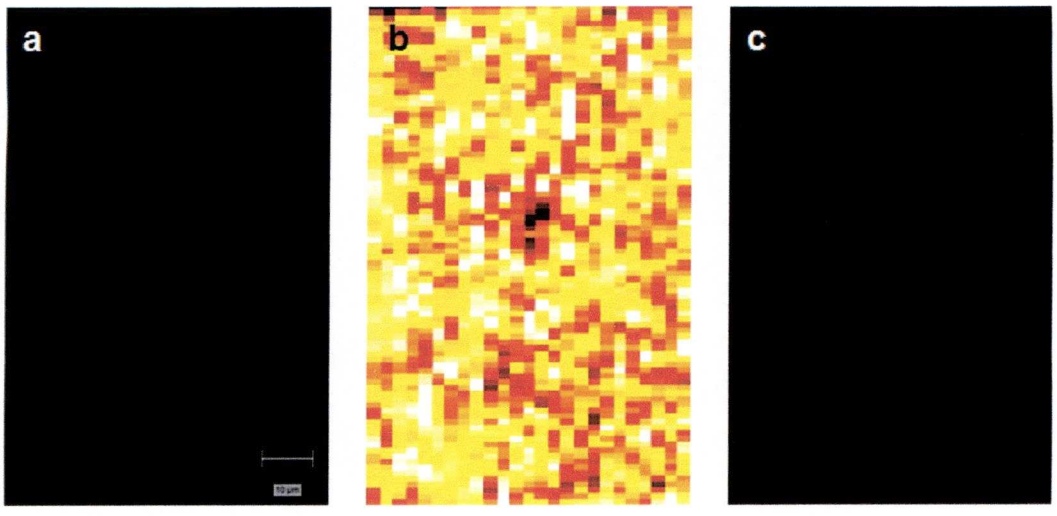

Figure 6. SERS maps of the Ag-Agar gel before (a) and after (b) CV addition, as well as after washing with 1% trisodium citrate in water (c).

To ensure that the effect is not an artifact due to the occasional measurement of hot spots, extended mapping was carried out on the blank polymer, after addition of the analyte and after washing (Figure 6). For charged species, it is very likely that sodium and citrate ions compete for the retention sites of the analyte on the nanoparticles, thus displacing it because of their much higher concentration and thereby cleaning the sensor. When the analyte was again in contact with the gel, it was retained, giving rise to signals of similar intensity. In the case of DDT, although the same washing process was followed, it was observed that the low affinity of this molecule toward metallic surfaces makes the citrate solution unnecessary, rendering the sensor ready for reutilization after simply washing with water. These results further demonstrate the trapping properties of the gel, together with its reversibility for a wide variety of substances with different chemical properties, within a material that is capable of generating dynamic hot spots with extremely high enhancing activity, which is comparable to that of aggregated silver colloids.

CONCLUSIONS

In summary, we devised a novel material that benefits from unique characteristics offering at the same time reversible sequestering properties and high SERS intensity, which allows for fast ultradetection of a wide range of molecular systems, while smoothing the way toward the generation of online sensors capable to monitor continuous flows in real time.

ACKNOWLEDGMENT

P.A.-P. and E.F. have contributed equally to the present work. R.A.A.-P. acknowledges the RyC (MEC, Spain) program. This work has been funded by the Spanish Ministerio de Ciencia e Innovación (Grants MAT2007-62696 and MAT2008-05755, Consolider Ingenio 2010-CSD2006-12) and the Xunta de Galicia (Grants PGIDIT06TMT31402PR, 08TMT008314PR). E.F. acknowledges financial support via an EPSRC quota Ph.D. studentship.

Received for review June 19, 2009. Accepted September 2, 2009.

AC901333P

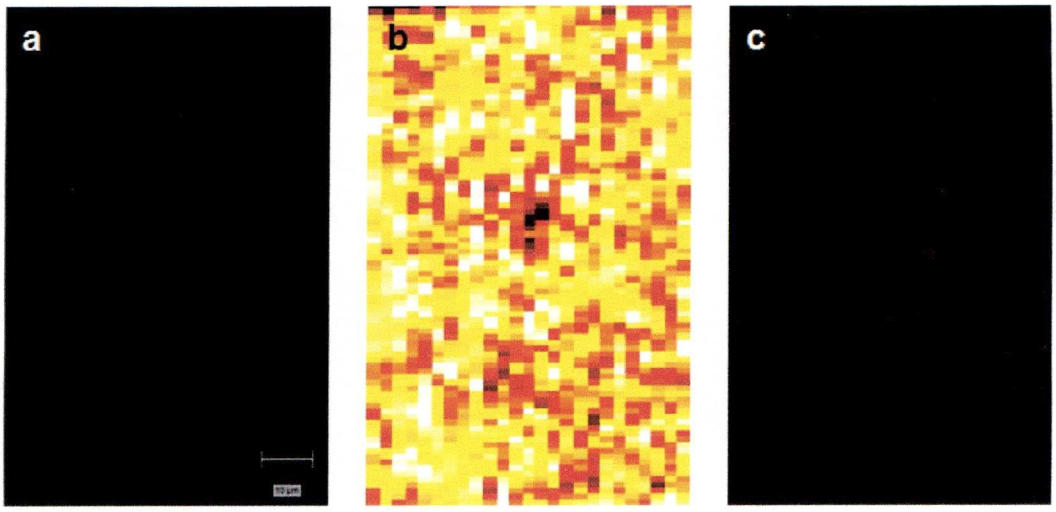

Figure 6. SERS maps of the Ag-Agar gel before (a) and after (b) CV addition, as well as after washing with 1% trisodium citrate in water (c).

To ensure that the effect is not an artifact due to the occasional measurement of hot spots, extended mapping was carried out on the blank polymer, after addition of the analyte and after washing (Figure 6). For charged species, it is very likely that sodium and citrate ions compete for the retention sites of the analyte on the nanoparticles, thus displacing it because of their much higher concentration and thereby cleaning the sensor. When the analyte was again in contact with the gel, it was retained, giving rise to signals of similar intensity. In the case of DDT, although the same washing process was followed, it was observed that the low affinity of this molecule toward metallic surfaces makes the citrate solution unnecessary, rendering the sensor ready for reutilization after simply washing with water. These results further demonstrate the trapping properties of the gel, together with its reversibility for a wide variety of substances with different chemical properties, within a material that is capable of generating dynamic hot spots with extremely high enhancing activity, which is comparable to that of aggregated silver colloids.

CONCLUSIONS

In summary, we devised a novel material that benefits from unique characteristics offering at the same time reversible sequestering properties and high SERS intensity, which allows for fast ultradetection of a wide range of molecular systems, while smoothing the way toward the generation of online sensors capable to monitor continuous flows in real time.

ACKNOWLEDGMENT

P.A.-P. and E.F. have contributed equally to the present work. R.A.A.-P. acknowledges the RyC (MEC, Spain) program. This work has been funded by the Spanish Ministerio de Ciencia e Innovación (Grants MAT2007-62696 and MAT2008-05755, Consolider Ingenio 2010-CSD2006-12) and the Xunta de Galicia (Grants PGIDIT06TMT31402PR, 08TMT008314PR). E.F. acknowledges financial support via an EPSRC quota Ph.D. studentship.

Received for review June 19, 2009. Accepted September 2, 2009.

AC901333P